

Multiscale Modelling of Structural Transformation in Metal Nanocatalysts for CO₂ Electroreduction

by

Feng Li

A thesis
presented to the University of Waterloo
in fulfillment of the
thesis requirement for the degree of
Doctor of Philosophy
in
Chemistry

Waterloo, Ontario, Canada, 2022

©Feng Li 2022

Examining Committee Membership

The following served on the Examining Committee for this thesis. The decision of the Examining Committee is by majority vote.

External Examiner	Dr. Byron Gates Professor Simon Fraser University, Burnaby, B.C., Canada
Internal Examiner	Dr. Michael Pope Associate Professor University of Waterloo, Waterloo, ON., Canada
Supervisor	Dr. Anna Klinkova Assistant Professor University of Waterloo, Waterloo, ON., Canada
Advisory Committee Member(s)	Dr. Pierre-Nicholas Roy Professor University of Waterloo, Waterloo, ON., Canada
	Dr. Rodney Smith Assistant Professor University of Waterloo, Waterloo, ON., Canada
	Dr. Leanne Chen Assistant Professor University of Guelph, Guelph, ON., Canada

Author's Declaration

This thesis consists of material all of which I authored or co-authored: see Statement of Contributions included in the thesis. This is a true copy of the thesis, including any required final revisions, as accepted by my examiners.

Statement of Contributions

This manuscript was written by Feng Li with critical comments and revisions by Dr. Anna Klinkova and corresponding collaborators. This thesis is based on key projects that have either published, submitted or are in preparation for peer-reviewed scientific journals. The contributions of all authors are provided in detail below.

(1) Cu(II)-nanoparticle-derived structures under CO₂ reduction conditions: a matter of shape

Authors: Amir Basiratnia, Jacob Rempel, Feng Li, Alexey Pogodaev, Thomas A. Zienchuk and Anna Klinkova

The contribution of Feng Li includes performing electrochemical experiments and product analysis. Amir Basiratnia and Jacob Rempel performed material synthesis and characterization. Alexey Pogodaev and Thomas A. Zienchuk developed the product analysis method and assisted with product analysis. Anna Klinkova designed the project and provided critical guidance on the experimental work and data interpretation and wrote the article.

(2) Interplay of electrochemical and electrical effects induces structural transformations in electrocatalysts

Authors: Feng Li, Xenia V. Medvedeva, Jury J. Medvedev, Evgeniia Khairullina, Helen Engelhardt, Skandan Chandrasekar, Yinzhou Guo, Jian Jin, Anna Lee, Héloïse Thérien-Aubin, Aftab Ahmed, Yuanjie Pang and Anna Klinkova

The contribution of Feng Li includes designing and carrying out the DFT calculations and the FEM simulations and assisting in manuscript writing. Xenia V. Medvedeva designed experiments and performed the nanoparticle synthesis, carried out the electrochemical experiments, conducted the SEM characterization and assisted in manuscript writing. Jury J. Medvedev performed electrochemical experiments and product analysis and conducted the literature survey summarized in Supplementary Tables 1–3. Evgeniia Khairullina performed the nanoparticle synthesis and the electrochemical experiments. Helen Engelhardt assisted with the nanoparticle synthesis and helped to organize the supplementary materials. Skandan Chandrasekar assisted with the FEM simulations. Jian Jin assisted with the Joule heating simulations. Aftab Ahmed assisted with running and analysing the FEM simulations. Yinzhou Guo assisted with the nanoparticle synthesis. Anna Lee assisted with data analysis. Héloïse

Thérien-Aubin, Aftab Ahmed and Yuanjie Pang contributed to data analysis and manuscript. Anna Klinkova conceived the idea, supervised the project and wrote the manuscript.

(3) Reaction-Intermediate-Induced Atomic Mobility in Heterogeneous Metal Catalysts for Electrochemical Reduction of CO₂

Authors: Feng Li, Ce Zhou, Eliana Feygin, Pierre-Nicholas Roy, Leanne D. Chen, Anna Klinkova

The contribution of Feng Li includes conceiving the idea, designing and carrying out all the DFT calculations and MD simulations, and writing the manuscript. Ce Zhou helped with the Python code for data processing, troubleshooting the NEB calculations and data interpretation. Eliana Feygin assisted in DFT calculations for metal alloys. Pierre-Nicholas Roy helped with Python code for MD simulation data processing and the calculations of MSD, RDF, Lindemann index, temperature and heat capacity. Leanne D. Chen and Anna Klinkova provided critical guidance and suggestions on data analysis, interpretation, and article writing.

(4) Simulating the E-field and current density for shape-specific nanoscale electrocatalysts under CO₂ reduction conditions.

Authors: Feng Li, Ce Zhou, Anna Klinkova.

The contribution of Feng Li includes designing the tutorial, carrying out the FEM simulations, and writing the manuscript. Ce Zhou assisted in FEM simulations and writing the manuscript, helped with equation derivation for PB, PNP, MPB and GMPNP models, and wrote the Python code for plotting the data. Anna Klinkova provided critical guidance and suggestions on data analysis, interpretation, and article writing.

Abstract

The precise control of nanostructure and surface atomic arrangement can be used to tune the electrocatalytic properties of materials and improve their performance. Unfortunately, the long-term structural stability of electrocatalysts with complex nanoscale morphology, a necessary requirement for industrial implementation, often remains elusive. This work explores structural changes in complex cathodic nanoscale electrocatalysts with and without oxidation state changes during CO₂ reduction reaction (CO₂RR) or hydrogen evolution reaction (HER). Based on the experimentally obtained structural and surface analyses, density functional theory (DFT) calculations and finite element method (FEM) simulations, I elucidate the mechanisms of the structural dynamics in electrocatalysts under bias, demonstrating that the reaction intermediates (RIs) of electrolysis reactions, the electrocatalyst material and the current density distribution are the crucial factors in influencing the structural transformations in electrocatalysts.

In chapter 3, I focus on the structural behaviour of hydroxide-derived copper during CO₂RR and well-defined gold and palladium core cages and branched nanoparticles in the course of CO₂RR and HER conditions using *ex situ* high-resolution scanning electron microscopy and electrochemical surface analysis *via* underpotential deposition of lead. First, the structural transformation with the oxidation state change were observed in Cu(II)-nanoparticle-derived copper electrodes when producing them by electrochemically reducing the precursor of Cu(OH)₂ under CO₂RR conditions, with the structural changes in this case directed by the interplay between facet stabilization by CO₂RR intermediates, electrochemical Ostwald ripening and field-induced reagent concentration effect. Moreover, the structural behavior of well-defined gold and palladium nanoparticles are explored under electrolysis reactions of CO₂RR and HER. The morphological changes were also observed in these well-defined nanoparticles without oxidation state change under both electrolysis conditions, with more pronounced morphological changes observed in specific localities of complex nanoscale electrocatalysts (e.g., narrow constrictions). More importantly, the structural changes of the studied nanoparticles are accelerated by the RIs of the electrolysis reactions, with the extent and rates of structural transformations depending on the material of the nanostructure and the nature of the environment and electrocatalytic reaction at its surface.

The experimental observations discussed in Chapter 3 revealed a significant influence of the surface reactions on the restructuring of nanoparticles, which motivated me to perform a DFT analysis of the RIs on the mobility of different metals. Thus, in chapter 4, I explore the parameters affecting the

mobility of the surface metal atoms using DFT and MD calculations. Specifically, I consider several electrocatalyst compositions of common interest in CO₂RR electrocatalyst design: Cu, Ag, Au, Pd, and Cu₃Pd, and the key RI associated with CO₂ reduction and accompanying reactions, i.e., HER and oxygen reduction reaction: *COOH, *H, and *OOH. Using DFT calculations, I demonstrate that that RIs may promote the thermodynamic process of vacancy formation (VF) and accelerate the migration kinetics of the adatom on crystallographic facets of Au and Pd. In addition to the thermodynamic VF assessment, I also expand the atomic mobility assessment method to enable the evaluation of both thermodynamics and kinetics of VF via DFT and to probe the stability of a complex surface structure (compared to low-index facets) mimicking nanostructured catalysts using *ab initio* molecular dynamic (AIMD) simulations. Based on the atomic mobility assessment for a series of metal and metal-alloy CO₂RR catalysts, this chapter provides a more comprehensive description of atomic mobility induced by RIs during CO₂RR electrolysis.

The DFT calculations performed in Chapter 4 demonstrated the influence of the RIs and material on the atomic mobility in electrocatalysts, however, which cannot explain the locality of the structural changes in the morphologically complex nanoparticles observed in Chapter 3. To understand the origins of the locality and directionality of atomic mobility in nanocatalysts, I decide to investigate the electrochemical physics effects of the studied nanostructures. Therefore, in chapter 5, I summarize the current status and recent advances in the theoretical models used for the electric field (E-field), reaction current density ($J_{electrolyte}$), electrode current density ($J_{electrode}$) simulations using FEM, propose the protocols for reliable simulations of these electrochemical effects, and study the electrochemical performances various nanostructured electrodes with complex morphologies. In section 2 of this chapter, I discuss the setup of the FEM simulation domains and the interfaces of Comsol Multiphysics required for the simulations performed in this chapter. In section 3, I introduce the fundamentals relevant to the essential electrochemical phenomena at the electrode-electrolyte interface, the classical theories for modelling these electrochemical effects, and the advanced modifications to these classical theories to account for the steric effect of the solution species and field-dependent dielectric function of the electrolyte. In section 4-6, I describe a protocol for simulating the E-field, $J_{electrolyte}$ and $J_{electrode}$ under different electrolysis conditions. In section 7, I demonstrate simulations on the specific electrode models with complex shapes that represent nanoparticle-based electrodes. In section 8, I compare the electrochemical performances, especially the current density, of various nanostructured electrodes including anchored nanostar, nanostar, core-cages and frames. In section 9, I discuss the application scope of the models involved in this work as well as their limitations. This chapter provides

a useful departure point for electrocatalysis researchers to begin implementing FEM in their work and will facilitate a wider adoption of computational studies and rational design of nanoscale effects in electrocatalysts to further improve the performance of the electrocatalysts for CO₂RR and other clean energy conversion reactions.

In summary, using a series of complex nanostructured electrodes, this thesis demonstrates that RIs of electrolysis reactions, the nature of the electrocatalyst material and the current density distribution are the important factors determining the extent of and trends in structural transformation of electrocatalysts under electrolysis conditions. Furthermore, the mechanistic descriptions of the impact of the factors mentioned above on the structural transformation are revealed using DFT and FEM simulations. Moreover, this thesis establishes a general framework for evaluating the structural transformations in cathodic metal nanocatalysts and explain specific qualitative trends. In chapter 6, I provide an outlook for future work on both improving the predictive power of the framework and expanding the scope of nanoscale electrocatalysts and reactions it is applied to. In conjunction with catalyst design rules, this mechanistic framework will facilitate the development of nanostructured electrocatalysts with sufficient stability for sustainable applications.

Acknowledgements

I would like to thank my supervisor Prof. Anna Klinkova for offering the chance to work and study in her group as well as her guidance, support, and patience throughout my Ph.D. program. She gave me the opportunity to explore electrochemical experiments, material characterization techniques, and theoretical studies, which made me have a more comprehensive understanding of scientific issues from both an experimental and theoretical perspective. In addition, she was very patient in teaching me how to prepare for a presentation and organize and write a paper, which helped me become better in presenting and writing.

I would like to thank my committee member Prof. Leanne D. Chen, Prof. Rodney Smith, and Prof. Pierre-Nicholas Roy for their guidance, advice, and productive conversations during my Ph.D. program.

I would like to thank Dr. Jury Medvedev for helping me troubleshoot experimental problems and interpret experimental data. I would like to thank Dr. Ana Sousa-Castillo for training me how to use the experimental equipment when I just entered Klinkova group. I would like to thank Xenia Medvedeva for her help in material synthesis and imaging. I would like to thank Stephen W. Tatarchuk for helping with my Python coding and Finite element method simulation. I would like to thank Thomas A. Zienchuk for his help in my Ph. D program. In addition, I would like to thank any unmentioned current and past members of the Klinkova lab for maintaining a wonderful environment for study and work in the lab.

I would like to thank Prof. Linda Nazar at the University of Waterloo for providing access to X-ray diffraction instrumentation and the license for Vienna Abinitio simulation package. I would like to thank Prof. Holger Kleinke at University of Waterloo for providing access to X-ray diffraction instrumentation. I would like to thank Prof. Marcel Nooijen for teaching me the quantum theories associated with theoretical studies that appear in this thesis. I would like to thank Prof. Aftab Ahmed at California State University Long Beach for helping me troubleshooting the problems with Finite Element Method simulation and Finite-Difference Time-Domain simulations. I would like to thank Prof. Yuanjie Pang at Huazhong University for training me how to perform Finite Element Method simulation.

I would like to thank my wife and my son. They are the biggest motivation for me to move on. In particular, I would like to give a huge thanks to my wife. She has been taking care of my son and family

when I am busy with my study and work. I would also like to thank my parents for their support and encouragement throughout my Ph.D. program.

Table of Contents

Examining Committee Membership.....	ii
Author's Declaration.....	iii
Statement of Contributions.....	iv
Abstract	vi
Acknowledgements	ix
List of Figures	xiv
List of Tables.....	xxxii
List of Abbreviations.....	xxxii
Chapter 1 Introduction.....	1
1.1 Significance of the cathodic electrosynthetic methods.....	1
1.2 Outstanding activity and selectivity of nanostructured electrocatalysts with complex shape	3
1.3 Poor structural stability of complex nanostructured electrocatalysts	5
1.4 Application of DFT calculations in designing advanced electrocatalysts	6
1.5 Application of FEM simulations in designing advanced electrocatalysts	9
1.6 Scope of this thesis	11
Chapter 2 Materials and methods	12
2.1 Materials.....	12
2.2 Methods	13
2.2.1 Experimental methods	13
2.2.2 DFT Calculations.....	18
2.2.3 MD simulations	20
2.2.4 FEM simulations	25
Chapter 3 Experimental observations of structural dynamics in various nanostructured catalysts.....	32
3.1 Introduction	32
3.2 Structural changes in Cu(II) nanoparticle-derived structures during CO ₂ RR	39
3.3 Structural changes in Au CCs and BNPs during CO ₂ RR.....	47
3.4 Effect of cathodic reactions on the structural changes in Au CCs	55
3.5 Effect of materials on the structural changes in CCs and BNP during CO ₂ RR.....	57
3.6 Summary	59
Chapter 4 Atomic- and molecular-scale mechanistic description of structural changes in CO ₂ RR electrocatalysts	60

4.1 Introduction.....	60
4.2 Application of DFT calculations in studying atomic mobility of metal surfaces	62
4.3 Application of AIMD simulations in studying the atomic mobility	64
4.4 Comparison of the atomic mobility on Au and Pd facets during HER and CO ₂ RR electrolysis	66
4.5 Comparison of the atomic mobility on Cu, Ag, Au, and Pd facets during HER, ORR and CO ₂ RR electrolysis	71
4.6 Comparison of the atomic mobility on Cu, Cu ₃ Pd and Pd facets during HER, ORR and CO ₂ RR electrolysis	89
4.7 Summary	91
Chapter 5 Continuum level mechanistic description of structural changes in CO ₂ RR electrocatalysts: Electrochemical physics.....	92
5.1 Introduction.....	92
5.2 Multiphysics simulations and electrode model	99
5.3 Fundamentals of the electrode-electrolyte system	102
5.3.1 Theories and models for EDL simulations.....	102
5.3.2 Theories and models for Jelectrolyte simulations	106
5.3.3 Theories and models for Jelectrode simulations	109
5.4 FEM simulations of E-field behavior.....	111
5.4.1 Potential reference for E-field simulation: point of zero charge	111
5.4.2 Effect of the EDL and relative permittivity of the electrolyte on computed E-field profile	112
5.4.3 Impact of the electrolyte nature and concentration on computed E-field profile.....	114
5.4.4 Comparison of the PNP, GMPNP, and MPB models in E-field simulation	115
5.5 FEM simulations of Jelectrolyte behavior	119
5.5.1 Comparison of various Jelectrolyte modelling approaches	119
5.5.2 Comparison of various electrode kinetic models in Jelectrolyte simulations	122
5.5.3 Other essential factors in Jelectrolyte simulations	125
5.6 FEM simulations of Jelectrode behavior	127
5.7 Electrochemical simulations for 3D model.....	130
5.8 Electrochemical performance of various nanostructured electrodes.....	133
5.9 Applicability and limitations of the discussed models.....	140
5.9.1 Potential and E-field simulations	140
5.9.2 Jelectrolyte simulations.....	141

5.9.3 Jelectrode simulations	143
5.9.4 Other considerations	143
5.10 Summary	146
Chapter 6 Conclusions and future work	148
Letters of Copyright Permission.....	150
Bibliography	213
Appendices	226
Appendix A: Optimized geometry structures	226
A.1 Optimized geometry structures for initial, transition and final states of metal atom migration	226
A.2 Optimized geometry structures for reaction-intermediate-adsorbed metal surfaces	231
A.3 Optimized geometry structures for metal surfaces with single atom vacancy.....	233
Appendix B: Calculated energy barriers	235
Appendix C: Calculated MSD, RDF, and Lindemann index	239
Appendix D: Derivation of PB, PNP, MPB and GMPNP models	254

List of Figures

Figure 1.1: Schematic showing sustainable electrochemical synthesis of renewable value-added products such as hydrocarbons, oxygenates, and ammonia. ¹ Reprinted from ref. [1]. Copyright 2017, with the permission from American Association for the Advancement of Science.	1
Figure 1.2: Various single- and multi-carbon gas and liquid products that can be produced in CO ₂ RR electrocatalysis. ³ Reprinted from ref. [3]. Copyright 2019, with the permission from Springer Nature.	2
Figure 1.3: Motifs on a metal electrode surface that may influence C—C bond formation in CO ₂ RR. Reprinted from ref. [11]. Copyright 2019, with the permission from Springer Nature.	3
Figure 1.4: Various electrochemical physics effects on nanoscale. (a) Field induced reagent concentration effect by concentrating the cations at the vicinity of a high-curvature feature. Reprinted from ref. [13]. Copyright 2016, with the permission from Springer Nature. (b) Cavity confinement effect that promotes C ₂ species binding and further conversion to C ₃ . C ₂ and C ₃ concentrations are shown in colour scale in millimoles and flux distributions are shown in arrows. Reprinted from ref. [14]. Copyright 2018, with the permission from Springer Nature.	4
Figure 1.5: Structural transformations observed in shape-specific nanostructured electrocatalysts with and without oxidation state change. (a) SEM images and schematic of the key structure features during the growth process of the electrochemically reduced Cu nanostructures at their specific applied potentials. Reprinted from ref. [51]. Copyright 2017, with the permission from The American Chemical Society (b) Schematic illustrating the transformation process of Cu NP ensembles to an active catalyst for C ₂ –C ₃ product formation. Reprinted from ref. [55]. Copyright 2017, with the permission from National Academy of Science of the United States of America. (c) Tomographic reconstruction of the CuNCs and corresponding schematic morphological models at different stages under CO ₂ RR electrolysis conditions. Reprinted from ref. [63]. Copyright 2018, with the permission from Springer Nature.	7
Figure 3.1: SEM (a) and TEM (b) images of Cu(OH) ₂ nanocages (Cu(II)-NCs). Reprinted with permission from ref. [111]. Copyright 2019, Royal Society of Chemistry.	39
Figure 3.2: Copper precursor: Cu(II)-NCs. Inset shows a 3D cartoon representation of the Cu(II)-NCs with core (x) and arms (y) size parameters. (a, b and d) SEM images and (c) TEM image of Cu(II)-NCs. Scale bars in (c and d) are 200 nm. Reprinted with permission from ref. [111]. Copyright 2019, Royal Society of Chemistry.	39

Figure 3.3: Characterization of the initial and electroreduced Cu(II)-NCs. (a) CV plot corresponding to the reduction of Cu(II)-NCs dispersed in CO₂-saturated 0.5 M KHCO₃ electrolyte at 20mV s⁻¹ scan rate. (b) Representative XRD plot of Cu(II)-NCs-derived Cu (black and red lines show standard XRD patterns for Cu₂O and Cu, respectively) (c) Cu₂p_{3/2} and (d) CuLMM representative XPS plots of the original Cu(II)-NCs (gray line) and electroreduced material (red). Reprinted with permission from ref. [111]. Copyright 2019, Royal Society of Chemistry. 40

Figure 3.4: SEM images of Cu nanostructures observed on the surface of carbon paper working electrode at different densities of precursor Cu(II)-NCs in CO₂-saturated 0.5M KHCO₃ electrolyte. (a) after 4 CV cycles at 20 mV/s in the electrolyte containing Cu(II)-NCs at [Cu]=0.001 M. (b) after 20 CV cycles at 20 mV/s in the electrolyte containing Cu(II)-NCs at [Cu]=0.001 M. (c) after 20 CV cycles at 20 mV/s with Cu(II)-NCs directly spin-coated on the working electrode (20 μL, [Cu]=0.085 M, 3000 rpm). (d,e) after 20 CV cycles at 20 mV/s in the electrolyte containing Cu(II)-NCs at [Cu]=0.02M. (f) after 20 CV cycles at 20 mV/s with Cu(II)-NCs directly spin-coated on the gas diffusion working electrode (Sigracet purchased from Fuel Cell Store) containing carbon black and PTFE particles (200 μL, [Cu]=0.085 M, 3000 rpm). Reprinted with permission from ref. [111]. Copyright 2019, Royal Society of Chemistry. 41

Figure 3.5: Pourbaix diagrams of Cu phases at 0.001 M (a) and 0.0001 M (b) copper concentration in bicarbonate aqueous solution. Obtained using “Pourbaix diagram” app by Materials Project.¹¹² Reprinted with permission from ref. [111]. Copyright 2019, Royal Society of Chemistry. 42

Figure 3.6: SEM analysis of structures obtained in electroreduction of Cu(II)-NCs and schematics of their formation processes. (a) Minimum [Cu(II)-NC]: single particle reduction to individual Cu NCs. (b) Low [Cu(II)-NC]: Cu cube-containing clump formation due to Cu(II)-NC diffusion spheres overlap (shown in blue) (c) intermediate [Cu(II)-NC]: Cu structure extrusion due to the FIRC effect (E-field enhancement shown at structure extrusions in red). Smoothing the surface due to electrochemical Ostwald ripening is shown in magenta. (d) High [Cu(II)-NCs]: Cu MUs obtained at full coverage of the working electrode substrate surface. (e) Phase-like diagram of the structures obtained at different [Cu] and number of CV cycles. Shaded areas correspond to the dominance of facet stabilization (orange) and FIRC effect (blue) as driving force determining the structure shape. Reprinted with permission from ref. [111]. Copyright 2019, Royal Society of Chemistry. 43

Figure 3.7: SEM images of Cu nanocubes observed on the surface of carbon paper working electrode after 4 CV cycles at 20 mV/s in CO₂-saturated 0.5M KHCO₃ electrolyte containing Cu(II)-NCs ([Cu]=0.0001 M). Reprinted with permission from ref. [111]. Copyright 2019, Royal Society of Chemistry. 44

Figure 3.8: The relative Gibbs free energy of COOH* and OCHO* on Cu(111) and Cu(100) surfaces.	44
Figure 3.9: SEM images of Cu nanostructures observed on the surface of carbon paper working electrode at different densities of precursor Cu(II)-NCs in Ar-saturated 0.5M KHCO ₃ electrolyte containing Cu(II)-NCs at [Cu]=0.0001 M (a) and [Cu]=0.001 M (b). Reprinted with permission from ref. [111]. Copyright 2019, Royal Society of Chemistry.	45
Figure 3.10: Electrochemical performance and stability of Au CCs and BNPs. a-c, CO ₂ reduction activity of Au BNPs (a,b) and Au CCs (c) over time during potentiostatic electrolysis at -0.6 V (a,c) and -1.2 V (b) vs RHE in CO ₂ saturated 0.5 M KHCO ₃ . d-g, Cyclic voltammograms of Au BNPs (d,e) and Au CCs (f,g) before and after 5 hours of potentiostatic electrolysis at -0.6 V vs RHE in CO ₂ saturated (d,f) or Ar saturated 0.5 M KHCO ₃ (e,g). Current densities correspond to currents normalized by the geometric area of the electrode. For surface roughness analysis of these electrodes see Table 3.4. Reprinted with permission from ref. [71]. Copyright 2021, Springer Nature.	47
Figure 3.11: Structural changes in gold nanoparticles during CO ₂ RR. a-h, SEM images of gold BNPs before (a-c) and after (d-h) 300 min of electrolysis in CO ₂ -saturated 0.5 M KHCO ₃ at -0.6 V versus RHE, with d and f-h showing magnified areas of the electrode with sintering of the BNPs with each other (d,f) and with the substrate (g,h). Scale bars, 100 nm. i-l,o,p, SEM images of gold CCs before (i,o) and after 60 min (j), 120 min (k,p) and 300 min (l) of electrolysis in CO ₂ saturated 0.5 M KHCO ₃ at -0.6 V versus RHE. Panels i-l and panels o and p show the behaviour of a close-packed array of CCs and sparsely distributed CCs, respectively. Scale bars, 100 nm. m,n, Lead UPD before (purple traces) and after 120 min (orange traces) of electrolysis using gold BNPs (m) and gold CCs (n). Black dashed traces correspond to lead UPD on the substrate gold foil without deposited particles. Reprinted with permission from ref. [71]. Copyright 2021, Springer Nature.	49
Figure 3.12: Illustration of Au BNPs sintering. SEM images of standard Au BNPs sintering in a pile (a), sintering of tips (b), and sintering of a tip with Au substrate (c); and of small Au BNPs sintering of tips (d), and sintering in a pile (e) after 300 min of CO ₂ RR reaction at -0.6V vs RHE. Reprinted with permission from ref. [71]. Copyright 2021, Springer Nature.	50
Figure 3.13: CO ₂ reduction activity of small Au BNPs over time during potentiostatic electrolysis at -0.6V vs RHE in CO ₂ -saturated 0.5M KHCO ₃ : changes in total current density (left axis) and Faradaic efficiencies (right axis) of CO (solid circles) and H ₂ (empty circles) are shown as a function of time. Reprinted with permission from ref. [71]. Copyright 2021, Springer Nature.	50

Figure 3.14: SEM images of small branched Au nanoparticle before (a,d), after 120 min (b,e), and after 300 min (c,f) of CO ₂ RR reaction at -0.6V vs RHE at different magnifications. Reprinted with permission from ref. [71]. Copyright 2021, Springer Nature.	51
Figure 3.15: Structural evolution of branched Au nanoparticles. SEM images of branched Au nanoparticles before (a,d) and after 300 min of CO ₂ RR reaction at -0.6V (b,e) and -1.2V (c,f) vs RHE at different magnifications. Reprinted with permission from ref. [71]. Copyright 2021, Springer Nature.	52
Figure 3.16: SEM images of Au-Au CCs before (a), after 120 min (b), and 300 min (c) of HER at -0.6V vs RHE, and after 60 min (d), 120 min (e), and 300 min (f) of CO ₂ RR reaction at -0.6V vs RHE. Reprinted with permission from ref. [71]. Copyright 2021, Springer Nature.	53
Figure 3.17: (a,b) SEM images of Au CCs after 30 min (a) and 60 min (b) of CO ₂ RR at -1.2V vs RHE. (c) Disfigurement of Au CCs observed after potential overload error when running electrolysis at -0.6V vs RHE for 30 min. Reprinted with permission from ref. [71]. Copyright 2021, Springer Nature.	53
Figure 3.18: (a,b) SEM images of Au CCs after 60 min of electrolysis under CO ₂ RR conditions in CO ₂ -saturated 0.5M KHCO ₃ at -0.6V vs RHE. The loading of CCs in these experiments is twice lower than in the standard fully covered electrode samples. Reprinted with permission from ref. [71]. Copyright 2021, Springer Nature.	54
Figure 3.19: Effect of electrochemical reaction and catalyst material on the structural stability of CCs. a–c, SEM images of gold CCs before (b) and after (a,c) 120 min of electrolysis at -0.6 V versus RHE: effect of HER (a) and CO ₂ RR (c). (d,e) SEM images of palladium CCs before (d) and after (e) 300 min under CO ₂ RR conditions at -1.2 V versus RHE. Scale bars in a–e, 100 nm. f,g, Evolution of electrocatalytic activity of gold and palladium CCs over five hours of potentiostatic electrolysis: gold CCs (f) under CO ₂ RR conditions (blue traces) and under HER reaction conditions (orange traces) at -0.6 V versus RHE, and palladium CCs (g) under CO ₂ RR conditions. Solid lines, current evolution over time; filled circles, FE(CO); open circles, FE(H ₂). CO ₂ RR and HER reaction conditions correspond to CO ₂ and argon-saturated 0.5 M KHCO ₃ , respectively. Reprinted with permission from ref. [71]. Copyright 2021, Springer Nature.	55
Figure 3.20: Structural stability of Pd CCs under CO ₂ reduction conditions. a-d, SEM images areas of Pd CCs before (a,c) and after (b,d) 300 min of CO ₂ RR reaction at -1.2 V vs RHE at different magnifications. e-h, SEM images of Pd CCs with a more open wall morphology before (e,g) and after (f,h) 300 min of CO ₂ RR reaction at -1.2 V vs RHE at different magnifications. Reprinted with permission from ref. [71]. Copyright 2021, Springer Nature.	57

Figure 3.21: Structural stability of BNPs under CO₂ reduction conditions. a-f, SEM images of Pd BNPs before (a,d), after 120 min (b,e), and after 300 min (c,f) of CO₂RR reaction at -1.2 V vs RHE at different magnifications. Reprinted with permission from ref. [71]. Copyright 2021, Springer Nature. 58

Figure 4.1: Adsorbed reaction intermediate facilitation of atomic mobility on different crystallographic facets. a, Atomic migration energy barrier and atomic vacancy formation energy calculated for different crystallographic facets of gold with and without surface-bound intermediates *COOH or *H and of palladium with and without surface-bound intermediate *COOH. The arrow shows the general trend of decreasing atomic mobility. The cartoons on the left illustrate the migration of a single metal adatom with bound reaction intermediates (*H, above; *COOH, below) to an adjacent surface site, and the cartoon scheme along the bottom illustrates the vacancy formation events for which the energies were calculated. IS, initial state; TS, transition state; FS, final state. b, Calculated binding energy of *COOH and *H intermediates to different crystallographic facets of gold. c, Calculated binding energy of *COOH intermediate to different crystallographic facets of palladium. d,e, Charge distribution for Au(100)-H (d) and for Au(100)-COOH (e); yellow and blue colors represent the charge accumulation and depletion, respectively, with an iso-surface value of 0.001 e Å⁻³ implemented. Reprinted with permission from ref. [71]. Copyright 2021, Springer Nature. 67

Figure 4.2: Charge distribution profiles for different Ay facets with surface-bound intermediates *COOH or *H. a-c, Side view of Au(111), Au(110) and Au(211). d-g, Top view of Au(111), Au(100), Au(110) and Au(211). Yellow and blue colors represent the charge accumulation and depletion, with an iso-surface value of 0.001 e/Å³ implemented.. Reprinted with permission from ref. [71]. Copyright 2021, Springer Nature. 68

Figure 4.3: Au atom mobility differentiation based on reaction intermediates present in the media. (a-d) the hooping paths studied for surface atom migration on Au(111), Au(100), Au(110) and Au(211) surfaces, with the olive colour atoms representing the Au surface and orange colour atoms representing the hooping Au atom and intermediate-bound Au atoms (Au-COOH and Au-H). (e-h) calculated energy barriers for migration path of Au atom, Au-COOH (CO₂RR) and Au-H (HER) intermediate-bound Au atoms on Au(111), Au(100), Au(110) and Au(211) surfaces, respectively. Reprinted with permission from ref. [71]. Copyright 2021, Springer Nature. 69

Figure 4.4: Calculated energy barriers for migration path of Pd atom and Pd-COOH (CO₂RR) intermediate-bound Au atom, with (a-d) for Pd(111), Pd(100), Pd(110) and Pd(211) surfaces, respectively. The paths studied for Pd are the same as that for Au. Reprinted with permission from ref. [71]. Copyright 2021, Springer Nature. 70

Figure 4.5: The interaction of different intermediates with various metal surfaces. (a) the optimized geometries of adsorbed *H, *OOH and *COOH on Cu surfaces of (111), (100), (110) and (211), and (b) the binding energies of *H, *OOH and *COOH on (111), (100), (110) and (211) surfaces of Cu, Ag, Au and Pd. White, H atom; red, O atom; gray, C atom; dark/light blue, Cu atom in outmost/inner layer. Reprinted with permission from ref. [132]. Copyright 2022, Royal Society of Chemistry. 72

Figure 4.6: The influence of the reaction intermediates and metal materials on vacancy formation energy. The (111), (100), (110), and (211) surfaces of Cu, Ag, Au, and Pd were studied with and without adsorbed RIs. Reprinted with permission from ref. [132]. Copyright 2022, Royal Society of Chemistry. 73

Figure 4.7: Comparison of the adsorption structures for *OOH and *COOH on Cu(111), Ag(111), Au(111), and Pd(111) without vacancy. Reprinted with permission from ref. [132]. Copyright 2022, Royal Society of Chemistry..... 74

Figure 4.8: Comparison of the adsorption structures for *OOH and *COOH on Cu(111), Ag(111), Au(111), and Pd(111) with single-atom vacancy. Reprinted with permission from ref. [132]. Copyright 2022, Royal Society of Chemistry..... 75

Figure 4.9: The influence of the RIs and metal nature on the one-atom and the two-atom VF mechanisms: the schematic of the two VF mechanisms (a) and the associated energy barriers (b) on (111), (100), (110), and (211) surfaces of studied metals with and without adsorbed RIs. Reprinted with permission from ref. [132]. Copyright 2022, Royal Society of Chemistry. 76

Figure 4.10: Comparison of the kinetic barriers for the two VF mechanisms on (111), (100), (110), and (211) surfaces of Cu, Ag, Au, and Pd. Reprinted with permission from ref. [132]. Copyright 2022, Royal Society of Chemistry..... 77

Figure 4.11: The comparison of atomic mobility on metal surfaces under different reaction conditions. (a) The migration pathway of a metal adatom on Cu(111) surface without and with different adsorbed RIs (*H, *OOH, and *COOH). (b) The energy barriers of surface adatom migration on (111), (100), (110), and (211) surfaces of studied metals with and without adsorbed RIs. White, H atom; red, O atom; gray, C atom; dark blue, Cu atom. Reprinted with permission from ref. [132]. Copyright 2022, Royal Society of Chemistry. 78

Figure 4.12: Optimized geometry structures for initial, transition, and final states of migration for Cu atom and intermediate-bound Cu atoms of Cu*H (HER), Cu*OOH (ORR), and Cu*COOH (CO₂RR) on the Cu(100) surface. Reprinted with permission from ref. [132]. Copyright 2022, Royal Society of Chemistry. 79

Figure 4.13: Optimized geometry structures for initial, transition and final states of migration for Cu atom and intermediate-bound Cu atoms of Cu*H (HER), Cu*OOH (ORR), and Cu*COOH (CO₂RR) on the Cu(110) surface. Reprinted with permission from ref. [132]. Copyright 2022, Royal Society of Chemistry. Reprinted with permission from ref. [132]. Copyright 2022, Royal Society of Chemistry. 79

Figure 4.14: Optimized geometry structures for initial, transition and final states of migration for Cu atom and intermediate-bound Cu atoms of Cu*H (HER), Cu*OOH (ORR), and Cu*COOH (CO₂RR) on the Cu(211) surface. Reprinted with permission from ref. [132]. Copyright 2022, Royal Society of Chemistry..... 80

Figure 4.15: Average values of adatom migration energy barriers on studied four metal surfaces for Cu, Ag, Au, and Pd without and with different adsorbed RIs (*H, *OOH, and *COOH). Reprinted with permission from ref. [132]. Copyright 2022, Royal Society of Chemistry..... 81

Figure 4.16: AIMD simulations of the metal cluster supported on extended metal surfaces. (a) Snapshots during the trajectories of AIMD for Cu cluster and H-, OOH- and COOH-bound Cu cluster on the Cu (111) surface. (b) The change of the averaged displacements of atoms in Cu, Ag, Au, and Pd clusters with and without bound RIs with time. White, H atom; red, O atom; black, C atom; dark blue, Cu atom. Reprinted with permission from ref. [132]. Copyright 2022, Royal Society of Chemistry. 83

Figure 4.17: Snapshots during the trajectories of AIMD for Ag, Au, Pd clusters with and without adsorbed reaction intermediates of *H, *OOH, and *COOH. Reprinted with permission from ref. [132]. Copyright 2022, Royal Society of Chemistry. 84

Figure 4.18: The change of the center of mass (COM) for Cu, Ag, Au, and Pd clusters with and without bound RIs with time. Reprinted with permission from ref. [132]. Copyright 2022, Royal Society of Chemistry..... 85

Figure 4.19: The temperature change of metal cluster and slab as a function of simulation time. Reprinted with permission from ref. [132]. Copyright 2022, Royal Society of Chemistry..... 86

Figure 4.20: The heat capacities of Cu, Ag, Au, and Pd cluster systems. Reprinted with permission from ref. [132]. Copyright 2022, Royal Society of Chemistry. 87

Figure 4.21: The influence of reaction intermediates on the energy barrier of VF processes and adatom migration on the (100) surface of Cu₃Pd alloy. The schematic and energy barriers for the VF via the one-atom mechanism (a) and via the two-atom mechanism (b), and the adatom migration on Cu₃Pd (100) surface with and without RIs (c). For the comparison purpose, the corresponding energy data on Cu(100) and Pd(100) surface are also included. Dark blue, Cu atom; dark cyan, Pd atom. Reprinted with permission from ref. [132]. Copyright 2022, Royal Society of Chemistry..... 89

Figure 4.22: The comparison of the lowest energy barriers of VF process and atom migration on Cu(100) and Cu₃Pd(100) surface. Reprinted with permission from ref. [132]. Copyright 2022, Royal Society of Chemistry. 90

Figure 5.1: Computed distribution of E-field distribution near the surface of various nanostructured electrodes. (a) Au nanoneedle with tip radii of 5 nm, 10 nm, and 15 nm.⁴² (b,c) Bismuth nanoflakes with sharp coner and edge: (b) three-dimensional and (c) two dimensional.⁴⁴ (d) CdS nanoparticle, rod, and needles.⁷² (e,f) CuO nano-prism with different (e) corner angle and edge length and (f) applied potential.⁴¹ (g) nanostructured Au-Bi₂O₃ fractals.⁷³ (h) Ni foams with different ridges and groove.⁷⁴ (i) MoS₂ nanoflower sheets without and with intercalated graphene sheets.⁴³ Reprinted from the data of the cited papers by the permission from The American Chemical Society, Elsevier, John Wiley and Sons, Royal Society of Chemistry, The Chinese Academy of Sciences. 94

Figure 5.2: Computed distribution of current density near the surface of various nanostructured electrodes. (a) Au needle, Au rod and Au hemispherical particle.¹³ (b) Fluorine doped carbon electrodes including fluorine-doped cagelike porous carbon (F-CPC) and fluorine-doped carbon sphere (F-CS).⁷⁵ (c,d) Indium electrodes including (c) an In porous foam and (d) In tip, rod and dendrite.⁴⁵ Reprinted from the data of the cited papers by the permission from Springer Nature, The American Chemical Society, and John Wiley and Sons. 95

Figure 5.3: Computed distribution of K⁺ density distribution on the surface of various nanostructured electrodes. (a) CdS needles with different gaps.⁷² (b) Au needle.¹³ (c) Fluorine doped carbon electrodes including fluorine-doped cagelike porous carbon (F-CPC) and fluorine-doped carbon sphere (F-CS).⁷⁵ (d) Cu@Sn electrodes including Cu@Sn nanocone and bulk Sn.⁴⁰ (e) Cu dendrites (Cu-D) and Cu particles (Cu-P).⁷⁶ Reprinted from the data of the cited papers by the permission from John Wiley and Sons, Springer Nature, The American Chemical Society, and Royal Society of Chemistry. 96

Figure 5.4: Computed distribution of electron density on the surface of various nanostructured electrodes. (a) CuPd electrodes including 7-nm CuPd tetrapods, 50-nm CuPd tetrapod, and CuPd nanoparticle.³⁹ (b) Au electrodes including Au needles, Au rods and Au particle.¹³ (c) Fluorine doped carbon electrodes including fluorine-doped cagelike porous carbon (F-CPC) and fluorine-doped carbon sphere (F-CS).⁷⁵ (d) Cu@Sn electrodes including Cu@Sn nanocone and bulk Sn.⁴⁰ Reprinted from the data of the cited papers by the permission from John Wiley and Sons, Springer Nature, The American Chemical Society, and Royal Society of Chemistry. 97

Figure 5.5: Computed concentration of species on various nanostructured electrodes. (a-f) Species of CO₂, C₁, C₂, and C₃ around multi-hollow Cu₂O electrode: the concentration distribution of (a) CO₂, (b) C₁, (c) C₂, (d) C₃, and the species C₂/C₁ ratio as a function of (e) different catalysts and (f) number of

holes, Color scale, in mol/L.⁷⁷ (g) hydroxide ion (OH⁻) around c-wrinkle cavities with different D parameters ranging 400nm to 2.2 μ m.⁷⁸ (h) Species of CO, CH₄ and C₂H₄ around copper-porphyrin frameworks, Color scale, in mol/m³.⁷⁹ (i) Species C₂/C₁ concentration ratio over single 1-shell, 2-shell and 3-shell hollow multi-shell structured copper.⁸⁰ (j) CO, C₂ and C₃ concentrations on the Cu nanocavity electrode, color scale, in mmol/L. Reprinted from the data of the cited papers by the permission from The American Chemical Society, Royal Society of Chemistry, Elsevier, and John Wiley and Sons. 98

Figure 5.6: the electrode geometries used in this work: (a) 2D nanostar, (b) 2D nanocone, and (c) 3D branched nanoparticle. 99

Figure 5.7: (a) FEM simulation domain setup and (b) the dimension of the nanostar electrode. 100

Figure 5.8: Schematic diagram of the Gouy-Chapman-Stern model..... 101

Figure 5.9: (a) the simplified CO₂RR pathway, (b) the dependencies of the electroreduction equilibrium, (c) The response of the electroreduction energy barriers to the applied overpotential.. 106

Figure 5.10: the interconnection between generalized Butler-Volmer (G. B-V) equation, standard Butler-Volmer (S. B-V) equation, linearized Butler-Volmer (L. B-V) equation and Tafel equation, and the associated conditions for linking B-V equation with other equations..... 108

Figure 5.11: The potential (ϕ) and electric field (E) distribution for nanostar electrode simulated under different conditions: (a, d) without considering the formation of EDL, (b,e) accounting for the effect of EDL using modified Poisson-Boltzmann (MPB) model, and (c, f) accounting for the effect of EDL using MPB model and the electrolyte field-dependent dielectric permittivity using Booth model. (d) potential drop from catalyst surface ($x=-0.33$ nm), (h) electric field drop from OHP ($x=0$). The results in this figure are for applied potential of -0.8 V vs. PZC with the electrolyte of 0.5 M KHCO₃. 112

Figure 5.12: The effect of (a) cation size and (b) electrolyte concentration on the electric field at OHP ($EOHP$). 0.5 M electrolyte of KHCO₃, NaHCO₃, and LiHCO₃ are compared in (a). KHCO₃ with different concentrations are compared in (b). The results in this figure are obtained using MPB & Booth for nanostar electrode with applied potential of -0.8 V vs. PZC..... 114

Figure 5.13: Comparison between the electric field results obtained from Poisson-Nernst-Planck (PNP) model, a generalized modified PNP (GMPNP) model and modified Poisson-Boltzmann model for (a) electric field at OHP and (b) electric field drop with the distance from OHP. Subscript OHP means the measurement at OHP. Considering the difficulty in solving GMPNP numerically, all results are obtained using a planar model with the applied potential of -0.4 V vs PZC and the electrolyte of 0.5 M KHCO₃..... 117

Figure 5.14: Comparison between results obtained from Poisson-Nernst-Planck (PNP) model, a generalized modified PNP (GMPNP) model and modified Poisson-Boltzmann model for (a,c) space charge density (ρ), (b,d) potential (ϕ). Subscript OHP means the measurement at OHP. Considering the difficulty in solving GMPNP numerically, all results are obtained using a planar model with applied potential of -0.4 V vs PZC and the electrolyte of 0.5 M KHCO₃..... 118

Figure 5.15: Comparison between results of current density obtained from G. B-V equation and S. B-V equation. The results from G. B-V are (a, e) CO₂ concentration drop from catalysts surface, (b, f) CO₂ concentration distribution and (c, g) current density distribution. Current density distributions from S. B-V equation are shown in (d, h). Applied potential of -0.3 V vs SHE is assigned to cathode in (a-d) while -0.6 V vs SHE used in (e-h). The results in this figure are obtained using Tertiary current density. 123

Figure 5.16: Comparison between results of current density obtained from (a, d) S. B-V equation, (b, e) L. B-V equation and (e, f) Tafel equation. Applied potential of -0.15 V vs SHE is assigned to cathode in (a-c), while -0.6 V vs SHE used in (d-f). The results in this figure are obtained using Tertiary current density. 124

Figure 5.17: Effect of CO₂ concentration on the magnitude and distribution of current density in electrolyte. (a) The magnitudes of current density at OHP ($JOHP$) are compared using different concentrations of CO₂ from 3 mM to 38 mM. The distribution of current density is shown in (b), (c), (d) and (e) for 8 mM, 18 mM, 28 mM and 38 mM CO₂, respectively. The results in this figure are obtained using Tertiary Current Density with the electrolyte of 500 mM KHCO₃ and the applied potential of -0.3 V vs SHE. 125

Figure 5.18: Effect of electrolyte concentration on the magnitude and distribution of current density in electrolyte. (a) The magnitudes of current density at OHP ($JOHP$) are compared using different concentrations of KHCO₃ from 0.1 mM to 500 mM. The distributions of current density are shown in (b), (c), (d) and (e) for 0.1 mM, 1mM, 10mM and 100mM KHCO₃, respectively. The results in this figure are obtained using Tertiary Current Density with applied potential of -0.3 V vs SHE. 126

Figure 5.19: Comparison between the results of current density in electrode for nanostar and nanocone. The results in this figure obtained using an average current density of 1 mA/cm² for cathode as boundary condition..... 128

Figure 5.20: Simulations performed for 3D branched nanoparticle: (a) potential, (b) electric field, (c) K⁺ concentration and (d) current density in metal ($J_{electrode}$) and adjacent electrolyte ($J_{electrolyte}$). $J_{electrode}$ is shown as color map. $J_{electrolyte}$ is shown as groups of cyan arrows, where the size and direction of each arrow represent the magnitude and direction of the current at the spatial position of

the arrow, respectively. The results in (a), (b) and (c) are obtained from MPB & Booth model with the electrolyte of 500 mM KHCO₃ and potential of -0.8V vs PZC, the reaction current density ($J_{electrolyte}$) in (d) is calculated using J_{Sec+M} 130

Figure 5.21: Simulations performed for 2D nanostar nanoparticle. (a) The potential (ϕ), (b) electric field (E-field) (c) K⁺ concentration and (d) current density in metal ($J_{electrode}$) and adjacent electrolyte ($J_{electrolyte}$). The results in (a), (b) and (c) are obtained from MPB & Booth model with the electrolyte of 500 mM KHCO₃ and potential of -0.8V vs PZC, the reaction current density ($J_{electrolyte}$) in (d) is calculated using J_{Sec+M} 131

Figure 5.22: Computed current-density distributions of various gold nanoshapes. The current-density distribution within the metal structures ($J_{electrode}$) is shown as colour maps; the current-density distribution in the electrolyte at the nanostructure surface ($J_{electrolyte}$) is shown as groups of yellow arrows, where the size and direction of each arrow represent the magnitude and direction of the current at the spatial position of the arrow, respectively; the average ($J_{electrolyte}$) was set at 0.1 A cm⁻². a–e, Structures shown are the symmetric branched (a), anchored branched (b), CC (c), thick (d) and thin (e) frames. f, A 2D-slice of the structure a showing the computed current density in a BNP and the surrounding electrolyte for an apparent comparison of current-density magnitudes in both the metal ($J_{electrode}$) and the adjacent electrolyte ($J_{electrolyte}$). g,h, BNP dimer (g) and CC dimer (h), where the two particles are in direct contact, showing the locations of current crowding at the interfaces between the particles and between a particle and the substrate. In h, the left CC is hidden from the view to reveal the $J_{electrode}$ distribution in the planes of contact, where the inset shows the full geometry of the corresponding CC dimer. All scale bars, 25 nm. Reprinted with permission from ref. [71]. Copyright 2021, Springer Nature. 134

Figure 5.23: Effects of geometry, material, and interelectrode distance on computed current density and E-field. a, Computed current density distribution in Pd BNPs. b-d, average current density within the Debye length, $J_{electrolyte}$ (b), average current density within the electrode, $J_{electrode}$ (c) and average E-field within the Stern layer (d), as the function of the distance between anode and cathode. e, Computed current density distribution in a Au CC tetramer with the geometry shown in the inset; three CCs in the front of the structure are hidden from the view to reveal the current distribution at the interfaces between the particles and at the particle-substrate interfaces. In (a) and (e) $J_{electrode}$ is shown as colour maps, and $J_{electrolyte}$ at the nanostructure surface is shown as a group of yellow arrows, where the size and direction of each arrow represent the magnitude and direction of current at the spatial

position of the arrow, respectively. Scale bars are 25 nm. Reprinted with permission from ref. [71]. Copyright 2021, Springer Nature. 135

Figure 5.24: Computed power density distribution (shown as colour map) in Au nanostructures of different shapes. The left CC in a dimer in (f) is hidden from view to show the power distribution at the interface between the CC and the substrate, and at the interface between the two CCs; the inset shows the geometry of the dimer. Scale bars are 25 nm. Reprinted with permission from ref. [71]. Copyright 2021, Springer Nature. 137

Figure 5.25: Computed current density (a) and power density (b) distributions in Pd BNPs. (a) $J_{electrolyte}$ in are shown as groups of arrows, where the size and direction of each arrow represent the magnitude and direction of current at the spatial position of the arrow; $J_{electrode}$ is shown with a colour map. (b) Power density distribution is shown as a colour map. Scale bars are 25 nm. Reprinted with permission from ref. [71]. Copyright 2021, Springer Nature. 138

Figure 5.26: The change of averaged temperature of Au BNPs with the average current density with the substrate temperature of 293.15 K as the reference temperature. Reprinted with permission from ref. [71]. Copyright 2021, Springer Nature. 139

Figure A.1: Optimized geometry structures for initial, transition and final states of migration for Au atom and intermediate-bound Au atoms of Au-COOH(CO₂RR) and Au-H(HER) on Au(111) surface respectively. The olive color atoms represent Au substrate surfaces, with yellow, grey, red and white color atoms representing hooping Au, C, O and H atoms respectively. Reprinted with permission from ref. [71]. Copyright 2021, Springer Nature. 226

Figure A.2: Optimized geometry structures for initial, transition and final states of migration for Au atom and intermediate-bound Au atoms of Au-COOH(CO₂RR) and Au-H(HER) on Au(100) surface, respectively. Reprinted with permission from ref. [71]. Copyright 2021, Springer Nature. 227

Figure A.3: Optimized geometry structures for initial, transition and final states of migration for Au atom and intermediate-bound Au atoms of Au-COOH(CO₂RR) and Au-H(HER) on Au(110) surface, respectively. Reprinted with permission from ref. [71]. Copyright 2021, Springer Nature. 227

Figure A.4: Optimized geometry structures for initial, transition and final states of migration for Au atom and intermediate-bound Au atoms of Au-COOH(CO₂RR) and Au-H(HER) on Au(211) surface, respectively. Reprinted with permission from ref. [71]. Copyright 2021, Springer Nature. 228

Figure A.5: Optimized geometry structures for initial, transition and final states of migration for Pd atom and intermediate-bound Pd atom of Pd-COOH(CO₂RR) on Pd(111) surface respectively. The lavender color atoms represent Pd surfaces, with teal, grey, red and white color atoms representing

hooping Au, C, O and H atoms, respectively. Reprinted with permission from ref. [71]. Copyright 2021, Springer Nature.....	228
Figure A.6: Optimized geometry structures for initial, transition and final states of migration for Pd atom and intermediate-bound Pd atom of Pd-COOH(CO ₂ RR) on Pd(100) surface, respectively. Reprinted with permission from ref. [71]. Copyright 2021, Springer Nature.....	229
Figure A.7: Optimized geometry structures for initial, transition and final states of migration for Pd atom and intermediate-bound Pd atom of Pd-COOH(CO ₂ RR) on Pd(110) surface, respectively. Reprinted with permission from ref. [71]. Copyright 2021, Springer Nature.....	229
Figure A.8: Optimized geometry structures for initial, transition and final states of migration for Pd atom and intermediate-bound Pd atom of Pd-COOH(CO ₂ RR) on Pd(211) surface, respectively. Reprinted with permission from ref. [71]. Copyright 2021, Springer Nature.....	230
Figure A.9: Optimized geometries of Ag(111), Ag(100), Ag(110), and Ag(211) surfaces without (top panels) and with (bottom panels) absorbed *H, *OOH and *COOH. Reprinted with permission from ref. [132]. Copyright 2022, Royal Society of Chemistry.....	231
Figure A.10: Optimized geometries of on Au(111), Au(100), Au(110), and Au(211) surfaces without (top panels) and with (bottom panels) absorbed *H, *OOH and *COOH. Reprinted with permission from ref. [132]. Copyright 2022, Royal Society of Chemistry.	232
Figure A.11: Optimized geometries of Pd(111), Pd(100), Pd(110), and Pd(211) surfaces without (top panels) and with (bottom panels) absorbed *OOH and *COOH. Reprinted with permission from ref. [132]. Copyright 2022, Royal Society of Chemistry.	232
Figure A.12: Optimized single-atom vacancy on Cu(111), Cu(100), Cu(110), and Cu(211) surfaces without (top panels) and with (bottom panels) absorbed *H, *OOH and *COOH. Reprinted with permission from ref. [132]. Copyright 2022, Royal Society of Chemistry.....	233
Figure A.13: Optimized single-atom vacancy on Ag(111), Ag(100), Ag(110), and Ag(211) surfaces without (top panels) and with (bottom panels) absorbed *H, *OOH and *COOH. Reprinted with permission from ref. [132]. Copyright 2022, Royal Society of Chemistry.....	233
Figure A.14: Optimized single-atom vacancy on Au(111), Au(100), Au(110), and Au(211) surfaces without (top panels) and with (bottom panels) absorbed *H, *OOH and *COOH. Reprinted with permission from ref. [132]. Copyright 2022, Royal Society of Chemistry.....	234
Figure A.15: Optimized single-atom vacancy on Pd(111), Pd((100), Pd((110), and Pd((211) surfaces without (top panels) and with (bottom panels) absorbed *OOH and *COOH. Reprinted with permission from ref. [132]. Copyright 2022, Royal Society of Chemistry.	234

Figure B.1: Calculated kinetic barriers of two VF mechanisms on Cu(111), Cu(100), Cu(110), and Cu(211) surfaces. Reprinted with permission from ref. [132]. Copyright 2022, Royal Society of Chemistry.	235
Figure B.2: Calculated kinetic barriers of two VF mechanisms on Ag(111), Ag(100), Ag(110), and Ag(211) surfaces. Reprinted with permission from ref. [132]. Copyright 2022, Royal Society of Chemistry.	236
Figure B.3: Calculated kinetic barriers of two VF mechanisms on Au(111), Au(100), Au(110), and Au(211) surfaces. Reprinted with permission from ref. [132]. Copyright 2022, Royal Society of Chemistry.	237
Figure B.4: Calculated kinetic barriers of two VF mechanisms on Pd(111), Pd(100), Pd(110), and Pd(211) surfaces. Reprinted with permission from ref. [132]. Copyright 2022, Royal Society of Chemistry.	238
Figure C.1: Profiles of time-averaged mean-square displacement (TA-MSD) and radial distribution function (RDF) for Cu cluster supported on Cu(111) surface. (a) TA-MSDs for cluster Cu atoms. TA-MSD for the first 2 most mobily cluster atoms is shown in solid line, with the rest shown in dash line. (b) Averaged TA-MSD for all substrate metal atoms. (c) RDF and Lindemann index of the metal cluster and substrate. Reprinted with permission from ref. [132]. Copyright 2022, Royal Society of Chemistry.	239
Figure C.2: Profiles of time-averaged mean-square displacement (TA-MSD), radial distribution function (RDF), and vvt for H-bound Cu cluster supported on Cu(111) surface. (a) TA-MSDs for cluster Cu atoms. TA-MSD for the first 2 most mobily cluster atoms is shown in solid line, with the rest shown in dash line. (b) Averaged TA-MSD for all substrate metal atoms. (c) RDF and Lindemann index of the metal cluster and substrate, and the RDF of the reaction intermediate. (d) vvt for reaction intermediate of H. Reprinted with permission from ref. [132]. Copyright 2022, Royal Society of Chemistry.	240
Figure C.3: Profiles of time-averaged mean-square displacement (TA-MSD), radial distribution function (RDF), and vvt for OOH-bound Cu cluster supported on Cu(111) surface. (a) TA-MSDs for cluster Cu atoms. TA-MSD for the first 2 most mobily cluster atoms is shown in solid line, with the rest shown in dash line. (b) Averaged TA-MSD for all substrate metal atoms. (c) RDF and Lindemann index of the metal cluster and substrate, and RDF of the reaction intermediate. (d) vvt for reaction intermediate of OOH. Reprinted with permission from ref. [132]. Copyright 2022, Royal Society of Chemistry.	241

Figure C.4: Profiles of time-averaged mean-square displacement (TA-MSD), radial distribution function (RDF), and v_{vt} for COOH-bound Cu cluster supported on Cu(111) surface. (a) TA-MSDs for cluster Cu atoms. TA-MSD for the first 2 most mobile cluster atoms is shown in solid line, with the rest shown in dash line. (b) Averaged TA-MSD for all substrate metal atoms. (c) RDF and Lindemann index of the metal cluster and substrate, and the RDF of the reaction intermediate. (d) v_{vt} for reaction intermediate of COOH. Reprinted with permission from ref. [132]. Copyright 2022, Royal Society of Chemistry..... 242

Figure C.5: Profiles of time-averaged mean-square displacement (TA-MSD) and radial distribution function (RDF) for Ag cluster supported on Ag(111) surface. (a) TA-MSDs for cluster Ag atoms. TA-MSD for the first 2 most mobile cluster atoms is shown in solid line, with the rest shown in dash line. (b) Averaged TA-MSD for all substrate metal atoms. (c) RDF and Lindemann index of the metal cluster and substrate. Reprinted with permission from ref. [132]. Copyright 2022, Royal Society of Chemistry. 243

Figure C.6: Profiles of time-averaged mean-square displacement (TA-MSD), radial distribution function (RDF), and v_{vt} for H-bound Ag cluster supported on Ag(111) surface. (a) TA-MSDs for cluster Ag atoms. TA-MSD for the first 2 most mobile cluster atoms is shown in solid line, with the rest shown in dash line. (b) Averaged TA-MSD for all substrate metal atoms. (c) RDF and Lindemann index of the metal cluster and substrate, and the RDF of the reaction intermediate. (d) v_{vt} for reaction intermediate of H. Reprinted with permission from ref. [132]. Copyright 2022, Royal Society of Chemistry..... 244

Figure C.7: Profiles of time-averaged mean-square displacement (TA-MSD), radial distribution function (RDF), and v_{vt} for OOH-bound Ag cluster supported on Ag(111) surface. (a) TA-MSDs for cluster Ag atoms. TA-MSD for the first 2 most mobile cluster atoms is shown in solid line, with the rest shown in dash line. (b) Averaged TA-MSD for all substrate metal atoms. (c) RDF and Lindemann index of the metal cluster and substrate, and the RDF of the reaction intermediate. (d) v_{vt} for reaction intermediate of OOH. Reprinted with permission from ref. [132]. Copyright 2022, Royal Society of Chemistry..... 245

Figure C.8: Profiles of time-averaged mean-square displacement (TA-MSD), radial distribution function (RDF), and v_{vt} for COOH-bound Ag cluster supported on Ag(111) surface. (a) TA-MSDs for cluster Ag atoms. TA-MSD for the first 2 most mobile cluster atoms is shown in solid line, with the rest shown in dash line. (b) Averaged TA-MSD for all substrate metal atoms. (c) RDF and Lindemann index of the metal cluster and substrate, and the RDF of the reaction intermediate. (d) v_{vt} for reaction

intermediate of OOH. Reprinted with permission from ref. [132]. Copyright 2022, Royal Society of Chemistry. 246

Figure C.9: Profiles of time-averaged mean-square displacement (TA-MSD) and radial distribution function (RDF) for Au cluster supported on Au(111) surface. (a) TA-MSDs for cluster Au atoms. TA-MSD for the first 2 most mobile cluster atoms is shown in solid line, with the rest shown in dash line. (b) Averaged TA-MSD for all substrate metal atoms. (c) RDF and Lindemann index of the metal cluster and substrate. Reprinted with permission from ref. [132]. Copyright 2022, Royal Society of Chemistry. 247

Figure C.10: Profiles of time-averaged mean-square displacement (TA-MSD), radial distribution function (RDF), and vvt for H-bound Au cluster supported on Au(111) surface. (a) TA-MSDs for cluster Au atoms. TA-MSD for the first 2 most mobile cluster atoms is shown in solid line, with the rest shown in dash line. (b) Averaged TA-MSD for all substrate metal atoms. (c) RDF and Lindemann index of the metal cluster and substrate, and the RDF of the reaction intermediate. (d) vvt for reaction intermediate of H. Reprinted with permission from ref. [132]. Copyright 2022, Royal Society of Chemistry. 248

Figure C.11: Profiles of time-averaged mean-square displacement (TA-MSD), radial distribution function (RDF), and vvt for OOH-bound Au cluster supported on Au(111) surface. (a) TA-MSDs for cluster Au atoms. TA-MSD for the first 2 most mobile cluster atoms is shown in solid line, with the rest shown in dash line. (b) Averaged TA-MSD for all substrate metal atoms. (c) RDF and Lindemann index of the metal cluster and substrate, and the RDF of the reaction intermediate. (d) vvt for reaction intermediate of OOH. Reprinted with permission from ref. [132]. Copyright 2022, Royal Society of Chemistry. 249

Figure C.12: Profiles of time-averaged mean-square displacement (TA-MSD), radial distribution function (RDF), and vvt for COOH-bound Au cluster supported on Au(111) surface. (a) TA-MSDs for cluster Au atoms. TA-MSD for the first 2 most mobile cluster atoms is shown in solid line, with the rest shown in dash line. (b) Averaged TA-MSD for all substrate metal atoms. (c) RDF and Lindemann index of the metal cluster and substrate, and the RDF of the reaction intermediate. (d) vvt for reaction intermediate of COOH. Reprinted with permission from ref. [132]. Copyright 2022, Royal Society of Chemistry. 250

Figure C.13: Profiles of time-averaged mean-square displacement (TA-MSD) and radial distribution function (RDF) for Pd cluster supported on Pd(111) surface. (a) TA-MSDs for cluster Ag atoms. TA-MSD for the first 2 most mobile cluster atoms is shown in solid line, with the rest shown in dash line. (b) Averaged TA-MSD for all substrate metal atoms. (c) RDF and Lindemann index of the metal cluster

and substrate. Reprinted with permission from ref. [132]. Copyright 2022, Royal Society of Chemistry.

..... 251

Figure C.14: Profiles of time-averaged mean-square displacement (TA-MSD), radial distribution function (RDF), and vvt for OOH-bound Pd cluster supported on Pd(111) surface. (a) TA-MSDs for cluster Au atoms. TA-MSD for the first 2 most mobile cluster atoms is shown in solid line, with the rest shown in dash line. (b) Averaged TA-MSD for all substrate metal atoms. (c) RDF and Lindemann index of the metal cluster and substrate, and the RDF of the reaction intermediate. (d) vvt for reaction intermediate of OOH. Reprinted with permission from ref. [132]. Copyright 2022, Royal Society of Chemistry..... 252

Figure C.15: Profiles of time-averaged mean-square displacement (TA-MSD), radial distribution function (RDF), and vvt for COOH-bound Pd cluster supported on Pd(111) surface. (a) TA-MSDs for cluster Au atoms. TA-MSD for the first 2 most mobile cluster atoms is shown in solid line, with the rest shown in dash line. (b) Averaged TA-MSD for all substrate metal atoms. (c) RDF and Lindemann index of the metal cluster and substrate, and the RDF of the reaction intermediate. (d) vvt for reaction intermediate of COOH. Reprinted with permission from ref. [132]. Copyright 2022, Royal Society of Chemistry..... 253

List of Tables

Table 3.1: Hollow and porous nanostructures as electrocatalysts for CO ₂ RR.	34
Table 3.2: Hollow and porous nanostructures as electrocatalysts for HER.....	36
Table 3.3: Hollow and porous nanostructures as electrocatalysts for NRR and ORR.	37
Table 3.4: Surface roughness assessment of the fabricated Au electrodes.....	48
Table 3.5: Statistical analysis of nanoparticle sizes before and 5 hours of CO ₂ RR electrolysis obtained using Image-J software. On average, 100 nanoparticles were analyzed for each measurement.	48
Table 5.1: Comparison of the major features of PNP, GMPNP, and MPB.....	116
Table 5.2: Essential effects accounted in the simulation of primary, secondary, tertiary current density and secondary current density coupled with mass transport effect, respectively. All results are obtained for applied potential of -0.3 V vs SHE with the electrolyte of 0.5 M KHCO ₃ . All scale bars, 50 nm.	120

List of Abbreviations

AIMD	Ab initio molecular dynamic
BNPs	Branched nanoparticles
CA	Chronoamperometry
CCs	Core-cages
CI-NEB	Climbing-image nudged elastic band
CO ₂ RR	Carbon dioxide reduction reaction
CPC	Cetylpyridinium chloride
CTAB	hexadecyltrimethylammonium bromide
CTAC	Hexadecyltrimethylammonium chloride
CV	Cyclic voltammetry
DFT	Density functional theory
EDL	Electric double layer
E-field	Electric field
EM	Electromigration
FDM	Finite difference method
FE	Faradaic efficiency
FEM	Finite element method
FID	Flame ionization detector
FIRC	Field-induced reagent concentration
FVM	Finite volume method
G. B-V	Generalized Butler-Volmer
GC	Gouy-Chapman
GCS	Gouy-Chapman-Stern

GGA	Generalized-gradient approximation
GMPNP	General modified Poisson-Nernst-Plank
HER	Hydrogen evolution reaction
L. B-V	Linearized Butler-Volmer
MD	Molecular dynamic
MPB	Modified Poisson-Boltzmann
MSDs	Mean square displacements
NCs	Nanocages
NRR	Nitrogen reduction reaction
OHP	Outer Helmholtz plane
ORR	Oxygen reduction reaction
PAW	Projector augmented wave
PB	Poisson-Boltzmann
PBE	Perdew-Burke-Ernzerhof
PNP	Poisson-Nernst-Plank
PVP	polyvinylpyrrolidone
PZC	Point of zero charge
RDFs	Radial distribution functions
RHE	Reversible hydrogen electrode
RI	Reaction intermediate
S. B-V	Standard Butler-Volmer
SEM	Scanning electron microscopy
SHE	Standard hydrogen electrode
TCD	Thermal conductivity detector
TEM	Transmission electron microscopy

UPD	underpotential deposition
VASP	Vienna Ab initio Simulation Package
VF	Vacancy formation
XPS	X-ray photoelectron spectroscopy
XRD	X-ray diffraction

Chapter 1

Introduction

1.1 Significance of the cathodic electrochemical synthesis methods

With rising global concerns about energy demand and climate change, sustainable synthesis of renewable fuels is becoming increasingly important. In particular, electrocatalytic approaches, including hydrogen evolution reaction (HER), nitrogen reduction reaction (NRR), and carbon dioxide reduction reaction (CO₂RR) are promising solutions for the sustainable production of synthetic fuels such as hydrogen, ammonia, hydrocarbons, and oxygenates while also representing a long-term storage strategy for intermittent renewable electricity.¹ HER can be used to produce hydrogen, which is an attractive energy carrier that can be used to produce clean electricity in fuel cells. NRR can be performed for electrochemically reducing the nitrogen (N₂) and water (H₂O) to ammonia (NH₃), which is an activated nitrogen building block for the manufacture of modern fertilizers, plastics, fibers,

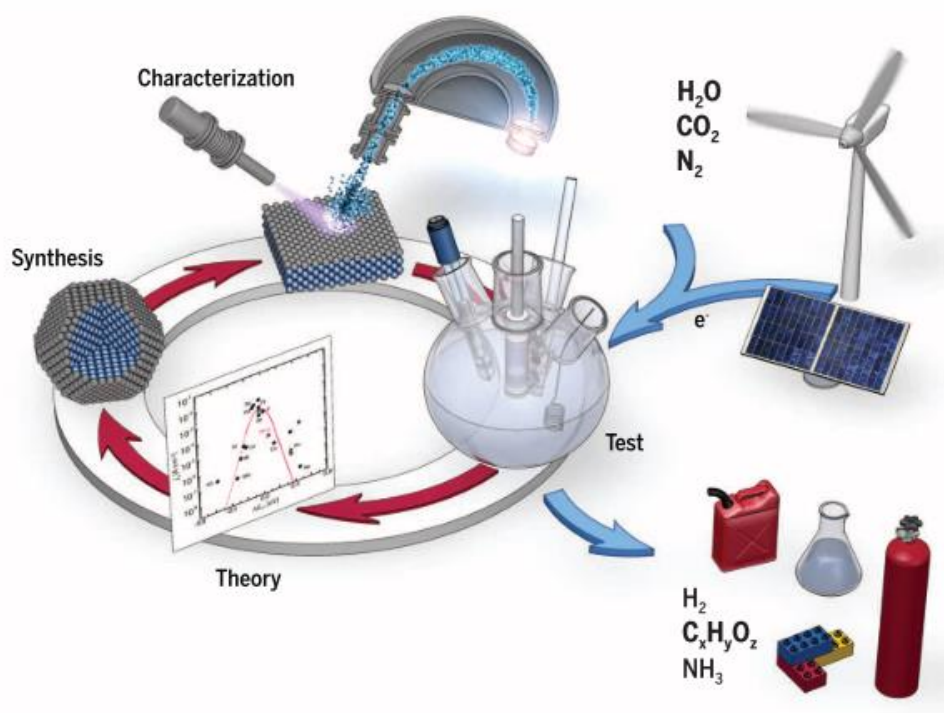


Figure 1.1: Schematic showing sustainable electrochemical synthesis of renewable value-added products such as hydrocarbons, oxygenates, and ammonia.¹ Reprinted from ref. [1]. Copyright 2017, with the permission from American Association for the Advancement of Science.

explosives, etc. Compared to HER and NRR, CO₂RR is attracting particular attention, as it can not only produce various value-added chemical products, but also can recycle the CO₂ released from burning fossil fuels back to fuels and mitigate the deteriorating environmental issues caused by global climate change.² However, various single- and multi-carbon gas and liquid products can be produced in CO₂RR electrocatalysis, with most of these products requiring multiple proton-electron transfers during their formation processes.³ A wide distribution of possible products as well as multi-proton-electron transfer mechanisms lead to poor selectivity and sluggish kinetics of CO₂RR. The reaction selectivity is further disrupted by the competing HER^{4,5} and oxygen reduction reaction (ORR), where the latter occurs when oxygen is present in the CO₂ feedstock⁶ as both H⁺ and O₂ can be easily reduced at the applied potentials required for CO₂RR. The key to improving the selectivity and kinetics of CO₂RR towards target products is rationally designed electrocatalysts, as they play a central role in determining the rate, efficiency, and selectivity of the chemical transformations involved in CO₂RR.¹ Thus, developing electrocatalysts with desired properties is necessary to realize the prospects of using CO₂RR to produce fuels and chemicals that we need for a sustainable energy future.

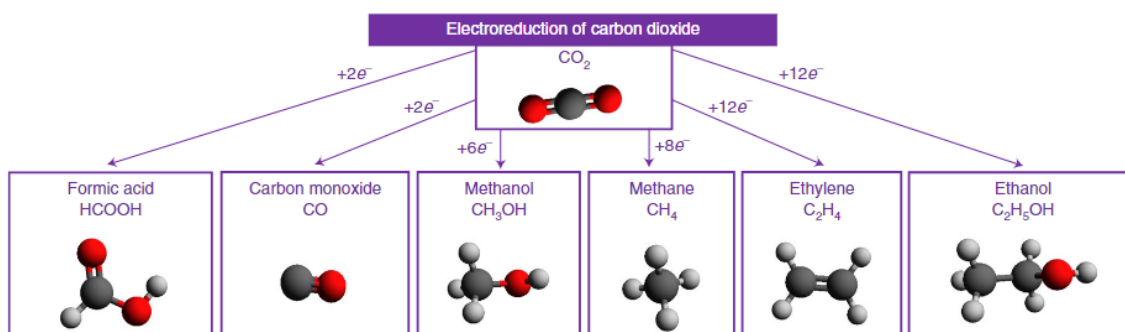


Figure 1.2: Various single- and multi-carbon gas and liquid products that can be produced in CO₂RR electrocatalysis.³ Reprinted from ref. [3]. Copyright 2019, with the permission from Springer Nature.

1.2 Outstanding activity and selectivity of nanostructured electrocatalysts with complex shape

In the past decades, developing nanostructured heterogeneous electrocatalysts has been on the rise due to their advantages over conventional heterogeneous electrocatalysts.⁷ Cathodic nanoscale electrocatalysts with structural complexity often show outstanding catalytic activity and selectivity towards target products.⁷ For example, nanostructured catalysts provide more degrees of freedom in adjusting their composition, surface chemistry and morphology, which enables finetuning the catalytic active sites via manipulating the atomic arrangement on the nanoscale electrode surface,^{8–10} as shown in Figure 1.3.¹¹ In particular, the electronic structures of nanostructured electrodes can be modulated to stabilize key reaction intermediates, thereby steering the reaction selectivity.¹² Furthermore, the nanostructured electrocatalysts are rich in active sites due to the presence of various surface defects including grain boundaries,⁸ subsurface oxides,⁹ and highly undercoordinated atoms,¹⁰ and which can act as enhanced active sites contributing to the improved activity.¹ In addition to the aforementioned

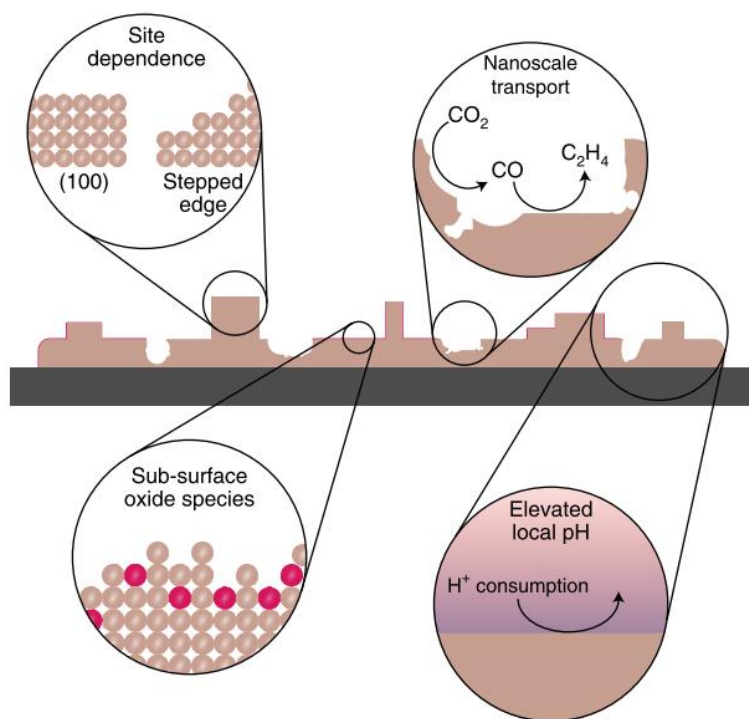


Figure 1.3: Motifs on a metal electrode surface that may influence C–C bond formation in CO₂RR. Reprinted from ref. [11]. Copyright 2019, with the permission from Springer Nature.

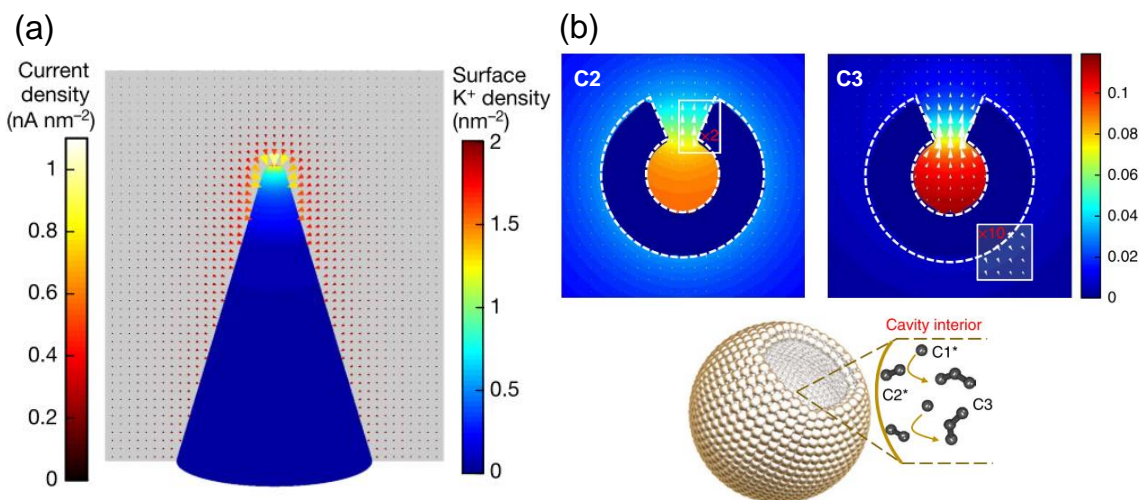


Figure 1.4: Various electrochemical physics effects on nanoscale. (a) Field induced reagent concentration effect by concentrating the cations at the vicinity of a high-curvature feature. Reprinted from ref. [13]. Copyright 2016, with the permission from Springer Nature. (b) Cavity confinement effect that promotes C2 species binding and further conversion to C3. C2 and C3 concentrations are shown in colour scale in millimoles and flux distributions are shown in arrows. Reprinted from ref. [14]. Copyright 2018, with the permission from Springer Nature.

effects on the atomic scale, the activity and selectivity of nanoparticle-based electrodes in surface reactions can also be modulated by varying their nanostructure due to various electrochemical physics effects on nanoscale. For instance, high-curvature nanoscale features in complex nanostructures can generate high electric fields (E-fields) in the electrolyte adjacent to their surface under an applied bias, which can increase the CO₂ concentration by accumulating the electrolyte cations in their vicinity and therefore promote the CO₂RR performance (Figure 1.4a).¹³ Moreover, the distribution of reaction species can also be affected by the nanoscale geometry of electrocatalysts: for example, nanocavities in nanostructured electrodes can confine the reaction intermediates during the CO₂RR electrolysis, steering the reaction towards more valuable multi-carbon products (Figure 1.4b).¹⁴ These specific electrocatalytic effects illustrate the significance of optimizing the geometry of catalytic nanostructures in improving the electrocatalytic performance of these materials.

Considering the advantages of the complex nanostructured electrodes in electrocatalysis, the electrocatalysts with various nanoscale shape have been designed, ranging from cages,^{15–19} frames,^{20–27}

cavities,^{14,28} multi-shell hollow^{29–33} and yolk–shell particles^{34,35} to various branched morphologies^{36,37} being reported as superior electrocatalysts compared with their more geometrically simple counterparts. Their exceptional electrocatalytic performance has been ascribed to high mass activity, the specificity of exposed crystalline facets, a high number of undercoordinated surface atoms, structural disorder and a high density of surface defects, confinement of the reactants in the pores of the structure, and the concentration of reagents at the surface due to local electric field (E-field) enhancement at high surface curvature features.^{13,14,38} The latter effect is specific to electrocatalysis, while the other factors may generally apply to any heterogeneous catalysis scenario. The electrocatalytic performance enhancement attributed specifically to local E-field behaviour is currently on the rise and has been reported for spherical,^{13,39} conical,⁴⁰ rod,¹¹ prism,⁴¹ needle-like^{13,42} and more complex structures, including three-dimensional hierarchic nanoflowers,⁴³ nanoflakes,⁴⁴ tetrapods,³⁹ porous foams⁴⁵ and cage-like porous spheres,⁴³ that have been used as catalysts for the electroreduction.

1.3 Poor structural stability of complex nanostructured electrocatalysts

Many researchers have focused on modifying the composition and morphology of metal nanostructured catalysts to increase their selectivity and activity in CO₂RR.⁴⁶ However, comparatively less attention has been given to the structural stability of nanoscale electrocatalysts under CO₂RR conditions. Understanding the factors determining their structural stability in the course of electrolysis is of paramount importance to the practical application of CO₂RR, as the long-term stability is another key performance parameter beyond activity and selectivity for real-world catalysts.^{47,48} Structural transformations have been observed in solid state materials with and without oxidation state change under cathodic electrolysis conditions. For example, structural evolutions were observed in oxide- and hydroxide-derived copper electrodes with obvious oxidation state change when Cu(II) precursors are electrochemically reduced to make copper electrodes (Figure 1.5a).^{45,49–51} The changes in the structure and oxidation state of Cu(II)-derived copper electrodes give rise to the formation of unique structural and compositional features, including grain boundaries,^{52,53} exposed surface facets,⁵⁴ presence of Cu(I) species (or subsurface oxygen),⁹ and high-curvature sites,¹³ which makes Cu(II)-derived copper electrodes with higher selectivity towards multicarbon products compared to polycrystalline copper. Moreover, it has been recently discovered that metal Cu nanoparticles can also undergo significant structural transformation in the course of CO₂RR with drastic effect on their catalytic performance,⁵⁵ suggesting that in situ formation of catalytic active sites and morphological changes are not unique to the electroreduction of oxidized copper (Figure 1.5 b and c). Furthermore, recent studies have revealed

the reconstruction of Au nanospheres under CO₂ electroreduction conditions,⁵⁵⁻⁵⁹ signifying the prominent mobility of the nanocatalyst material during electrolysis. Further structural and mechanistic elucidation of the structural dynamics under electrical bias is necessary to ensure that the catalytically active features of complex nanostructures are not transient states of their evolving morphology, which is very important for engineering long-term catalyst performance and stability in CO₂RR and beyond.

The evolution of the metal structures could proceed *via* different mechanisms,⁶⁰ such as dissolution, electrodeposition, electrochemical Ostwald ripening, fragmentation, and agglomeration, to name a few, and most of them are accompanied by a prominent atomic mobility. During the electrolysis conditions, atomic mobility could change the particle size, crystalline phase, and morphology of the heterogeneous metal catalysts, which does not only affect their stability and activity,⁶¹ but also cause the active sites to be dynamically evolving.⁶² Therefore, understanding the factors affecting the atomic mobility under electrolysis conditions is the key to reveal the structural transformations mechanisms of the electrocatalysts.

1.4 Application of DFT calculations in designing advanced electrocatalysts

To date, the known factors affecting the atomic mobility of metal surfaces include the reaction intermediate (RI), electrolyte, applied potential, local pH, nanostructure size, and catalyst support.^{57-59,62-64} Among them, RI is one of the key parameters in driving the atomic mobility during CO₂RR electrolysis. In principle, the ability to remove a metal atom from a surface is determined by the bonding strength of an atom to its neighbouring atoms in lattice, and thus correlates with the number of valence electrons that the metal atom has to form the metallic bond. As an essential step for the CO₂RR on the electrode surface, the bond formation between the RI and the catalytic metal atom on the surface may distract the valence electrons of the atom from metallic bonding and eventually influence its mobility on the metallic surface. The investigation of the impact of CO₂RR-associated RIs on the atomic mobility is of significant importance not only to reveal the mechanisms of structural degradation and subsequently develop solutions to prolonging the catalyst lifetime for metal catalysts used in CO₂RR, but also to shine more light on the dynamic nature of the catalyst surface during electrochemical reactions. Density functional theory (DFT) calculations is a commonly used tool to explore the interaction of RIs with metal surfaces as well as the migration of the RI and RI-bound metal atom on metal surface at the atomic scale.⁶⁵⁻⁶⁷

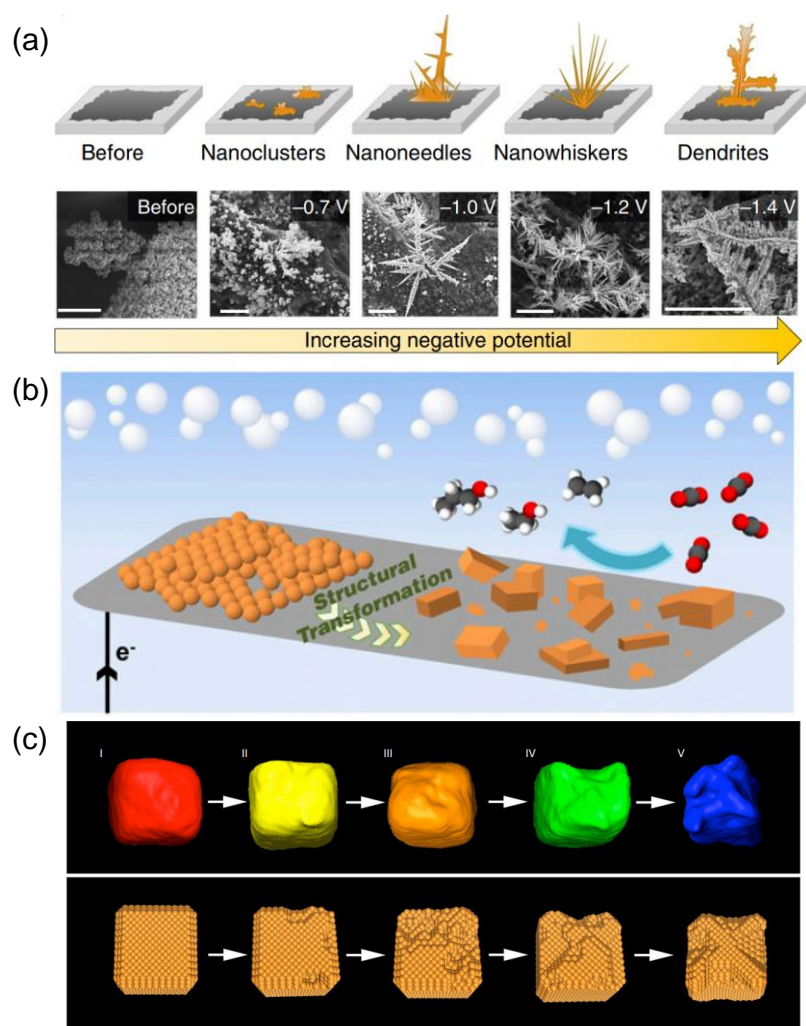


Figure 1.5: Structural transformations observed in shape-specific nanostructured electrocatalysts with and without oxidation state change. (a) SEM images and schematic of the key structure features during the growth process of the electrochemically reduced Cu nanostructures at their specific applied potentials. Reprinted from ref. [51]. Copyright 2017, with the permission from The American Chemical Society (b) Schematic illustrating the transformation process of Cu NP ensembles to an active catalyst for C2–C3 product formation. Reprinted from ref. [55]. Copyright 2017, with the permission from National Academy of Science of the United States of America. (c) Tomographic reconstruction of the CuNCs and corresponding schematic morphological models at different stages under CO_2RR electrolysis conditions. Reprinted from ref. [63]. Copyright 2018, with the permission from Springer Nature.

First, DFT calculations can be performed to investigate the energetically favourable geometries of (111) (100), (110), and (211) surfaces for the commonly used metals in CO₂RR such as Cu, Ag, Au, and Pd with adsorbed CO₂RR-related RIs, including *COOH, *H, and *OOH, key RIs for CO₂RR itself, competing HER, and competing ORR from traces of air/oxygen present in CO₂, respectively. Optimized geometries of RI-bound metal surfaces can be used to calculate the binding energy of adsorbed RIs on metal surfaces. Binding energy reflects the binding strength of the adsorbates on a surface, which can be performed for studying the interaction strength and likelihood of RIs adsorption on metal surfaces.

Furthermore, DFT calculations can be applied to explore the impact of the adsorbed RIs on the chemical bonds of RI-bound metal atom with its neighbours in the lattice by studying thermodynamic and kinetic aspects of extracting a metal atom on different crystallographic facets of the studied metals with and without surface-bound RIs. The thermodynamic profile can be assessed by calculating the vacancy formation energy (E_{VF}). The kinetic aspects can be accessed by searching for the energy favourable paths of extracting a metal atom on metal facets and the energy barriers associated with them using the climbing-image nudged elastic band (CI-NEB) method.⁶⁸ Moreover, DFT calculation can be performed to explore the migration profile of a metal adatom on different metal surfaces with and without bound RI. The migration pathway of the surface adatom on metal surfaces and the energy barriers associated with it can also be studied using CI-NEB method.

In addition to DFT calculation, molecular dynamic (MD) simulation is another a powerful tool to monitor the structural dynamics of a complex multiatomic surface structure⁶⁹ and the influence of adsorbed species.⁷⁰ In contrast to DFT calculation, MD simulation can be used to probe the stability of a complex surface structure (compared to low-index facets) mimicking nanostructured catalysts such as surface model comprised of a metal cluster bound to an extended metal surface. The trajectory for the morphology evolution of the studied metal clusters can be obtained from MD simulations. Based on the trajectory file, the averaged displacement, mean square displacements (MSDs), radial distribution functions (RDFs), and Lindemann indices of the atoms in a metal cluster can be assessed, which can be used to analyse the atomic mobility of a metal qualitatively and quantitatively. Moreover, the trajectory file can also be used for calculating the temperature and heat capacity of the metal system, which can reveal the influence of the heat transfer efficiency and heat capacity of a metal on its atomic mobility.

The DFT and MD approaches mentioned above can be applied to a series of metal and metal-alloy CO₂RR catalysts to provide a more comprehensive description of atomic mobility induced by RIs during CO₂RR electrolysis. Therefore, the influence of the RIs on the atomic mobility and their specific mechanisms, along with the trends in atomic mobility in the series of metals and their correlations with their chemical and physical nature are revealed. These studies can not only shine light on the atomic mobility trends in the commonly used CO₂RR metal electrocatalysts and the influence of the RIs under electrolysis conditions, but also enables the evaluation of the atomic mobility in a cathodic catalyst of a new composition and provides another step in guiding experiments toward designing more stable electrocatalysts for industrial applications.

1.5 Application of FEM simulations in designing advanced electrocatalysts

As discussed above, the influence of the RIs and metal nature on the atomic mobility can be well characterized by DFT and MD calculations at atomic scale. However, the DFT and MD approaches do not reflect the impact of the morphology of nanostructured electrocatalysts on the atomic mobility and the structural stability in the electrocatalysts. Conversely, experimental reports suggested that metal catalysts with complex nanostructures can take advantage of the field-induced reagent concentration near high-curvature nanoscale features¹³ or the confinement of reaction intermediates in a nanocavity, promoting both activity and selectivity of CO₂RR.¹⁴ These specific electrochemical physics effects generated by the specific nanoscale features of the electrocatalysts can not only affect the catalytic activity and selectivity of the electrocatalysts, but also affect the structural stability of electrocatalysts since these electrocatalytic phenomena could promote the electrolysis reactions proceeding on the electrode surfaces. Electrolysis reactions have been proven to have significant impacts on the structural transformations of the electrocatalysts under electrolysis conditions. These specific electrochemical physics effects illustrate the significance of the nanoscale morphology of the electrocatalysts in the structural stability of the electrode under the electrolysis conditions.

To understand how the nanoscale shapes structurally affect the structural stability of the electrocatalysts under bias conditions, one needs to get the quantitative spatial analysis of physicochemical properties adjacent to and in the morphologically complex electrocatalysts. Finite element method (FEM) is a well-known numerical engineering tool for modelling various multiphysics systems and processes, therefore, which has been increasingly applied to electrocatalytic systems to quantitatively and spatially describe their electrocatalytic performance on nanoscale.

First, FEM has been performed for studying the E-field profiles of various nanostructured electrodes including geometries of nanoneedles,^{42,71–73} nanorods,⁷² nanoflakes,⁴⁴ nanoprisms,⁴¹ nanogrooves,⁷⁴ and nanoflowers.⁴³ The distribution of E-field at the electrode-electrolyte interface is one of the crucial metrics in evaluating the electrochemical performance of the electrode. The interfacial E-field could significantly impact the reactivity of the electrode in CO₂RR by accelerating the electron transfer. Moreover, E-field can greatly affect the adsorption energy of an adsorbate that is uncharged, but has a significant dipole moment and/or a large polarizability. More recently, Liu et al. demonstrated that E-field generated by nanostructures with high curvature can also promote CO₂RR by concentrating K⁺ ions at the electrode surface and thereby enhancing CO₂ adsorption and decreasing the thermodynamic energy barrier for CO₂RR.¹³

Furthermore, FEM has also been used to study the reaction current density ($J_{electrolyte}$) for various nanostructured electrodes including nanoneedles,^{13,45} nanocones,^{13,45} nanorods,^{13,45} nanocages,⁷⁵ branched nanoparticles⁷¹ and nanoframes.⁷¹ The $J_{electrolyte}$ near the electrode surface is another important indicator for evaluating the electrochemical performance of an electrode, as it reflects the reaction rate of the electroactive species on the electrode surface. Therefore, a high $J_{electrolyte}$ on the surfaces of an electrode indicates a high electrochemical activity at these areas, which can be regarded as an electrochemical activity indicator to guide the electrocatalyst design.

In addition to the E-field and $J_{electrolyte}$, FEM has also been reported to evaluate the electron density^{13,39,40,75} on the electrode surface and the concentration of the electrolyte ions^{13,40,72,75,76} and other species^{14,77–80} in the electrolyte adjacent to the electrode surface. These parameters are also the important factors for evaluating the electrochemical performance of an electrode, as they reflect the properties of the electrode kinetics and mass transport of an electrode.

Although the application of FEM simulation in analysing the electrochemical performance of nanostructured electrodes is on the rise, less attention has been given in this area in comparison to the DFT calculations in designing advanced electrocatalysts for CO₂RR. In these limited reports on studying the electrochemical behavior of nanostructured electrodes using FEM, there are some inaccurate and inconsistent results. This is due to a lack of established best practices and consistent protocols in setting and solving the necessary equations for determining the distributions of the local E-field, current density and active species at electrodes with complex nanoscale morphologies. The protocols for reliable simulations of these electrochemical effects are required to facilitate a wider adoption of FEM simulations in analysing the electrochemical performance of morphologically

complex nanostructured electrodes and rational design of advanced electrocatalysts for CO₂RR and other clean energy conversion reactions.

1.6 Scope of this thesis

This thesis provides the mechanistic elucidation of the structural dynamics in electrocatalysts under bias based on structural and surface analyses, DFT/MD calculations and FEM simulations for the cathodic nanostructured electrocatalysts with complex morphologies. In the next chapter, I describe the experimental and theoretical methods used in the thesis. Chapter 3 explores the structural behaviour of Cu(II)-derived copper electrodes during the oxidation state change and well-defined Au and Pd branched nanoparticles (BNPs) and core-cage nanoparticles (CCs) without oxidation state changes using *ex situ* high-resolution scanning electron microscopy (SEM) and electrochemical surface analysis via underpotential deposition of lead (UPD). Chapter 4 explores the influence of RIs and nanostructure materials on the atomic mobility of the surface metal atoms in commonly used CO₂RR electrocatalyst, including Cu, Ag, Au, Pd, and Cu₃Pd, using DFT and MD simulations. Chapter 5 summarizes the state-of-the-art theoretical models for the E-field, $J_{electrolyte}$, electrode current density ($J_{electrode}$) simulations using FEM, proposes the protocols for reliable simulations of these electrochemical effects, and applies these models to study current density behavior of real electrochemical nanoparticles with complex morphologies, including anchored nanostar, nanostar, CCs and frames, and understand how their nanoscale shapes structurally affect the structural dynamics of the electrocatalysts. Chapter 6 provides the conclusions of the work presented in this thesis and the future works.

Chapter 2

Materials and methods

2.1 Materials

Copper (II) chloride (CuCl_2 , other details), polyvinylpyrrolidone (PVP), sodium borohydride (NaBH_4), were purchased from TCI America. Gold foil (99.95%, thickness 0.05mm), palladium foil (99.9%, thickness 0.025mm), sodium salicylate (NaSal, 99%), BrijL23, and palladium(II) chloride (PdCl_2 , 99.9%) were purchased from Alfa Aesar. Potassium bicarbonate (KHCO_3 , 99.5-101.0%), hexadecyltrimethylammonium bromide (CTAB, $\geq 99.0\%$, BioUltra, for molecular biology), cetylpyridinium chloride monohydrate (CPC, UPS grade), L-Ascorbic acid (AA, $\geq 99\%$, anhydrous, ACS grade), gold(III) chloride trihydrate ($\text{HAuCl}_4 \cdot 3\text{H}_2\text{O}$, $\geq 99.9\%$, used for the synthesis of Au BNPs), sodium borohydride (NaBH_4 , $\geq 98.0\%$), copper(II) sulfate (CuSO_4 , $\geq 99.99\%$), gold(III) chloride solution (HAuCl_4 , 99.99%, 30 wt. % solution in dilute HCl), hydrogen peroxide (H_2O_2 , 30 wt. % solution in H_2O), and sodium hydroxide (NaOH , $\geq 97\%$, ACS grade) were purchased from Sigma Aldrich. Hexadecyltrimethylammonium chloride (CTAC, $> 95.0\%$) was purchased from TCI America. Silver nitrate (AgNO_3 , 99.98%) was purchased from Engelhard Industries. Toray carbon paper (060, Wet Proofed) was purchased from FuelCellStore. All chemicals were used without further purification. All solutions were aqueous and freshly prepared before use. Ultrapure water (Millipore, $18.2 \text{ M}\Omega \cdot \text{cm}$) was used for all experiments.

2.2 Methods

2.2.1 Experimental methods

2.2.1.1 Synthesis of Cu(II)-nanoparticle-derived structures

To synthesize the Cu(II)-nanoparticle-derived structures, Cu(OH)₂ nanocages (Cu(II)-NCs) were first synthesized according to the procedure reported elsewhere.⁸¹ Briefly, a solution of CuCl₂ in ethanol (40 mL, 5.5 mM) was mixed with a solution of polyvinylpyrrolidone (PVP, M_n = 55000), and the resultant mixture was sonicated for 10 min, followed by stirring for 30 min at room temperature. Nanoparticle formation was initiated by a quick addition of a freshly prepared NaBH₄ solution (20 mL, 20 mM) to the mixture of CuCl₂ and PVP in ethanol under vigorous stirring. The solution color immediately changed to dark brown, the stirring was stopped, and the reaction mixture was aged without agitation for at least 48 h. In this method, the formation of Cu(II)-NCs proceeds through the oxidation of initially formed copper clusters.⁸¹ The final blue colloid of Cu(OH)₂ nanocages were purified with ethanol using three centrifugation cycles (7200 g, 10 min), and dispersed in 2 mL of methanol to provide [Cu]=0.085M final concentrated Cu(II)-NCs colloidal solution. Elongated 17±4 nm-wide bundles comprising the structure can be observed in high magnification SEM and TEM images. The formation of these bundles is due to the anisotropic nature of Cu(OH)₂, as it consists of complex chains formed through coordination of OH⁻ and Cu²⁺, while the bundle organization and the overall size of the particles is dictated by the stabilizing surfactant.⁸²

Then, Cu(II)-NCs were dispersed in CO₂-saturated 0.5 M KHCO₃ electrolyte, and reductive cyclic voltammetry (CV) was performed in a three-electrode configuration cell with carbon paper used as a working electrode. Cu(II)-NCs were electroreduced to Cu(II)-nanoparticle-derived structures once they came in contact with the working electrode, with their morphologies depending on the concentration of Cu(II)-NCs dispersed in the electrolyte.

2.2.1.2 Synthesis of Au CCs

The synthesis of Au-Au CCs was previously reported by our group elsewhere.⁸³ Briefly, (i) 3 nm Au nanoparticles were synthesized by the addition of 0.6 mL of ice-cold 10mM NaBH₄ solution into the vigorously stirred mixture of 0.167 mL of 15mM HAuCl₄ and 10 ml of aqueous 0.1M CTAB. After two hours of aging, seed solution was diluted to 50 mL; 6 mL of this solution was added into the diluted to 1 L mixture of 100mL of 0.2M CTAB, 2.66 mL of 15mM HAuCl₄, and 50 mL of 0.12M AA under

mild stirring. Resultant was left to react overnight undisturbed. As prepared Au octahedrons were concentrated to 5 mL, washed twice with water, and redispersed in 5 mL of water. (ii) Au@Ag CCs were synthesized by the consequent addition of 1 mL of 10mM AgNO₃ and 4 mL of 1M AA into the preheated to 60 °C mixture of 2.5 mL of concentrated Au octahedrons and 5 mL of 0.3 M aqueous CPC solution. Reaction was left to proceed under intense stirring on the thermomixer for 1h, then cooled down, washed once, and redispersed in 62.5 mL of water. (iii) 0.1 mL of 1mM HAuCl₄ was added dropwise into 1 mL of the Au@Ag cubes at a rate of 2 mL/min under vigorous stirring on thermomixer, followed by the addition of 0.05 mL of H₂O₂. Resultant – Au-Au CCs – were washed once at a high speed, once at a low speed, concentrated, and used as prepared for the electrode preparation.

2.2.1.3 Synthesis of Pd CCs

Pd CCs were synthesized following a modified procedure described for the synthesis of Au CCs, where in step (iii) 0.1 mL of the 1mM Na₂PdCl₄ was used instead of HAuCl₄ and in step (ii) surfactant-rich solution was used to top up Ag cubes. Specifically, when 0.1M CTAC solution was used, a more closed cage structured was obtained (a) and when 0.1M CTAB solution was used more open frame-like cage structure was obtained (b).

2.2.1.4 Synthesis of Au BNPs

Au BNPs were prepared according to the previously reported procedure.⁸⁴ Au seeds were synthesized by the addition of the 1 mL ice-cold 100mM NaBH₄ into the mixture of 1 mL of 10mM HAuCl₄, 1 mL of 10mM sodium citrate, and 36 mL of water under stirring. The resulting mixture was left undisturbed for 3 hours. Au BNP growth has been done in two steps. First, 0.1 mL of Au seeds were added to the aqueous mixture of 1 mL of 0.2M BrijL23, 1 mL of 0.1 M CTAB, 0.08 mL of 10 mM HAuCl₄, 0.01 mL of 5mM AgNO₃, 0.2 mL of NaSal, and 0.02 mL of 0.1 M AA. Second, 0.1 mL of the solution that was prepared on the first step was added to the mixture of 10 mL of 0.2 M BrijL23, 10 mL of 0.1 M CTAB, 0.8 mL of 10 mM HAuCl₄, 0.1 mL of 5 mM AgNO₃, 2 mL of NaSal, and 0.2 mL of 0.1 M AA. Resultant was vigorously shaken for 1 min, left undisturbed for 8 h, washed twice, concentrated, and then used for the electrode preparation.

For the small Au BNPs, they were synthesized following the procedure for Au BNPs, but addition of NaSal was replaced by the addition of equimolar AA.

2.2.1.5 Synthesis of Pd BNPs

The synthesis was performed according to the procedure reported elsewhere.⁸⁵ Firstly, Pd polygonal seeds were synthesized. 345 mg of CTAB was dissolved in 10 mL of 0.25 mM solution of Na₂PdCl₄ in a 50 mL two-neck round-bottom flask, the solution was bubbled with Ar for 30 minutes under stirring at 30 °C, followed by the injection of 0.22 mL of 15 mM ice-cold NaBH₄ aqueous solution. Then 0.168 mL of this solution was added to the mixture of 690 mg CTAB, 20 mL of 0.25 mM Na₂PdCl₄, and 0.156 mL of 0.1 M AA. Resultant was shaken for 1 minute and left undisturbed for 2 h. Secondly, seed-mediated growth of branched Pd nanoparticles was performed. 1g of CTAB was dissolved in 6.8 mL of water and stirred at 30 °C, then 1 mL of 100 mM CuSO₄ was added, followed by the consequent addition of 3.2 mL of a solution containing 100 mM of Na₂PdCl₄ and 0.25 M of HCl, and 10 mL of the polygonal seeds, and 5 mL of 1 M AA. Resulting mixture was stirred for 24 hours at 45 °C, washed 2 times, concentrated, and then used for the electrode preparation.

2.2.1.6 Electrode fabrication

Fabrication of the working electrodes with Cu(II)-nanoparticle-derived structures

To prepare a series of electrodes with different distribution density of the Cu(II)-nanoparticle-derived structures at the surface, solution regime (a) and spin-coating regime (b) were used:

(a) In the solution regime, a certain volume of the concentrated Cu(II)-NCs solution in methanol was centrifuged to remove methanol and subsequently dried, following redispersion and quick sonication in 50 ml of CO₂-saturated 0.5M KHCO₃ to obtain a homogeneous solution. The final concentration of Cu(II)-NCs in the series of experiments varied from [Cu]=0.0001-0.02 M. This solution was transferred into a three-electrode configuration cell with carbon paper (typical working area: 0.5 cm²), Pt mesh (2 cm²), and saturated Ag/AgCl as a working, counter and reference electrodes, respectively. The solution was purged with CO₂ for 15 min, followed by a number of CV scans at 20 mV/s, typically from 0 to -1.2 V (using Biologic SP300 electrochemical workstation). After the CV scans, the working electrode was removed from the electrolyte, rinsed thoroughly with deionized water, dried in air, and analyzed using SEM and other characterization methods, as described below. Variables controlling the material density at the electrode surface in this method included (I) precursor amount added to the electrolyte, as described above; (II) number of CV cycles: increasing the number of cycles resulted in the increase of material density; (III) CV potential range: increasing the range from 0V: -1.2 V to 0 V : -1.4 V resulted in the increase of material density obtained in the same number of CV scans.

(b) In the spin-coating regime, a certain volume (from 20 to 200 μL) of the concentrated Cu(II)-NCs solution in methanol was spin-coated at 3000 rpm on the surface of carbon paper (typical area: 0.5 cm^2), followed by the deposition of 10 μL of 0.5 wt% Nafion 117 solution in methanol. The resultant electrode and dried in a vacuum oven at 500 $^\circ\text{C}$ for 10 min. Finally, as-prepared working electrode was immersed into CO_2 -saturated 0.5M KHCO_3 in a three-electrode configuration cell with Pt mesh (2 cm^2) and saturated Ag/AgCl as a counter and reference electrodes, respectively. The electrolyte was purged with CO_2 for 15 min, followed by at least 20 CV scans at 20 mV/s, typically from 0 to -1.2 V, followed by applying -1.2 V for at least 10 min to allow for the system to reach equilibrium and ensure that all Cu(II) was electroreduced. Finally, working electrode was removed from the electrolyte, rinsed thoroughly with deionized water, dried in air, and analyzed using SEM and other characterization methods, as described below. The variable controlling the material density at the electrode surface in this method was the precursor amount spin-coated on the electrode surface.

Fabrication of the working electrodes with gold (Au CCs and BNPs) or palladium (Pd CCs and BNPs) nanoparticles

All electrodes were prepared by drop-casting a concentrated gold or palladium nanoparticle solution onto the gold or palladium foil substrate, respectively. For the product analysis of potentiostatic electrolysis, carbon paper was used as a support in place of noble metal foils to eliminate the contribution of the foil electrochemical activity and to increase the working electrode area for accurate product analysis. All prepared electrodes were dried, washed with methanol and water to clean their surface from the surfactants used in the nanoparticle synthesis, and then used as prepared or stored under argon. The thermogravimetric analysis measurements were conducted to assess the purity of the electrode surface from the organic surfactants using a Mettler-Toledo TGA/SDTA-851 thermobalance (room temperature to 1,000 $^\circ\text{C}$, at a heating rate of 10 $^\circ\text{C min}^{-1}$, under a nitrogen atmosphere; the sample weight was about 10 mg).

Unless otherwise specified, the particle loading of the fabricated electrodes was such that a full coverage of the substrate surface was achieved while minimizing the formation of multi-layer structures, which was confirmed by SEM analysis. Specifically, approximately 0.02 and 0.01 mg cm^{-2} mass loadings of gold and palladium CCs, respectively, were needed to achieve a densely packed monolayer coverage on a flat surface. Owing to a more complex geometry and packing mode, a three-times higher mass loading of BNPs compared with CCs was required to achieve full substrate coverage, as was determined empirically. When carbon paper was used as a support for potentiostatic electrolysis

and product analysis (see the paragraph above), the loading was increased sixfold for all particle types to account for the higher surface area of the support.

2.2.1.7 Electrochemical cell assembly

Electrochemical experiments were performed using a three-electrode system connected to an electrochemical workstation (Bio-Logic SP300). Au and Pd nanoparticles supported on Au and Pd foils, respectively, were used as a working electrode, Pt mesh was used as a counter electrode, and double junction saturated Ag/AgCl was used as a reference electrode. The experiments were performed in a gas-tight undivided cell. For electrolysis product analysis, a divided cell with Nafion 117 proton exchange membrane (FuelCellStore) was employed, which was integrated with in-line gas chromatographer. Gases were delivered at a rate of 20 sccm. All recorded potentials (vs Ag/AgCl) were converted to the reversible hydrogen electrode (RHE) scale using the Nernst equation: $E_{\text{RHE}} = E_{\text{Ag/AgCl}} + E_{\text{Ag/AgCl}}^0 + 0.059 \cdot \text{pH}$, where $E_{\text{Ag/AgCl}}^0 = 0.1976\text{V}$ at 25°C . All potentials are reported as measured, without resistance (iR) corrections.

For CO₂RR experiments, the reactions were performed in the constant potential regime – chronoamperometry (CA). CO₂ saturated 0.5 M KHCO₃ was used as an electrolyte, CO₂ was delivered into the electrochemical cell throughout all reaction. Cyclic voltammetry was performed prior to and following the potentiostatic electrolysis to assess the electrode performance in a wide potential range. After a certain time (30 min to 5 hours) reaction was stopped. Working electrode was washed with water and ethanol, dried, and characterized.

For HER experiments, the reactions were performed similarly to the CO₂ electroreduction, but Ar-saturated electrolyte and Ar bubbling was used instead of CO₂ saturated electrolyte and CO₂ bubbling.

2.2.1.8 Electrochemical assessment

For the electroreduction experiments performed for the Cu(II)-nanoparticle-derived nanoparticle, gas products were analyzed using MG5 GC system (SRI Instruments), equipped with a packed MolSieve 5A column and a packed Haysep D column. Argon (Praxair, 99.999%) was used as a carrier gas. A flame ionization detector, equipped with a methanizer, was used to quantify CO, methane, and ethylene yields, and a thermal conductivity detector was used to quantify hydrogen yield.

For the electroreduction experiments performed for the Au or Pd nanoparticles, gas products were analyzed using Agilent 7890B GC System, equipped with multiple columns sequence (two HP-PLOT

Q PT columns, HP-PLOT Molesieve column and deactivated fused silica restrictor) for efficient separation of electrolysis major products (H₂ and CO) and bypassing CO₂. The gas composition in the headspace of the cell was analyzed using in-line gas chromatography analysis every 20 minutes. The quantitative analysis of the gas products was performed using a thermal conductivity detector (TCD) and flame ionization detector (FID).

Concentration of liquid products was analyzed using Bruker 500 MHz nuclear magnetic resonance spectrometer. In a typical experiment, 0.8 mL sample of the electrolyte after 1 hour of electrolysis was mixed with 0.1 mL D₂O and 2×10⁻⁷ M dimethyl sulfoxide solution in water, used as an internal standard. 1D 1H spectra were measured using water suppression technique.

2.2.1.9 SEM analysis of structural changes

SEM imaging was performed using a Hitachi S-5200 microscope operating at 30 kV (0.5 nm resolution). Samples for imaging were prepared by attaching the electrode (a foil with deposited particles) to the SEM holder using conductive tape (NEM tape, Nisshin EM).

2.2.1.10 UPD analysis of structural and surface changes

The lead underpotential deposition was performed according to the procedure reported elsewhere.⁸⁶ Briefly, lead UPD was conducted by cyclic voltammetry in the argon-saturated solution of 0.1 M NaOH containing 1 mM Pb(NO₃)₂ over a potential range of -0.7 V to -0.2 V (versus Ag/AgCl) at a scan rate of 50 mV s⁻¹.

2.2.1.11 XPS analysis of surface chemistry changes

The surface analysis of the electrodes comprised of metal nanoparticles with different shapes was performed using X-ray photoelectron spectroscopy with an Thermo Fisher Scientific K-Alpha system.

2.2.2 DFT Calculations

All DFT calculations in this work were performed within Vienna Ab initio Simulation Package (VASP).⁸⁷⁻⁸⁹ The electronic exchange-correlation energy was treated by the spin-polarized generalized-gradient approximation (GGA) of Perdew-Burke-Ernzerhof (PBE).⁹⁰ The electron-ion interaction was described by projector augmented wave (PAW) potentials.^{91,92} The kinetic energy cutoff for the plane-wave expansion was set to 500 eV. For geometry optimizations, the convergence criteria of electronic

and ionic iterations were 10^{-5} eV and 10^{-2} eV \AA^{-1} , respectively. To decouple the interaction between periodic surfaces, 15 \AA of vacuum space was set among them in the z -direction.

For the DFT calculations in section 4.4, the $3 \times 3 \times 1$ and $4 \times 4 \times 1$ Monkhorst–Pack k -point meshes were applied for geometry optimization and electronic structural calculation, respectively. The (3×3) cells with four atomic layers were used to simulate various gold and palladium surfaces, including (111), (100), (110) and (211).

For the DFT calculations in section 4.5 and 4.6, the Monkhorst-Pack⁹³ k -point mesh was set to $(4 \times 4 \times 1)$. The metal surface was modelled using a (3×3) supercell structure with five atomic layers consisting of 45 metal atoms, including (111), (100), (110), and (211) fcc metal facets. To model $\text{Cu}_3\text{Pd}(100)$ surface, the bulk structure of Cu_3Pd (mp-580357) was first obtained from the Material Project.⁹⁴ Then $\text{Cu}_3\text{Pd}(100)$ surface was constructed based on the optimized Cu_3Pd bulk structure using a (3×3) supercell with four atomic layers consisting of 72 atoms.

2.2.2.1 Binding energy calculations

In section 4.4, the binding energy E_b was calculated as follows:

$$E_b = E_M + E_i - E_a \quad 2.1$$

where E_M is the energy of metal surface, E_i the energy of isolated reaction intermediates and E_a the energy of the adsorbed metal surface.

In section 4.5 and 4.6, the binding energy E_b of RIs on metal surface was calculated based on the optimized geometries of the metal surfaces bound RIs as follows:

$$E_b = E_a - (E_M + E_i) \quad 2.2$$

where E_a is the energy of reaction-intermediate-bound metal surface, E_M is the energy of the metal surface, and E_i is the energy of the gas phase reaction intermediate including H, OOH, and COOH, with $E_H = \frac{1}{2} E_{H_2}$, $E_{OOH} = \frac{1}{2} E_{H_2} + E_{O_2}$, and $E_{COOH} = \frac{1}{2} E_{H_2} + E_{CO_2}$. In essence, everything is referenced to CO_2 , H_2 , and O_2 to avoid the calculation of gas-phase fragments.

2.2.2.2 Vacancy formation calculations

The vacancy formation energy E_f of a pure metal surface and an intermediate-adsorbed metal surface were calculated according to equations 2.3 and 2.4, respectively:

$$E_f = E_{V_M} - E_M \quad 2.3$$

$$E_f = E_{V_M_X} - E_a \quad 2.4$$

where E_{V_M} is the energy of the metal surface with the metal atom adsorbed near the atomic vacancy and $E_{V_M_X}$ is the energy of a metal surface with an intermediate-bound metal atom adsorbed near the atomic vacancy.

2.2.2.3 Kinetic energy barrier calculations for vacancy formation or atom migration

The kinetic energy barrier E_{EB} for the vacancy formation and atom migration on different metal surfaces with and without the bound RI was calculated as follows:

$$E_{EB} = E_{TS} - E_{IS} \quad 2.5$$

where E_{IS} and E_{TS} are the energies of the initial state and transition state of the vacancy formation or atom migration on the metal surface, respectively. The initial-state structure was obtained from structure optimization; the transition-state structure was searched by using the climbing-image nudged elastic band (CI-NEB),⁶⁸ which were then verified by analysis of the normal modes and contain only one imaginary frequency.

2.2.2.4 Charge-density difference calculations

A charge-density difference^{95,96} was applied to investigate the charge transfer between the adsorbates and the catalyst surfaces. The charge-density differences were generated in the program named Visualization for Electronic and Structural Analysis (VESTA) by subtracting the charge density of isolated catalytic substrate and a gas-phase adsorbate from the total charge density of an adsorbed system. The charge density of the adsorbed system, the isolated catalytic substrate and gas-phased adsorbate was obtained from VASP output.

2.2.3 MD simulations

AIMD simulations were performed for metal clusters on metal (111) surfaces without and with different adsorbed RIs in the canonical ensemble (NVT) with the Nosé-Hoover thermostat.⁹⁷⁻⁹⁹ The initial velocities of the atoms were sampled from the Maxwell-Boltzmann distribution for the target temperature. Even though a single trajectory is computed for each of the systems, we have used time averaging in order to estimate ensemble average properties such as mean square displacements (MSDs), radial distribution functions (RDFs), and Lindemann indices. Our tests indicate that the systems are

ergodic enough for the timescales of interest here. The simulation was set to be 2000 steps with a 1.0 fs time step at 300 K. As it is hugely computational demanding for a large system with above 100 atoms, a (2×2×1) k-point mesh was used in the calculations for the Brillouin-zone integration. Based on the trajectory of the AIMD simulations, the displacement, MSD, RDF, Lindemann index, temperature, and heat capacity of the metal surfaces were calculated.

2.2.3.1 Mean square displacement (MSD) of the cluster

The mean squared displacement (MSD) for coordinate r is time dependent quantity defined as

$$MSD(t) = \langle |r(t) - r(t = 0)|^2 \rangle \quad 2.6$$

In practice, the ensemble average in the above definition is computed using time averaging and the MSD at some time step t_j is now,

$$MSD(t_j) = \frac{1}{N_i} \sum_i^{N_i} |r(t_{i+j}) - r(t_i)|^2 \quad 2.7$$

where N_i is the number of time origins used in the averaging procedure. In terms of the simulation time step Δ , the time origins are $t_i = i \cdot \Delta t$.

The coordinate r can be that of a single atom. It can also be a collective coordinate. In the present work, we have computed the $MSD(t)$ for all the atoms composing the substrate slab and averaged over those atoms. It should be noted that due to the fact the system is only periodic in the two x and y dimensions, only the x and y components are used in the definition of r for the substrate. In the case of the 13 metal atoms forming the initial cluster, the $MSD(t)$ is computed using the full 3-dimensional r vector of each atom. For each simulation, we have identified which of the 13 cluster atoms have the largest $MSD(t)$. For the RIs, the centre-of-mass of the RI was used as a coordinate.

2.2.3.2 Velocity autocorrelation function

The velocity autocorrelation function is defined as

$$C_{vv}(t) = \langle v(t = 0) \cdot v(t) \rangle \quad 2.8$$

where the velocity vector at time t , $v(t)$, is correlated to its value at time zero. The ensemble averaging is performed using the time averaging procedure described above for the MSD calculations. We have computed the velocity of the RI's Center of Mass (CMRI) in the present calculations. The $C_{vv}(t)$

correlation function is related to the RI's contribution to the density of states (DOS) via a Fourier transform.

2.2.3.3 Radial distribution function (RDF) of the cluster

The radial distribution function for a system of N atoms is defined as

$$g(r) = C \sum_{i < j} \langle \delta(r - r_{ij}) \rangle \quad 2.9$$

where C is a proportionality factor and r_{ij} is the distance between atoms i and j . The sum is over all pairs of atoms and the ensemble averaging is performed via time averaging as above. We have separately computed the $g(r)$'s of the substrate atoms, and those of the 13 metal atom clusters, and that of the atom distances of the RI's. The radial distribution function is a measure of the solid-like or liquid-like nature of a system. We observe that for the substrate, the $g(r)$ is that of a solid lattice in good agreement with literature values.¹⁰⁰ For the 13 atom clusters, the $g(r)$ is much less structured due to the fluxional nature of the cluster where the atoms are more mobile.

2.2.3.4 Lindemann indices of the cluster

As an additional measure of atom mobility, we have also computed the Lindemann index of the substrate and cluster atoms. The Lindemann index is defined as:

$$\lambda = \frac{1}{N-1} \sum_{i < j} \frac{\sqrt{\langle r_{ij}^2 \rangle - \langle r_{ij} \rangle^2}}{\langle r_{ij} \rangle} \quad 2.10$$

The quantity λ is a measure of how much the distance between a specific pair of atoms can grow. In a solid, atoms stay around their lattice sites and λ is small. However, for a system where atomic mobility is increased, λ will be larger. This is observed for the 13 atom clusters. For all the systems studied here, $\lambda_{cluster}$ is 2 to 3 times larger than $\lambda_{substrate}$. This is a clear indicator of the enhanced mobility of the cluster atoms compared to their substrate counterpart.

2.2.3.5 Averaged displacement of metal atoms in the cluster

The displacement $s_j(t)$ of the j^{th} metal atom in the cluster was calculated by comparing its position $r_j(t)$ at reaction time t with its initial position $r_j(0)$ according to:

$$s_j(t) = \|r_j(t) - r_j(0)\| = \sqrt{[(x_j(t) - x_j(0))^2 + (y_j(t) - y_j(0))^2 + (z_j(t) - z_j(0))^2]} \quad 2.11$$

Then the displacement of the metal cluster $s_{cluster}(t)$ at reaction time t was calculated by averaging the displacement of the cluster metal atoms according to:

$$s_{cluster}(t) = \frac{1}{13} \left[\sum_{j=1}^{j=13} d_j(t) \right] \quad 2.12$$

2.2.3.6 Displacement of the cluster center of mass (COM)

The displacement of the metal cluster COM $s_{cluster_com}(t)$ was calculated by comparing its COM $R(t)$ at reaction time t with its initial COM $R(0)$ according to:

$$s_{cluster_com}(t) = \frac{1}{M} \sum_{j=1}^{13} m_j r_j(t) - \frac{1}{M} \sum_{j=1}^{13} m_j r_j(0) \quad 2.13$$

where m_j is the mass of the j^{th} metal atom and $s_{cluster_com}(t) = \frac{1}{M} \sum_{j=1}^{13} m_j r_j(t) - \frac{1}{M} \sum_{j=1}^{13} m_j r_j(0)$ is the total mass of all of the atoms in the cluster.

2.2.3.7 Kinetic temperature of the cluster

The instantaneous temperature $T_j(t)$ of the j^{th} metal atom at reaction time t was calculated according to the equipartition theorem as follows:

$$T_j(t) = \frac{2}{3} \left[\frac{E_{KE-j}(t)}{k_B} \right] \quad 2.14$$

where $k_B = 1.38 \times 10^{-23} \text{ J} \cdot \text{K}^{-1}$ is the Boltzmann constant and $E_{KE-j}(t) = \frac{1}{2} m_j [v_{jx}^2(t) + v_{jy}^2(t) + v_{jz}^2(t)]$ is the kinetic energy of the j^{th} metal atom at time t . In the kinetic energy equation, m_j is the mass of the j^{th} metal atom and $v_{jx}(t)$, $v_{jy}(t)$, and $v_{jz}(t)$, are the speeds of the j^{th} metal atom along x , y , and z directions, respectively, at reaction time t . $v_{jx}(t)$ was calculated as follows:

$$v_{jx}(t) = [x_j(t+1) - x_j(t)]/1 \quad 2.15$$

$x_j(t)$ and $x_j(t+1)$ are the positions of the j^{th} atom at reaction time t and $t+1$, respectively, along the x direction. $v_{jy}(t)$ and $v_{jz}(t)$ were obtained with analogous equations for the y and z directions.

The temperatures of the metal cluster, the metal slab, and the overall system at reaction time t , $T_{cluster}(t)$, $T_{slab}(t)$, and $T_{sys}(t)$, were obtained by averaging the $T_j(t)$ of the metal atoms in the cluster, the slab, and the whole metal system, respectively.

2.2.3.8 Heat capacity of the metal system

The kinetic energy $E_{KE}(t)$ of the whole metal system at the reaction time t is the sum of the kinetic energy of each atom,

$$E_{KE}(t) = \sum_j E_{KE_j}(t) \quad 2.16$$

Therefore, the total energy $E_{tot}(t)$ of the whole system at reaction time t was calculated as follows:

$$E_{tot}(t) = E_{KE}(t) + E_{PE}(t) \quad 2.17$$

where $E_{PE}(t)$ is the potential energy of the whole metal system, which can be collected from VASP output.

The total energy $E_{tot_a}(t)$ of each atom at reaction time t was set to be

$$E_{tot_a}(t) = E_{tot}(t)/n \quad 2.18$$

where n is the number of the metal atoms in the system.

The heat capacity C_V of the metal system at the reaction time t was calculated according to the following equation:

$$C_V = \frac{\langle E_{tot_a}(t)^2 \rangle - \langle E_{tot_a}(t) \rangle^2}{k_B T_{sys}^2} * n \quad 2.19$$

where $\langle E_{tot_a}(t)^2 \rangle$ is the expected value of the squared $E_{tot_a}(t)$ and $\langle E_{tot_a}(t) \rangle^2$ is the square of the expected value of $E_{tot_a}(t)$. They were calculated as follows:

$$\langle E_{tot_a}(t)^2 \rangle = \frac{\sum_{t=t_1}^{t=t_2} E_{tot_a}(t)^2}{m} \quad 2.20$$

$$\langle E_{tot_a}(t) \rangle^2 = \left[\frac{\sum_{t=t_1}^{t=t_2} E_{tot_a}(t)}{m} \right]^2 \quad 2.21$$

where m is the number of the reaction steps between t_1 and t_2 . t_1 and t_2 are the time points when the system first reaches an equilibrated state, and when the simulation was finished, respectively.

2.2.4 FEM simulations

All FEM simulations in this work were performed in COMSOL Multiphysics package based on the finite-element-method solver (<https://www.comsol.com/>). For different purposes described in the text, six interfaces were applied in the simulation, including ‘Primary Current Distribution’, ‘Secondary Current Distribution’, ‘Tertiary Current Distribution’, ‘Transport of Diluted Species’, ‘Electrostatics’, as well as ‘Electric Currents’, and the details of these interfaces and the corresponding electrochemical theories are also discussed.

2.2.4.1 EDL simulation

Poisson-Boltzmann model

In the GCS model, the distribution of ionic species in the diffuse layer at equilibrium is determined by the Boltzmann distribution:¹⁰¹

$$\rho(\mathbf{r}) = \sum_i \rho_i(\mathbf{r}) = \sum_i z_i F C_i^* e^{-\left(\frac{z_i F \phi(\mathbf{r})}{RT}\right)} \quad 2.22$$

In equation (2.22), $\rho(\mathbf{r})$ denotes the charge density within the electrolyte; z_i and C_i^* are the charge and the bulk concentration of the i^{th} ionic species, respectively; T is the temperature of the electrolyte; F and R is the Faradaic constant and the ideal gas constant, respectively. The unevenly distributed charged ionic species could generate a non-uniform potential in the diffuse layer, which is denoted as $\phi(\mathbf{r})$. The local potential profile $\phi(\mathbf{r})$ is related with the charge density $\rho(\mathbf{r})$ as described by the Poisson equation:¹⁰¹

$$\nabla \cdot (\varepsilon_0 \varepsilon_r \nabla \phi(\mathbf{r})) = -\rho(\mathbf{r}) \quad 2.23$$

In equation (2.23), ε_0 and ε_r are the vacuum permittivity and the relative permittivity of the solution, respectively.

To solve the $\rho(\mathbf{r})$ and $\phi(\mathbf{r})$ numerically, equation (2.22) has to combined with equation (2.23) to get the equation (2.24), which is the well-known Poisson-Boltzmann (PB) equation.¹⁰¹

$$\nabla \cdot (\varepsilon_0 \varepsilon_r \nabla \phi(\mathbf{r})) = - \sum_i z_i F C_i^* e^{-\left(\frac{z_i F}{RT} \phi(\mathbf{r})\right)} \quad 2.24$$

However, for a symmetric binary electrolyte, where valence charge (z_+) and bulk concentration (C_+^*) of the cation are equal to that (z_- and C_-^*) of the anion ($z_+ = -z_-$, $C_+^* = C_-^*$),- equation (2.24) can be simplified to a hyperbolic function:^{101,102}

$$\nabla \cdot (\varepsilon_0 \varepsilon_r \nabla \phi(\mathbf{r})) = 2zFC^* \sinh\left(\frac{zF}{RT} \phi(\mathbf{r})\right) \quad 2.25$$

The charge density at Outer Helmholtz plane (OHP), σ_{OHP} , in GCS model is given by:

$$\sigma_{OHP} = \frac{\varepsilon_0 \varepsilon_r (\phi_M - \phi_{OHP})}{d_s} \quad 2.26$$

where ϕ_M and ϕ_{OHP} are the potentials at the electrode surface and OHP, respectively; d_s denotes the Stern layer thickness. Since there is no charge presented in the Stern layer, the potential is assumed to drop linearly from ϕ_M to ϕ_{OHP} in the Stern layer.

Poisson-Nernst-Plank model

The distribution of ionic species in diffuse layer at the steady-state conditions can also be described by the Nernst-Plank (NP) equation. Provided that the magnetic interaction and convection are absent, and the electrolyte is inert (i.e., no electrolysis is associated with the ionic species), the resulting NP equation has the following form:¹⁰³

$$\frac{\partial C_i(\mathbf{r})}{\partial t} = -\nabla \cdot \mathbf{J}_i(\mathbf{r}) = -\nabla \cdot \left(-D_i \nabla C_i(\mathbf{r}) - \frac{D_i z_i F C_i(\mathbf{r})}{RT} \nabla \phi(\mathbf{r}) \right) = 0 \quad 2.27$$

In equation (2.27), $J_i(\mathbf{r})$ and D_i refer to the total flux and the diffusion constant for the i^{th} ionic species, respectively, while the other terms are defined the same way as in the PB equation. Similarly to the PB model, equation (2.27) has to combine with the Poisson equation given by equation (2.28) to solve $C_i(\mathbf{r})$ and $\phi(\mathbf{r})$ numerically. The combination of equation (2.27) and (2.28) is the so-called Poisson-Nernst-Plank (PNP) model.¹⁰³

$$\nabla \cdot (\varepsilon_0 \varepsilon_r \nabla \phi(\mathbf{r})) = -F \sum_i z_i C_i \quad 2.28$$

Modified Poisson-Boltzmann model

Mathematically, the maximum concentration of the species in the space can be expressed by:

$$C_{max} = \sum_i \frac{1}{N_A a_i^3} \quad 2.29$$

Here N_A is the Avogadro constant and a_i is the effective solvent diameter of the i^{th} species.

If we further assume that the effective solvent diameter of all species is the same (and is denoted a), the entropy of the electrolyte system considering the steric effect is:¹⁰³

$$S = -\frac{k_B}{a^3} \int d\mathbf{r} \left(\sum_i N_A a^3 C_i \ln(N_A a^3 C_i) + \left(1 - \sum_i N_A a^3 C_i \right) \ln \left(1 - \sum_i N_A a^3 C_i \right) \right) \quad 2.30$$

In equation (2.30), the first term is the entropy of each species. The second term is the entropy of the solvent molecules, which can introduce steric corrections to the PB or PNP equations. Here, the term of $1 - \sum_i N_A a^3 C_i$ can be regarded as the probability for a system with the concentration of species $\sum_i C_i$, while the term of $\ln(1 - \sum_i N_A a^3 C_i)$ is the interaction intensity between species in this system. When $\sum_i C_i$ approaches C_{max} , the terms of $1 - \sum_i N_A a^3 C_i$ and $\ln(1 - \sum_i N_A a^3 C_i)$ reach zero and infinity, respectively, meaning that in this system the interaction between species is infinitely strong and its probability is zero. Therefore, the concentration of the species in the simulations cannot beyond C_{max} .

To take into account the steric effect, equation (2.30) is incorporated into the PB model as demonstrated in the work of Borukhov et al.,¹⁰⁴ generating modified PB (MPB) model. For a symmetric binary electrolyte where $z_+ = -z_- = z$, the resulting MPB equation becomes equation (2.31).

$$\nabla \cdot (\varepsilon_0 \varepsilon_r \nabla \phi(\mathbf{r})) = -ze \frac{N_A C^* e^{-\frac{zF\phi(\mathbf{r})}{RT}} - N_A C^* e^{\frac{zF\phi(\mathbf{r})}{RT}}}{1 - 2zN_A a^3 C^* + N_A a^3 C^* e^{-\frac{zF\phi(\mathbf{r})}{RT}} + N_A a^3 C^* e^{\frac{zF\phi(\mathbf{r})}{RT}}} \quad 2.31$$

For $KHCO_3$, $z = 1$, and equation 2.31 can be further simplified to a hyperbolic form:

$$\nabla \cdot (\varepsilon_0 \varepsilon_r \nabla \phi(\mathbf{r})) = \frac{2eN_A C^* \sinh\left(\frac{F\phi(\mathbf{r})}{RT}\right)}{1 + 2N_A a^3 C^* \sinh^2\left(\frac{F\phi(\mathbf{r})}{2RT}\right)} \quad 2.32$$

Modified Poisson-Nernst-Plank model

Similar to the MPB equation, equation (2.30) is incorporated into the PNP models as demonstrated in the work of Kilic et al.,¹⁰³ generating modified PNP (General Modified PNP, or GMPNP) models. For a symmetric binary electrolyte where $z_+ = -z_- = z$, the resulting MPB and GMPNP equations become equation (2.33), respectively.

$$\frac{\partial C_i}{\partial t} = -\nabla \cdot \mathbf{J}_i = -\nabla \cdot \left(D_i \nabla C_i - \frac{D_i C_i z F}{RT} \nabla \phi(\mathbf{r}) - D_i C_i \frac{N_A a^3 \sum_i \nabla C_i}{1 - N_A a^3 \sum_i C_i} \right) = 0 \quad 2.33$$

Booth model

To account for the dependence of the dielectric permittivity on E-field, the Booth model, equation (2.34), can be employed.^{102,105,106}

$$\varepsilon_r(E; \beta) = n^2 + (\varepsilon_r(0) - n^2) \frac{3}{\beta E} \left[\coth(\beta E) - \frac{1}{\beta E} \right] \quad 2.34$$

In equation (2.34), $E = |-\nabla \phi(\mathbf{r})|$ is the local E-field strength, n is the electrolyte refractive index, and β is a parameter given by:¹⁰⁷

$$\beta = \frac{5\mu}{2kT} (n^2 + 2) \quad 2.35$$

where μ is the dipole moment of the water molecule.

In addition, there is another way of expressing the Booth model, equation (2.34a):¹⁰⁸

$$\varepsilon_r(E) = n^2 + \frac{a}{|E|} L(b|E|), L(x) = \coth(x) - 1/x \quad 2.34a$$

$$a = \frac{7 N_0 \mu (n^2 + 2)}{3\sqrt{73} \varepsilon_0}, b = \frac{\sqrt{73} \mu (n^2 + 2)}{6kT}$$

where n is the optical refractive index, $N_0 = 3.343 \times 10^{28} \text{ m}^{-3}$ is the number of molecules per unit volume, μ is the water molecule dipole moment, k is the Boltzmann constant, T is the absolute temperature, L is the Langevin function. To make sure that the ε_r of electrolyte equals to 78 in regions of weak electric field, μ was set up to $6.6621 \times 10^{-30} \text{ C m}$.¹⁰⁸

2.2.4.2 $J_{\text{electrolyte}}$ calculations

Nernst equation

The overall free energy change of the half-cell reaction, ΔG_r , on the electrode surface, is usually expressed in electrochemistry in terms of the electrode potential, ϕ :¹⁰¹

$$\Delta G_r = (G_{CO} - G_{CO_2}) = -nF\phi \quad 2.36$$

In equation (2.36), n is the number of electrons transferred in the half-cell reaction and F is the Faradaic constant.

For a half-cell reaction, its electrode potential, ϕ , is governed by the Nernst equation:¹⁰¹

$$\phi_{CO_2RR} = \phi_{CO_2RR}^0 + \frac{RT}{nF} \ln \left(\frac{\gamma_{CO_2}}{\gamma_{CO}} \right) + \frac{RT}{nF} \ln \left(\frac{C_{CO_2}}{C_{CO}} \right) \quad 2.37$$

In equation (2.37), $\phi_{CO_2RR}^0$ is the standard potential of CO₂RR, γ and C are the activity coefficient and the concentration of the species, respectively. However, dealing with the activities in the evaluation of the electrode potential is complicated by the fact that the activity coefficients remain unknown for most species. One way to avoid dealing with the activities in the simulations is to rearrange equation (2.37) into equation (2.38):

$$\phi_{CO_2RR} = \phi_{CO_2RR}^{0'} + \frac{RT}{nF} \ln \left(\frac{C_{CO_2}}{C_{CO}} \right) \quad 2.38$$

In equation (2.38), $\phi_{CO_2RR}^{0'}$ is the formal potential of CO₂RR, which is given by:

$$\phi_{CO_2RR}^{0'} = \phi_{CO_2RR}^0 + \frac{RT}{nF} \ln \left(\frac{\gamma_{CO_2}}{\gamma_{CO}} \right) \quad 2.39$$

In contrast to $\phi_{CO_2RR}^0$, $\phi_{CO_2RR}^{0'}$ can be measured experimentally, when the ratio of C_{CO_2}/C_{CO} in equation is equal to unity.

Generalized Butler-Volmer equation

The dependence of the reaction current on the activation overpotential η can be characterized by the various Butler-Volmer equations. Generalized Butler-Volmer equation is given by equation (2.40):¹⁰¹

$$i(\eta) = i_0 \left\{ \left(\frac{C_O(0,t)}{C_O^*} \right) e^{-\frac{\alpha n F \eta}{RT}} - \left(\frac{C_R(0,t)}{C_R^*} \right) e^{\frac{(1-\alpha) n F \eta}{RT}} \right\} \quad 2.40$$

where i_0 is the exchange current; $C(0,t)$ and C^* terms denote the concentration of a species at the electrode surface and in the bulk electrolyte, respectively; α is the transfer coefficient, which is a

measure of the symmetry of the energy barrier; T is the temperature, and F, R are the Faradaic constant and the ideal gas constant, respectively.

Standard Butler-Volmer equation

Standard Butler-Volmer equation is given by equation (2.41):

$$i(\eta) = i_0 \left\{ e^{-\frac{\alpha n F \eta}{RT}} - e^{\frac{(1-\alpha) n F \eta}{RT}} \right\} \quad 2.41$$

Linearized Butler-Volmer equation

Linearized Butler-Volmer equation is given by equation (2.42):

$$i(\eta) = -\frac{i_0 n F \eta}{RT} \quad 2.42$$

Tafel equation

Tafel equation is given by equation (2.43):

$$i(\eta) = i_0 e^{\frac{\alpha n F \eta}{RT}} \quad 2.43$$

2.2.4.3 $J_{electrode}$ calculations

The current density in a metal obeys Ohm's law, therefore, $J_{electrode}$ is solved as follows:

$$J_{electrode} = \sigma E \quad 2.44$$

where the σ is electrical conductivity of the material, which is $4.42 \times 10^7 \text{ S m}^{-1}$ for gold¹⁰⁹ and $0.93 \times 10^7 \text{ S m}^{-1}$ for palladium.¹¹⁰

2.2.4.4 Heat power density and temperature calculations

The heat power density is calculated as follows:

$$Q = J_{electrode}^2 \rho \quad 2.45$$

where ρ is the resistivity of a metal.

To calculate the temperature of the electrode, the Au branched nanoparticle is defined as the heat source, with the heat power density as described above. The convective heat flux is applied to the liquid-solid interface of the electrolyte and the electrode according to the equation

$$q_0 = h \cdot (T_{ext} - T) \quad 2.46$$

where h is the heat transfer coefficient of the electrolyte, and T_{ext} and T are the temperature of the electrolyte and the electrode, respectively. h was set to $50 \text{ W}/(\text{m}^2 \cdot \text{K})$. T_{ext} is assumed to be a constant of 293.15 K due to the high heat capacity of water. To simulate the temperature profile of Au branched electrode, I assume that the substrate is covered by monolayer of Au branched nanoparticles. Therefore, the electrode can be represented by a periodic model, in which the computation domain can be restricted to a single unit cell.

Chapter 3

Experimental observations of structural dynamics in various nanostructured catalysts

Partially reprinted with permission from *Phys.Chem.Chem.Phys.* **2019**, 21,5894. Copyright 2019, Royal Society of Chemistry

Contribution: performed electrochemical experiments and product analysis.

Partially reprinted with permission from *Nature Catal.* **2021**, 4, 479. Copyright 2021, Springer Nature.

Contribution: designed and carried out the DFT calculations and the FEM simulations, assisted in manuscript writing.

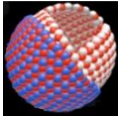
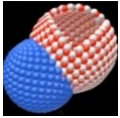



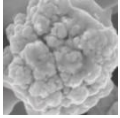
3.1 Introduction

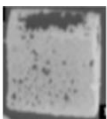
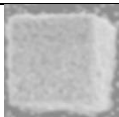


Cathodic nanoscale electrocatalysts with structural complexity often show outstanding catalytic activity and selectivity towards target products.⁷ Current advancements in nanoparticle synthesis have enabled control over nanoscale shape to a high degree, with complex nanostructures ranging from cages, frames, cavities, multi-shell hollow and yolk-shell particles to various branched morphologies being reported as superior electrocatalysts compared with their more geometrically simple counterparts (Tables 3.1–3.3). More complex structures, including three-dimensional hierarchic nanoflowers,⁴³ nanoflakes,⁴⁴ tetrapods,³⁹ porous foams⁴⁵ and cage-like porous spheres,⁴³ that have been used as catalysts for the electroreduction of CO₂ (CO₂RR)^{13,39–42,44,45} and O₂ (ORR)⁷⁵ and the hydrogen evolution reaction (HER).⁴³ Considering the application scope of cathodic nanoelectrocatalysts with complex shapes, understanding the factors determining their structural stability in the course of electrocatalysis is of paramount importance to the field. So far, only a fraction of the reports on nanocatalysts with complex shapes has included notes on their structural stability or observed morphological changes after continuous electrolysis (Tables 3.1–3.3), with somewhat contradictory and inconclusive general trends.

The structural transformations could occur in solid state materials with and without oxidation state change. Typically, the oxidation state change occurs in the structural transformation of oxide- and hydroxide-derived metals such as copper, which have been reported as effective copper electrocatalysts with higher selectivity towards multicarbon products compared to polycrystalline copper.^{45,50,51} Oxide-hydroxide-derived copper catalysts is fabricated by electrochemically reducing the Cu(II), in which the unique structural and compositional features could form, including grain boundaries,^{52,53} exposed surface facets,⁵⁴ presence of Cu(I) species (or subsurface oxygen),⁹ and high-curvature sites.¹³ These active features could benefit from field-induced reagent (FIRC) concentration that enhances CO₂RR. Moreover, it has been recently discovered that metal Cu and other metal nanoparticles⁵⁵⁻⁵⁹ can also undergo significant structural transformation in the course of CO₂RR with drastic effect on their catalytic performance, suggesting the prominent mobility of the nanocatalyst material during electrolysis which is not unique to the electroreduction of oxidized copper. Further structural and mechanistic elucidation of the structural dynamics under electrical bias is necessary for engineering long-term catalyst performance and stability in CO₂RR and beyond.

Here I explore the structural behavior of hydroxide-derived copper during CO₂RR¹¹¹ and well-defined gold and palladium core cages (CCs) and branched nanoparticles (BNPs) in the course of CO₂RR and HER conditions using *ex situ* high-resolution scanning electron microscopy (SEM) and electrochemical surface analysis via underpotential deposition (UPD)⁷¹. I found that structural evolution of Cu(II)-nanoparticle-derived copper electrodes with oxidation state change under CO₂RR conditions is directed by the interplay between facet stabilization by CO₂RR intermediates, electrochemical Ostwald ripening and field-induced reagent concentration (FIRC) effect; morphological changes of well-defined gold and palladium nanoparticles without oxidation state change can be accelerated by the RIs of the electrolysis reactions, with the extent and rates of structural transformations depending on the material of the nanostructure and the nature of the environment and electrocatalytic reaction at its surface.




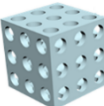



Table 3.1: Hollow and porous nanostructures as electrocatalysts for CO₂RR.


Electrocatalyst composition	Overall Size	Structure	Structure description	Test of stability	Ref.
CuSnO₂	26.5±3.5 nm		Hollow nanospheres	Stable current density and FEs of the products during 10h electrolysis in CO ₂ -saturated 0.1M KHCO ₃ at -0.7V vs RHE. No significant changes in the morphology of nanoparticles (TEM data) were observed.	29
CuSnO₂	32.5±4.5 nm		Cu NPs/Hollow SnO ₂ Janus structures	Stable current density and FEs of the products during 10h electrolysis in CO ₂ -saturated 0.1M KHCO ₃ at -0.7V vs RHE. Changes in morphology have not been studied.	29
AuCu	50-100 nm		Thin-walled hollow nanospheres	Current density and FE of the CO decreased slightly during 12h electrolysis in CO ₂ -saturated 0.5M KHCO ₃ at -0.7V vs RHE. No obvious changes in the morphology of nanoparticles (TEM data) were observed.	30
Cu	110±20 nm		Nanocavities	Current density and FEs of C ₃ -products significantly decreased after 2.5h of electrolysis in a flow-cell configuration with GDE (1M KOH electrolyte) at -0.56V vs RHE. Catalyst reconstructed to form aggregated Cu nanoparticles (SEM data).	14
Au	120 nm		Concave rhombic dodecahedral nanoparticles	Current density was stable during 8.3h electrolysis in CO ₂ -saturated 0.5M KHCO ₃ (potential not specified). The concave features were maintained (SEM data).	28
Cu	≈ 700 nm		Porous microspheres	Current density increased without significant changes in average FE of C ₂ H ₄ during 10h electrolysis in CO ₂ -saturated 0.05M KHCO ₃ + 0.05M KI at -1.1V vs RHE. No significant changes in the morphology of nanoparticles (SEM data) were observed.	36

Au	≈ 1 μm		Hollow cubic NPs	Stability of the catalyst has not been studied.	31
Cu₂O@Au	≈ 1 μm		Hollow cubic nanocomposites	Stability of the catalyst has not been studied.	31
Ag	≈ 1.2 μm		Hollow porous microspheres	Current density was stable, and FE of CO slightly decreased after 10h of electrolysis in 0.1M NaHCO ₃ at -0.845V vs RHE. No significant changes in the morphology of nanoparticles (SEM and TEM data) were observed.	32
(CoOH)₂CO₃	≈ 2 μm		Hollow urchin-like structures	Stable current density and FE of MeOH during 10h electrolysis in CO ₂ -saturated 0.1M NaHCO ₃ at -0.25V vs RHE. No significant changes in the morphology of nanoparticles (SEM and TEM data) were observed.	37

Reprinted from the cited papers with the permission from Springer Nature, Royal Society of Chemistry, The American Chemical Society, John Wiley and Sons, and Nanoscale Research Letters.

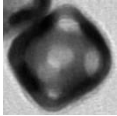
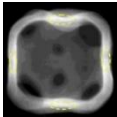



Table 3.2: Hollow and porous nanostructures as electrocatalysts for HER.

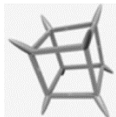
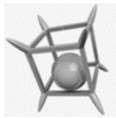


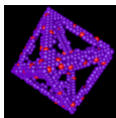
Electrocatalyst composition	Size	Structure	Structure description	Test of stability	Ref.
PtCu	17.7 nm		Dodecahedral nanoframes	Little changes in polarization curves after 1000 CV cycles. Current density decreased slightly after 2.8h electrolysis in 0.5M H ₂ SO ₄ at -0.05V vs RHE. No significant changes in the structure of nanoparticles, except the broken of some ultrathin edges (TEM data).	26
PdPt	17.5-21.5 nm		Bilayer nanocages with sub-nanometer thin shells	The mass activities of nanocages given as kinetic current densities at -0.05V vs RHE reduced by 24% after 10000 CV cycles in 0.5M H ₂ SO ₄ . Changes in morphology have not been studied.	15
CuNi	62 nm		Mesoporous nanocages	Little changes in polarization curves after 2000 CV cycles. Current density slightly during 8h electrolysis in 1M KOH at -0.022V vs RHE. Changes in morphology have not been studied.	16
RuCoP	200 nm		Ru NPs doped into CoP nanocage	Little changes in polarization curves after 1000 CV cycles in 0.5M H ₂ SO ₄ . Initial current was decreased by 16% after continuous operation of 10h . No significant changes in the morphology of nanoparticles (TEM data) were observed.	17
CoFeSeP	300 nm		Mesoporous nanostructured frames	No changes in polarization curves after 1000 CV cycles in 0.5M H ₂ SO ₄ . Current density was relatively stable during 40h electrolysis in 0.5M H ₂ SO ₄ at constant overpotential of 0.07V vs RHE. No significant changes in the morphology of nanoparticles (SEM data) were observed.	27
CoSP	450 nm		Yolk-shell microspheres	Current density was stable during 20h electrolysis in 0.5M H ₂ SO ₄ at constant overpotential of 0.135V vs RHE. Changes in morphology have not been studied.	34
NiCo₂S₄	550 nm		Double-shelled hollow nanospheres	Little changes in polarization curves after 2000 CV cycles in 1M KOH. No significant changes in the morphology of nanoparticles (SEM and TEM data) were observed.	35

CoSe₂/(NiCo) Se₂	400-600 nm		Box-in-box hollow nanocubes	Little changes in polarization curves after 2000 CV cycles in 1M NaClO ₄ . Small changes in the morphology of nanoparticles (SEM and TEM data) were observed.	33
---	------------	---	-----------------------------	---	----

Reprinted from the cited papers with the permission from The American Chemical Society, Springer Nature, and Royal Society of Chemistry.

Table 3.3: Hollow and porous nanostructures as electrocatalysts for NRR and ORR.

Electrocatalyst composition	Size	Structure	Structure description	Test of stability	Ref.
Electrocatalysts for <i>Nitrogen</i> Reduction Reaction					
Au	35 nm		Nanocages	Current density was stable, and FE of the NH ₃ decreased slightly during 12h (5 runs) electrolysis in N ₂ -saturated 0.5M LiClO ₄ at -0.4V vs RHE. At more negative than -0.6V potentials current density was not stable. Changes in morphology have not been studied.	18
Au-Ag₂O	40 nm		Bimetallic nanocages	Current density was relatively stable during 12h electrolysis in N ₂ -saturated 0.5M LiClO ₄ at -0.3V and -0.4V vs RHE, but not stable at -0.5V . Changes in morphology have not been studied.	19
Electrocatalysts for <i>Oxygen</i> Reduction Reaction					
Pt₄PdCu_{0.4}	10 nm		Alloy nanoframes	Little changes in polarization curves after 2000 CV cycles in 0.1M HClO ₄ . Nanoframes largely maintained original structures while a few nanoboxes have been slightly fractured after stability test (TEM data).	20
Pt	18nm		Cubic nanoframes	No significant aggregation after 30000 CV cycles in O ₂ sat. 0.1M HClO ₄ . Nanoframes slightly deformed, but their open structure was still retained (TEM data) after stability test. However, the cubic nanoframes shrank in terms of particle size and the average thickness of their ridges increased from 1.7 to 2.6 nm.	21
PtNi₃	20.1±1.9 nm		Nanoframes	Negligible changes in polarization curves after 10000 CV cycles in 0.1M HClO ₄ . No significant changes in morphology of nanoparticles	22

				(bright- and dark-field STEM data) were observed.	
PtCu	20 nm		Octopod nanoframes	Small changes in polarization curves after 10000 CV cycles in O ₂ sat. 0.1M HClO ₄ . No significant changes in the morphology of nanoparticles (STEM and TEM data) were observed.	23
PtCuPd	20 nm		Yolk-shell octopod nanoframe	Significant changes in polarization curves after 10000 CV cycles in O ₂ sat. 0.1M HClO ₄ . Changes in morphology have not been studied.	23
CuPt	30 nm		Rhombic dodecahedral nanoframes	A few segregated nanocrystals were observed (TEM data) after 1200 CV cycles in O ₂ sat. 0.1M HClO ₄ , but frame skeletons were still well-defined.	24
CuPt	30 nm		Spiny rhombic dodecahedral nanoframes	Nanoparticles distorted in their frame structure (TEM data) after 1200 CV cycles in O ₂ sat. 0.1M HClO ₄ , and the extended {100} vertices evolved rounded.	24
PtCu	40 nm		Spiny alloy octahedral nanoframes	Small changes in polarization curves after 8000 CV cycles in O ₂ sat. 0.1M HClO ₄ . The XPS characterization showed that the chemical state of PtCu structure did not change. No significant changes in the morphology of nanoparticles (TEM data) were observed.	25

Reprinted from the cited papers with the permission from Elsevier, The American Chemical Society, John Wiley and Sons, and American Association for the Advancement of Science.

3.2 Structural changes in Cu(II) nanoparticle-derived structures during CO₂RR

Structural changes in oxide-derived Cu have been generally studied in shape-undefined nanomaterials.^{47–49} To better understand the structural evolution associated with changing oxidation state of Cu from II to 0 during CO₂RR, this project was focussed on well-defined Cu(OH)₂ nanoparticles that were reduced at a substrate in the course of electrolysis. Thus, different Cu morphologies were obtained to separate the factors affecting the structural evolution of the precursor during the reduction process.

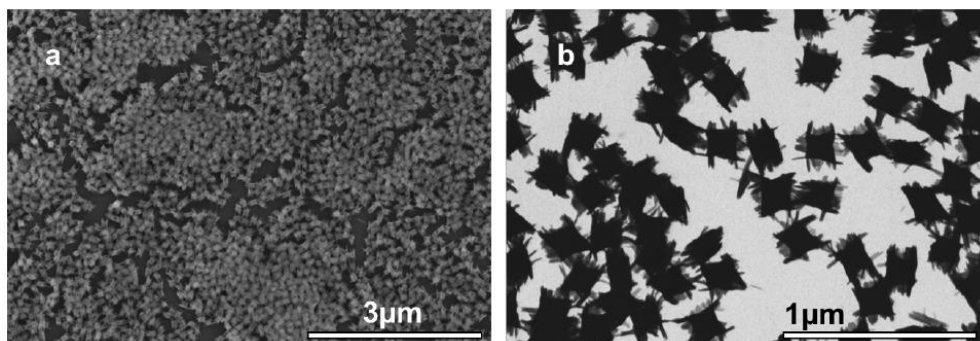


Figure 3.1: SEM (a) and TEM (b) images of Cu(OH)₂ nanocages (Cu(II)-NCs). Reprinted with permission from ref. [111]. Copyright 2019, Royal Society of Chemistry.

Amorphous Cu(OH)₂ nanocages (Cu(II)-NCs)⁸¹ with narrow size distribution and regular structure were selected as a copper precursor material (Figure 3.1). Scanning and transmission electron microscopy (SEM and TEM) images of the Cu(II)-NCs with average core size $x = 165 \pm 10$ and arm size $y = 51 \pm 17$ nm are shown in Figure 3.2 and Figure 3.1. Elongated 17 ± 4 nm-wide bundles

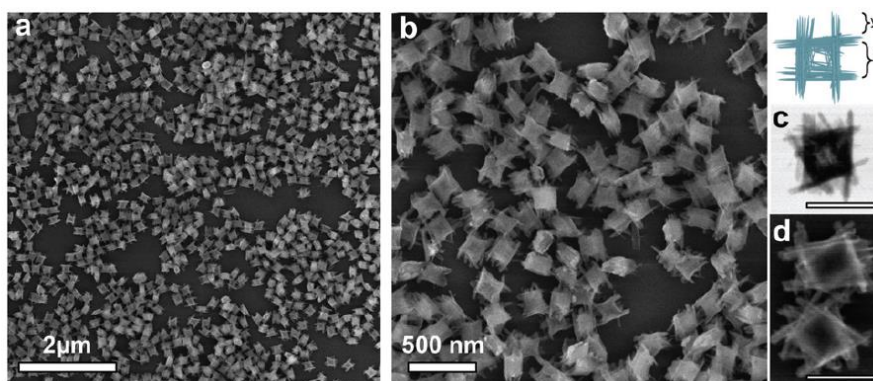


Figure 3.2: Copper precursor: Cu(II)-NCs. Inset shows a 3D cartoon representation of the Cu(II)-NCs with core (x) and arms (y) size parameters. (a, b and d) SEM images and (c) TEM image of Cu(II)-NCs. Scale bars in (c and d) are 200 nm. Reprinted with permission from ref. [111]. Copyright 2019, Royal Society of Chemistry.

comprising the structure can be observed in high magnification SEM and TEM images (Figure 3.2c and d).

For the electrode fabrication with varied surface density of the precursor nanoparticles, different concentrations of Cu(II)-NCs were dispersed in CO₂-saturated 0.5 M KHCO₃ electrolyte, and reductive cyclic voltammetry (CV) was performed in a three electrode configuration cell with carbon paper used as a working electrode. The potential was scanned at 20 mV s⁻¹ rate from 0 to -1.2 V vs. RHE for 4–20 cycles. Cu(II)-NCs were electroreduced once they came in contact with the working electrode. The density of the nanoparticles at the surface could be increased by increasing the concentration of Cu(II)-NCs in solution or the number of CV cycles. Figure 3.3a show representative CV plots corresponding to the Cu(II)-NCs electroreduction. Alternative way to vary the precursor surface density consisted in

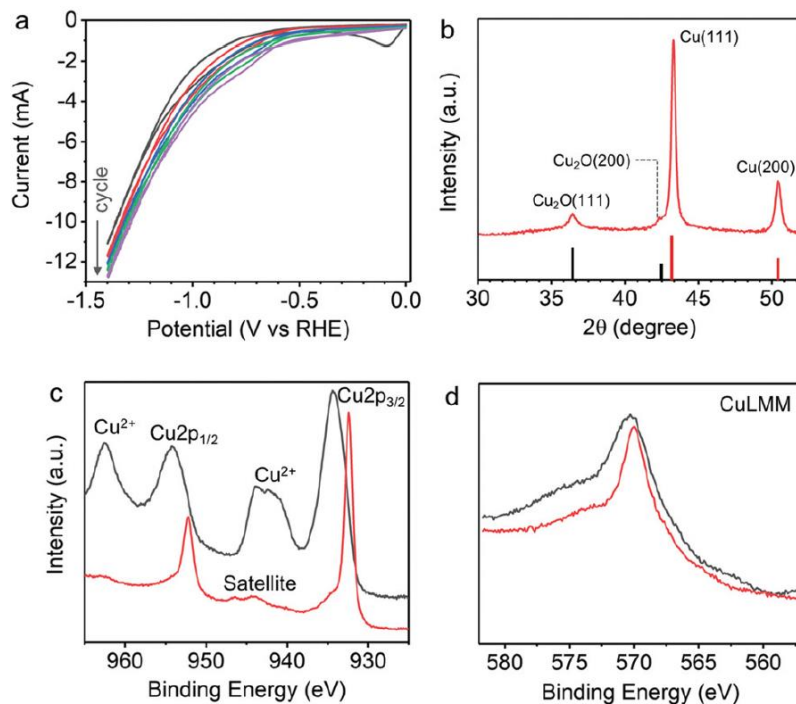


Figure 3.3: Characterization of the initial and electroreduced Cu(II)-NCs. (a) CV plot corresponding to the reduction of Cu(II)-NCs dispersed in CO₂-saturated 0.5 M KHCO₃ electrolyte at 20mV s⁻¹ scan rate. (b) Representative XRD plot of Cu(II)-NCs-derived Cu (black and red lines show standard XRD patterns for Cu₂O and Cu, respectively) (c) Cu2p_{3/2} and (d) CuLMM representative XPS plots of the original Cu(II)-NCs (gray line) and electroreduced material (red). Reprinted with permission from ref. [111]. Copyright 2019, Royal Society of Chemistry.

spin-coating of a solution containing Cu(II)-NCs and Nafion (as a binder) onto carbon paper substrate, followed by subsequent electroreduction in CO₂-saturated 0.5 M KHCO₃ electrolyte. In this method, Cu(II)-NCs surface density was controlled by varying the concentration of Cu(II)-NCs in the spin-coating solution and the number of spin-coating cycles. Similar general trends in the morphological

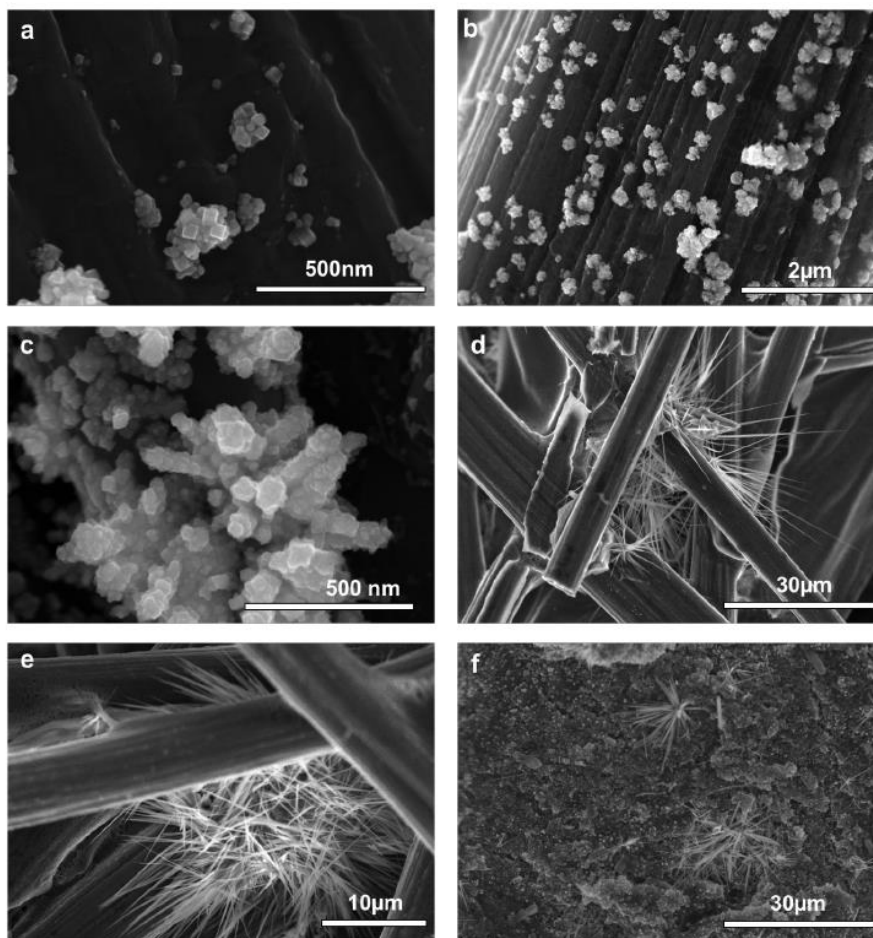


Figure 3.4: SEM images of Cu nanostructures observed on the surface of carbon paper working electrode at different densities of precursor Cu(II)-NCs in CO₂-saturated 0.5M KHCO₃ electrolyte. (a) after 4 CV cycles at 20 mV/s in the electrolyte containing Cu(II)-NCs at [Cu]=0.001 M. (b) after 20 CV cycles at 20 mV/s in the electrolyte containing Cu(II)-NCs at [Cu]=0.001 M. (c) after 20 CV cycles at 20 mV/s with Cu(II)-NCs directly spin-coated on the working electrode (20 μL, [Cu]=0.085 M, 3000 rpm). (d,e) after 20 CV cycles at 20 mV/s in the electrolyte containing Cu(II)-NCs at [Cu]=0.02M. (f) after 20 CV cycles at 20 mV/s with Cu(II)-NCs directly spin-coated on the gas diffusion working electrode (Sigracet purchased from Fuel Cell Store) containing carbon black and PTFE particles (200 μL, [Cu]=0.085 M, 3000 rpm). Reprinted with permission from ref. [111]. Copyright 2019, Royal Society of Chemistry.

changes were observed using Cu(II)-NCs-containing electrolyte and in spin-coating method (Figure 3.4). Below I describe the structural transformations observed using the former approach.

According to the Pourbaix diagrams¹¹² (Figure 3.5), only solid-state transitions took place during electroreduction of Cu(OH)₂ to Cu(0) through Cu(I) (Cu₂O and/or CuOH₂)¹¹³ in CO₂-saturated 0.5 M KHCO₃ at pH = 7.23 (or higher, when a negative potential was applied¹¹⁴). After CV cycling, all the resultant electroreduced structures consisted primarily of metal Cu(0), with small fraction of Cu(I), according to X-ray diffraction analysis (Figure 3.3b). X-ray photoelectron spectroscopy results (Figure 3.3c and d) also showed a complete reduction of Cu(II) and a presence of a mixture of Cu(0) and Cu(I) states based on the satellite peak in Cu2p region (Figure 3.3c) and the peak shift in the Auger spectrum (Figure 3.3d). Peak features and ratios were the same for the samples obtained in the Cu(II)-NCs concentration and CV scan numbers ranges studied here. The final electrode morphologies were analyzed using SEM to examine the structural transformations as a function of Cu(II)-NCs surface density. These transformations were “mapped” by a phase-like diagram in concentration of [Cu] – number of CV cycles parameter space (Figure 3.6e).

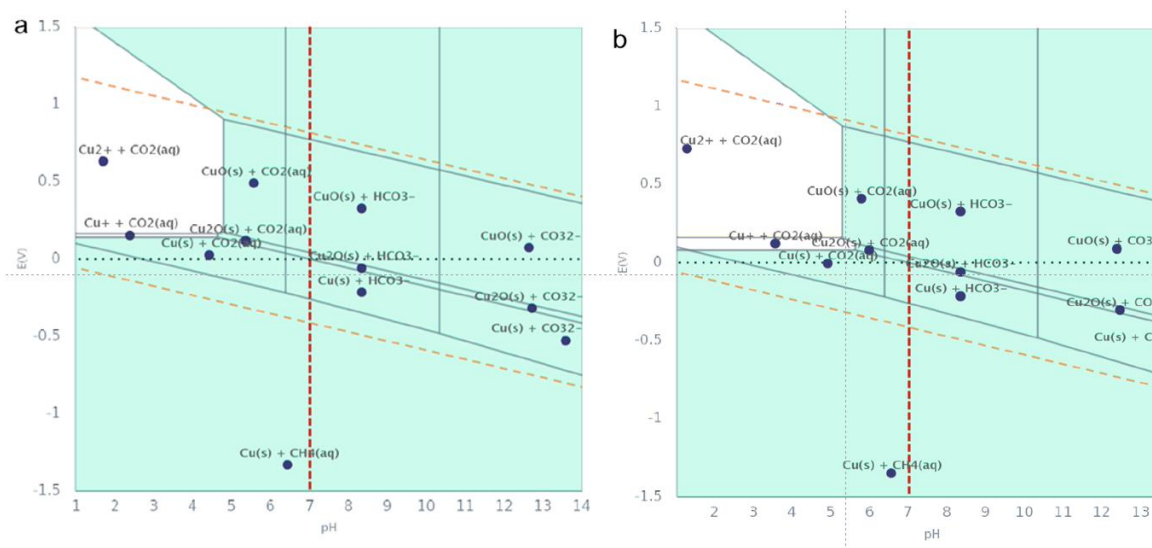


Figure 3.5: Pourbaix diagrams of Cu phases at 0.001 M (a) and 0.0001 M (b) copper concentration in bicarbonate aqueous solution. Obtained using “Pourbaix diagram” app by Materials Project.¹¹² Reprinted with permission from ref. [111]. Copyright 2019, Royal Society of Chemistry.

At a low Cu(II)-NCs surface density, a single particle regime was achieved, where each electroreduced structure on the substrate originated from a single Cu(II)-NC. Figure 3.6a and 3.7 show the individual nanocubes (NCs) of $94 \pm 19 \text{ nm}$ edge length observed after 4 CV cycles in solution regime at a low concentration of Cu(II)-NCs in the electrolyte ($[\text{Cu}] = 0.0001 \text{ M}$). The decrease in the average size of the nanoparticles upon electroreduction agrees with the mass loss and crystallization associated with the transition of the amorphous void-containing Cu(II)-NCs into metal Cu. Copper NCs enclosed by $\{100\}$ facets have been shown to exhibit higher catalytic activity in CO_2 electroreduction reaction.^{54,115,116} As the experiments were conducted in a CO_2 -saturated electrolyte, Cu(II)-NCs electroreduction co-occurred with CO_2RR at the reduced copper sites. Higher catalytic activity of the $\{100\}$ facet is related to its stronger binding to key CO_2RR intermediates¹¹⁷ compared to the most thermodynamically stable $\{111\}$ surface of fcc metal.¹¹⁸ The DFT calculations in Figure 3.8 also demonstrate the CO_2RR reaction intermediates (COOH^* and OCHO^*) prefer the adsorption on Cu(100) surface instead of Cu(111) surface. Thus, CO_2RR intermediates can stabilize $\{100\}$ facet over $\{111\}$ facet during crystal formation, essentially allowing these moieties to act as shape-directing

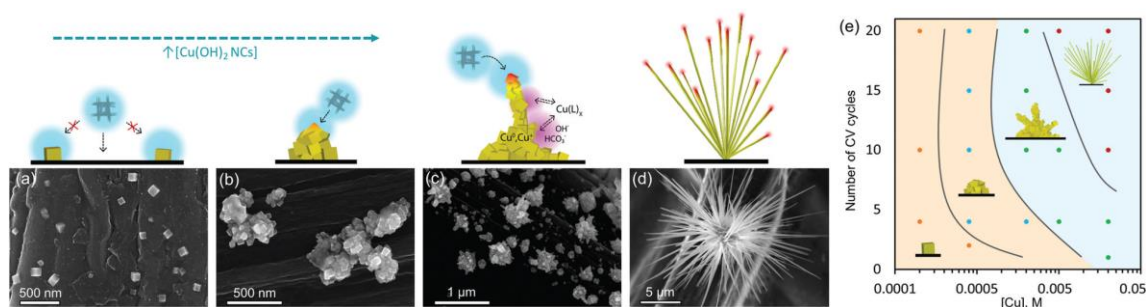


Figure 3.6: SEM analysis of structures obtained in electroreduction of Cu(II)-NCs and schematics of their formation processes. (a) Minimum $[\text{Cu(II)-NC}]$: single particle reduction to individual Cu NCs. (b) Low $[\text{Cu(II)-NC}]$: Cu cube-containing clump formation due to Cu(II)-NC diffusion spheres overlap (shown in blue) (c) intermediate $[\text{Cu(II)-NC}]$: Cu structure extrusion due to the FIRC effect (E-field enhancement shown at structure extrusions in red). Smoothing the surface due to electrochemical Ostwald ripening is shown in magenta. (d) High $[\text{Cu(II)-NCs}]$: Cu MUs obtained at full coverage of the working electrode substrate surface. (e) Phase-like diagram of the structures obtained at different $[\text{Cu}]$ and number of CV cycles. Shaded areas correspond to the dominance of facet stabilization (orange) and FIRC effect (blue) as driving force determining the structure shape. Reprinted with permission from ref. [111]. Copyright 2019, Royal Society of Chemistry.

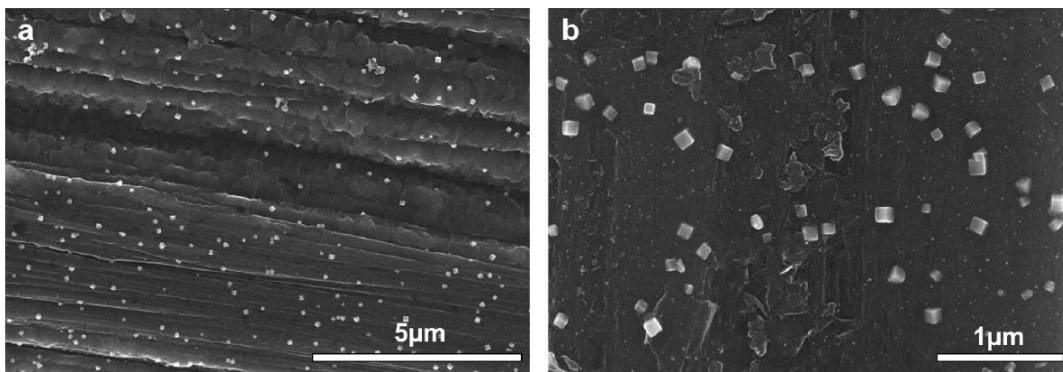


Figure 3.7: SEM images of Cu nanocubes observed on the surface of carbon paper working electrode after 4 CV cycles at 20 mV/s in CO₂-saturated 0.5M KHCO₃ electrolyte containing Cu(II)-NCs ([Cu]=0.0001 M). Reprinted with permission from ref. [111]. Copyright 2019, Royal Society of Chemistry.

surface stabilizers.^{119,120} In Ar-saturated 0.5 M KHCO₃ electrolyte, spherical Cu nanoparticles were observed instead, further supporting that forming CO₂RR intermediates are responsible for the Cu NCs formation when CO₂ is present (Figure 3.9a).

At a higher Cu(II)-NCs concentration in the electrolyte ([Cu] =0.001 M), which allowed for the overlap of Cu(II)-NCs diffusion spheres at the substrate surface, a formation of submicron Cu clumps with defined cubic elements with edge length ≤ 50 nm was observed (Figure 3.6b and Figure 3.4a, b,). The presence of these cubic elements suggests that the forming structures still experienced the

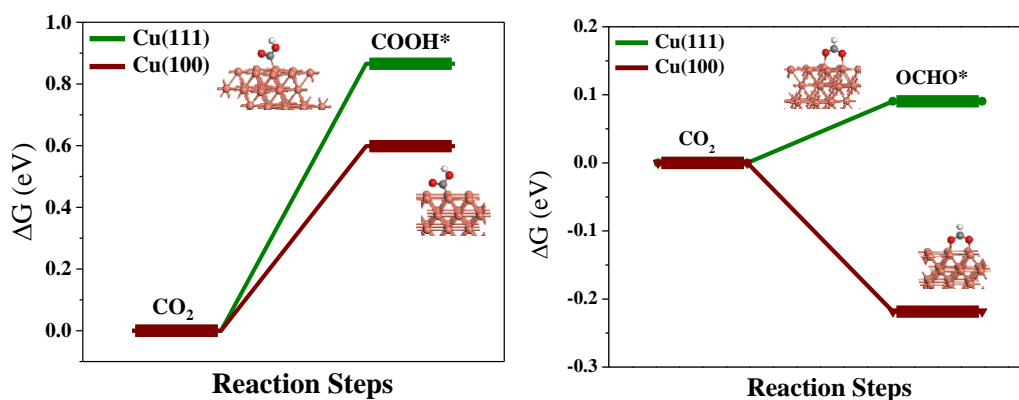


Figure 3.8: The relative Gibbs free energy of COOH* and OCHO* on Cu(111) and Cu(100) surfaces.

thermodynamic drive to develop features with more stable under CO₂RR conditions {100} facets, while their multiparticle origin hindered the formation of a single submicron cube.

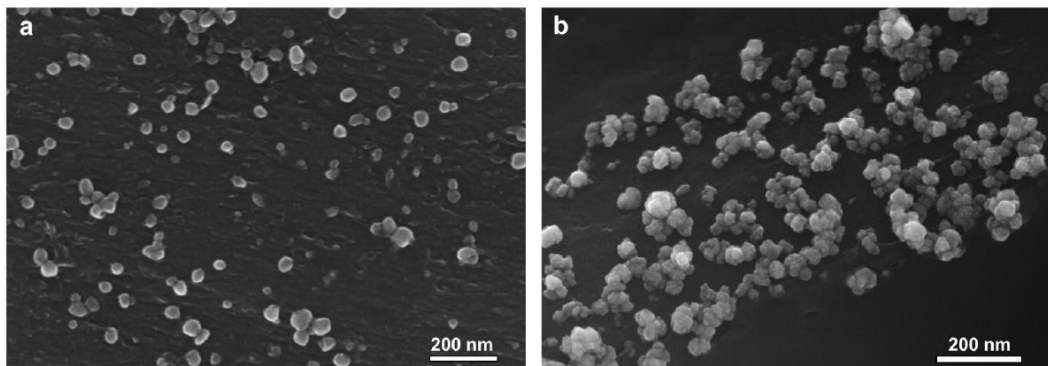


Figure 3.9: SEM images of Cu nanostructures observed on the surface of carbon paper working electrode at different densities of precursor Cu(II)-NCs in Ar-saturated 0.5M KHCO₃ electrolyte containing Cu(II)-NCs at [Cu]=0.0001 M (a) and [Cu]=0.001 M (b). Reprinted with permission from ref. [111]. Copyright 2019, Royal Society of Chemistry.

With a further increase in Cu(II)-NCs surface density, the reduced Cu clumps became more polydisperse and increased in size (Figure 3.6c, [Cu] = 0.005 M). Notably, a prominent shape anisotropy in a form of extrusions was observed for the larger Cu clumps. This anisotropic structure development is ascribed to the FIRC effect,¹³ that is responsible for promoting electrochemical reactions at high-curvature features of the electrode surface. Such high-curvature features could already be seen in the cube-containing clumps obtained at a lower precursor surface density: their exposed cubic vertices result in a local negative electric field enhancement, thereby attracting Cu(II)-NCs to these parts of the surface and causing their preferential deposition (see the cartoon in Figure 3.6b). This process differentiated nucleation sites not only within, but also between the copper islands on the substrate surface, promoting the growth of more anisotropic depositions and suppressing the growth of less anisotropic ones, resulting in the broadening of their size distribution. The extruding features experienced further field enhancement at their vicinity and in turn higher affinity to the next precursor particle attachment; this oriented attachment further increased structure anisotropy, and propagated the extrusion of the features. Due to the FIRC-based self-propagating and accelerating feedback loop in Cu(II)-NCs electroreduction process, a drastic increase in the aspect ratio of extruded features was observed with a further increase of the concentration of the precursor ([Cu] = 0.02 M), producing sparsely-spaced Cu microurchins (MUs; Figure 3.6d and Figure 3.4d–f).

In addition to the structure extrusion, smoothening of the features with increasing the precursor Cu(II)-NCs concentration was observed. This morphological change can be ascribed to electrochemical Ostwald ripening,¹²¹ i.e., local nanoscale surface reconstruction via copper dissolution and redeposition. The standard electrode potential of sub-50 nm metal features on conductive substrates shifts negatively with decreasing size, meaning that smaller features are more easily oxidized than larger ones. The work function of metal nanoparticles also decreases with particle size due to their reduced electron affinity.¹²² As a result, nanoscale surface inhomogeneities are more susceptible to electroreposition to minimize surface energy than larger surface features. Interestingly, based on our experimental results observed at single precursor particle regime and the recent report on the sub-10 nm Cu nanoparticle ensemble transformations into cubes during electrolysis,⁶² electrochemical surface reconstruction into the most thermodynamically stable spherical shape is less favorable than {100} facet development, likely through the facet stabilization with CO₂RR intermediates discussed above. These observations agreed with an earlier report demonstrating that structural reformation on nanoscale could be shut off by the addition of a surface stabilizing agent.¹²¹ With the precursor concentration increase, the more surface smearing was observed in the obtained structures the higher was the aspect ratio of the extruded features. This trend suggests that high-curvature surface extrusions (“needles”) are more stabilized under CO₂RR conditions than {100} surfaces, in line with their reported outstanding activity in CO₂RR ascribed to the efficient physical removal of CO₂RR products¹²³ in combination with the aforementioned FIRC effect. As a result of the extremely high CO₂RR rates and efficient mass transfer at the tips of the needles, CO₂ concentration at the base of the structure (i.e., further from the tips and closer the substrate) became depleted, while further CO₂ access to these surfaces from the bulk of the solution was hindered, virtually suppressing CO₂RR at these surfaces. Thus, Ostwald ripening at the needles’ sides and base could take place due to the lack of the stabilizing effect of the CO₂RR intermediates, directing the observed morphological transformations to smoother surfaces.

3.3 Structural changes in Au CCs and BNPs during CO₂RR

Another way of fabricating the electrode is to deposit the pre-synthesized metal nanoparticles on a substrate. In this approach, the catalyst is already present in metal form, so no oxidation state change (except for the oxidized surface when it is exposed to air in some materials) and no mass loss associated with it occurs in this case. However, when the nanoparticles have complex morphologies, structural changes could be observed in metal nanoparticles under electrolysis conditions, which is described below and in section 3.4 and 3.5.

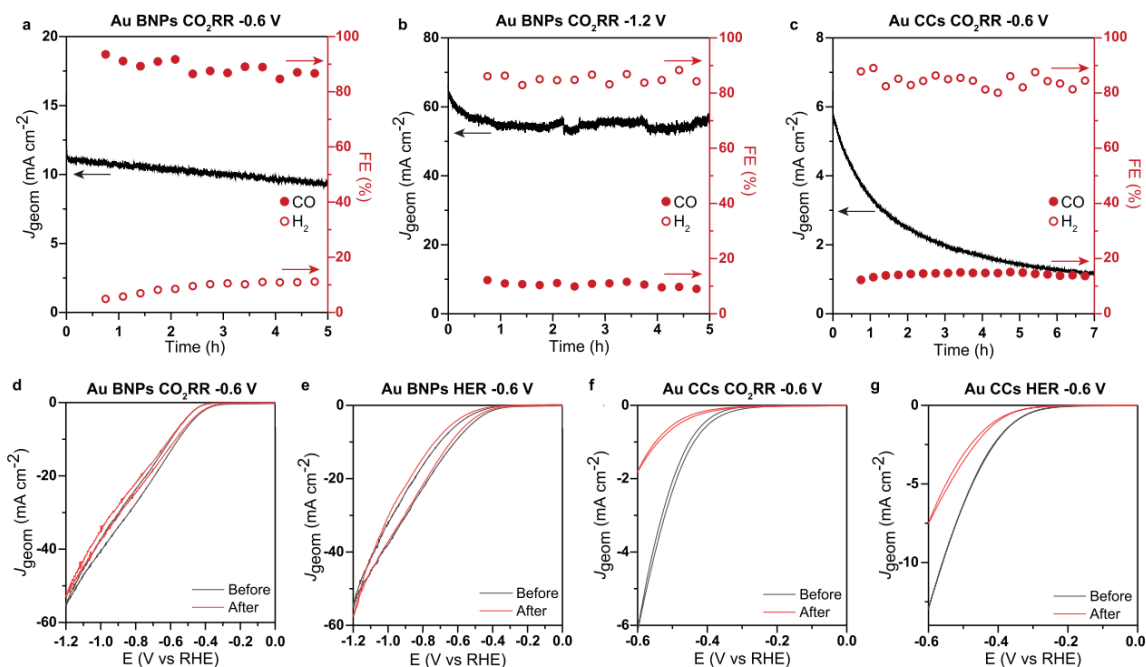


Figure 3.10: Electrochemical performance and stability of Au CCs and BNPs. a-c, CO₂ reduction activity of Au BNPs (a,b) and Au CCs (c) over time during potentiostatic electrolysis at -0.6 V (a,c) and -1.2 V (b) vs RHE in CO₂ saturated 0.5 M KHCO₃. d-g, Cyclic voltammograms of Au BNPs (d,e) and Au CCs (f,g) before and after 5 hours of potentiostatic electrolysis at -0.6 V vs RHE in CO₂ saturated (d,f) or Ar saturated 0.5 M KHCO₃ (e,g). Current densities correspond to currents normalized by the geometric area of the electrode. For surface roughness analysis of these electrodes see Table 3.4. Reprinted with permission from ref. [71]. Copyright 2021, Springer Nature.

Table 3.4: Surface roughness assessment of the fabricated Au electrodes.

Material	$Q_{\text{Pb stripping}}$ ($\mu\text{C cm}^{-2}$)	Roughness factor
Au (111) ¹²³	272	1
Au CCs	1479	5.44
Au BNPs	2453	9.02

Reprinted with permission from ref. [71]. Copyright 2021, Springer Nature.

The first series of experiments was performed with gold BNPs and CCs under potentiostatic CO₂RR electrolysis conditions at -0.6 V versus the reversible hydrogen electrode (RHE; the typical potential for CO₂RR on gold⁷). For surface roughness analysis of these electrodes see Table 3.4. While gold BNPs generally preserved their overall structure and showed minor decay in current density over time (Figure 3.10a), after five hours of electrolysis I observed structural changes (Figure 3.11a–h), with pronounced sintering between a BNP and the substrate (Figure 3.11g,h) and between multiple BNPs (Figure 3.11f,d and Figure 3.12a–c). Only slight surface smoothing was observed in the external BNP arms facing the electrolyte (Figure 3.11e–h), and their average length and width decreased negligibly

Table 3.5: Statistical analysis of nanoparticle sizes before and 5 hours of CO₂RR electrolysis obtained using Image-J software. On average, 100 nanoparticles were analyzed for each measurement.

Nanoparticle shape type	As-synthesized size, nm \pm SD	Size after 5h CO ₂ RR, nm \pm SD
Standard Au BNPs (overall diameter arm length arm width)	265 \pm 51 127 \pm 31 31 \pm 8	256 \pm 35 124 \pm 20 29 \pm 7
Small Au BNPs (overall diameter arm length arm width)	112 \pm 15 54 \pm 13 15 \pm 4	113 \pm 14 50 \pm 16 19 \pm 4
Au CCs (side length)	29 \pm 3	N/A***
Pd BNPs (overall diameter arm length arm width)	133 \pm 12 45 \pm 12 17 \pm 4	139 \pm 16 46 \pm 16 21 \pm 5****
Standard Pd CCs (side length)*	25 \pm 2	26 \pm 2****
Pd CCs – more open structure (side length)**	26 \pm 2	27 \pm 2****

*These measurements correspond to Pd CCs with a closed wall structure (see Figure 3.20 a-d).

** These measurements correspond to Pd CCs with an open wall structure (see Figure 3.21 e-h).

Reprinted with permission from ref. [71]. Copyright 2021, Springer Nature.

(Table 3.5). Smaller BNPs followed a similar trend (Table 3.5 and Figure 3.12d,e, 3.13 and 3.14). In potentiostatic experiments at the more negative potential of -1.2 V (Figure 3.10b), only surface smoothing and minor sintering close to the substrate was observed after five hours of electrolysis (Figure 3.15). Interestingly, at -1.2 V, which favoured the HER (with the Faradaic efficiency for H_2 (FE_{H_2}) over 80%), the current decay was less pronounced than at -0.6 V, which favoured the CO_2RR

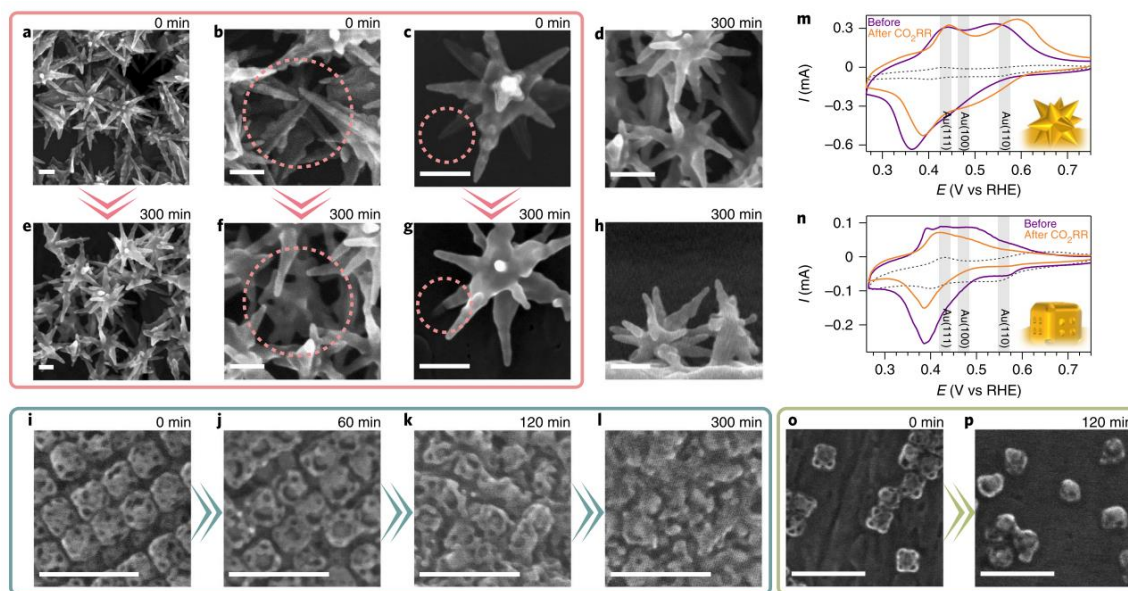


Figure 3.11: Structural changes in gold nanoparticles during CO_2RR . a–h, SEM images of gold BNPs before (a–c) and after (d–h) 300 min of electrolysis in CO_2 -saturated 0.5 M KHCO_3 at -0.6 V versus RHE, with d and f–h showing magnified areas of the electrode with sintering of the BNPs with each other (d,f) and with the substrate (g,h). Scale bars, 100 nm. i–l,o,p, SEM images of gold CCs before (i,o) and after 60 min (j), 120 min (k,p) and 300 min (l) of electrolysis in CO_2 saturated 0.5 M KHCO_3 at -0.6 V versus RHE. Panels i–l and panels o and p show the behaviour of a close-packed array of CCs and sparsely distributed CCs, respectively. Scale bars, 100 nm. m,n, Lead UPD before (purple traces) and after 120 min (orange traces) of electrolysis using gold BNPs (m) and gold CCs (n). Black dashed traces correspond to lead UPD on the substrate gold foil without deposited particles. Reprinted with permission from ref. [71]. Copyright 2021, Springer Nature.

(FE_{CO} over 80%), even though the more negative potential resulted in higher currents (Figure 3.10a,b). This observation suggested the influence of the surface reaction nature on the degradation rate.

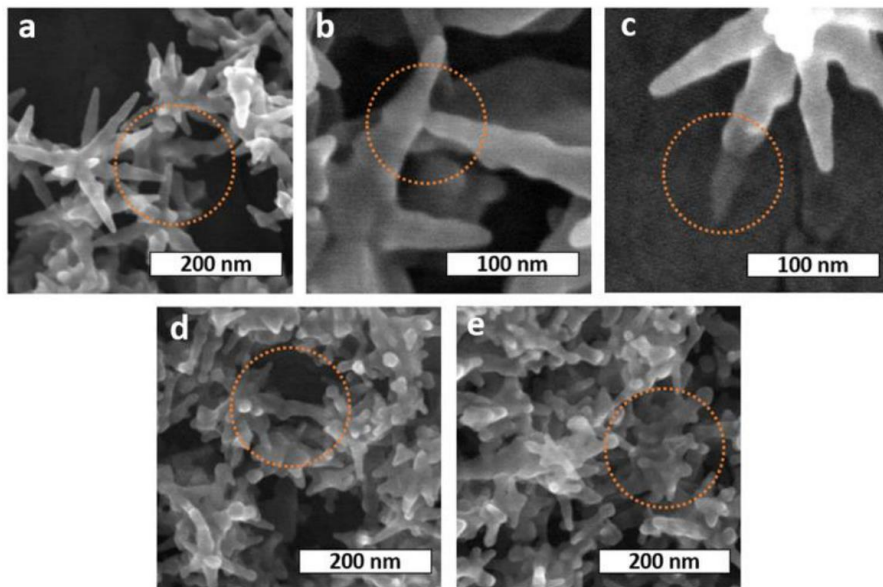


Figure 3.12: Illustration of Au BNPs sintering. SEM images of standard Au BNPs sintering in a pile (a), sintering of tips (b), and sintering of a tip with Au substrate (c); and of small Au BNPs sintering of tips (d), and sintering in a pile (e) after 300 min of CO₂RR reaction at -0.6V vs RHE. Reprinted with permission from ref. [71]. Copyright 2021, Springer Nature.

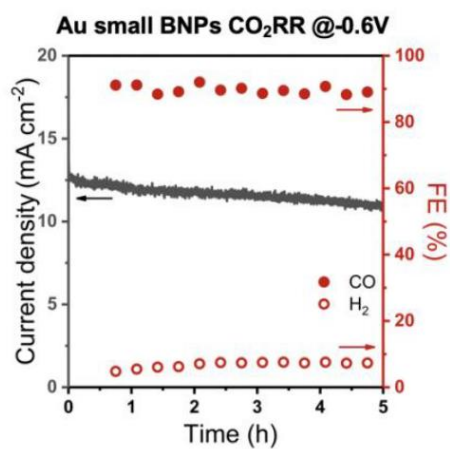


Figure 3.13: CO₂ reduction activity of small Au BNPs over time during potentiostatic electrolysis at -0.6V vs RHE in CO₂-saturated 0.5M KHCO₃; changes in total current density (left axis) and Faradaic efficiencies (right axis) of CO (solid circles) and H₂ (empty circles) are shown as a function of time. Reprinted with permission from ref. [71]. Copyright 2021, Springer Nature.

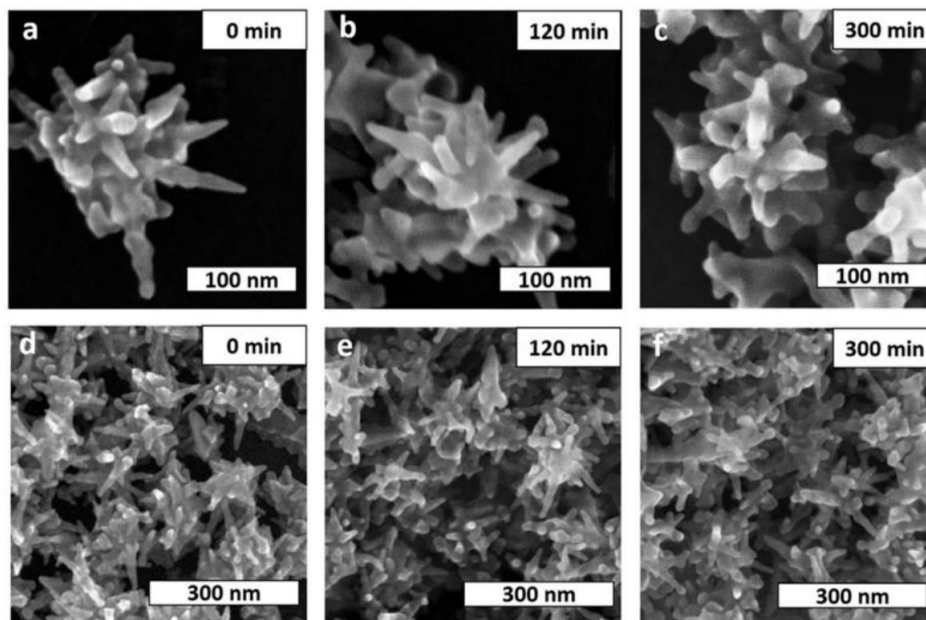


Figure 3.14: SEM images of small branched Au nanoparticle before (a,d), after 120 min (b,e), and after 300 min (c,f) of CO₂RR reaction at -0.6V vs RHE at different magnifications. Reprinted with permission from ref. [71]. Copyright 2021, Springer Nature.

To obtain further insight into the surface smoothing observed in gold BNPs, electrochemical surface characterization was performed before and after electrolysis. The crystallographic orientation of the gold surface can be assessed by the electrochemical adsorption of foreign metal atoms:¹²⁴ lead UPD on gold enables the assignment of the voltammetric peaks to lead stripping occurring on {111}, {110} or {100} gold terraces or steps^{125–129} (Figure 3.11m). The lead UPD voltammogram of gold BNPs before electrolysis shows that the initial surface was rich in {110} and {111} terraces, with broad peaks consistent with the presence of steps and kinks associated with the nanoscale surface curvature. After two hours of CO₂RR electrolysis at -0.6 V versus RHE, {111} and {110} UPD features remained dominant and became more pronounced, and a minor shift in the peaks was observed, suggesting that some surface restructuring took place (Figure 3.11m).¹²⁷ This evidence, along with chronoamperometric data (Figure 3.10a), highlighted the presence of an ongoing structural surface morphing on a smaller timescale not detected by SEM analysis.

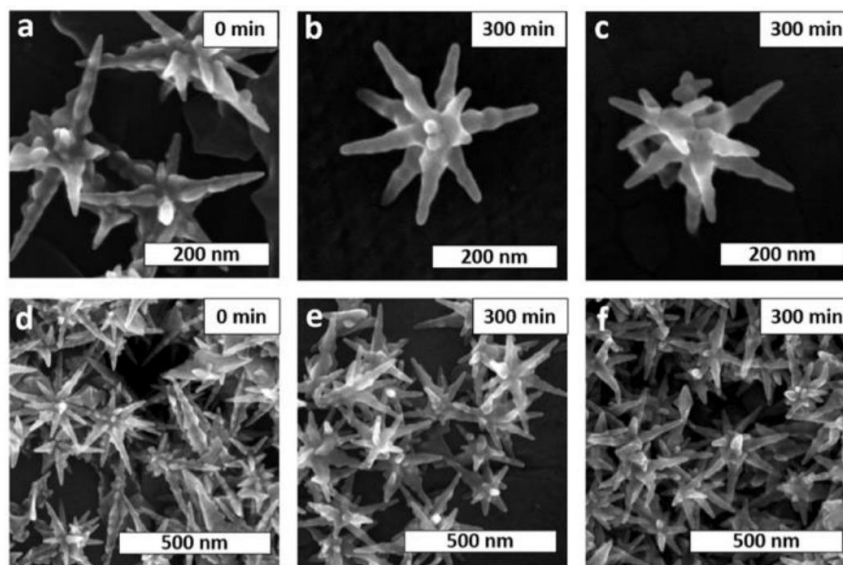


Figure 3.15: Structural evolution of branched Au nanoparticles. SEM images of branched Au nanoparticles before (a,d) and after 300 min of CO₂RR reaction at -0.6V (b,e) and -1.2V (c,f) vs RHE at different magnifications. Reprinted with permission from ref. [71]. Copyright 2021, Springer Nature.

The structural transformations observed by SEM in gold CCs were substantially more pronounced than in the case of gold BNPs, which was also evidenced by a notable current decay in potentiostatic electrolysis (Figure 3.10c). Already after one hour of electrolysis under CO₂RR conditions at -0.6 V versus RHE, a breakage of the structural integrity of the CC walls facing the electrolyte and a sintering of the adjacent CCs could be seen (Figure 3.11i,j and 3.16). After two hours, complete disfigurement of the CC shape was observed (Figure 3.11k), although the structural deformation continued beyond this point (Figure 3.11l). At a more negative applied potential, this process was further accelerated (Figure. 3.17). Therefore, after 5 hours of CO₂RR electrolysis, no definitive side measurements could be obtained due to the disfigurement of Au CCs in Table 3.5. In contrast to BNPs, layers of CCs form close-packed structures due to their more compact geometry (Figure 3.11i-l and 3.16). To assess whether or not the observed degradation is a consequence of the ensemble behaviour due to interparticle interactions, electrodes with a reduced CC loading were tested (Figure 3.11 o,p and 3.18). The individual CCs still underwent some structural degradation, while CCs that were touching each other exhibited sintering at the interface. The beginning of interparticle sintering could be observed in both small particle assemblies and close-packed arrays already during the first hour of electrolysis under

CO₂RR conditions, further deteriorating with time. The lead UPD voltammogram revealed that the initial gold CCs were rich in {100} and {111} terraces, with the leftmost shoulder peak in the voltammogram associated with the presence of high-index surfaces (Figure 3.11n). After two hours of

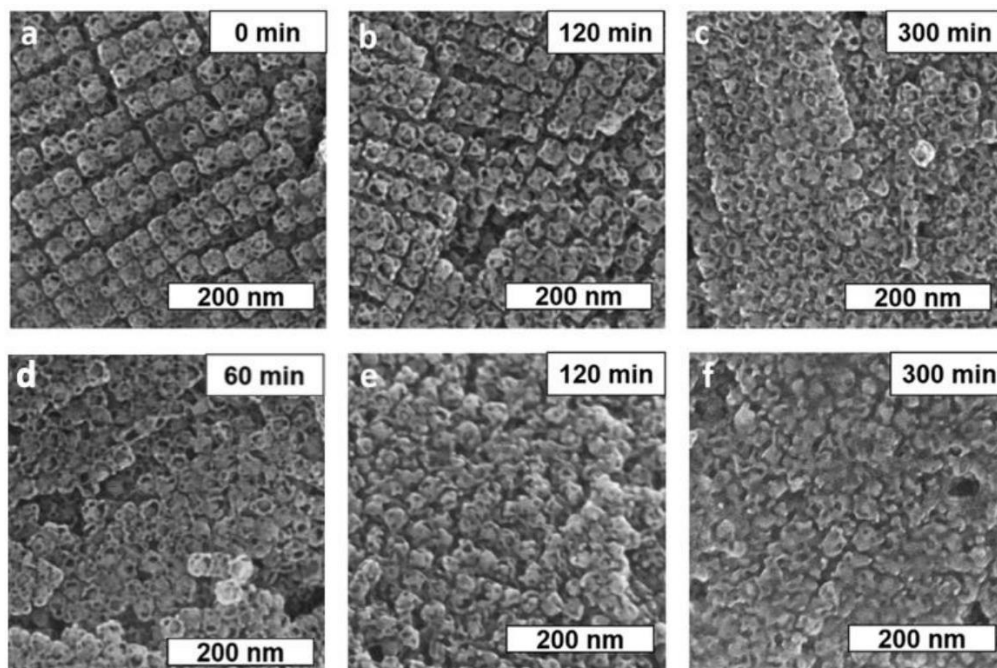


Figure 3.16: SEM images of Au-Au CCs before (a), after 120 min (b), and 300 min (c) of HER at -0.6V vs RHE, and after 60 min (d), 120 min (e), and 300 min (f) of CO₂RR reaction at -0.6V vs RHE. Reprinted with permission from ref. [71]. Copyright 2021, Springer Nature.

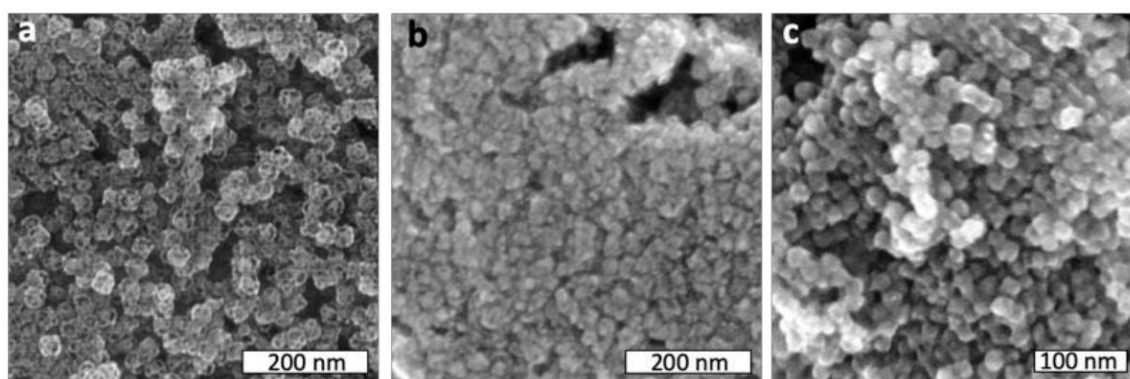


Figure 3.17: (a,b) SEM images of Au CCs after 30 min (a) and 60 min (b) of CO₂RR at -1.2V vs RHE. (c) Disfigurement of Au CCs observed after potential overload error when running electrolysis at -0.6V vs RHE for 30 min. Reprinted with permission from ref. [71]. Copyright 2021, Springer Nature.

CO₂RR electrolysis at -0.6 V versus RHE, the lead UPD voltammogram revealed the dominance of {111} terraces in the resultant structure, indicating a change in crystallographic surface structure in the course of electrolysis towards a different stable state than that observed for gold BNPs (Figure 3.11m,n). This difference in lead UPD behaviour for gold BNPs and CCs suggested that the thermodynamic stability of the final surface may not be the only factor driving these structural transformations.

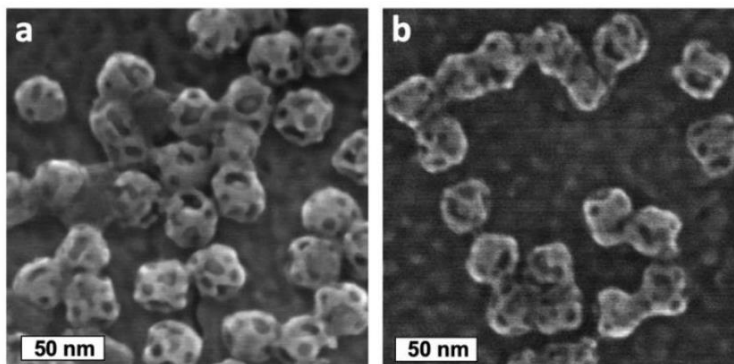


Figure 3.18: (a,b) SEM images of Au CCs after 60 min of electrolysis under CO₂RR conditions in CO₂-saturated 0.5M KHCO₃ at -0.6 V vs RHE. The loading of CCs in these experiments is twice lower than in the standard fully covered electrode samples. Reprinted with permission from ref. [71]. Copyright 2021, Springer Nature.

3.4 Effect of cathodic reactions on the structural changes in Au CCs

To elucidate the effect of electrochemical reactions on the structural behaviour of the particles, the outcomes of electrolysis under CO₂RR and HER conditions were compared (Figure 3.19). Figure 3.19a–c shows the SEM images of the gold CCs before (Figure 3.19b) and after two hours of electrolysis at –0.6 V versus RHE under HER (Figure 3.19a) and CO₂RR (Figure 3.19c) reaction conditions (see also Figure 3.16). The disfigurement and sintering of the CC structures along with a drop in the current density, J_{geom} , were more pronounced under CO₂RR than under HER conditions, although the current density measured for the same electrode sizes was lower in CO₂RR than in HER (Figure 3.19f and 3.10d–g) due to the difference in kinetics between these two reactions.^{130,131} Importantly, the Faradaic efficiency (FE) of CO under CO₂RR conditions was only under 20%, showing that a relatively minor contribution of the CO₂RR resulted in different structural degradation rates,

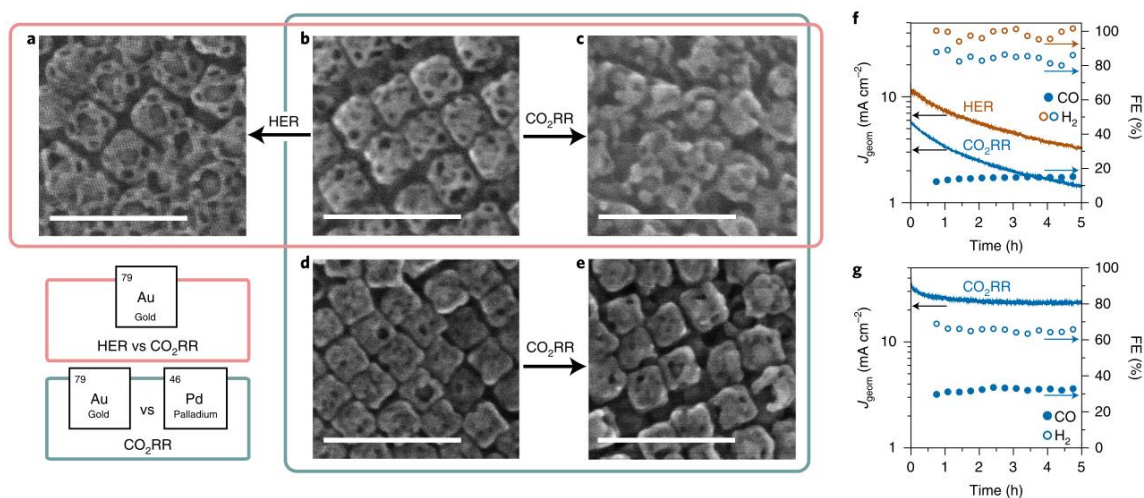


Figure 3.19: Effect of electrochemical reaction and catalyst material on the structural stability of CCs. a–c, SEM images of gold CCs before (b) and after (a,c) 120 min of electrolysis at –0.6 V versus RHE: effect of HER (a) and CO₂RR (c). (d,e) SEM images of palladium CCs before (d) and after (e) 300 min under CO₂RR conditions at –1.2 V versus RHE. Scale bars in a–e, 100 nm. f,g, Evolution of electrocatalytic activity of gold and palladium CCs over five hours of potentiostatic electrolysis: gold CCs (f) under CO₂RR conditions (blue traces) and under HER reaction conditions (orange traces) at –0.6 V versus RHE, and palladium CCs (g) under CO₂RR conditions. Solid lines, current evolution over time; filled circles, FE(CO); open circles, FE(H₂). CO₂RR and HER reaction conditions correspond to CO₂ and argon-saturated 0.5 M KHCO₃, respectively. Reprinted with permission from ref. [71]. Copyright 2021, Springer Nature.

although hydrogen evolution was still the dominant process on the catalyst surface (FE over 80%). The observed stability trends for both CCs and BNPs suggested that the surface chemistry (adsorbed reaction intermediates) has a strong effect on the process of structural transformation of the electrocatalyst material.

3.5 Effect of materials on the structural changes in CCs and BNP during CO₂RR

To further probe the effect of surface chemistry interactions during electrolysis on the structural behaviour of the electrocatalyst, CO₂RR electrocatalysis on palladium CCs of comparable sizes to gold CCs were performed. In contrast to gold CCs, palladium CCs did not undergo noticeable structural transformation or interparticle sintering even after five hours of electrolysis at -1.2 V versus RHE and with an FE_{CO} over 30% (Figure 3.19d,e, Figure 3.20 and Table 3.5), and only a minor decrease in the current density was observed (Figure 3.19g). Similarly, palladium BNPs preserved their overall shape after five hours of CO₂RR electrolysis under the same conditions, although some minor dulling of the sharp BNP tips was observed (Figure 3.21 and Table 3.5). A slight increase in the size of Pd nanoparticles after electrolysis in aqueous medium was observed in Table 3.5, which is related to Pd hydride formation and associated lattice expansion from 388.9 pm to 402.5 pm.

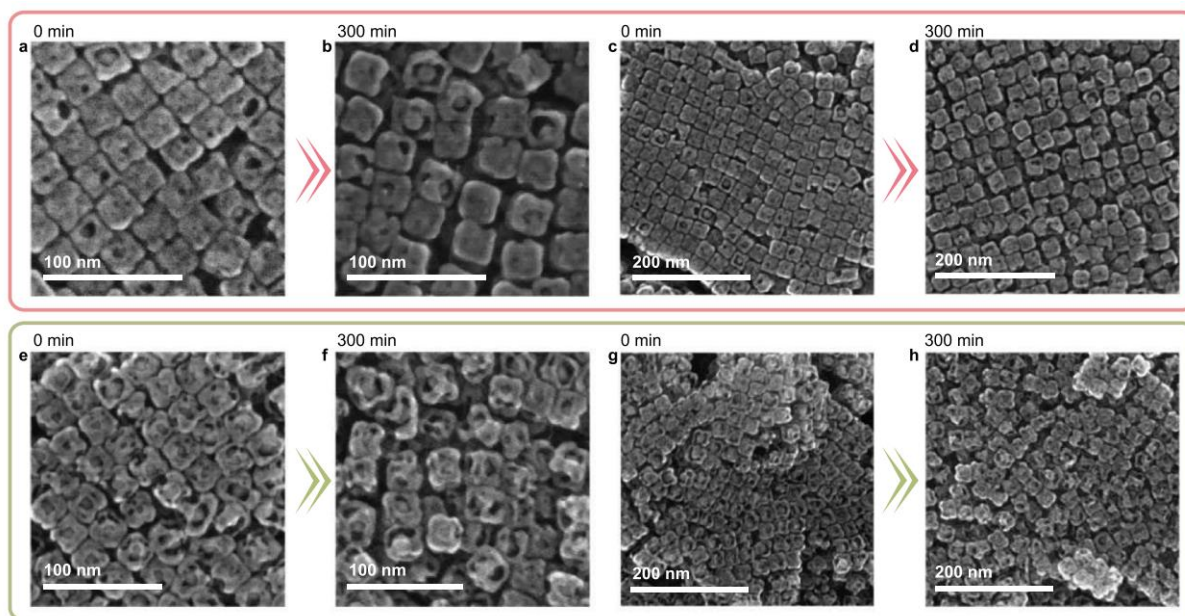


Figure 3.20: Structural stability of Pd CCs under CO₂ reduction conditions. a-d, SEM images areas of Pd CCs before (a,c) and after (b,d) 300 min of CO₂RR reaction at -1.2 V vs RHE at different magnifications. e-h, SEM images of Pd CCs with a more open wall morphology before (e,g) and after (f,h) 300 min of CO₂RR reaction at -1.2 V vs RHE at different magnifications. Reprinted with permission from ref. [71]. Copyright 2021, Springer Nature.

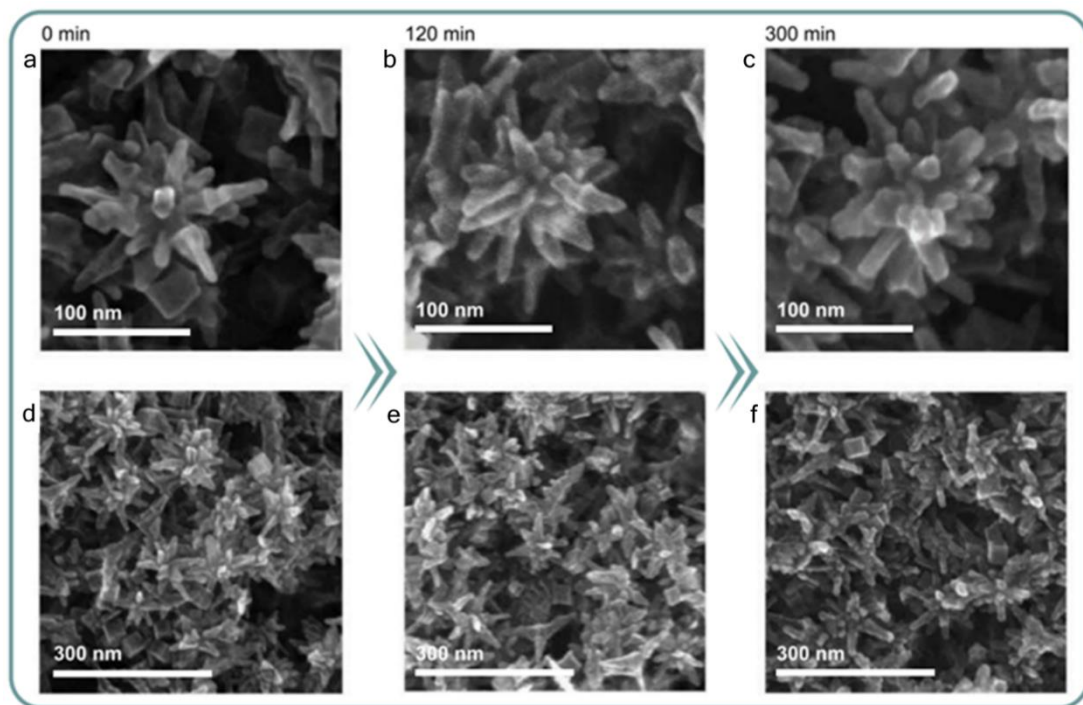


Figure 3.21: Structural stability of BNPs under CO₂ reduction conditions. a-f, SEM images of Pd BNPs before (a,d), after 120 min (b,e), and after 300 min (c,f) of CO₂RR reaction at -1.2 V vs RHE at different magnifications. Reprinted with permission from ref. [71]. Copyright 2021, Springer Nature.

3.6 Summary

In this chapter, I explored the structural behavior in the nanostructured electrocatalysts with and without oxidation state changes during electrolysis conditions. To study the cases with oxidation state changes, Cu(II)-nanoparticle-derived copper electrodes were prepared by electrochemically reducing the Cu(OH)₂ nanoparticles under CO₂RR electrolysis conditions. Structural transformations were observed in the Cu(II)-nanoparticle-derived copper electrodes under CO₂RR conditions, with the structural evolution of the electrodes being found to be directed by the facet stabilization by CO₂RR intermediates, electrochemical Ostwald ripening and FIRC effect. Furthermore, to investigate the cases without oxidation state changes, as-synthesized well-defined Au and Pd CCs and BNPs nanoparticles were used to fabricate electrodes that were subjected to CO₂RR and HER electrolysis. The experimental observations revealed that the morphological changes of the electrodes were accelerated by the RIs of the electrolysis reactions, with CO₂RR having a more pronounced effect than HER. In addition, Pd showed higher stability against the structural changes than Au under electrolysis conditions. Based on the experiments performed for Cu(II)-nanoparticle-derived copper electrodes, well-defined Au and Pd CCs and BNPs nanoparticles, the structural transformations in the electrocatalyst with and without oxidation state changes were demonstrated to be strongly affected by the surface reactions (RIs), the material nature and applied bias, showing the properties of locality and directionality in structural evolution of the electrocatalysts under the electrolysis conditions. The works included in this chapter reveals the crucial factors affecting the structural dynamics in the electrocatalysts, paving the way for understanding the stories behind the structural transformations in electrocatalysts under bias conditions.

Chapter 4

Atomic- and molecular-scale mechanistic description of structural changes in CO₂RR electrocatalysts

Partially reprinted with permission from *Nature Catal.* **2021**, 4, 479. Copyright 2021, Springer Nature.

Contribution: designed and carried out the DFT calculations and the FEM simulations, assisted in manuscript writing.

Partially reprinted with permission from *Phys.Chem.Chem.Phys.* **2022**, DOI: 10.1039/d2cp02075k.

Copyright 2022, Royal Society of Chemistry

Contribution: conceived the idea, designed and carried out all the DFT calculations and MD simulations, and wrote the manuscript.

4.1 Introduction

To date, the known factors affecting the atomic mobility of metal surfaces include the reaction intermediate (RI), electrolyte, applied potential, local pH, nanostructure size, and catalyst support.^{57-59,62-64} Furthermore, based on the experimental observations discussed in Chapter 3, RIs have significant impact on the structural transformations of various nanoparticles under the electrolysis of HER and CO₂RR. In principle, the ability to remove a metal atom from a surface is determined by the bonding strength of an atom to its neighbouring atoms in lattice, and thus correlates with the number of valence electrons that the metal atom has to form the metallic bond. As an essential step for CO₂RR on the electrode surface, the bond formation between a RI and the catalytic metal atom on the surface may attract the valence electrons of the atom from metallic bonding and eventually influence its mobility on the metallic surface. The investigation of the impact of CO₂RR-associated RIs on the atomic mobility is of significant importance not only to reveal the mechanisms of structural degradation and subsequently develop solutions to prolonging the catalyst lifetime for metal catalysts used in CO₂RR, but also to shine more light on the dynamic nature of the catalyst surface during electrochemical reactions. Density functional theory (DFT) calculation is a commonly used tool to explore the migration of the RI and RI-bound metal atom on metal surface at the atomic scale.⁶⁵⁻⁶⁷

In this chapter, I show that RIs may promote the thermodynamic process of vacancy formation (VF) and accelerate the migration kinetics of the adatom on crystallographic facets of Au and Pd using DFT

calculations. This VF assessment from the thermodynamic standpoint provided the initial mechanistic insight into the impact of RIs on the atomic mobility in metal electrocatalysts. In addition to the thermodynamic VF assessment, I also expand the atomic mobility assessment method to enable the evaluation of both thermodynamics and kinetics of VF via DFT and to probe the stability of a complex surface structure (compared to low-index facets) mimicking nanostructured catalysts using *ab initio* molecular dynamic (AIMD) simulations¹³². This approach was applied to a series of metal and metal-alloy CO₂RR catalysts to provide a more comprehensive description of atomic mobility induced by RIs during CO₂RR electrolysis. Specifically, I considered several electrocatalyst compositions of common interest in CO₂RR electrocatalyst design^{133–137}: Cu, Ag, Au, Pd, and Cu₃Pd, and the key RI associated with CO₂ reduction and accompanying reactions, i.e., hydrogen evolution reaction (HER) and oxygen reduction reaction (ORR): *COOH, *H, and *OOH. In this chapter the relative trends in increased atomic mobility by these RI and their specific mechanisms, along with the trends in atomic mobility in the series of metals and their correlations with their chemical and physical nature are discussed in detail, which I present in the following.

4.2 Application of DFT calculations in studying atomic mobility of metal surfaces

The structural stability of metal surfaces depends on the chemical bonds of surface atom with its neighboring lattice atoms as well as the migration difficulty of an adatom on a metal surface. In the case of surface-catalysed reactions, RIs can affect the structural stability of metal surfaces from both aspects due to their intimate interactions with metal surfaces. DFT is a well-established tool to study the influence of a RI on the atomic mobility in a metal catalyst.

The influence of a RI on the atomic mobility in a metal catalyst starts with its adsorption on the catalyst surface. To reveal the interaction of various RIs with metal surfaces, I should first investigate the energetically favorable geometries of (111) (100), (110), and (211) surfaces for the commonly used metals in CO₂RR with adsorbed CO₂RR-related RIs. Optimized geometries of RI-bound metal surfaces can be obtained using DFT calculations, which can reveal the most favorable adsorption structures of CO₂RR-related RIs on various different metal surfaces.

Binding energy of the RIs on the metal surfaces

To understand the binding strength between the RIs and the metal surfaces, the binding energies (E_b) of the studied RIs can be calculated according to equation (2.1) or (2.2) based on the optimized geometries of the metal surfaces bound with the RIs. The binding energy reflects strength and likelihood of RIs on metal surfaces. Therefore, binding energy is an appropriate parameter for describing the formation of adsorbed surface species during CO₂RR, which can help me understand the favorable adsorbed surface species during CO₂RR and its dependences on the materials and surfaces.

Vacancy formation on the metal surfaces

To understand the impact of the adsorbed RIs on the chemical bonds of RI-bound metal atom with its neighbors in the lattice, both the thermodynamic and kinetic aspects of extracting a metal atom can be explored on different crystallographic facets of the studied metals with and without surface-bound RIs. The thermodynamic profile can be assessed by calculating the vacancy formation energy (E_{VF}) according to the equation (2.3) or (2.4). Then, the kinetic aspects of extracting a metal atom from the metal surface can be studied by calculating the energy barriers of single-atom vacancy formation (VF) process according to the equation (2.5). The calculations of E_{VF} and energy barrier of VF process can reveal the influence of the RIs on the interactions of RI-bound metal atom with its neighbors in the lattice.

Atom migration on the metal surfaces

To further understand the impact of RIs on the atomic mobility, the kinetic energy barriers for the migration of a metal adatom can be assessed on different metal surfaces with and without the bound RI, which can be calculated according to equation (2.5). The kinetic energy barrier reflects the minimum kinetic energy required to drive the migration of a metal adatom on metal surfaces, which is another important parameter for understanding the atomic mobility of a metal surface.

4.3 Application of AIMD simulations in studying the atomic mobility

Considering real nanoscale electrocatalysts attainable experimentally, which typically have complex nanomorphology and a high number of undercoordinated sites, the calculations for single-atom VF and migration may not fully reveal the nuances of atomic mobility in the realistic catalysts during CO₂RR. Specifically, possible processes include VF, migration of multiple atoms, and the mutual interactions between the migrating atoms and their neighbors in the lattice. Therefore, the structures and surface behavior description presented above serve only as ideal, hypothetical models to the real catalytic systems, allowing me to roughly assess the comparative surface stability of different compositions and facets in the presence of different RIs. The complexity of multi-atom mechanisms makes it very difficult to study the impact of surface reactions on the structural behavior of realistic catalysts by using the DFT calculations of the VF and atom migration. In contrast, molecular dynamic (MD) simulation is a powerful tool to monitor the structural dynamics of a complex multiatomic surface structure⁶⁹ and the influence of adsorbed species.⁷⁰ Previously, the displacement of atoms in MD simulations has been used to evaluate the atomic mobility in metal materials.¹³⁸ Thus, to have a more comprehensive understanding of the atomic mobility induced by adsorbed RIs in a multiatomic system, I can investigate the dynamical behavior and the displacement of metal atoms on a complex metal surface with and without bound RIs using AIMD simulations. To reflect the complexity and atomic coordination of shaped nanoparticle surface features, I should use a surface model comprised of a metal cluster bound to an extended metal surface. Based on the trajectory of the AIMD simulations, the averaged displacement, mean square displacements (MSDs), radial distribution functions (RDFs), Lindemann index, temperature, and heat capacity of the metal surfaces can be calculated.

Averaged displacement and MSD

The averaged displacement of a metal system defines the average value of the differences between the positions of the metal atoms at reaction time t and the initial time, which is calculated according to equations (2.12) and can be used to qualitatively describe the atomic mobility of a metal. MSD is a measure of the deviation of the position of a particle with respect to a reference position over time, which is calculated according to equation (2.6) and can be applied to quantitatively evaluate the atomic mobility in a metal. The ensemble average in MSD is computed using time averaging according to equation (2.7).

RDF and Lindemann index

RDF describes how density varies as a function of distance from a reference particle, which is calculated according to equation (2.9) and can reveal the feature of a particle: ordered solid behavior or disordered liquid behavior. Lindemann index is a measure of thermally driven disorder in atoms, which is defined in equation (2.10) and can be used to evaluate the atomic order in a solid material.

Temperature and heat capacity

The temperature calculation can be performed to access the heat transfer between RIs and the metal slab, which can be further used to calculate the heat capacity C_V of the metal system. The temperature and heat capacity calculations can reveal the influence of the heat transfer efficiency and heat capacity of a metal on its atomic mobility, which are calculated according to the equation (2.14) and (2.19), respectively.

4.4 Comparison of the atomic mobility on Au and Pd facets during HER and CO₂RR electrolysis

The restructuring of gold and palladium nanoparticles and the surface reactions influencing this process (discussed in Chapter 3) motivated me to perform DFT calculations to study the influence of the RIs on the mobility of the surface metal atoms in the studied systems. More specifically, I investigated the thermodynamics of extracting a metal atom from the metal surface as well as the binding energy and charge distribution between RIs and metal surfaces. Furthermore, kinetic energy barrier of atom migration on metal surfaces was also discussed in this section.

First, I assessed the thermodynamics of extracting a metal atom from the metal surface by calculating the vacancy formation energies on different crystallographic facets of gold and palladium with and without surface-bound CO₂RR and HER reaction intermediates, that is, *COOH and *H, respectively (Figure 4.1a, x-axis, and the scheme underneath). I observed that the vacancy formation energy was considerably reduced by bound *COOH and *H on all studied gold and palladium surfaces, with the adsorbed *COOH having a more pronounced effect than *H. Notably, the material of the metal surface had a marked effect on how strongly the atoms are bound with their neighbors. In addition, the vacancy formation energy was lower on high-index surfaces with undercoordinated sites, such as Au (211). Simultaneously, these sites had higher *COOH and *H binding energies (Figure 4.1b,c) and therefore were more likely to capture the reaction intermediates during the reaction, which in turn reduced the vacancy formation energy, as discussed above. These factors result in high-index surfaces being less thermodynamically stable compared with their low-index counterparts.

To explore further the impact of adsorbed intermediates on the surface atomic mobility, I performed DFT calculations of the charge-density difference for gold surfaces with bound *H and *COOH intermediates (Figure 4.1d,e, respectively, and Figure 4.2). The results showed that *COOH, as an electron acceptor, stabilized its adsorption by pulling the electron density from the gold surface and accumulating it between *COOH and the gold surface along the C–Au bond (Figure 4.1e and 4.2). Consequently, this electron depletion weakened the interaction of the *COOH-bound gold atom with its neighbors in the lattice, making it easier to extract that *COOH-bound gold atom from the surface. Similar to *COOH, *H also caused an electron density accumulation between *H and *H-bound gold along the H–Au bond (Figure 4.1d and 4.2). However, *H is less efficient in displacing the electron density in this way, as can be seen by a smaller cyan area compared with *COOH-bound gold. Thus, the bonds between *H-bound gold and its neighbors in the lattice are less affected by this adsorbed

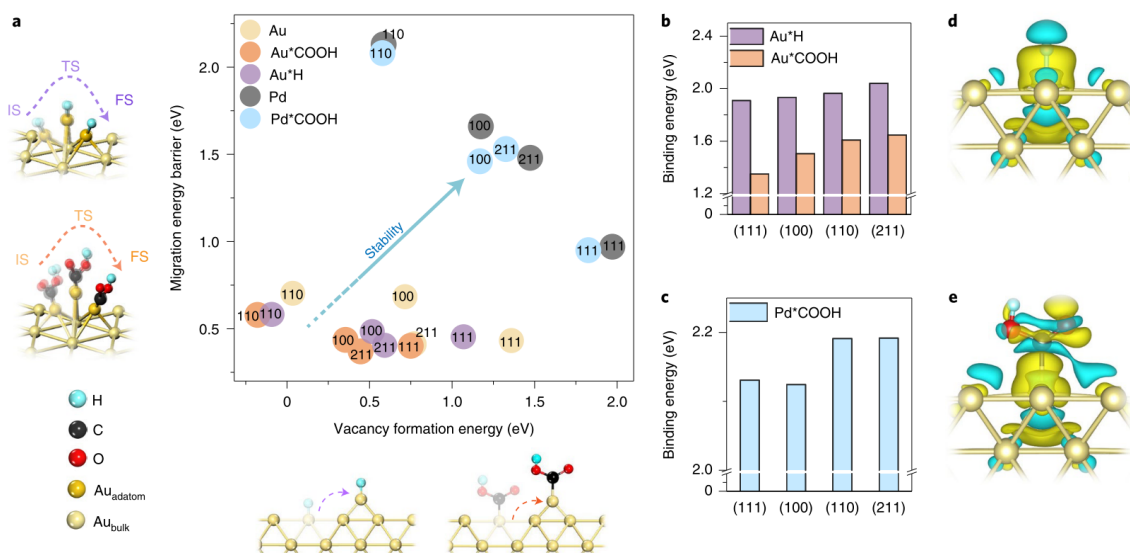


Figure 4.1: Adsorbed reaction intermediate facilitation of atomic mobility on different crystallographic facets. a, Atomic migration energy barrier and atomic vacancy formation energy calculated for different crystallographic facets of gold with and without surface-bound intermediates *COOH or *H and of palladium with and without surface-bound intermediate *COOH. The arrow shows the general trend of decreasing atomic mobility. The cartoons on the left illustrate the migration of a single metal adatom with bound reaction intermediates (*H, above; *COOH, below) to an adjacent surface site, and the cartoon scheme along the bottom illustrates the vacancy formation events for which the energies were calculated. IS, initial state; TS, transition state; FS, final state. b, Calculated binding energy of *COOH and *H intermediates to different crystallographic facets of gold. c, Calculated binding energy of *COOH intermediate to different crystallographic facets of palladium. d,e, Charge distribution for Au(100)–H (d) and for Au(100)–COOH (e); yellow and blue colors represent the charge accumulation and depletion, respectively, with an iso-surface value of $0.001 \text{ e} \text{ \AA}^{-3}$ implemented. Reprinted with permission from ref. [71]. Copyright 2021, Springer Nature.

intermediate due to the lower electron depletion by bound *H. These results also correlate with the relatively higher stability of gold structures in HER electrolysis than in CO₂RR electrolysis under the same operating conditions.

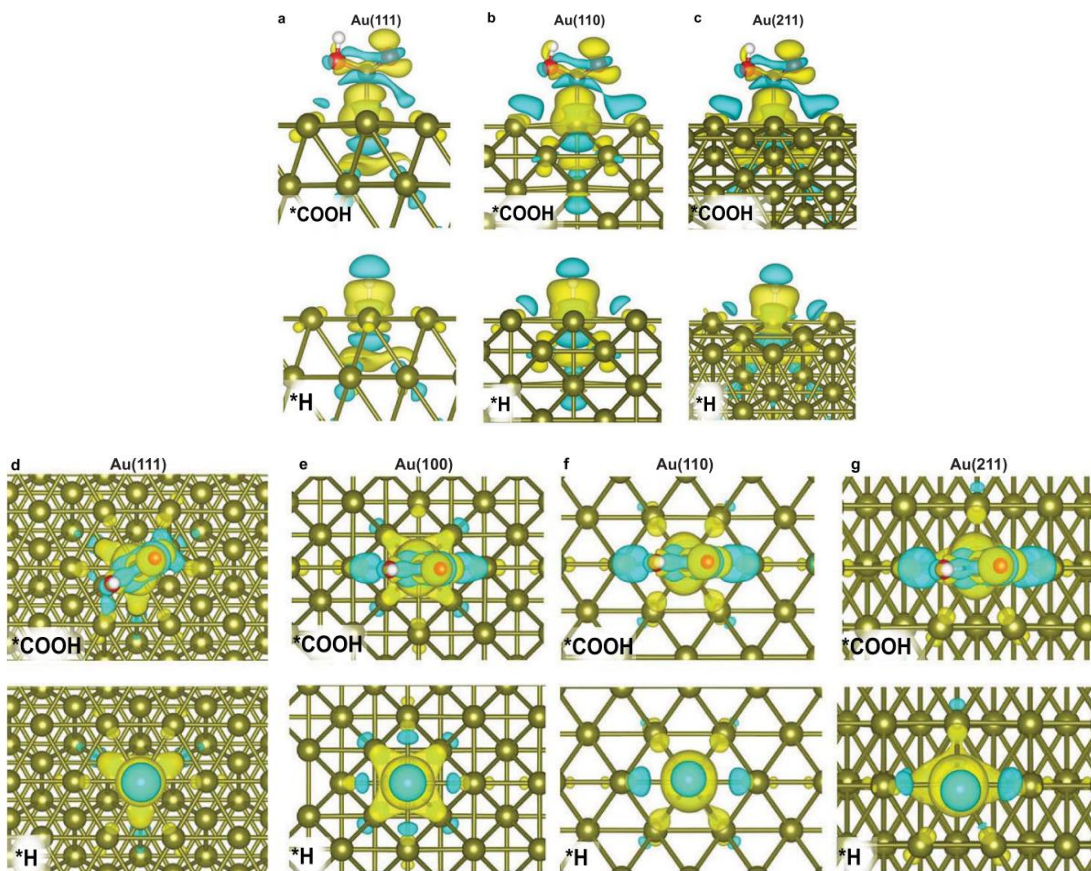


Figure 4.2: Charge distribution profiles for different Au facets with surface-bound intermediates *COOH or *H. a–c, Side view of Au(111), Au(110) and Au(211). d–g, Top view of Au(111), Au(100), Au(110) and Au(211). Yellow and blue colors represent the charge accumulation and depletion, with an iso-surface value of $0.001 \text{ e}/\text{\AA}^3$ implemented. Reprinted with permission from ref. [71]. Copyright 2021, Springer Nature.

Next, I assessed the kinetic aspect of the surface atomic mobility by calculating the migration energy barriers on different surfaces with and without the bound electrocatalytic reaction intermediates (Figure 4.1a, y-axis, and Figure 4.3, 4.4, A.1-A.8). As in the vacancy formation energy calculations, palladium suggested a comparatively higher stability than gold, based on the relatively lower migration energy barriers of the latter. Bound reaction intermediates were shown to decrease the migration energy barrier for the studied gold and palladium surfaces, with the adsorbed *COOH having a more pronounced effect than *H on all calculated crystallographic facets of gold. The relative positions of the facets on the migration energy barrier axis showed a different trend than the vacancy formation energy axis (Figure 4.1a). Specifically, despite the lowest vacancy formation energy, Au (110) had the highest

migration energy barrier among the studied gold surfaces, which correlates with the experimental evidence of gold BNPs maintaining their dominant (110) surfaces after continuous electrolysis (Figure 3.11m).

Considering the migration energy barriers and vacancy formation energies together, the plot in Figure 4.1a shows the comparatively higher stability of the surface atomic structures in the top-right corner, whereas the structures in the bottom-left corner are relatively more likely to reconstruct. However, these thermodynamic and kinetic aspects consider random hopping of surface atoms and do not reflect any locality or directionality of atomic mobility on the nanoscale. Conversely, the experimental data implied that in some localities of complex nanoscale electrocatalysts the atoms were hopping about more than in other otherwise identical features, suggesting that the impacts exerted on them are associated with the applied bias. Moreover, the experimental evidence revealed structural changes at the interfaces of the particles with the substrate and each other, where the electrolysis is hindered due to apparent mass-transport limitations, further suggesting the presence of additional driving forces for atomic migration.

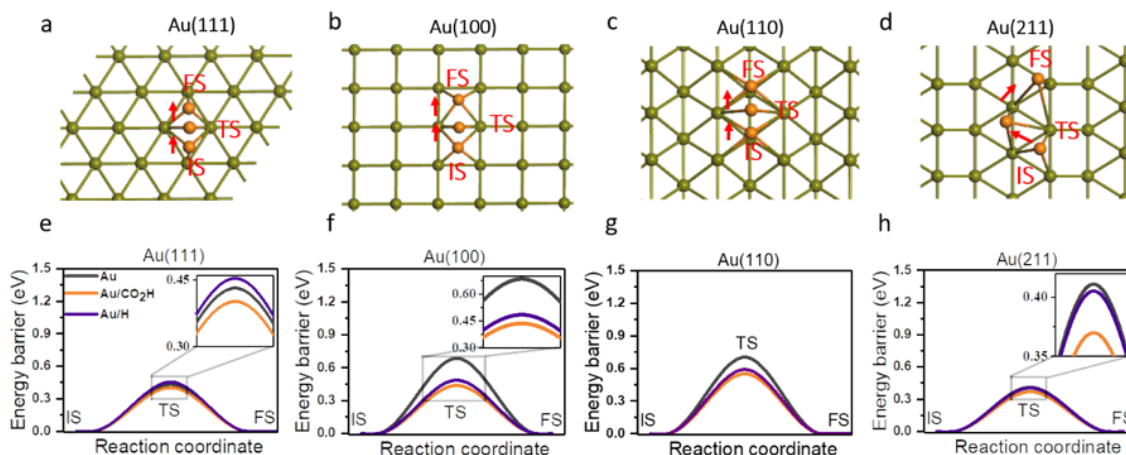


Figure 4.3: Au atom mobility differentiation based on reaction intermediates present in the media. (a-d) the hopping paths studied for surface atom migration on Au(111), Au(100), Au(110) and Au(211) surfaces, with the olive colour atoms representing the Au surface and orange colour atoms representing the hopping Au atom and intermediate-bound Au atoms (Au-COOH and Au-H). (e-h) calculated energy barriers for migration path of Au atom, Au-COOH (CO₂RR) and Au-H (HER) intermediate-bound Au atoms on Au(111), Au(100), Au(110) and Au(211) surfaces, respectively. Reprinted with permission from ref. [71]. Copyright 2021, Springer Nature.

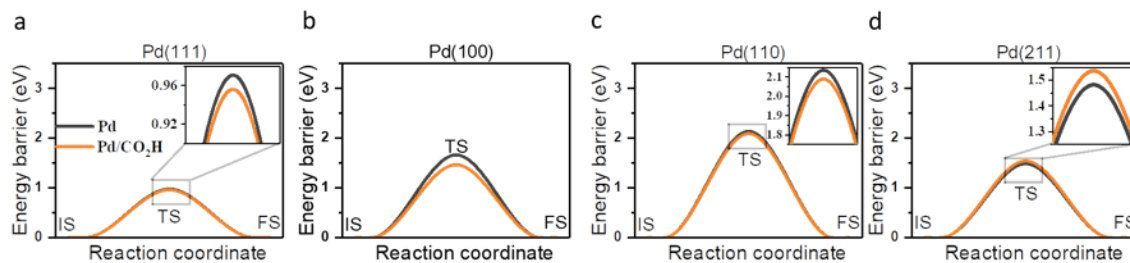


Figure 4.4: Calculated energy barriers for migration path of Pd atom and Pd-COOH (CO₂RR) intermediate-bound Au atom, with (a-d) for Pd(111), Pd(100), Pd(110) and Pd(211) surfaces, respectively. The paths studied for Pd are the same as that for Au. Reprinted with permission from ref. [71]. Copyright 2021, Springer Nature.

4.5 Comparison of the atomic mobility on Cu, Ag, Au, and Pd facets during HER, ORR and CO₂RR electrolysis

In the previous section 4.4, I showed that the RI may promote the thermodynamic process of vacancy formation (VF) and accelerate the migration kinetics of the adatom on crystallographic facets of Au and Pd using DFT calculations. This VF assessment from the thermodynamic standpoint provided the initial mechanistic insight into the impact of RIs on atomic mobility in metal electrocatalysts. A more detailed description of RI-induced VF mechanism on metal surfaces, which includes kinetic considerations of VF pathways, however, has not been explored to date. In addition, more complex structural models reflecting the complexity of nanostructured metal catalysts and accounting for all possible RIs are necessary to accurately predict the atomic mobility trends in a series of electrocatalysts with various compositions.

To address this knowledge gap, in this section 4.5, I expanded the atomic mobility assessment method to enable the evaluation of both thermodynamics and kinetics of VF via DFT and to probe the stability of a complex surface structure (compared to low-index facets) mimicking nanostructured catalysts using *ab initio* molecular dynamic (AIMD) simulations. This approach was applied to a series of metal CO₂RR catalysts to provide a more comprehensive description of atomic mobility induced by RIs during CO₂RR electrolysis. Specifically, I considered several electrocatalyst compositions of common interest in CO₂RR electrocatalyst design:^{133–137} Cu, Ag, Au, Pd, and the key RI associated with CO₂ reduction and accompanying reactions, i.e., HER and ORR: *COOH, *H, and *OOH. In this work, the relative trends in increased atomic mobility by these RI and their specific mechanisms, along with the trends in atomic mobility in the series of metals and their correlations with their chemical and physical nature are discussed in detail, which I present in the following.

The influence of a RI on the atomic mobility in a metal catalyst starts with its adsorption on the catalyst surface. To reveal the interaction of various RIs with metal surfaces, I first investigated the energetically favorable geometries of (111) (100), (110), and (211) surfaces for the commonly used metals in CO₂RR such as Cu, Ag, Au, and Pd with adsorbed CO₂RR-related RIs, including *COOH, *H, and *OOH, key RIs for CO₂RR itself, competing HER, and competing ORR from traces of air/oxygen present in CO₂, respectively. Optimized geometries of RI-bound metal surfaces are shown in Figure 4.5a and Figure A.9-A.11. I found that the *H tends to adsorb at a three-fold or four-fold hollow site, except for the case of (110) facet where it prefers a bridge site; the *OOH interacts with the metal surfaces through both oxygen atoms; and the *COOH prefers a stabilization via forming C-

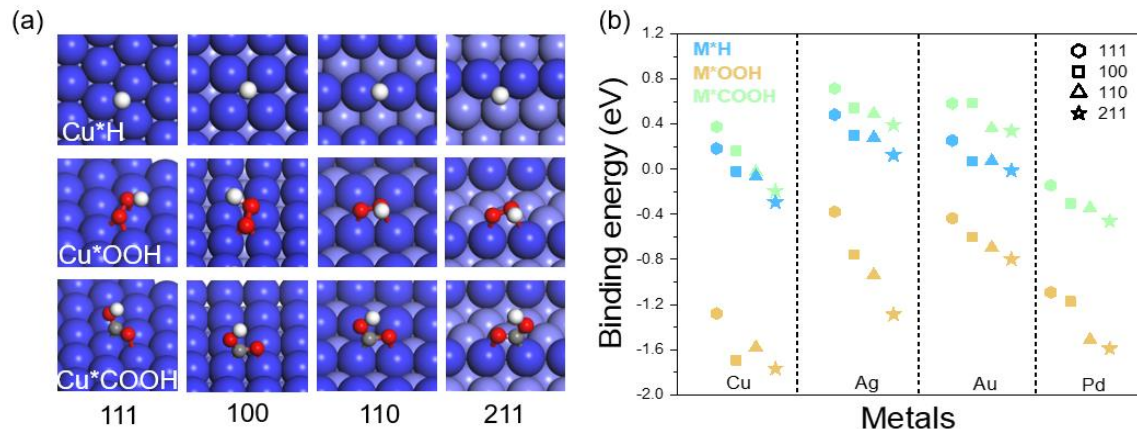


Figure 4.5: The interaction of different intermediates with various metal surfaces. (a) the optimized geometries of adsorbed $^*\text{H}$, $^*\text{OOH}$ and $^*\text{COOH}$ on Cu surfaces of (111), (100), (110) and (211), and (b) the binding energies of $^*\text{H}$, $^*\text{OOH}$ and $^*\text{COOH}$ on (111), (100), (110) and (211) surfaces of Cu, Ag, Au and Pd. White, H atom; red, O atom; gray, C atom; dark/light blue, Cu atom in outmost/inner layer. Reprinted with permission from ref. [132]. Copyright 2022, Royal Society of Chemistry.

M and O-M bonds. I note that the calculations of the $^*\text{H}$ on Pd surfaces was not performed due to the complexity of simulating Pd-H interactions associated with the formation of palladium hydride.^{139,140} To further understand the binding strength between the RIs and the metal surfaces, the binding energies of the studied RIs were calculated according to equation 2.2 based on the optimized geometries of the metal surfaces bound with the RIs (Figure 4.5b).

Note that the formation of adsorbed surface species is not only dependent on the binding energy, but also on other factors such as chemical potentials. However, in an aqueous electrolyte at ambient conditions typical for CO_2RR , the influence of chemical potentials on the presence of $^*\text{H}$ and $^*\text{OOH}$ is minor to that of binding energies. To illustrate it, I considered the formation of $^*\text{OOH}$ (for ORR) and $^*\text{COOH}$ (for CO_2RR) as an example. Assuming both O_2 and CO_2 reach their saturation (23 ppm and 615 ppm, respectively),¹⁴¹ the resulting correction to the binding energy difference between the $^*\text{OOH}$ and the $^*\text{COOH}$ is estimated to be 0.08 eV, while the absolute binding energy difference is about 1 eV (Figure 4.5b). Therefore, the binding energy is an appropriate parameter for describing the formation of adsorbed surface species during CO_2RR .

The binding energy results in Figure 4.5b revealed that the interaction between a RI and a metal surface strongly depends on the nature of the RI. Specifically, $^*\text{OOH}$ showed the most negative binding

energy on all studied facets of different metals, followed by *H, and finally by *COOH, which suggests that RIs of *OOH and *H from side reactions during CO₂RR can interact more strongly with the metal surfaces compared to the interaction between metal surfaces and CO₂RR reaction intermediate (*COOH), and therefore affect the structure of the metal surfaces more significantly. Moreover, the preferable adsorption of *OOH and *H can compete with the adsorption of *COOH and disturb the selectivity of CO₂RR. In this regard, considering the contribution of *OOH is particularly important due to its binding being the strongest on all studied metal surfaces (Figure 4.5b). Besides *OOH, *H also has stronger interactions with metal surfaces than the interaction between the metal surfaces and *COOH. The formation of *H is unavoidable in aqueous conditions in which CO₂RR is generally carried out. So, it has been a challenge to inhibit the competing HER against CO₂RR in aqueous electrolytes. Furthermore, the formation of *H on metal surfaces is also needed for the hydrogenation steps in CO₂RR process. As a good candidate of CO₂RR catalyst, it should be able to balance the formation of *COOH and *H. On this subject, Cu is the best choice among studied metals since the

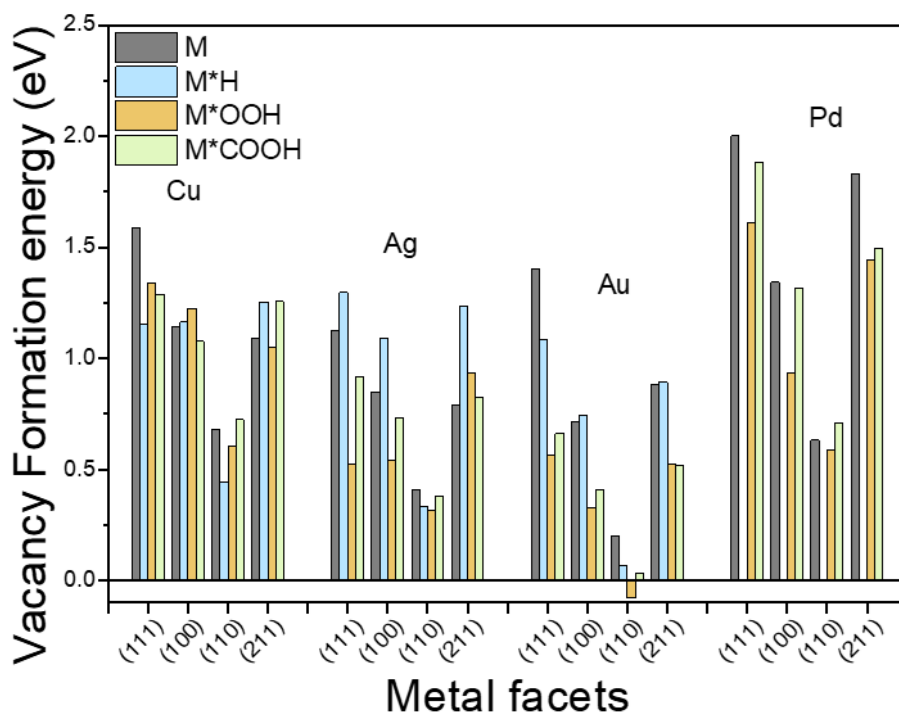


Figure 4.6: The influence of the reaction intermediates and metal materials on vacancy formation energy. The (111), (100), (110), and (211) surfaces of Cu, Ag, Au, and Pd were studied with and without adsorbed RIs. Reprinted with permission from ref. [132]. Copyright 2022, Royal Society of Chemistry.

difference between binding energies of *H and *COOH on Cu surfaces is smaller compared to that on other metals. Due to the moderate binding affinity to the CO₂RR intermediate and H atom, Cu is able to stabilize CO₂RR intermediates and its further hydrogenation simultaneously, which may contribute to its unique ability to produce a variety of hydrocarbons and oxygenates during the CO₂RR, in agreement with earlier studies.¹⁴² In addition to the nature of the RIs, our results indicated that the material composition and facet type of the metal can alter the observed binding energy of RI by about 0.5 - 1.0 eV (Figure 4.5b). Among the studied metals, Pd and Cu have more negative binding energies to the studied RIs compared to Ag and Au, suggesting a generally stronger interaction of the RIs with Pd and Cu metal surfaces. The various facets of a certain metal also show different binding energies to the RIs, with high-index facets showing more negative binding energies, consistent with chemical intuition as the metal atoms on high-index facets are generally more undercoordinated.

To understand the impact of the adsorbed RIs on the chemical bonds of RI-bound metal atom with its neighbors in the lattice, I then explored both the thermodynamic and kinetic aspects of extracting a metal atom on different crystallographic facets of the studied metals with and without surface-bound RIs. The thermodynamic profile was first assessed by calculating the vacancy formation energy (E_{VF}), shown in Figure 4.6. I found the adsorbed RIs can greatly affect E_{VF} on all studied metal surfaces. Among those RIs, *COOH and *OOH are prone to reduce the E_{VF} by around 0.25 eV on the majority

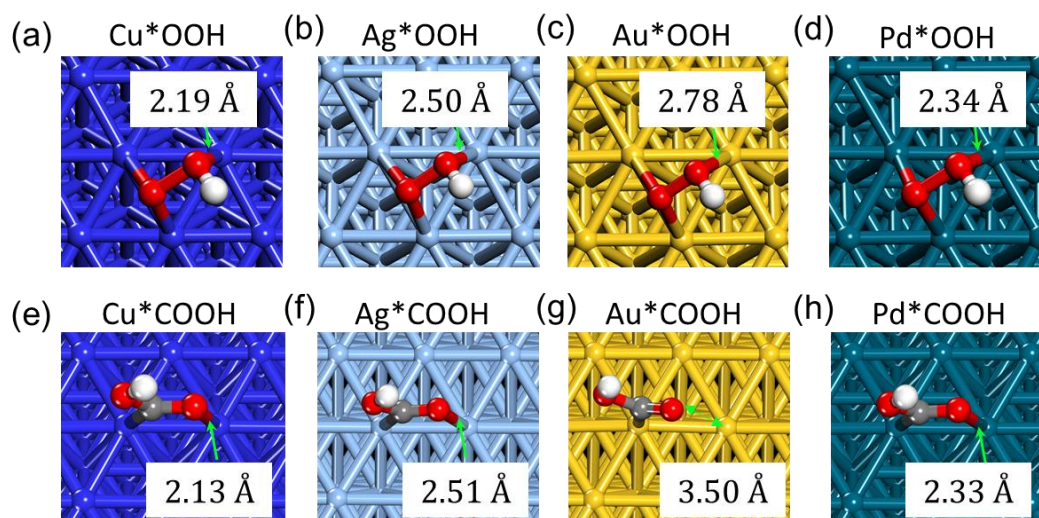


Figure 4.7: Comparison of the adsorption structures for *OOH and *COOH on Cu(111), Ag(111), Au(111), and Pd(111) without vacancy. Reprinted with permission from ref. [132]. Copyright 2022, Royal Society of Chemistry.

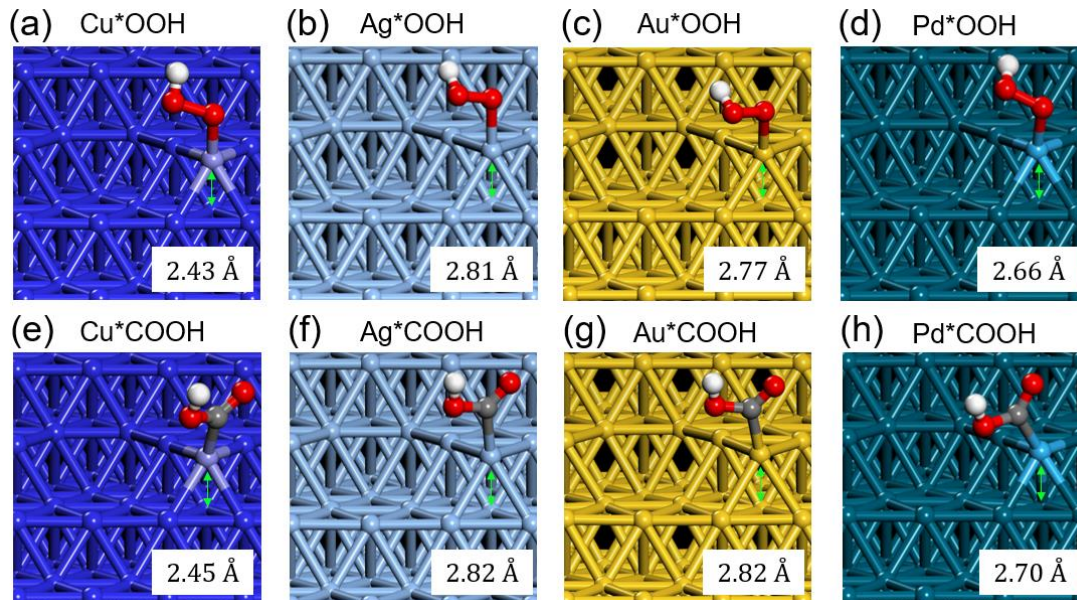


Figure 4.8: Comparison of the adsorption structures for *OOH and *COOH on Cu(111), Ag(111), Au(111), and Pd(111) with single-atom vacancy. Reprinted with permission from ref. [132]. Copyright 2022, Royal Society of Chemistry.

of the studied metals and therefore promote the process of extracting a metal atom from the surface thermodynamically. Note that a more obvious E_{VF} drop (around 0.75 eV) is observed on *COOH- and *OOH-bound Au surfaces, suggesting Au surfaces are more affected by *COOH and *OOH thermodynamically compared to other three metals. The large E_{VF} drop may be attributed to the relative inertness of the neighboring Au atoms around the catalytic center compared to those in other metals. As shown in Figure 4.7, on both the *OOH- and *COOH-bound Au(111) surfaces, the Au-O bond length (Figure 4.7c and g) is longer than the corresponding M-O bond lengths on other metal surfaces. This indicates a stronger interaction between RI and Au catalytic center and therefore more interference between RI and the valence electrons of the Au catalytic center from the bound RIs than that on other metals, leading to a lower E_{VF} on *COOH- and *OOH-bound Au surfaces. Furthermore, a negative E_{VF} is observed in the case of OOH-bound Au(110) surface with a single-atom vacancy, suggesting that this structure is more favorable thermodynamically than the other structures. This may be due to the stronger interaction between the removed Au atom and Au(110) surface than that on other metals. For instance, as shown in Figure 4.8, the distance between the removed atom and the metal surface is much shorter on OOH-bound Au(110) surface (Figure 4.8c) than that on Ag*OOH (Figure 4.8b) despite the two metals having very similar valence electron configurations and atomic radii. This stronger

interaction in gold could lower the energy of OOH-bound Au(110) surface with vacancy and eventually lead to a negative E_{VF} . Interestingly, *H exhibited a more complex behavior in terms of E_{VF} on different metal materials: *H can either reduce the E_{VF} on (111) and (110) surfaces or increase it on (100) and (211) surfaces for Cu, Ag, and Au. This difference in the effect of *H RI on E_{VF} is likely due to the inconsistent binding motif it adopts in the explored cases. Furthermore, E_{VF} substantially varied on different metals, with Pd surfaces having relatively higher E_{VF} than the surfaces of other metals, i.e., the VF is less favoured on Pd compared to other metals.

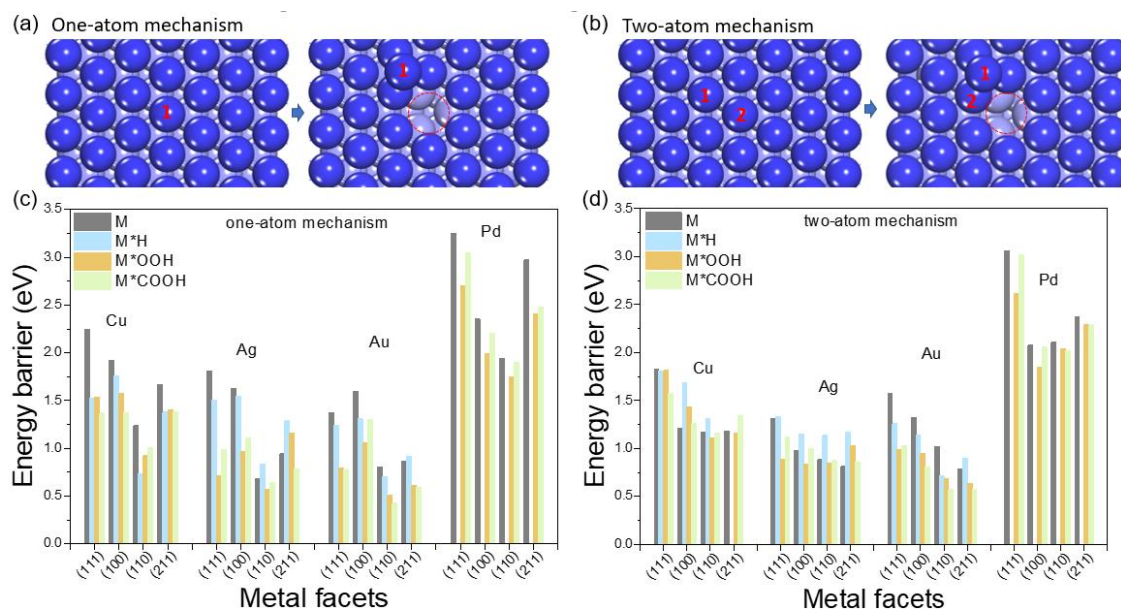


Figure 4.9: The influence of the RIs and metal nature on the one-atom and the two-atom VF mechanisms: the schematic of the two VF mechanisms (a) and the associated energy barriers (b) on (111), (100), (110), and (211) surfaces of studied metals with and without adsorbed RIs. Reprinted with permission from ref. [132]. Copyright 2022, Royal Society of Chemistry.

To further elucidate the process of VF, I also assessed the kinetic aspects of extracting a metal atom from the metal surface by calculating the energy barriers of single-atom VF process on different crystallographic facets of the studied metals with and without surface-bound RIs. (Figure 4.9, A.12-A.15) There are multiple ways for generating a single-atom vacancy on metal surfaces. One of the conceptually simplest approaches is to move a surface atom over a bridge site to its nearest adsorption site, referred to as “one-atom mechanism” below (Figure 4.9a). To have a more comprehensive profile of VF process, I also considered another plausible VF mechanism, referred to as “two-atom

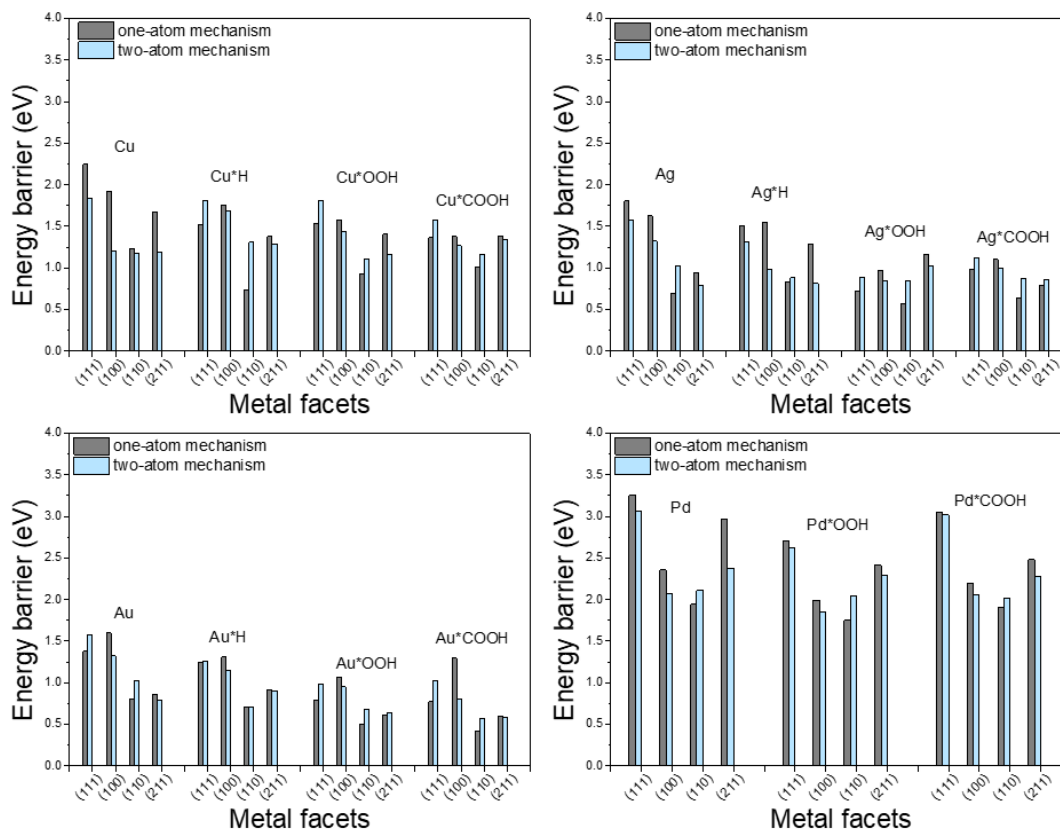


Figure 4.10: Comparison of the kinetic barriers for the two VF mechanisms on (111), (100), (110), and (211) surfaces of Cu, Ag, Au, and Pd. Reprinted with permission from ref. [132]. Copyright 2022, Royal Society of Chemistry.

mechanism”, in which one atom (atom 1) moves up toward a three-fold site, while another neighboring atom (atom 2) moves toward the original position of the first atom (atom 1 Figure 4.9b). I compared the energy barriers for these two VF mechanisms on the same metal surfaces with and without adsorbed RIs in Figure 4.10, with their corresponding detailed kinetic energy profiles of VF shown in Figure A.16-A.19. The results revealed that the VF of one-atom mechanism had higher energy barrier compared to that of two-atom mechanism on most of the metal surfaces without adsorbed RIs, making the two-atom mechanism more likely in this case. This trend correlates with the fact that the two-atom mechanism minimizes the travel distance the migrating atom has to travel by, in contrast to the one-atom mechanism. However, for RI-bound metal surfaces, the trends in the energy barrier showed a more complex behavior with either the one-atom or the two-atom mechanism having the higher energy barrier. This result suggests that the adsorbed RIs may have a significant influence on the VF

mechanism, and in some cases can decrease the barrier toward VF. Geometrically, the adsorbed RIs can facilitate the migrating atom to move over the bridge site, and therefore make the one-atom mechanism VF more accessible on the metal surfaces with adsorbed RIs. Similar to the trends observed in the relative VF energies, I found that the surface-bound RIs (*H, *OOH, and *COOH) reduced the energy barriers of VF in both mechanisms, with *OOH and *COOH having a more pronounced effect than *H (Figure 4.9c, d). In addition, VF processes were found to have lower energy barriers on high-index surface such as (110) and (211) compared to (111) and (100), implying that the high-index surfaces are less stable compared to their low-index counterparts both kinetically and thermodynamically.

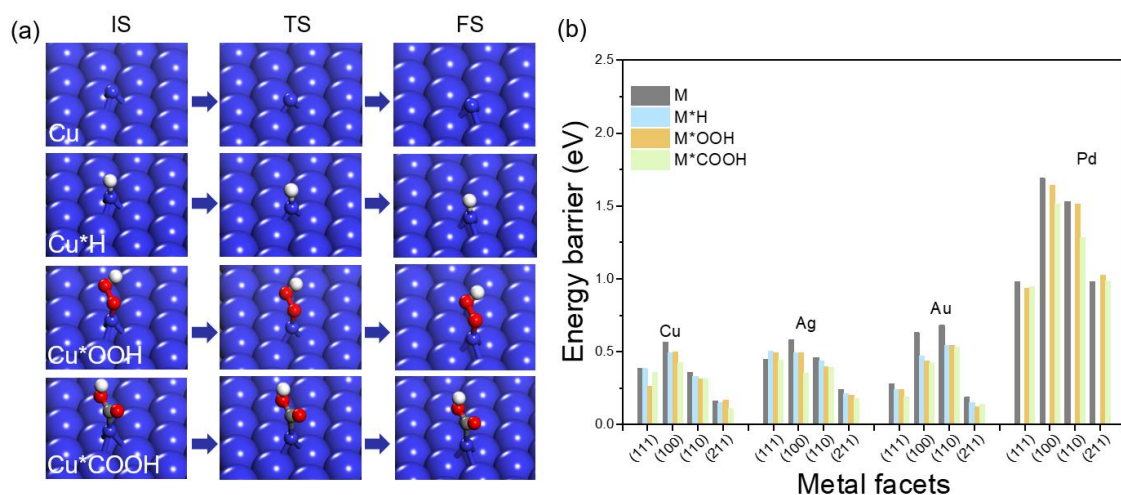


Figure 4.11: The comparison of atomic mobility on metal surfaces under different reaction conditions. (a) The migration pathway of a metal adatom on Cu(111) surface without and with different adsorbed RIs (*H, *OOH, and *COOH). (b) The energy barriers of surface adatom migration on (111), (100), (110), and (211) surfaces of studied metals with and without adsorbed RIs. White, H atom; red, O atom; gray, C atom; dark blue, Cu atom. Reprinted with permission from ref. [132]. Copyright 2022, Royal Society of Chemistry.

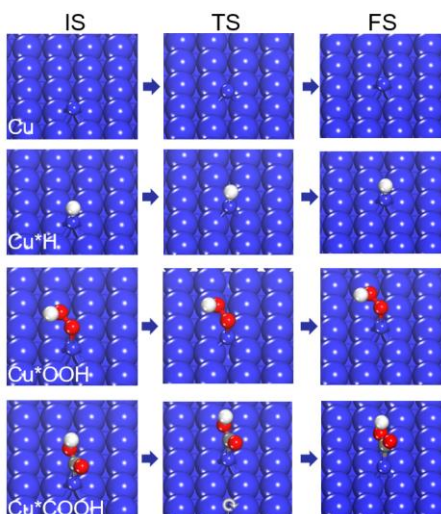


Figure 4.12: Optimized geometry structures for initial, transition, and final states of migration for Cu atom and intermediate-bound Cu atoms of Cu*H (HER), Cu*OOH (ORR), and Cu*COOH (CO₂RR) on the Cu(100) surface. Reprinted with permission from ref. [132]. Copyright 2022, Royal Society of Chemistry.

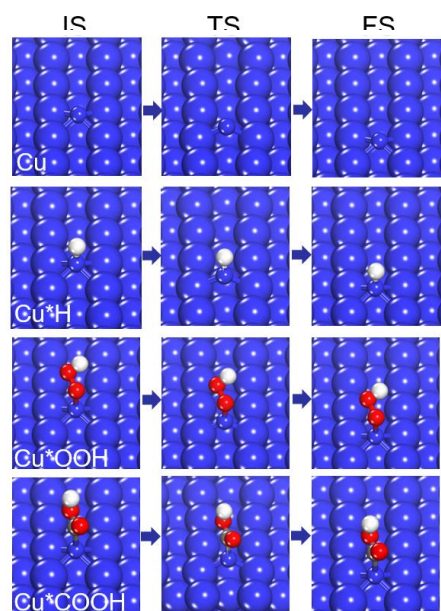


Figure 4.13: Optimized geometry structures for initial, transition and final states of migration for Cu atom and intermediate-bound Cu atoms of Cu*H (HER), Cu*OOH (ORR), and Cu*COOH (CO₂RR) on the Cu(110) surface. Reprinted with permission from ref. [132]. Copyright 2022, Royal Society of Chemistry. Reprinted with permission from ref. [132]. Copyright 2022, Royal Society of Chemistry.

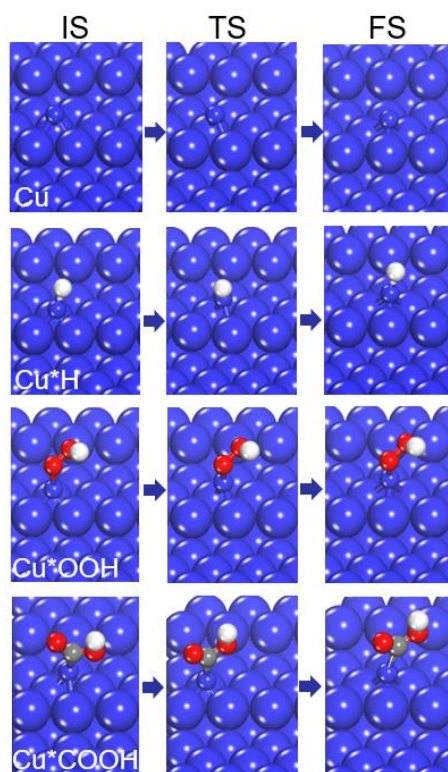


Figure 4.14: Optimized geometry structures for initial, transition and final states of migration for Cu atom and intermediate-bound Cu atoms of Cu*H (HER), Cu*OOH (ORR), and Cu*COOH (CO₂RR) on the Cu(211) surface. Reprinted with permission from ref. [132]. Copyright 2022, Royal Society of Chemistry.

To further understand the impact of RIs on the atomic mobility, I assessed the kinetic energy barriers for the migration of a metal adatom on different metal surfaces with and without the bound RI. The migration pathway of the surface adatom with and without the bound RI on different Cu surfaces is shown in Figure 4.11a and Figure 4.12-4.14. The same migration pathway was considered on different surfaces of the other metals in this study, Ag, Au, and Pd. The surface adatom was considered to be moving from one energetically favorable surface site to another one nearby by moving directly over a bridge site. Similar to the trends observed in the thermodynamic and kinetic analysis of VF, I found that the surface atom migration can be significantly affected by the nature of adsorbed RIs and the facet and material of the metal during CO₂RR electrolysis. The results indicated that the bound RIs reduce the energy barriers of the surface atom migration on different surfaces of the studied metals to varying degrees (Figure 4.11b), with *COOH having the most pronounced effect (ca. 0.1 eV drop), followed by *OOH (ca. 0.04 eV drop), and finally *H (ca. 0.03 eV drop) as shown in Figure 4.15. Note that energy barrier drops on Au surfaces are different compared to that on other metal surfaces, with a decrease of 0.12 eV, 0.1 eV and 0.09 eV for *COOH, *OOH, and *H, respectively. As discussed before, the difficulty of surface atom migration is another factor that can determine the structural stability of metal surfaces, which can be characterized by the energy barrier of surface atom migration: a metal surface with a higher migration energy barrier tends to be more stable than that with a lower barrier. Our results suggested the adsorbed RIs can contribute to the acceleration of the surface atom migration,

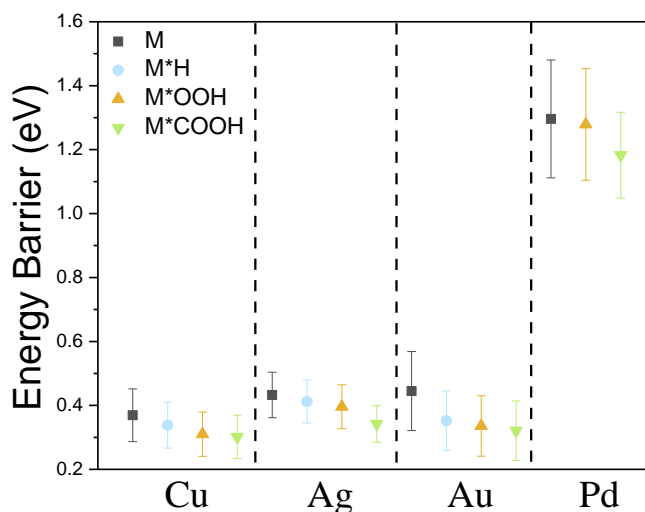


Figure 4.15: Average values of adatom migration energy barriers on studied four metal surfaces for Cu, Ag, Au, and Pd without and with different adsorbed RIs (*H, *OOH, and *COOH). Reprinted with permission from ref. [132]. Copyright 2022, Royal Society of Chemistry.

thereby promoting atomic mobility and lowering the structural stability on metal surfaces. Moreover, among the studied metals, Pd exhibited the highest (least favorable) migration energy (1.18 eV – 1.29 eV) with Au, Ag, and Cu having lower and similar migration energy barriers (0.30 eV – 0.44 eV) in Figure 4.15. As suggested by our results, Pd catalysts should have a higher stability than the other three metals including Au, Ag, and Au under CO₂RR electrolysis, which is consistent with the existing experimental observations.^{63,71} For Au, Ag, and Au, they shared a similar structural stability. Additionally, the migration energy barrier also varied on the different surfaces of all the *fcc* metals studied here, with (100) and (110) surfaces having relatively higher kinetic barriers than (111) and (211) surfaces.

Considering real nanoscale electrocatalysts attainable experimentally, which typically have complex nanomorphology and a high number of undercoordinated sites, the calculations for single-atom VF and migration may not fully reveal the nuances of atomic mobility in the realistic catalysts during CO₂RR. Specifically, possible processes include VF, migration of multiple atoms, and the mutual interactions between the migrating atoms and their neighbors in the lattice. Therefore, the structures and surface behavior description presented above serve only as ideal, hypothetical models to the real catalytic systems, allowing me to roughly assess the comparative surface stability of different compositions and facets in the presence of different RIs. The complexity of multi-atom mechanisms makes it very difficult to study the impact of surface reactions on the structural behavior of realistic catalysts by using the DFT calculations of the VF and atom migration. In contrast, molecular dynamic (MD) simulation is a powerful tool to monitor the structural dynamics of a complex multiatomic surface structure⁶⁹ and the influence of adsorbed species.⁷⁰ Previously, the displacement of atoms in MD simulations has been used to evaluate the atomic mobility in metal materials.¹³⁸ Thus, to have a more comprehensive understanding of the atomic mobility induced by adsorbed RIs in a multiatomic system, I investigated the dynamical behavior and the displacement of metal atoms on a complex metal surface with and without bound RIs using AIMD simulations. To reflect the complexity and atomic coordination of shaped nanoparticle surface features, I built a surface model comprised of a metal cluster bound to an extended metal surface. The 13-atom metal cluster and its interface with the substrate was used to represent highly undercoordinated features of a nanoparticle. The number of atoms was set at 13 because a cluster with more atoms becomes too computationally demanding.

The snapshots of the trajectories for the morphology evolution of the studied metal clusters with and without bound RIs are shown in Figure 4.16a and Figure 4.17. For Cu clusters, I observed the a *COOH-bound Cu atom was extracted from Cu cluster faster (at around 0.5 ps) than a bare Cu atom or a Cu atom bound with the other RI (*H or *OOH). In addition to the RI-bound Cu atom, Cu atoms

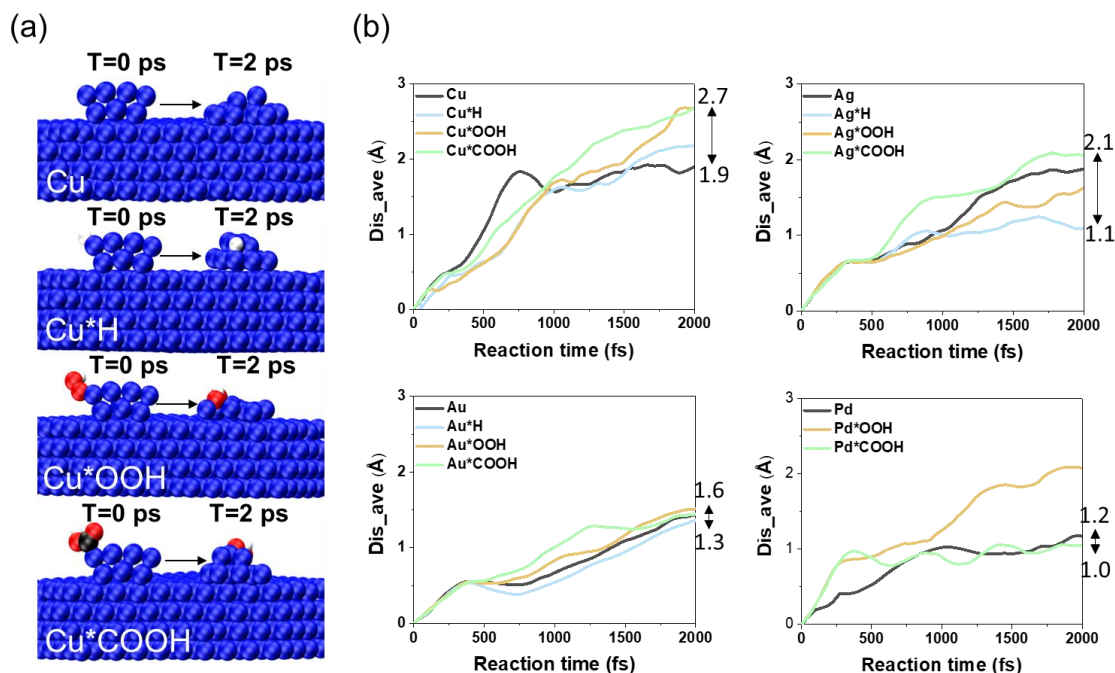


Figure 4.16: AIMD simulations of the metal cluster supported on extended metal surfaces. (a) Snapshots during the trajectories of AIMD for Cu cluster and H-, OOH- and COOH-bound Cu cluster on the Cu (111) surface. (b) The change of the averaged displacements of atoms in Cu, Ag, Au, and Pd clusters with and without bound RIs with time. White, H atom; red, O atom; black, C atom; dark blue, Cu atom. Reprinted with permission from ref. [132]. Copyright 2022, Royal Society of Chemistry.

around it also moved from their original positions when RI-bound Cu atom was separated from the metal cluster. A similar trend was observed on the other metal clusters. Therefore, the atomic mobility in the metal clusters was difficult to evaluate by only visualizing the morphology change. To qualitatively assess the atomic mobility, the averaged displacement of metal atoms in the cluster was considered to evaluate the atomic mobility in a metal cluster. The material of the metal exhibited a great impact on the averaged displacement of the cluster metal atoms during MD simulation. The results revealed the averaged displacement ranges of a Cu, Ag, Au, and Pd cluster atoms were 1.9-2.7 Å, 1.1-

2.1 Å, 1.3-1.6 Å, and 1.0-1.2 Å, respectively. (*OOH-bound Pd cluster is a special case and is discussed in the text below.) The variation in the averaged displacement on different metals reflects the difference in the atomic mobilities on these metals, with Pd having the lowest atomic mobility, followed by Au, Ag, and finally Cu. In addition, smaller averaged displacement ranges for Au and Pd clusters suggest that the atomic mobility in these metal clusters is less affected by the RI compared to Cu and Ag clusters.

Furthermore, the averaged displacement of cluster atoms was also sensitive to the nature of the adsorbed RI. The averaged displacements of *COOH-bound and *OOH-bound metal clusters were greater than that of *H-bound clusters on all metals. Interestingly, I found that the averaged displacements in the Cu and Pd clusters with bound *OOH were larger than in the Cu and Pd clusters with bound *COOH, respectively, resulting from the O-O bond cleavage and the formation of *O or *OH species, which further facilitated the atomic mobility. The displacement increased sharply after the cleavage of O-O bond at 1.5 ps and 1.0 ps on Cu and Pd clusters with adsorbed *OOH, respectively

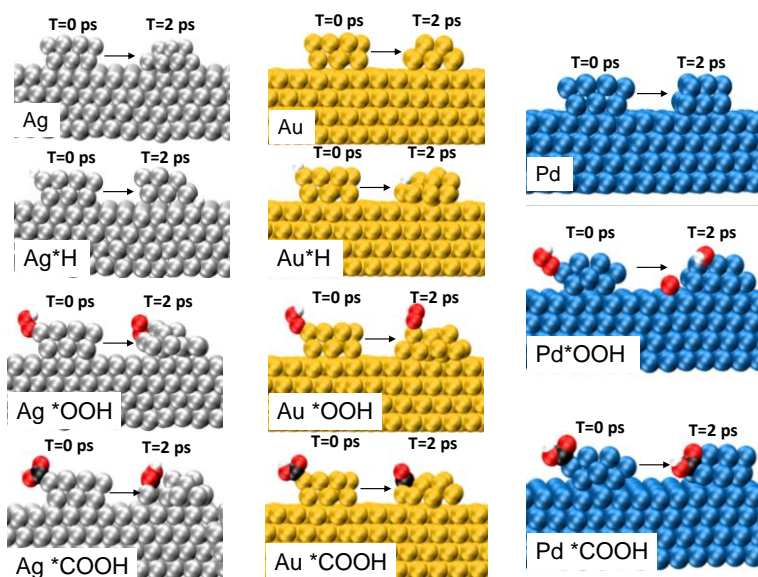


Figure 4.17: Snapshots during the trajectories of AIMD for Ag, Au, Pd clusters with and without adsorbed reaction intermediates of *H, *OOH, and *COOH. Reprinted with permission from ref. [132]. Copyright 2022, Royal Society of Chemistry.

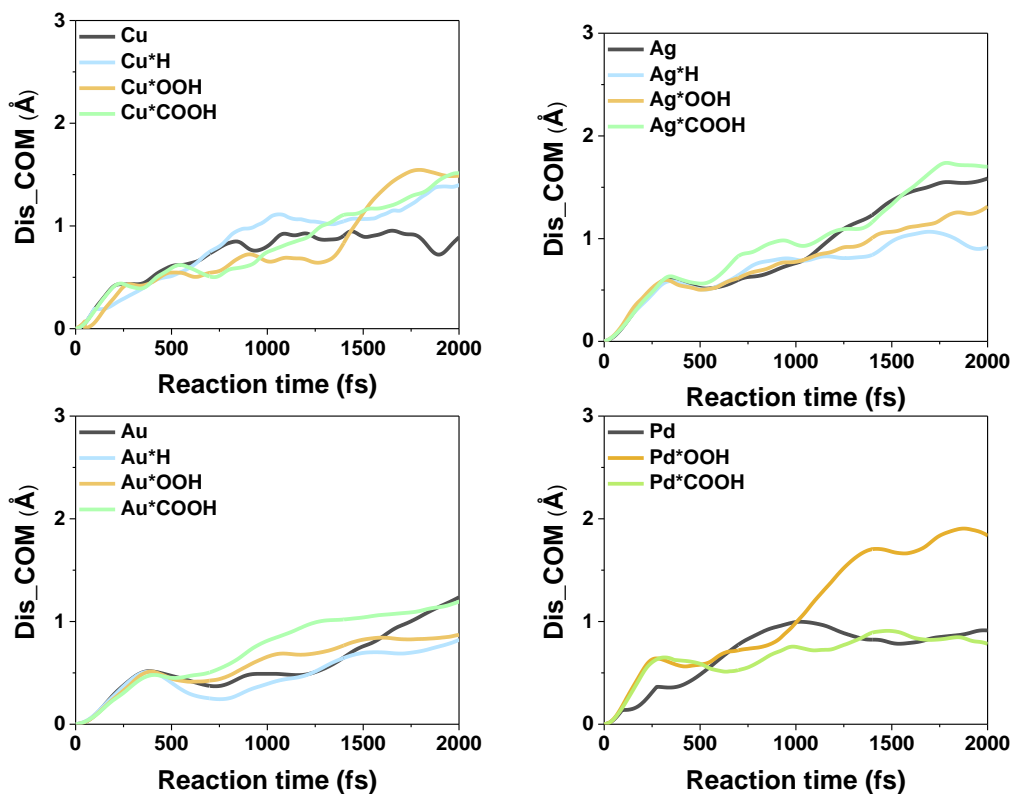


Figure 4.18: The change of the center of mass (COM) for Cu, Ag, Au, and Pd clusters with and without bound RIs with time. Reprinted with permission from ref. [132]. Copyright 2022, Royal Society of Chemistry.

(Figure 4.16b). This suggests that, compared to *COOH, a more pronounced reconstruction in metal nanoparticle catalysts can be induced by *O and *OH species formed via cleavage of the O–O bond from the *OOH adsorbate, highlighting detrimental effects of O₂ presence on the catalyst stability during CO₂RR electrocatalysis. Note that the Ag cluster without bound RI showed greater averaged displacement than Ag clusters bound with RIs: this trend is associated with the top-middle Ag atom in the cluster going down to the bottom of the cluster and pushing other Ag atoms way from their original position, which does not affect the overall morphology of the metal cluster.

In addition to the average displacement, the displacement of the cluster center of mass (COM) (Figure 4.18) was also considered to evaluate the movement of cluster atoms. The COM results showed a similar trend as observed in the study of average displacement in terms of the effect of the RI and the material on the atomic mobility. It should be noted that the displacements in Figure 4.16b and 4.18

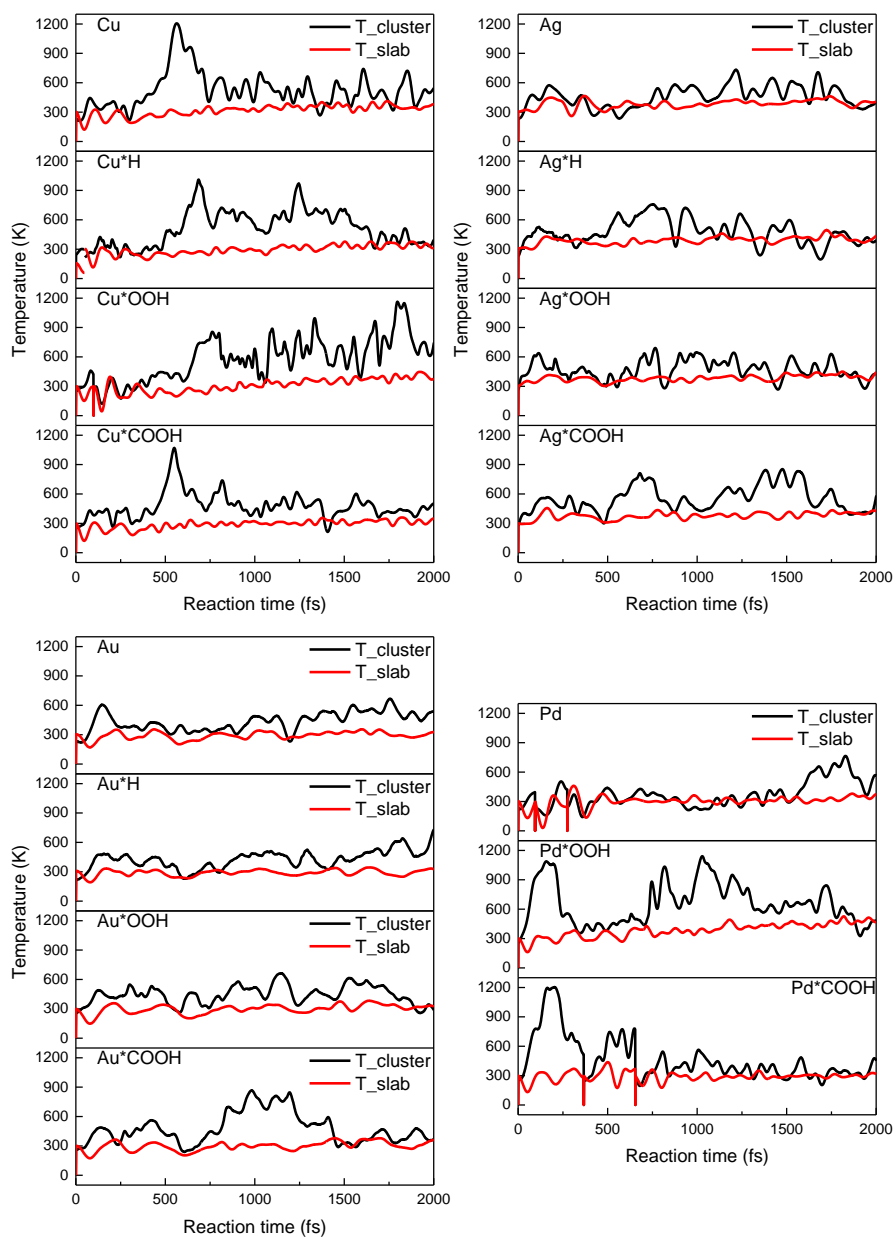


Figure 4.19: The temperature change of metal cluster and slab as a function of simulation time. Reprinted with permission from ref. [132]. Copyright 2022, Royal Society of Chemistry.

were obtained from a single trajectory and are intended as an illustration of the mobilities. To further support the displacement results, a time averaging method was used to estimate the ensemble average properties, including MSD, RDF, and Lindemann index, which can quantitatively measure the atomic mobility and order (Figure C.1-C.15). The MSD of the substrate atoms exhibited the typical features of

the solid state with nearly periodic distributions with low amplitude, while the MSD of the cluster atoms displayed liquid-state-like features, with larger amplitude and linear slopes at longer times, indicative of diffusive behavior. I found that the MSD of the cluster atoms depend on the RIs and materials, reflecting the effect of the latter on atomic mobility. The computed radial distribution functions also revealed that the substrates exhibit ordered solid behavior while the clusters display disordered liquid behavior. As shown in Figure C.1c-C.15c, RDFs of the substrates had broadened peaks with zero probability of finding a particle between peaks due to the regular spatial distribution of the atoms. However, RDFs of the clusters have non-zero separations between peaks as the atoms have higher mobility. Furthermore, I also found that the clusters have higher Lindemann indices than the substrates, further suggesting a higher atomic mobility of the metal cluster than that of the substrate. A sharp increase in Lindemann index was observed for Cu and Pd clusters after the adsorption of *OOH (from 0.067 to 0.112 for Cu; from 0.038 to 0.052 for Pd), which supports the significantly increased atomic mobility induced by *OOH on Cu and Pd clusters as demonstrated in Figure 4.16 and 4.18.

We used our estimated kinetic temperatures in order to assess the heat transfer between RIs and the metal slab. Results are shown in Figure 4.19 for all the systems under investigation. For the case of

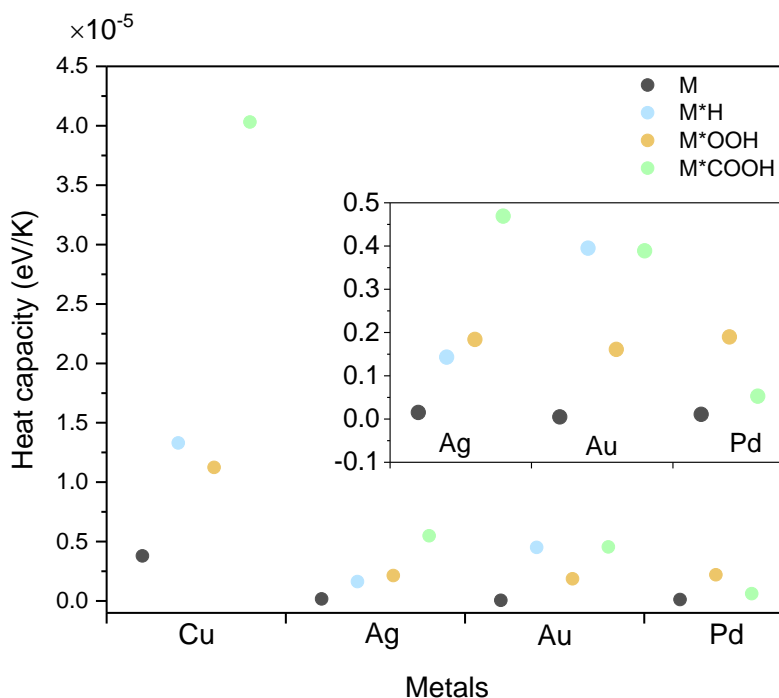


Figure 4.20: The heat capacities of Cu, Ag, Au, and Pd cluster systems. Reprinted with permission from ref. [132]. Copyright 2022, Royal Society of Chemistry.

copper, I observe that at short times, the RIs and have the same kinetic temperature. This is because, initial velocities are sampled from a Maxwell-Boltzmann distribution. As time evolves, the thermostat steers the velocity components, and overall kinetic energy, towards the target temperature. This equilibration process is accompanied by structural changes and large differences are observed between the kinetic temperatures of the cluster/RIs and that of the slab at around 500 fs and beyond. This is indicative of slow energy or inefficient energy transfer between the cluster/RIs and the slab for the case of copper. Only at around 2 ps does the kinetic temperature of the cluster/RIs appear to have reached the target temperature of 300 K. In the case of Au, the temperature equilibration process appears more efficient with less overall fluctuations. A similar situation is observed for Ag while Pd exhibits more pronounced fluctuations in the presence of RIs but lesser in the case of a surface cluster. I also estimated the heat capacities of the various systems and present our results in Figure 4.20. As a general trend, I observe that the presence of RIs increases the heat capacity in all cases as these RIs increase energy fluctuations. This observation is also consistent with the pronounced kinetic temperature fluctuations discussed above. Because of the limited length of our MD trajectories, the magnitude of our standard errors prevents a quantitation comparison of the effects of different RIs for a given metal.

4.6 Comparison of the atomic mobility on Cu, Cu₃Pd and Pd facets during HER, ORR and CO₂RR electrolysis

Considering the importance of the bimetallic electrocatalysts in CO₂RR, I investigated the influence of the CO₂RR-related RIs on the atom mobility in a model bimetallic catalyst, with the aim to develop a better understanding of the mobility trends. Specifically, considering a unique role of Cu in CO₂RR along with its higher propensity towards atomic mobility as described above, I chose a Cu-based alloy in order to verify whether its structural stability would be improved compared to pure Cu. To this end, as Pd is comparably more stable against migration compared to Cu, I selected the Cu₃Pd system, which has been experimentally shown to be a promising CO₂RR electrocatalyst¹³⁷. In order to evaluate the stability of the Cu atom in this alloy, the RI was considered to bind with Cu atom on the surface. Among various facets, Cu₃Pd(100) was selected as a case study in this work, considering that Cu(100) facet and bimetallic Cu₃Pd systems are of a great interest in the field of CO₂RR due to its selectivity to C₂ products.^{137,143–145} To see whether the stability of Cu(100) surface can be enhanced by introducing Pd element, I calculated the energy barrier for the VF processes and the adatom migration on Cu₃Pd (100) surface with and without adsorbed RIs *H, *OOH, and *COOH (Figure 4.21). Our calculations

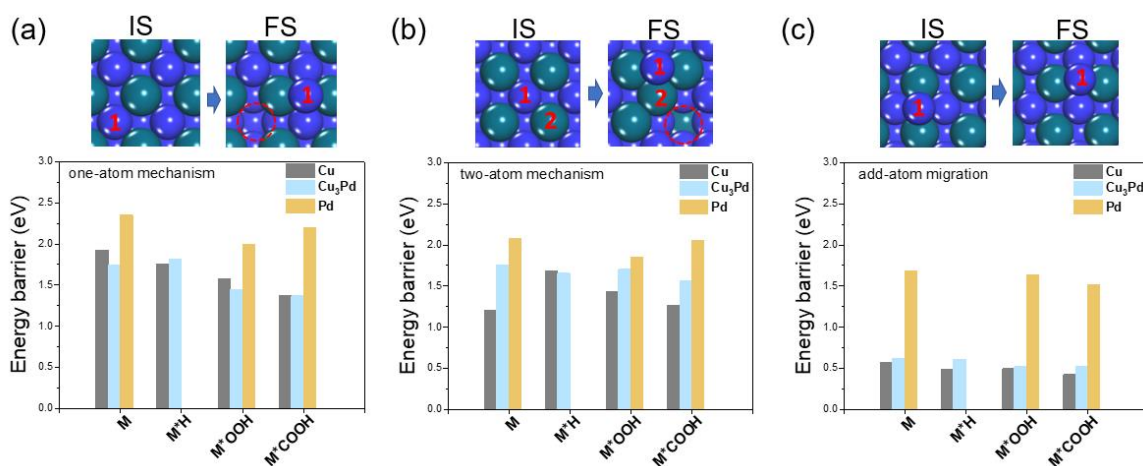


Figure 4.21: The influence of reaction intermediates on the energy barrier of VF processes and adatom migration on the (100) surface of Cu₃Pd alloy. The schematic and energy barriers for the VF via the one-atom mechanism (a) and via the two-atom mechanism (b), and the adatom migration on Cu₃Pd (100) surface with and without RIs (c). For the comparison purpose, the corresponding energy data on Cu(100) and Pd(100) surface are also included. Dark blue, Cu atom; dark cyan, Pd atom. Reprinted with permission from ref. [132]. Copyright 2022, Royal Society of Chemistry.

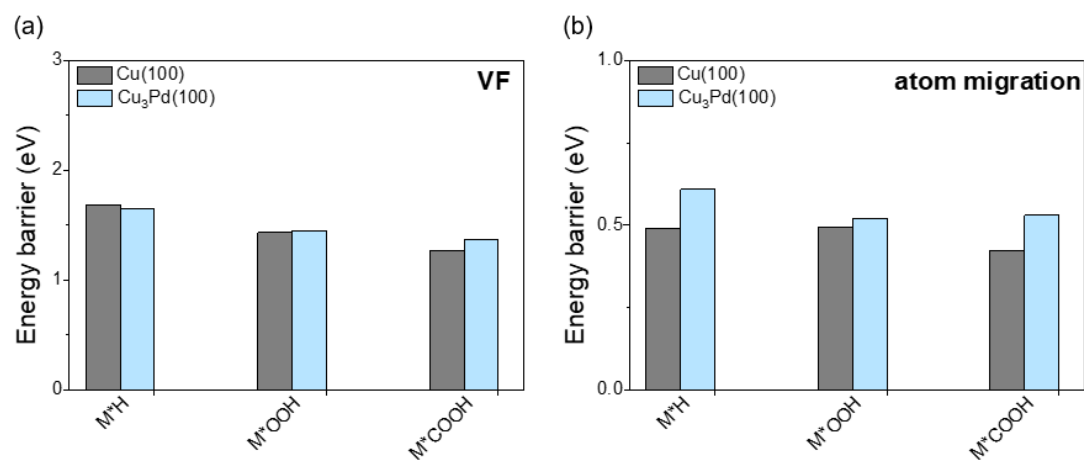


Figure 4.22: The comparison of the lowest energy barriers of VF process and atom migration on Cu(100) and Cu₃Pd(100) surface. Reprinted with permission from ref. [132]. Copyright 2022, Royal Society of Chemistry.

revealed that the adsorbed RIs can reduce the energy barrier for the two VF mechanisms and the atom migration on the Cu₃Pd (100) surface, similarly to the trends observed on the pure metal surfaces discussed above. More importantly, I found that the energy barrier of two-atom-mechanism VF and atom migration increased on Cu₃Pd (100) compared to that on Cu (100) (Figure 4.21 and 4.22), which suggests that optimizing the composition of bimetallic catalysts can not only tune the activity and selectivity of the catalysts, but also improve the structural stability of the catalysts.

4.7 Summary

In summary, I elucidated the influence of adsorbed reaction intermediates and the materials composition on the structural reconstructions in the common cathodic electrocatalysts during CO₂RR electrolysis by conducting a detailed computational study of thermodynamic, kinetic, and structural dynamics aspects of the atomic mobility in these electrocatalysts. Based on static DFT calculations, the adsorbed reaction intermediates tend to promote the atomic mobility in the metallic electrocatalysts by accelerating (1) the thermodynamics of vacancy formation; (2) the kinetic barriers of vacancy formation through two pathways; (3) the kinetic barriers of the atom migration on the metal surfaces. Depending on the nature of the adsorbed reaction intermediates, they facilitate the atomic mobility in varying degrees. For instance, *COOH has a more pronounced effect than *H, while *OOH could induce a more pronounced effect than *COOH, especially when the O-O bond breaks on metal surfaces. In addition, the AIMD simulations revealed that Pd has the lowest atomic mobility, then sequentially followed by Au, Ag, and Cu. This work highlights the side reaction intermediate such as *OOH can not only cause the waste of the input energy, but also facilitate the structural reconstruction in the cathodic electrocatalysts during CO₂RR. I also found that alloying less stable Cu with Pd renders a material with decreased atomic mobility of Cu surface atoms compared to pure Cu, which illustrates that alloying can not only be used to tailor the catalyst activity and selectivity, but also to improve their structural stability. These findings provide a more comprehensive picture of the atomic mobility trends in the commonly used CO₂RR metal electrocatalysts and the influence of the RIs under electrolysis conditions. The extended surface mobility assessment discussed here enables the evaluation of the atomic mobility in a cathodic catalyst of a new composition and provide guidance for experimental design of more stable electrocatalysts for industrial applications.

Chapter 5

Continuum level mechanistic description of structural changes in CO₂RR electrocatalysts: Electrochemical physics

Partially reprinted with permission from *Nature Catal.* **2021**, *4*, 479. Copyright 2021, Springer Nature.

Contribution: designed and carried out the DFT calculations and the FEM simulations, assisted in manuscript writing.

5.1 Introduction

As introduced in Chapter 4, the migration energy barriers and vacancy formation energies together, can be used to predict the relative stability of the surface atomic structures in various metals under different electrolysis conditions. However, these thermodynamic and kinetic aspects consider random hopping of surface atoms and do not reflect any locality or directionality of atomic mobility on the nanoscale. Conversely, the experimental data implied that in some localities of complex nanoscale electrocatalysts the atoms were hopping about more than in other otherwise identical features, suggesting that the impacts exerted on them are associated with the applied bias. Moreover, the experimental evidence revealed structural changes at the interfaces of the particles with the substrate and each other, (Figure 3.11 and 3.12) where the electrolysis is hindered due to apparent mass-transport limitations, further suggesting the presence of additional driving forces for atomic migration, which are related to the electrochemical behavior of the nanoparticles. To understand the origins of the locality and directionality of atomic mobility in nanocatalysts during electrolysis, one needs to study how the nanoscale shapes structurally participate in the electrochemical process.

Electrochemical physics effects on nanoscale can not only affect the atomic migration, but also impact the activity and selectivity of nanoparticle-based electrodes in surface reactions due to their complex nanostructures. For instance, high-curvature nanoscale features in complex nanostructures can generate high electric fields (E-fields) in the electrolyte adjacent to their surface under an applied bias, which can increase the CO₂ concentration by accumulating the electrolyte cations in their vicinity and therefore promote the CO₂RR performance.¹³ Moreover, the distribution of reaction species can also be affected by the nanoscale geometry of electrocatalysts: for example, nanocavities in nanostructured electrodes can confine the reaction intermediates during the CO₂RR electrolysis, steering the reaction towards more valuable multi-carbon products.¹⁴ These specific electrocatalytic

effects illustrate the significance of optimizing the geometry of catalytic nanostructures in improving the electrocatalytic performance of these materials.

However, the theoretical studies in this area have been given considerably less attention in comparison to the *ab initio* studies on the atomic structure design mentioned above. Typically, modelling above-mentioned electrochemical physics effects on nanoscale requires continuum descriptions of migration, diffusion and reaction processes in the electrolyte and current flow in the electrode by solving a set of partial differential equations with certain boundary conditions.^{71,146} As a result, currently there is a lack of established best practices and consistent protocols in setting and solving the necessary equations for determining the distributions of the local E-field, current density and active species at electrodes with complex nanoscale morphologies. In addition to being a challenging area to navigate for electrochemists, the computational analysis of these physicochemical parameters at electrocatalytic interfaces can lead to misleading data when performed without sufficient understanding of the underlying phenomena and the assumptions of the applied computational models, thereby hindering rational development of electrocatalysts on nanoscale.

To get the quantitative spatial analysis of physicochemical properties adjacent to and in the morphologically complex electrocatalysts, a set of partial differential equations has to be solved spatially (in 1D, 2D or 3D depending on how complex the structure is) using numerical method. Bohra et al.¹⁴⁶ and Chen et al.¹⁴⁷ simulated the distribution of E-field on the electrode surfaces using their custom numerical codes. What is more convenient is to use well-established numerical solvers of multiphysics problems developed for these purposes. Various numerical methods developed for solving partial differential equations can be used to perform the spatial analysis of the electrochemical parameters on nanoscale at continuum level, including finite difference method, finite volume method and finite element method (FEM). Finite difference method provides the least acceptable approximate for minimal computation cost while finite volume method provides best approximate with high computational cost. FEM provides acceptable approximation with lower computations. In addition, FEM advantages in dealing with arbitrary geometries, which makes the FEM being the best-known numerical engineering tool for modelling various multiphysics systems and processes. Therefore, FEM has been increasingly applied to electrocatalytic systems to quantitatively and spatially describe their electrocatalytic performance on nanoscale. There are more than 40 software packages that implement the FEM, with MATLAB, ANSYS and COMSOL Multiphysics being the most commonly used packages for the FEM simulations. Recent literature provides numerous examples of FEM being

applied to compute spatial distribution of E-field,^{41–44,71–74} electron density,^{13,39,40,75} reaction current density ($J_{electrolyte}$),^{13,45,71,75} electrolyte ion density,^{13,40,72,75,76} and concentration distribution of other species^{14,77–80} (Figure 5.1-5.5).

Figure 5.1 summarizes the E-field simulations performed for various nanostructured electrodes using the FEM method, covering geometries of nanoneedles,^{42,71–73} nanorods,⁷² nanoflakes,⁴⁴ nanoprisms,⁴¹

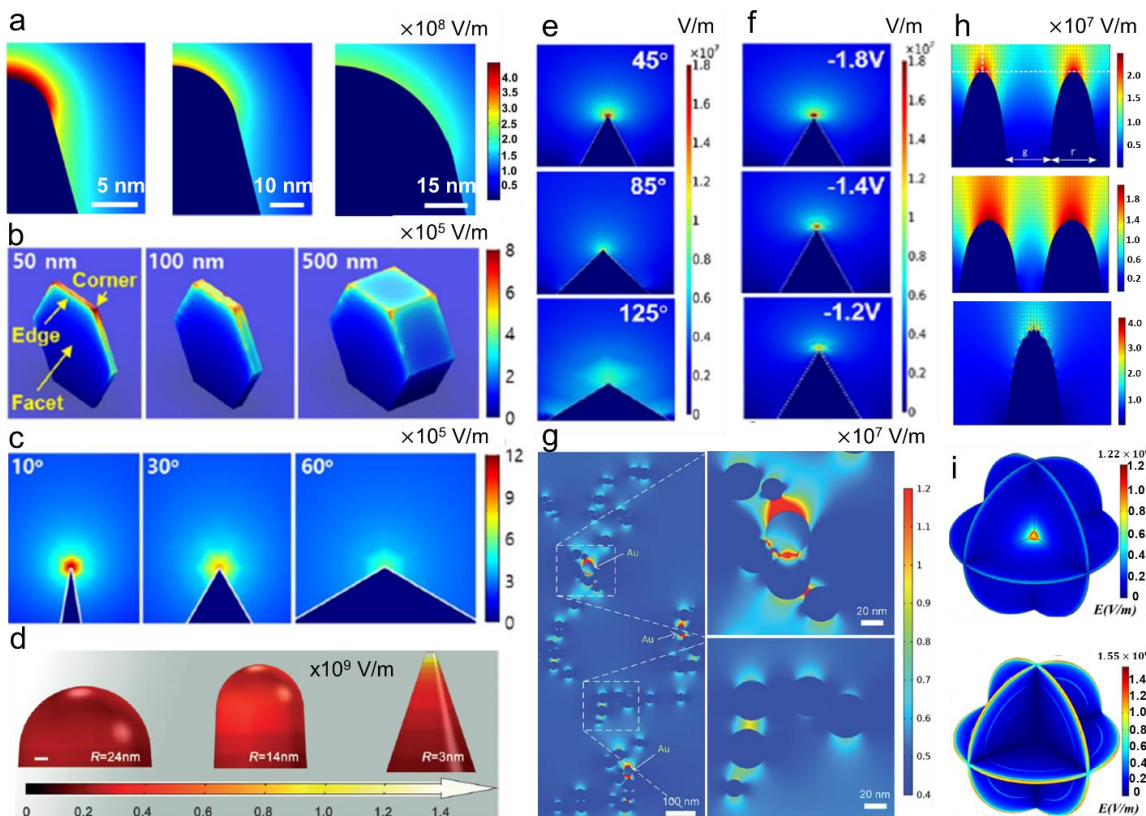


Figure 5.1: Computed distribution of E-field distribution near the surface of various nanostructured electrodes. (a) Au nanoneedle with tip radii of 5 nm, 10 nm, and 15 nm.⁴² (b,c) Bismuth nanoflakes with sharp coner and edge: (b) three-dimensional and (c) two dimensional.⁴⁴ (d) CdS nanoparticle, rod, and needles.⁷² (e,f) CuO nano-prism with different (e) corner angle and edge length and (f) applied potential.⁴¹ (g) nanostructured Au-Bi₂O₃ fractals.⁷³ (h) Ni foams with different ridges and groove.⁷⁴ (i) MoS₂ nanoflower sheets without and with intercalated graphene sheets.⁴³ Reprinted from the data of the cited papers by the permission from The American Chemical Society, Elsevier, John Wiley and Sons, Royal Society of Chemistry, The Chinese Academy of Sciences.

nanogrooves,⁷⁴ and nanoflowers⁴³. Most of these simulations were performed at applied potentials between -0.25 V to -1.2 V vs SHE, with only one example using an applied potential up to -3 V vs SHE (Figure 5.1g). The electrolytes used in the simulations were 1 M KOH, 0.5 M H₂SO₄ (Figures 5.1g, i) and 0.1 M KHCO₃ (Figures 5.1a-f,h). Widespread distributions of E-field with relatively low magnitudes (10⁵ V/m to 10⁸ V/m) were observed in the examples in Figure 5.1. However, based on the Debye length theory,¹⁴⁸ the interfacial E-field should be confined within 1 nm to 2 nm from the electrode surface, with a large magnitude (at least over 10⁸ V/m), at the potentials and the electrolyte concentrations applied in these simulations. This inaccuracy can be ascribed to a widespread simplification of the interface, where electric double layer (EDL) is not considered in the simulations. In addition to the E-field simulations, there is also a number of examples in the literature of applying FEM for studying the $J_{electrolyte}$ for various nanostructured electrodes including nanoneedles,^{13,45} nanocones,^{13,45} nanorods,^{13,45} nanocages,⁷⁵ branched nanoparticles⁷¹ and nanoframes⁷¹ (Figure 5.2).

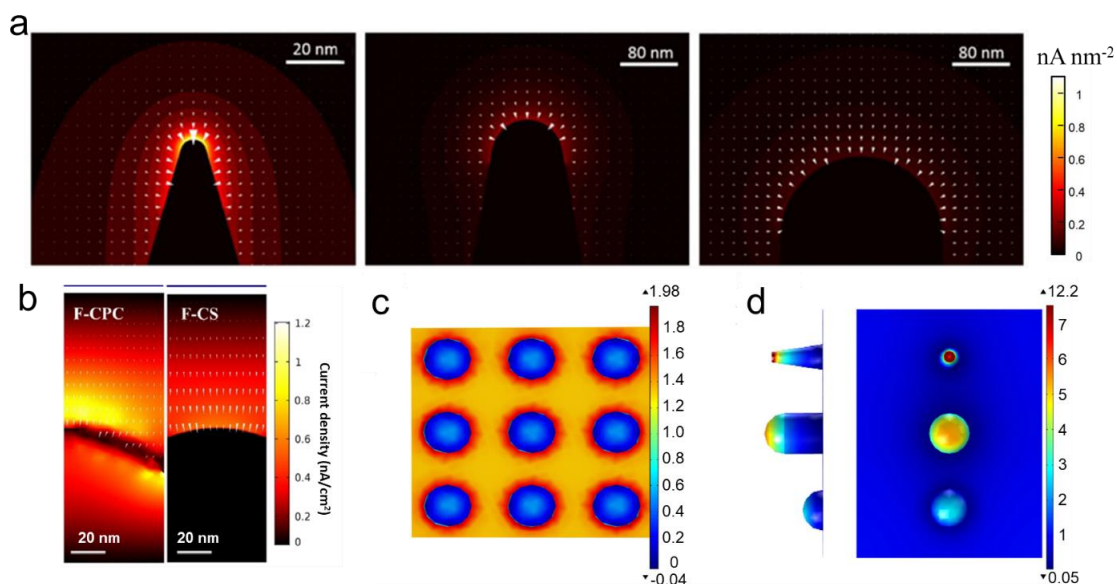


Figure 5.2: Computed distribution of current density near the surface of various nanostructured electrodes. (a) Au needle, Au rod and Au hemispherical particle.¹³ (b) Fluorine doped carbon electrodes including fluorine-doped cage-like porous carbon (F-CPC) and fluorine-doped carbon sphere (F-CS).⁷⁵ (c,d) Indium electrodes including (c) an In porous foam and (d) In tip, rod and dendrite.⁴⁵ Reprinted from the data of the cited papers by the permission from Springer Nature, The American Chemical Society, and John Wiley and Sons.

Although these simulations shown in Figure 5.2a-d were performed under similar conditions: in 0.5 M KHCO_3 electrolyte with an applied potential in the range of -1.0 V to -1.4 V vs SHE, the calculated $J_{\text{electrolyte}}$ still varied widely, from 10^{-9} A/cm² to 10^5 A/cm². Instead, one would expect the resulting values to be similar when simulations are performed under similar conditions. The discrepancy in simulated and expected values of $J_{\text{electrolyte}}$ can be remedied by applying more advanced electrode kinetics models.

The information about the structure of the EDL and the electrode kinetic properties are very important for modelling the E-field and $J_{\text{electrolyte}}$ of a nanoscale electrode numerically, as discussed above. EDL formed at the electrode surfaces due to the accumulation of the counter-ions, which has a strong shielding effect on the potentials generated near the electrode surface and, thus, significantly affects the distribution of the interfacial potential and E-field.⁷¹ Furthermore, the electrode kinetics, which determines the kinetic rate of the electrolysis reactions processing at the electrode-electrolyte interface and, consequently, plays an important role in the distribution of $J_{\text{electrolyte}}$.^{13,71} In addition to

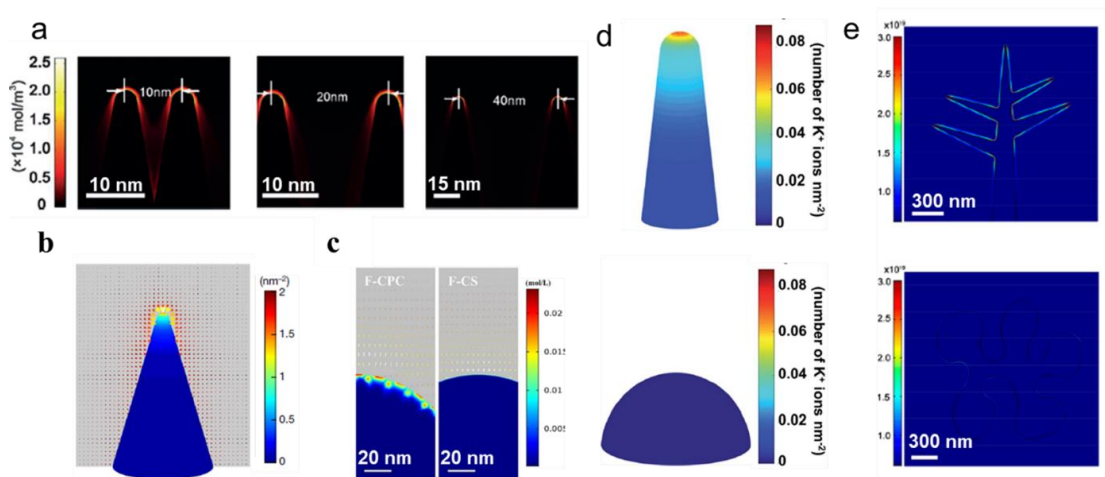


Figure 5.3: Computed distribution of K⁺ density distribution on the surface of various nanostructured electrodes. (a) CdS needles with different gaps.⁷² (b) Au needle.¹³ (c) Fluorine doped carbon electrodes including fluorine-doped cagelike porous carbon (F-CPC) and fluorine-doped carbon sphere (F-CS).⁷⁵ (d) Cu@Sn electrodes including Cu@Sn nanocone and bulk Sn.⁴⁰ (e) Cu dendrites (Cu-D) and Cu particles (Cu-P).⁷⁶ Reprinted from the data of the cited papers by the permission from John Wiley and Sons, Springer Nature, The American Chemical Society, and Royal Society of Chemistry.

the E-field and $J_{electrolyte}$, another crucial electrochemical physics effect in nanoscale electrocatalysts is the structural transformations induced by the high $J_{electrode}$ via electromigration. The crucial parameters for simulating the $J_{electrode}$ are the morphology and electric conductivity of the nanoscale electrocatalysts, as $J_{electrode}$ obeys ohm's law in metal.⁷¹ Understanding the key parameters affecting these electrochemical physics effects would help understand the state-of-the-art approaches and associated essential equations for describing these electrochemical effects, and further establish the protocols of modelling these electrochemical phenomena using FEM.

The aim of this chapter is to summarize the current status and recent advances in the theoretical models used for the E-field, $J_{electrolyte}$, $J_{electrode}$ simulations using FEM, propose the protocols for reliable simulations of these electrochemical effects, and study the electrochemical performances various nanostructured electrodes with complex morphologies. In section 2 of this chapter, I discuss the setup of the FEM simulation domains and the interfaces of Comsol Multiphysics required for the

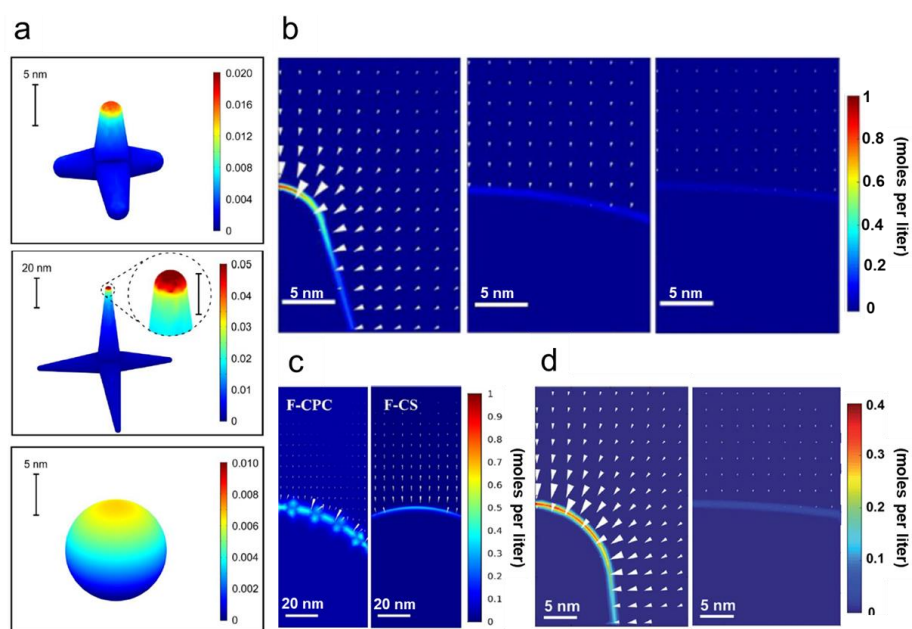


Figure 5.4: Computed distribution of electron density on the surface of various nanostructured electrodes. (a) CuPd electrodes including 7-nm CuPd tetrapods, 50-nm CuPd tetrapod, and CuPd nanoparticle.³⁹ (b) Au electrodes including Au needles, Au rods and Au particle.¹³ (c) Fluorine doped carbon electrodes including fluorine-doped cagelike porous carbon (F-CPC) and fluorine-doped carbon sphere (F-CS).⁷⁵ (d) Cu@Sn electrodes including Cu@Sn nanocone and bulk Sn.⁴⁰ Reprinted from the data of the cited papers by the permission from John Wiley and Sons, Springer Nature, The American Chemical Society, and Royal Society of Chemistry.

simulations performed in this chapter. In section 3, I introduce the fundamentals relevant to the essential electrochemical phenomena at the electrode-electrolyte interface, the classical theories for modelling these electrochemical effects, and the advanced modifications to these classical theories to account for the steric effect of the solution species and field-dependent dielectric function of the electrolyte. In section 4-6, I describe a protocol for simulating the E-field, $J_{electrolyte}$ and $J_{electrode}$ under different electrolysis conditions. In section 7, I demonstrate simulations on the specific electrode models with complex shapes that represent nanoparticle-based electrodes. In section 8, I compare the electrochemical performances, especially the current density, of various nanostructured electrodes including anchored nanostar, nanostar, core-cages and frames. In section 9, I discuss the application scope of the models involved in this work as well as their limitations. This chapter provides a useful

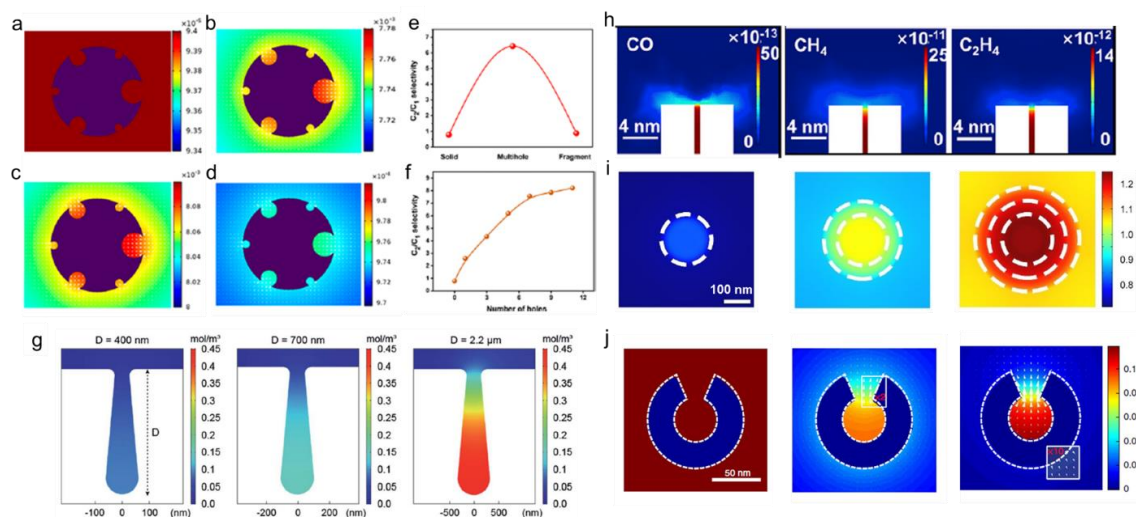


Figure 5.5: Computed concentration of species on various nanostructured electrodes. (a-f) Species of CO₂, C₁, C₂, and C₃ around multi-hollow Cu₂O electrode: the concentration distribution of (a) CO₂, (b) C₁, (c) C₂, (d) C₃, and the species C₂/C₁ ratio as a function of (e) different catalysts and (f) number of holes, Color scale, in mol/L.⁷⁷ (g) hydroxide ion (OH⁻) around c-wrinkle cavities with different D parameters ranging 400nm to 2.2 μm.⁷⁸ (h) Species of CO, CH₄ and C₂H₄ around copper-porphyrin frameworks, Color scale, in mol/m³.⁷⁹ (i) Species C₂/C₁ concentration ratio over single 1-shell, 2-shell and 3-shell hollow multi-shell structured copper.⁸⁰ (j) CO, C₂ and C₃ concentrations on the Cu nanocavity electrode, color scale, in mmol/L. Reprinted from the data of the cited papers by the permission from The American Chemical Society, Royal Society of Chemistry, Elsevier, and John Wiley and Sons.

departure point for electrocatalysis researchers to begin implementing FEM in their work and will facilitate a wider adoption of computational studies and rational design of nanoscale effects in electrocatalysts to further improve the performance of the electrocatalysts for CO₂RR and other clean energy conversion reactions.

5.2 Multiphysics simulations and electrode model

As an illustrative study object in this chapter, I selected an electrode formed by a branched nanoparticle (“nanostar”) placed on a substrate to reflect the complexity of the physical features in electrodes comprised of geometrically shaped nanoparticle electrocatalysts (Figure 5.6a). This nanostar model with complex morphology has a complicated distribution of E-field and current density. Generally speaking, simulating electrochemical behaviour in a 3D model of a nanoscale electrocatalyst is computationally demanding. However, often it is sufficient to consider a 2D model to elucidate certain geometric trends. Thus, the FEM simulations in section 5.4-5.5 shown in this chapter are performed using a 2D model, with a simulation domain setup shown in Figure 5.7a. Since our reaction of interest is the electrochemical reduction of CO₂, I consider that the nanostar particle placed on a substrate represents a working electrode and a cathode, where a negative potential or current density is assigned as a boundary condition for the simulation. A planar electrode is used for the anode throughout this chapter. Since the anode is far away from the cathode, the composition of the solution near the anode is not affected by the cathode, therefore, the concentration of each species, such as the electrolyte and CO₂, is set to be constant at the working electrode.

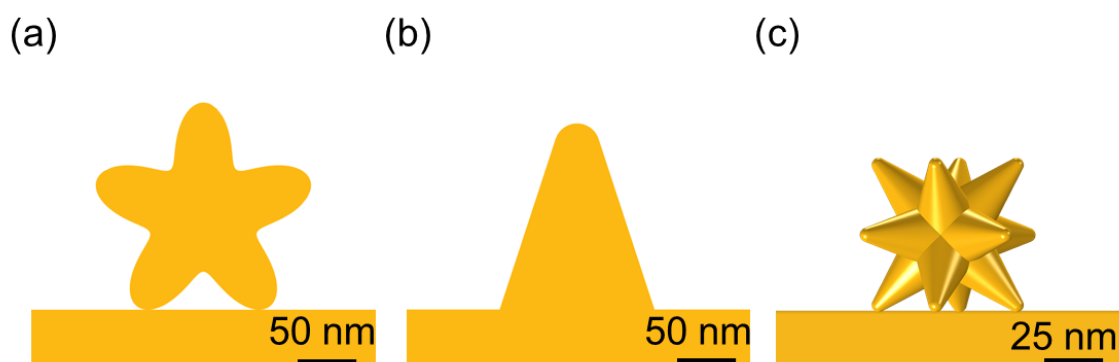


Figure 5.6: the electrode geometries used in this work: (a) 2D nanostar, (b) 2D nanocone, and (c) 3D branched nanoparticle.

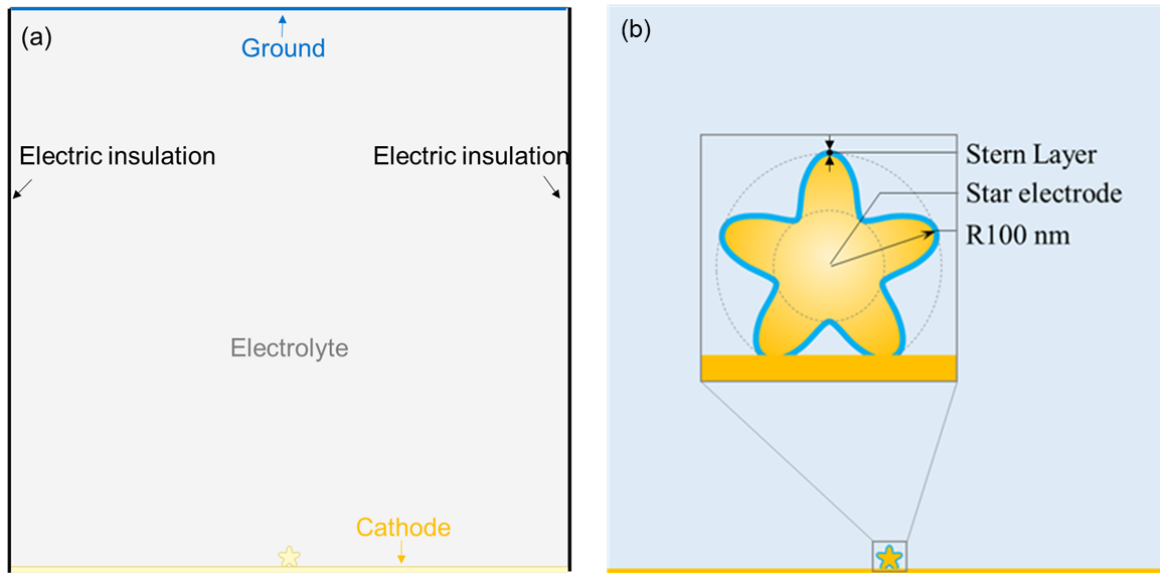


Figure 5.7: (a) FEM simulation domain setup and (b) the dimension of the nanostar electrode.

Briefly, the electrochemical cell is a $5000 \text{ nm} \times 5000 \text{ nm}$ square with a 50 nm -thick substrate placed at the bottom as shown in Figure 5.7a. A nanostar electrode is placed at the middle of the substrate. The shape of the nano-star electrode is generated from the function: $R_{\text{star}}(r, \theta; R_0, r_0) = r_0 + (R_0 - r_0) \cos^2 \frac{5\theta}{2}$, with two parameters, R_0 and r_0 , being 100 nm and 50 nm , respectively. The distance of the star center above the substrate surface is 83.66 nm , which is slightly smaller than the geometric height of the star center. As a result, the contacts of the nano-star with the substrate surface are two segments of *ca.* 3.6 nm rather than two points. The Stern layer is a uniform layer that is 0.33 nm above the electrode surface, as is indicated by the blue border in Figure 5.7b. The material for the nano-electrode and substrate is chosen gold. The electrolyte is 0.5 M KHCO_3 aqueous solution saturated with CO_2 (38 mM). The temperature of the system is 293.15 K and the electrolyte is unstirred.

As a model CO_2 electrolysis reaction, I selected CO_2 reduction to CO (equation (5.1)) on a gold cathode and 0.5 M KHCO_3 as the electrolyte (unless otherwise specified), in which water is used to balance this reaction assuming the electrolyte pH to be 7.2 .⁴⁵ Since the electrocatalytic behaviour of nanoscale catalysts is of the main interest, reaction 1 is confined to the nanoparticle surface. Therefore, I only construct an electric double layer (EDL) at the interface of the nanoparticle and the electrolyte based on the Gouy-Chapman-Stern model, with the thickness of the Stern layer determined by the radius of the solvated ions in the studied solution (Figure 5.8). In this simplification, the model loosely represents a repeat unit of an electrode comprised of a layer of nanoparticles placed on a substrate. It is

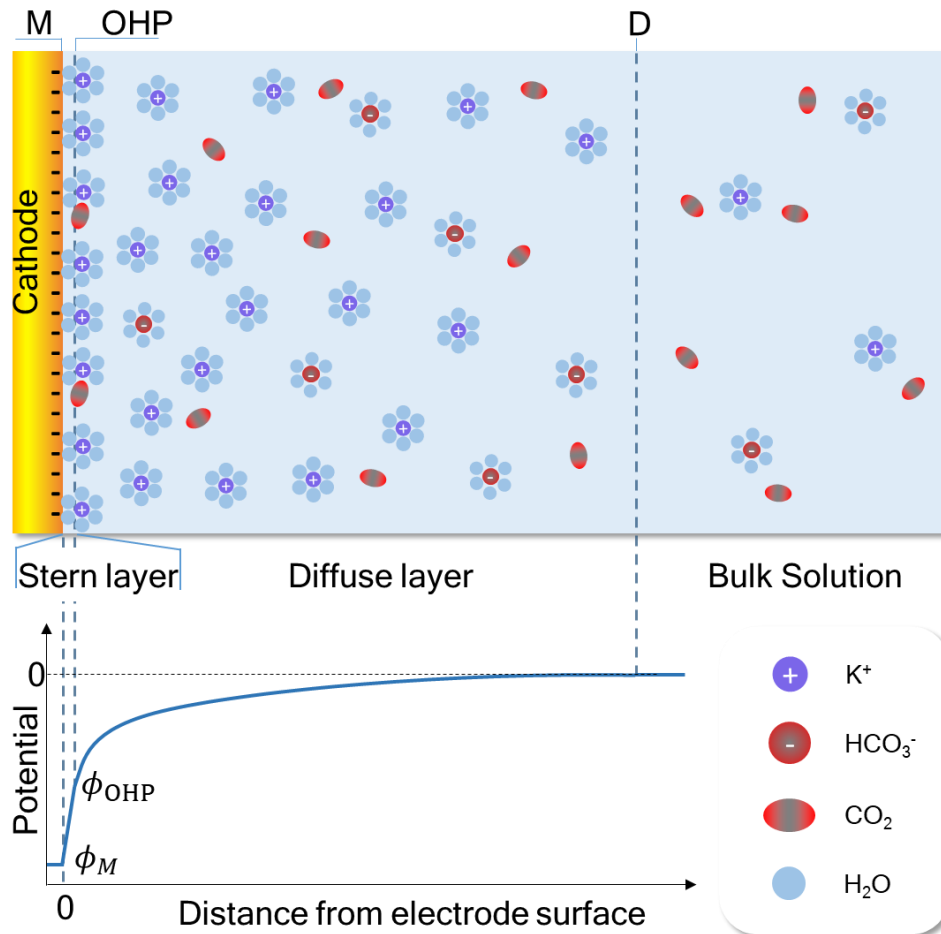
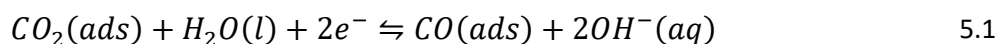


Figure 5.8: Schematic diagram of the Gouy-Chapman-Stern model

worth noting that considering multiple nanoparticles placed on a substrate in direct contact with each other can reveal electrochemical behaviour at the interfaces between the particles, which is often important to consider for both catalyst activity and stability studies. An accurate simulation of EDL is the key to exploring the E-field behaviour of a nanoparticle-based electrode under electrolysis conditions: various EDL models and their nuances are discussed in the section 5.3.1. In addition, the correct description of the thermodynamic and kinetic properties is important for revealing the $J_{electrolyte}$ of a nanostructured electrode: the details of the thermodynamic and kinetic properties of CO_2RR are discussed in section 5.3.2. For the comparative analysis and an illustration of the geometry effects, a 2D nanocone (Figure 5.6b), a 3D nanostar (Figure 5.6c) and other 3D models, including anchored nanostar, core-cages, frames, are also discussed in this chapter. A simulation domain similar to that for 2D nanostar electrode in 3 dimensions is applied for 3D models. All FEM simulations in this

work were performed in COMSOL Multiphysics package based on the finite-element-method solver (<https://www.comsol.com/>). For different purposes described in the text, six interfaces are applied in the simulation, including ‘Primary Current Distribution’, ‘Secondary Current Distribution’, ‘Tertiary Current Distribution’, ‘Transport of Diluted Species’, ‘Electrostatics’, as well as ‘Electric Currents’, and the details of these interfaces and the corresponding electrochemical theories are also discussed.



5.3 Fundamentals of the electrode-electrolyte system

The electrode-electrolyte interface affects the reaction rates and product selectivity of many electrocatalytic processes. Careful optimization of the electrode-electrolyte interface is essential for improving the reaction efficiency towards desired high-value products, which requires basic knowledge of this catalytic interface. The two crucial processes that occur at the catalytic interface during the electrolysis are: the formation of EDL and the electrocatalytic reaction (here I consider the electroreduction of CO_2 to CO) at the electrode-electrolyte interface. Accurate simulations on these two processes enable understanding of the impact of the catalytic interface in electrocatalysis. Typically, the structure of EDL is characterized in terms of the potential profile and the concentration profile of each ionic species within the electrolyte domain, while the electroreduction is usually characterized by the Faradaic current density at the electrode surface. In principle, the EDL formation and electroreduction occur simultaneously at the electrode-electrolyte interface for a given applied potential. To simplify the problem, I ignore the electrolysis when simulating the EDL formation and *vice versa*, which leads to two sets of FEM simulations below. In this section, I discuss theories and models for simulating the EDL and electroreduction current.

5.3.1 Theories and models for EDL simulations

The term “double layer” comes from the pioneering works of Helmholtz, and refers to the simultaneous aggregation or depletion of electrons within the electrode and counter-ionic species in the vicinity of the electrode surface under an applied potential,¹⁴⁹ as demonstrated in Figure 5.8. To model EDL using FEM, I require the potential profile (ϕ) and the concentration profile of K^+ (c_{K^+}) and HCO_3^- ($c_{HCO_3^-}$) within the electrolyte. Depending on the arrangement and the conformation of the solvated ionic species, several EDL models have been proposed in the literature. The earliest model is the Helmholtz

model¹⁴⁹, which presumes that a single layer of solvated counter-ions is formed at the surface of the electrode. The capacitance is assumed to be constant in the Helmholtz model. However, earlier experiments¹⁵⁰ demonstrated that the capacitance of EDL is potential- and ion-concentration-dependent. To account for this interdependence, the Gouy-Chapman (GC) model^{151,152} proposes a diffuse layer around the electrode in which the counter-ions are accumulated and the co-ions are depleted to balance the charge on the electrode. Although the GC model accounts for the dependence of the EDL capacitance on the potential and ion concentration, it still fails to describe EDL at large potentials. The predicted capacitance by GC model rises very rapidly at an extreme potential, which is against the flattening capacitance observed experimentally.¹⁵³ The reason for the unlimited rise in the GC model is that the location of the ions is not restricted to the solution, the point charges can approach the electrode surface arbitrarily closely, which is not realistic since the ions have a finite size and cannot approach the surface any closer than the ionic radius. To better describe the EDL capacitance, Stern suggested a combination of the Helmholtz model with the Gouy-Chapman model¹⁵⁴, forming the Gouy-Chapman-Stern (GCS) model (Figure 5.8), which considers a presence of a Stern layer and a diffuse layer and defines a plane of the closest approach for the centres of the ions to the electrode surface, called the outer Helmholtz plane (OHP). In the GCS model, the ions in the Stern layer are assumed to have a full hydration shell. However, the hydration shell could be partially shed, leading to the chemical adsorption of these ions on the electrode surface, also referred to as “specific adsorption”. More advanced models are required when specific adsorption occurs.¹⁵⁵ However, the capacitance predicted by the GCS model is consistent with the experimental observations due to accounting for finite size ions in the Stern layer.¹⁵⁶ Therefore, below I am focusing on the applications of the GCS model and discuss the theory behind it in more detail.

As discussed above, EDL is formed due to the accumulation of the ionic species in the vicinity of the electrode, therefore, an accurate description of the distribution of ionic species within EDL is the first important step for modelling EDL. In the GCS model, the distribution of ionic species in the diffuse layer at equilibrium is determined by the Boltzmann distribution (equation (2.22)). The unevenly distributed charged ionic species could generate a non-uniform potential in the diffuse layer, which is denoted as $\phi(\mathbf{r})$. The local potential profile $\phi(\mathbf{r})$ is related with the charge density $\rho(\mathbf{r})$ as described by the Poisson equation (equation (2.23)). To solve the $\rho(\mathbf{r})$ and $\phi(\mathbf{r})$ numerically, equation (2.22) has to be combined with equation (2.23) to get the equation (2.24), which is the well-known Poisson-Boltzmann (PB) equation.¹⁰¹ For a symmetric binary electrolyte, in which the valence charge (z_+) and

bulk concentration (C_+^*) of the cation are equal to that (z_- and C_-^*) of the anion ($z_+ = -z_-$, $C_+^* = C_-^*$), equation (2.24) can be simplified to a hyperbolic function (equation (2.25)).

I have discussed the equations that govern the ion distribution and the potential profile within the diffuse layer considered in the GCS model, which is the region beyond the OHP in Figure 5.8. Another important element in the GCS model is the Stern layer, *i.e.*, the region between the electrode surface (M) and OHP (Figure 5.8). As defined in the GCS model, OHP is the closest proximity of ions to the electrode, therefore, the Stern layer contains no charged species but water. Thus, the charge density at OHP, σ_{OHP} , is given by equation (2.26)

In addition to PB model I focused on above, another model for describing the potential and ion concentration distribution profiles in the EDL is Poisson-Nernst-Plank (PNP) model. In contrast to the PB model, the PNP model can not only simulate EDL at equilibrium, but also outside of equilibrium when EDL is dynamically changes due to the external perturbation. The detailed description of the PNP model is introduced below. As I did for the PB model, I first discuss the distribution of ionic species in diffuse layer at the steady-state conditions, which is described by the Nernst-Plank (NP) equation. Provided that the magnetic interaction and convection are absent, and the electrolyte is inert (*i.e.*, no electrolysis is associated with the ionic species), the resulting NP equation is shown in equation (2.27). Similarly to the PB model, equation (2.27) has to combine with the Poisson equation given by equation (2.28) to solve $C_i(\mathbf{r})$ and $\phi(\mathbf{r})$ numerically. The combination of equation (2.27) and equation (2.28) is the so-called PNP model.¹⁰³ As seen in equation (2.27), the ion concentration change with reaction time is accounted in the PNP model, suggesting that the dynamic evolution of the EDL structure can be captured by the PNP model, in contrast to the PB model that only describes the equilibrium state of EDL. Note that if $J_i(\mathbf{r})$ is set to 0, one can find that the ion concentration follows the Boltzmann distribution, *i.e.*, the results obtained from the MPB and GMPNP models become identical.

For the PB and PNP equations, one of their major drawbacks is the absence of the steric effect consideration, which can lead to the over-accumulation of the ions close to the electrode surface under conditions of a high electric potential or a high electrolyte concentration. One way to incorporate the steric effect into the PB and PNP equations is to account for the effective solvent diameter of each species in the simulations. Once the size effect of the species is considered in the simulations, the number of particles that can be accommodated in a specific space is fixed, therefore, the space has a maximum value with respect to the concentration of the species. For all studied species, they can coexist

in a certain area and affect distributions of one another. For example, if one position in a space is occupied by one species, another species cannot occupy that position anymore. Mathematically, the maximum concentration of the species in the space can be expressed by equation (2.29). If one further assumes that the effective solvent diameter of all species is the same (and is denoted a), the entropy of the electrolyte system considering the steric effect is expressed by equation (2.30).

To take into account the steric effect, equation (2.30) is incorporated into the PB and PNP models as demonstrated in the works of Borukhov et al.¹⁰⁴ and Kilic et al.¹⁰³, generating modified PB (MPB) and PNP (General Modified PNP, or GMPNP) models. For a symmetric binary electrolyte where $z_+ = -z_- = z$, the resulting MPB and GMPNP equations become equation (2.31) and (2.33), respectively. For the detailed derivation process of the MPB and GMPNP model, please refer to Appendix D. A notable change in equation (2.31) and (2.33) compared to their precursor equation (2.24) and (2.27) is the inclusion of the repulsive terms at a high ion concentration. The repulsion terms originate from the last term of equation (2.30), which is used to take the concentration of pure solvent into account.

Furthermore, the electrolyte dielectric permittivity, ϵ_r , is assumed to be constant in the MPB and GMPNP equations. However, ϵ_r of polar electrolytes is known to significantly decrease as E-field increases, especially when it is over $10^7 V/m$. To account for the dependence of the dielectric permittivity on E-field, the Booth model, equation (2.34) or (2.34a), can be employed, which was first proposed in work of Booth on studying the effective dielectric constant of water when orientation polarization of water molecules becomes saturated under high applied E-fields.^{102,105,106} Lastly, it should be noted that the potential is only first-order continuous at the OHP in GCS model, which means the OHP electric field, $\nabla\phi_{OHP}$, calculated from the diffuse layer and $\nabla\phi_{OHP}$ calculated at the Stern layer may not be the same.

To summarize, in this subsection I first compared three structure models for depicting EDL: the Helmholtz, GC and GCS models, with the GCS model adopted in this chapter due to its accuracy in predicting the EDL properties. I also discussed the PB and PNP models used for describing the ion and potential distribution in EDL. Furthermore, I highlighted the limitation of the PB and PNP models, specifically, the lack of the steric effect consideration, and introduced the strategy to incorporate the steric effect into the simulations by using the MPB and GMPNP models. Finally, I comment on the absence of the E-field dependence of the electrolyte permittivity in the MPB and GMPNP models and the way to solve this issue by adopting the Booth model.

5.3.2 Theories and models for $J_{electrolyte}$ simulations

Electrolysis occurs at the surface of the electrode and serves as a converter from electron current inside the circuit to ionic current within the electrolyte. The behaviour of such converter depends mostly on the thermodynamic and kinetic properties of the half-cell reaction at the electrode surface. To elucidate these properties, the reaction energy profile of the electroreduction is required. A reaction energy profile is usually established in three steps: first, one needs to identify the initial state, the final state, and the possible intermediate states along the reaction process. Then the thermodynamic properties of the reaction are obtained via calculations (or measurements) of the relative free energies of the states. Lastly, the kinetic properties are obtained once the activation energy for each reaction step is determined (e.g., from transition state calculations) or approximated.

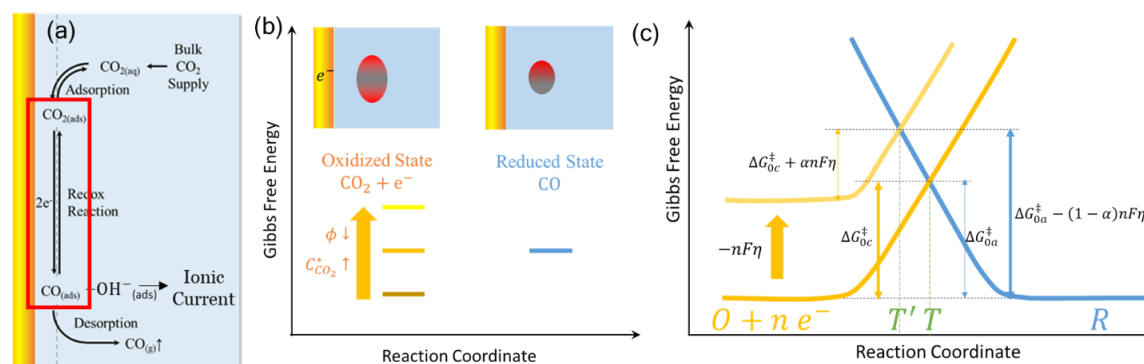


Figure 5.9: (a) the simplified CO₂RR pathway, (b) the dependencies of the electroreduction equilibrium, (c) The response of the electroreduction energy barriers to the applied overpotential.

For CO₂RR considered in this chapter, I treat it as a one-step reaction with no reaction intermediates. The associated states for the reaction profile are shown in Figure 5.9a. Firstly, the CO₂ molecules diffuse along the concentration gradient to the vicinity of the electrode and are then adsorbed at the electrode surface to facilitate the electron transfer. The second and most crucial step is electroreduction, in which each CO₂ molecule receives two electrons and is reduced to CO. The OH⁻ generated during this process leaves the electrode surface due to the electrostatic repulsion and constitutes the ionic current within the electrolyte. Lastly, the adsorbed CO leaves the electrode surface into the bulk of the electrolyte. The half-cell reaction presented in Figure 5.9a involves the adsorption of CO₂, the electroreduction, the migration of OH⁻, and the desorption of CO. The associated free energy change of these steps constitutes the overall free energy change of the half-cell reaction, ΔG_r, which is usually

expressed in electrochemistry in terms of the electrode potential, ϕ , as shown in equation (2.36). The dependence of ΔG_r on the electrode potential ϕ is illustrated in Figure 5.9b. When ϕ becomes more negative, G_{CO_2} increases and therefore ΔG_r decreases, resulting in a more favourable reduction reaction. For a half-cell reaction, its electrode potential, ϕ , is governed by the Nernst equation (equation (2.37)-(2.39))

While the electrode potential of a half-cell reaction, ϕ , is the thermodynamically determined potential to drive an electrochemical reaction, a different potential, ϕ' , is required to drive the electrochemical reaction in practice. The potential difference between the thermodynamic potential ϕ and the experimental potential ϕ' is called an activation overpotential, η , which determines the reaction rate and, consequently, the reaction current, as demonstrated in Figure 5.9c. When a negative η is applied to a cathode, the electroreduction reaction would change in two ways: firstly, the free energy change of this reaction becomes negative, meaning that the rate of the electroreduction reaction is increased; secondly, the activation energy barrier of the forward reaction is reduced by $|\alpha n F \eta|$, while that for the backward reaction increases by $|(1 - \alpha) n F \eta|$. These two changes together speed up the forward reaction and increase the reaction current at the electrode surface. More specifically, the dependence of the reaction current on the activation overpotential η can be characterized by the Generalized Butler-Volmer (G. B-V) equation, (equation (2.40)).

There are several key parameters in equation (2.40) that should be highlighted. The first parameter is the exchange current, i_0 , which is derived from the magnitude of the forward and backward reaction rates, and is thus related to the activation energy barrier (denoted by T in Figure 5.9c) when the net current is zero at equilibrium. The $C(0, t)$ and C^* terms denote the concentration of a species at the electrode surface and in the bulk electrolyte, respectively, while the 'O' and 'R' subscripts represent the oxidized and reduced forms of the reagent during electroreduction. For CO₂RR studied here, 'O' stands for CO₂ and 'R' stands for CO. Note that since CO has a very low solubility in water, I assume $C_{CO} = C_{CO}^*$ at equilibrium. The transfer coefficient, α , denotes the skewness of the energy curve, which determines the symmetry of the energy barrier for the reaction in Figure 5.9c. Typically, in most systems, the transfer coefficient is between 0.3 and 0.7, and it can usually be approximated by 0.5 in the absence of experimentally determined accurate values. The α value is set to be 0.5 in throughout this chapter, which corresponds to a symmetric energy barrier in Figure 5.9c. The parameter of n is the number of electrons transferred per half-cell reaction, T is the temperature, and F, R are the Faradaic constant and the ideal gas constant, respectively. In addition to the G. B-V equation, several other

versions of equations describing the electrode kinetics exist, including the standard Butler-Volmer (S. B-V), linearized Butler-Volmer (L. B-V), and the Tafel equation (Figure 5.10). These simplified models can be used in some specific reaction conditions to get accurate results in reaction current simulation while lowering the requirements for computational resources. The mathematical forms of the latter three models are shown in equation (2.41-2.43): equation (2.41) and (2.42) describe S. B-V and L. B-V, respectively, while equation (2.43) describes Tafel equation.¹⁰¹

$$\begin{array}{c}
 \text{Generalized Butler-Volmer (G. B-V)} \\
 i = i_0 \left[\frac{C_O(0,t)}{C_O^*} e^{-\frac{\alpha n F \eta}{RT}} - \frac{C_R(0,t)}{C_R^*} e^{\frac{(1-\alpha) n F \eta}{RT}} \right] \\
 \frac{C_O(0,t)}{C_O^*} = 1 \quad \downarrow \quad \frac{C_R(0,t)}{C_R^*} = 1 \\
 \text{Standard B-V (S. B-V)} \\
 i = i_0 \left[e^{-\frac{\alpha n F \eta}{RT}} - e^{\frac{(1-\alpha) n F \eta}{RT}} \right] \\
 \begin{array}{cc}
 \text{Low } \eta \swarrow & \searrow \text{High } \eta \\
 \text{Linearized B-V (L. B-V)} & \text{Tafel equation} \\
 i = \frac{-i_0 n F \eta}{RT} & i = i_0 e^{-\frac{\alpha n F \eta}{RT}}
 \end{array}
 \end{array}$$

Figure 5.10: the interconnection between generalized Butler-Volmer (G. B-V) equation, standard Butler-Volmer (S. B-V) equation, linearized Butler-Volmer (L. B-V) equation and Tafel equation, and the associated conditions for linking B-V equation with other equations.

The S. B-V model in equation (2.41) can be derived from equation (2.40) by assuming the reagent is present in high concentration in the vicinity of the electrode and thus $\frac{C}{C^*} = 1$ for both the oxidized and the reduced species. This model is a good approximation for depicting the kinetic performance of an electrode in an electrochemical cell, where the surface concentration of the reactant does not vary significantly from the bulk values due to the efficient mass transfer (e.g., well-stirred solution) or low current conditions. The L. B-V model in equation (2.41) can be obtained from equation (2.42) when the activation overpotential η is small, such that $e^{k\eta} \approx 1 + k\eta$. When the electrode kinetics is fairly fast, the electrolysis reactions are typically performed at low overpotentials to avoid the effect of mass-

transfer limitations. In this case, the L. B-V model is efficient to describe the electrode kinetic performance. The Tafel equation in equation (2.43) is obtained by ignoring the backward reaction (the $1 - \alpha$ term) in equation (2.41) when the activation overpotential η is high. Thus, when electrode kinetics is sluggish and high overpotentials are required for the electrolysis, the Tafel equation is a reasonable choice for modelling the electrode kinetics.

To summarize, in this section, I first discussed the influence of the reaction thermodynamics on the reaction current, and the interconnection between the reaction thermodynamics, the reaction free energy change (ΔG_r), the electrode potential (ϕ), and the ratio of the reactant and product concentrations (C_{CO_2}/C_{CO}). I also illustrated the impact of the electrode kinetics on the reaction current and the connection between the electrode kinetics and the reaction energy barrier (T) and overpotential (η). Furthermore, I introduced the commonly used electrode kinetics models for describing the dependence of the reaction current on the overpotential, including the G. B-V, S. B-V, L. B-V, and the Tafel equations.

5.3.3 Theories and models for $J_{electrode}$ simulations

To enable the practical application of CO₂RR technology, advanced electrocatalysts should not only be improved in terms of their activity and selectivity, but also be made more stable in long-term electrolysis. The structural stability of nanoscale electrocatalysts is closely related to the current density in the electrode ($J_{electrode}$).⁷¹ Consider that in an electrocatalytic reaction the electrons generated during the anodic electrochemical reaction have to flow through the anodic catalysts to cathodic catalysts via an external circuit, and then go through the interface of the cathodic catalyst to participate in the electrochemical reactions on its surface. If these electrons have to flow through a narrow constriction, such as the one at the interface between a branched particle and a flat substrate, it leads to high $J_{electrode}$, or so-called current crowding in these constricted areas. Sufficiently high current crowding can result in the mass transport of solid metal matter via electromigration (EM)¹⁵⁷ and Joule heating effects¹⁵⁸, which can further lead to the deformations and sintering in nanoscale features of an electrode with such geometric features. More specifically, the mass transport via EM is caused by the momentum transfer between the current carriers and the metal atoms on their scattering. The number of the current carriers scattering against the metal atoms can be increased by high $J_{electrode}$, thus, EM generally occurs at the areas with current crowding. Typically, EM on surfaces can be observed at ≥ 10 A/cm², and it is associated with the mobility of under-coordinated surface atoms.¹⁵⁷ The composition of the material and presence of any phase impurities can further accelerate EM. In addition to the EM,

the heat produced by the passage of the $J_{electrode}$ through the metal due to the resistance, also named as Joule heating, can also lead to the atomic movement in solid metal material. This phenomenon occurs only when the metal atoms obtain enough thermal energy to diffuse due to localized temperature rise caused by Joule heating, with the diffusion degree depending on the achievable temperature.¹⁵⁸ Among the complex nanostructured catalysts used for CO₂RR, there are often limited contact areas at the interfaces of the catalysts with the substrate and each other, constricting the current path and potentially leading to EM. Considering the effects described above and the increasing complexity of nanoscale electrocatalysts, investigating the local $J_{electrode}$ in these structures is instrumental for understanding and optimizing their structural stability. Suggested by our previous work,⁷¹ FEM simulation is also a powerful tool to study the $J_{electrode}$ distribution as well as its dependence on the electrode shape and the applied bias. The current density in a metal obeys Ohm's law, therefore, $J_{electrode}$ is solved according to equation (2.44).

5.4 FEM simulations of E-field behavior

The distribution of E-field at the electrode-electrolyte interface is one of the crucial metrics in evaluating the electrochemical performance of the electrode. The interfacial E-field could significantly impact the reactivity of the electrode in CO₂RR by accelerating the electron transfer. Moreover, E-field can greatly affect the adsorption energy of an adsorbate that is uncharged, but has a significant dipole moment and/or a large polarizability. More recently, Liu et al. demonstrated that E-field generated by nanofeatures with high curvature can also promote CO₂RR by concentrating K⁺ ions at the electrode surface and thereby enhancing CO₂ adsorption and decreasing the thermodynamic energy barrier for CO₂RR.¹³ Accurate E-field simulations could accelerate the development of electrode nanostructures with superior performance in CO₂RR and other clean energy reactions. In this section, I highlight the key parameters that need to be considered for the E-field simulation and relevant theoretical models proposed to date.

5.4.1 Potential reference for E-field simulation: point of zero charge

Accurate simulations of E-field rely on the correct evaluation of the surface charge density on the electrode surface, therefore, it has to be simulated first. For the surface charge density simulation, the potential at the point of zero charge (PZC) of the electrode has to be introduced. For an electrode at the potential of PZC, the surface charge density of the electrode is zero, and, consequently, no EDL is present at the electrode-electrolyte interface.^{159,160} Therefore, the potential can be assumed to be constant throughout the entire domain, providing a natural reference potential for the surface charge density study. For PZC reference, the surface charge on the electrode surface is generated only due to the variation of the applied potential, since no initial surface charge is present on the electrode surface at the potential of PZC. Thus, the surface charge density can be described by equation (2.26). Other potential references such as standard hydrogen electrode (SHE) can also be used,⁵¹ however, for any reference potential other than PZC, the surface charge of an electrode consists not only of the charge generated due to the applied potential variation, but also of the initially existing surface charge, which generally remains unknown in the most cases. To describe surface charge density accurately and conveniently, the applied potentials refer to PZC in this chapter. Note that the PZC of an electrode depends on the electrode material, crystal facet, as well as the electrolyte composition. For a single crystalline metallic surface, PZC can be well described by the DFT-based molecular dynamics proposed by Le et al. in 2017.⁵¹ However, for a polycrystalline metallic surface, PZC is not a known value, but is estimated using the minimum of the measured differential capacitance.¹⁴⁶ Here, I assume the PZC

for Au electrode is 0.5 V vs SHE, which corresponds to the PZC of Au(111) surface.⁵¹ Thus, for example, when the potential applied at the cathode in our E-field simulations is -0.3 V vs SHE, it translates to -0.8V vs PZC.

5.4.2 Effect of the EDL and relative permittivity of the electrolyte on computed E-field profile

Next, the consideration of the EDL is a must for the E-field simulation to accurately describe the spatial distribution of E-field due to the significant impact of the EDL on the potential distribution. To explain the implications of not taking into account EDL on the E-field behaviour, I provide an illustrative

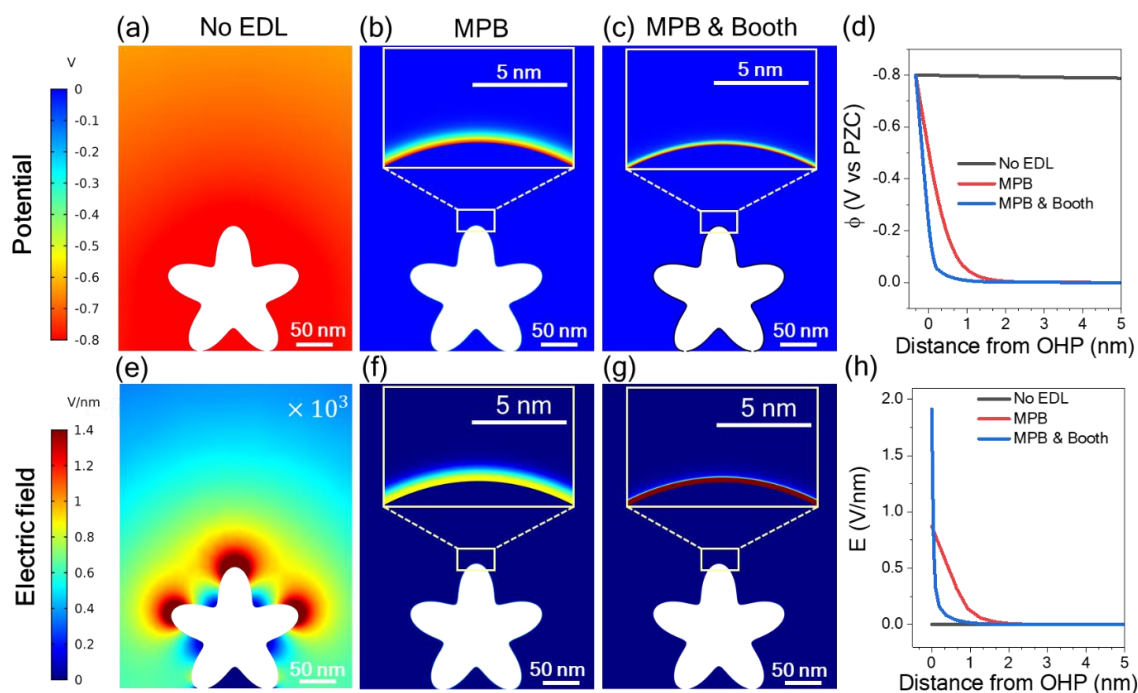


Figure 5.11: The potential (ϕ) and electric field (E) distribution for nanostar electrode simulated under different conditions: (a, d) without considering the formation of EDL, (b,e) accounting for the effect of EDL using modified Poisson-Boltzmann (MPB) model, and (c, f) accounting for the effect of EDL using MPB model and the electrolyte field-dependent dielectric permittivity using Booth model. (d) potential drop from catalyst surface ($x=-0.33$ nm), (h) electric field drop from OHP ($x=0$). The results in this figure are for applied potential of -0.8 V vs. PZC with the electrolyte of 0.5 M KHCO_3 .

example using a gold nanostar electrode, shown in Figure 5.11. As the magnitude of E-field is a negative gradient of potential ϕ , $E = -\nabla\phi$, I first calculate the potential distribution for the nanostar electrode without and with EDL. These calculations show that the potential drop is very slow when EDL is not taken into account in the simulation (Figure 5.11a and d). In contrast, a sharp drop in potential is observed (Figure 5.11b and d) when EDL is considered using the GCS model with the space charge density in the diffuse layer described by the MPB equation to account for the effect of finite ion size in the electrolyte solution (see details in section 5.3.1). More specifically, when EDL is not considered (Figure 5.11e and h), it results in large hotspots of E-field with a relatively low magnitude ($\sim 10^{-3} V/nm$) near the tips of the nanostar facing the anode, while the simulation using MPB model (Figure 6f and h) results in a narrow distribution of E-field with a relatively high magnitude ($\sim 0.9 V/nm$). According to the experimental observations and Debye length theory, for 0.5 M $KHCO_3$, E-field is confined within 1-2 nm from the electrode surface with the magnitude over 0.1 V/nm,^{148,156,161} suggesting that the results obtained from MPB model are more accurate.

The relative permittivity (ϵ_r) of a polar electrolyte is another crucial factor that can impact ϕ and E-field, since ϵ_r is the function of E-field, which decreases as E-field increases (especially for E-field over $10^{-2} V/nm$). The Booth model (equation (2.34)) accounts for this interrelationship between permittivity and E-field, therefore integrating equation (2.34) in the simulation provides more accurate values of E-field, as illustrated in Figures 5.11g,h. Specifically, while MPB model results without applying Booth model show a wider distribution of E-field with lower magnitudes (Figure 5.11f ,h) compared to the results obtained from the model corrected by the Booth model, the integration of the Booth model corrects the results by screening the potential more efficiently (Figure 5.11c, d). Compared to the results obtained from MPB, the potential decreased more significantly (Figure 5.11c, d), leading to the E-field screened in a narrower region but with a higher magnitude ($\sim 1.8 V/nm$). This E-field screening when applying the Booth model can be ascribed to the polarization of water molecules induced by E-field and, consequently, a uniform orientation of water molecules, which can screen the potential more effectively and confine the E-field to the electrode surface. According to the experimental observations, E-field at OHP is on the order of 0.1 - 1 V/nm in the potential range of -1 to 0 V vs Ag/AgCl, for Mn^{2+} cations.¹⁶¹ For K^+ cation that I consider in the simulations presented here, a higher E-field than 1V/nm could be generated due to the smaller effective solvation radius of K^+ compared to that of Mn^{2+} , which is in line with our simulations results when using MPB method corrected with the Booth model ($\sim 1.8 V/nm$). This experimentally observed high E-field suggests that the widely reported E-field distributions with low magnitude ($\sim 10^{-3} V/nm$) in Figure 5.1 and Figure

5.11a,e are not reasonable in magnitude, which resulted from not accounting for EDL in the simulations.

5.4.3 Impact of the electrolyte nature and concentration on computed E-field profile

Another important parameter of an electrochemical system that affects the accuracy of E-field simulations is the electrolyte, or more specifically for cathodic electrocatalysis, the nature and the concentration of the cations in the electrolyte. To illustrate the dependence of the E-field distribution on the electrolyte, I compared the impact of three electrolytes: KHCO_3 , NaHCO_3 , and LiHCO_3 , on E-field using the combination of the MPB and the Booth models (Figure 5.12). The influence of different cations in the electrolyte solution on E-field originates from their different solvated size and hydration number. The hydration number of each cation reflects its polarizability towards the surrounding water molecules and, therefore, affect the relative permittivity of the electrolyte. Bohra et al. introduced a simplified approach to describe the dependence of the relative permittivity of an electrolyte on the hydration number and the concentration of cations.¹⁴⁶ Although this approach accounts for the impact

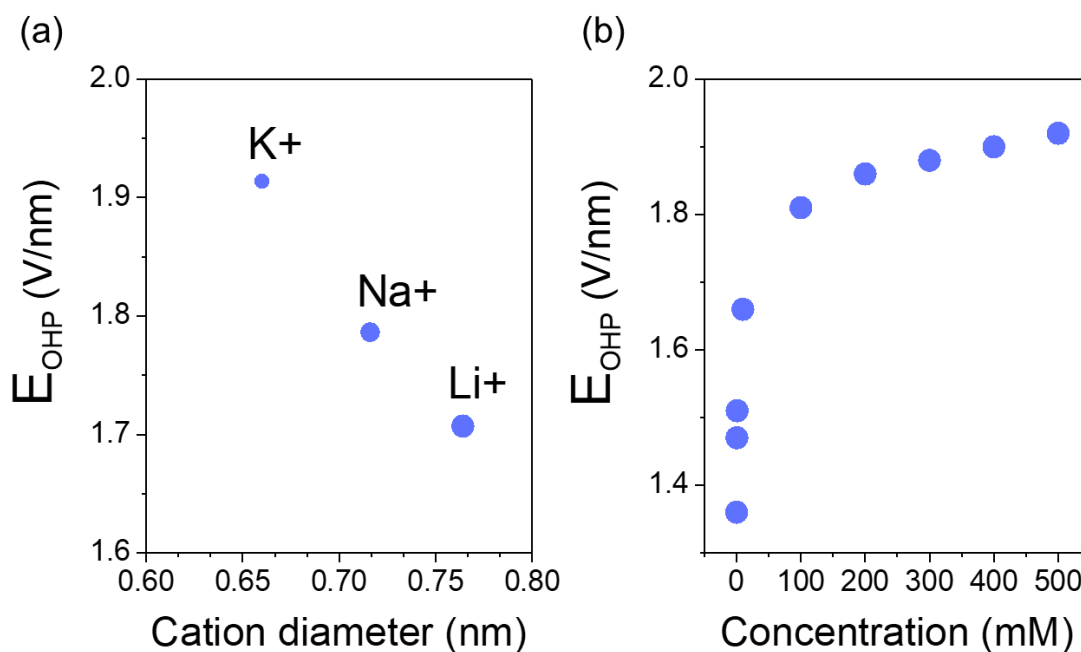


Figure 5.12: The effect of (a) cation size and (b) electrolyte concentration on the electric field at OHP (E_{OHP}). 0.5 M electrolyte of KHCO_3 , NaHCO_3 , and LiHCO_3 are compared in (a). KHCO_3 with different concentrations are compared in (b). The results in this figure are obtained using MPB & Booth for nanostar electrode with applied potential of -0.8 V vs. PZC.

of the hydration number on the relative permittivity of the electrolyte and E-field, it assumes the permittivity linearly changes with E-field. The impact of E-field on the permittivity results from the dependence of the orientational polarization of water molecules on E-field. The orientational polarization of water is nearly saturated when E-field is higher than 1 V/nm, suggesting a non-linear relation between the permittivity and E-field. To accurately describe the dependence of permittivity on E-field, the Booth model considers the water saturation effect at high E-field. Therefore, the Booth model is applied in the examples shown in Figure 5.11c,g, 5.12 and 5.13 to describe the dependence of permittivity of the electrolyte medium on E-field. The effect of the hydration number of a cation is not considered in this model, i.e., this example only considers the impact of the solvated cation size on the E-field. The trend of the solvated sizes of the examined cations in aqueous media follows the order $K^+ < Na^+ < Li^+$, which is the inverse of the trend for the corresponding neutral atoms sizes due to the difference in the hydration properties among alkali metal cations.^{161,162} In the context of the combined MPB and Booth model, the solvated size of a cation affects the surface charge density (equation (2.26)) and the steric limit of the ion concentration (equation (2.29)). The simulation results show that K^+ has the strongest E-field at the OHP, then followed by Na^+ and Li^+ in that order (Figure 5.12a). This trend can be explained by the solvated sizes of the studied cations. Since K^+ has the smallest solvated size among these three cations, it can reach the highest ion concentration at OHP compared to that of Na^+ and Li^+ according to the steric limit of the ion concentration (equation (2.29)). Therefore, K^+ can cause the sharpest potential drop and generate the highest electric field at the OHP. In addition, the bulk concentration of the electrolyte can also affect E-field at the OHP by affecting the space charge density distribution (equation (2.31) and (2.33)). I also compare the E-field at OHP in $KHCO_3$ electrolyte at different concentrations (0.1 mM-500 mM). The results show that the E-field at the OHP increases with increasing bulk concentration of the electrolyte, and gradually saturates when the concentration is over 100 mM (Figure 5.12b) due to the ionic strength change of the electrolyte with its concentration. Specifically, the ionic strength is proportional to the inverse square root of the electrolyte concentration. When the electrolyte concentration is over 100 mM, the ionic strength increases slowly, leading to a slow increase in the rate of the potential drop and, therefore, a gradual saturation of E-field.

5.4.4 Comparison of the PNP, GMPNP, and MPB models in E-field simulation

There are many examples in the literature where the PNP and GMPNP models^{13,146} are applied instead of the MPB model discussed above to obtain the spatial distribution of E-field of the EDL when it is perturbed from equilibrium. The PNP and GMPNP models were developed to describe linear-response

Table 5.1: Comparison of the major features of PNP, GMPNP, and MPB.

	MPB	PNP	GMPNP
Numerical Stability	Stable	Stable	Unstable
Computation Efficiency	High	High	Low
Allowed bias	High and Low	low	High and Low
Ion Steric Effect	Considered	Not considered	Considered
Electrolyte Symmetry	symmetric	symmetric and asymmetric	symmetric and asymmetric
System state	Equilibrium	Dynamic	Dynamic

dynamics of EDL perturbed from equilibrium, while MPB can only describe the equilibrium of the EDL. To demonstrate the limitations and applicability of these three models, their main features are summarized in Table 5.1. The “numerical stability” describes whether a theoretical model can find the solution of the potential or E-field for an electrode model (“stable” refers to a converging solution, and unstable refers to failure to find the numerical solution); the “computational efficiency” refers to the time required for a theoretical model to get a solution (the convergence speed). The MPB model is very stable and efficient in numerical simulations while simultaneously considering the steric effect of the ions. However, it is only applicable to a system at equilibrium state and with a symmetric electrolyte, i.e., an electrolyte with an equal number of cations and anions upon dissociation (e.g., KHCO_3 and KOH). In contrast, the PNP model can treat a dynamic system without the electrolyte nature limitation. At the same time, the PNP model is stable and efficient numerically. However, the ion steric effect is not considered in the PNP model, which makes it only valid for low electric potentials, because the ions tend to over-accumulate on the electrode surfaces at high potentials in the PNP model. Compared to the MPB and PNP models, the advantage of the GMPNP model is that it can deal with a dynamic system with an asymmetric electrolyte (i.e., an electrolyte with an unequal number of cations and anions upon dissociation) within a wide range of applied potential, making this model the most numerically accurate of the three models. The downside of the GMPNP model is that solving it numerically is highly computationally demanding due to its mathematical complexity and is not stable in 2D or 3D simulations. The magnitudes of E-field at OHP calculated using the GMPNP, MPN and PNP models are compared in Figure 5.13. These results correspond to a 1D electrode with applied potential of -0.4 V vs PZC and 0.5 M KHCO_3 as the electrolyte. In order to calculate E-field, the space charge density and potential distribution are first calculated using these three models in Figure 5.14. The concentration

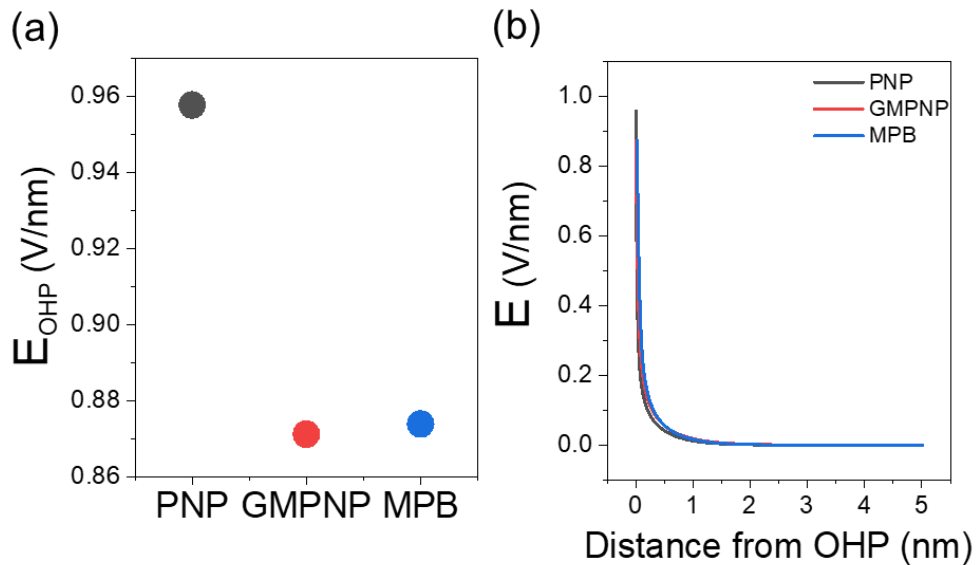


Figure 5.13: Comparison between the electric field results obtained from Poisson-Nernst-Planck (PNP) model, a generalized modified PNP (GMPNP) model and modified Poisson-Boltzmann model for (a) electric field at OHP and (b) electric field drop with the distance from OHP. Subscript OHP means the measurement at OHP. Considering the difficulty in solving GMPNP numerically, all results are obtained using a planar model with the applied potential of -0.4 V vs PZC and the electrolyte of 0.5 M KHCO_3

of K^+ at OHP ($\sim 14\text{M}$) obtained from the PNP model is about three times higher than that obtained from the GMPNP and MPB ($\sim 5\text{M}$) due to the lack of the steric effect consideration in the PNP model. In the PNP model, K^+ is over-accumulating at OHP, which strongly screens the electric potential generated by the electrons at the electrode surface. As shown in Figure 5.14, the potential at OHP obtained from the PNP equation (equation (2.27) and (2.28)) is about -0.084 V, which is lower than those obtained from the GMPNP and MPB equations (about -0.112 V and -0.110 V, respectively). The faster potential drop in the PNP equation then leads to a higher E-field at OHP (about 0.96 V/nm), compared to the results obtained from the GMPNP and MPB models (about 0.870 V/nm and 0.875 V/nm, respectively). The over-estimated E-field becomes even more pronounced when using a more negative potential or a higher concentration of the electrolyte. For the configurations considered here, the results obtained from the GMPNP and MPB models are very similar as I performed the simulations for a system with symmetric electrolyte at the equilibrium state. However, the GMPNP model can only be used for 1D simulations, while the MPB model can be applied for 2D and 3D simulations as seen in Figure 5.11

and 5.20. As summarized in Table 5.1, for given operation conditions, the main differences between the GMPNP and MPB equations are in the efficiency and stability of numerical computations associated with the mathematical equations of the GMPNP and MPB models and the numerical algorithms used for solving these equations.

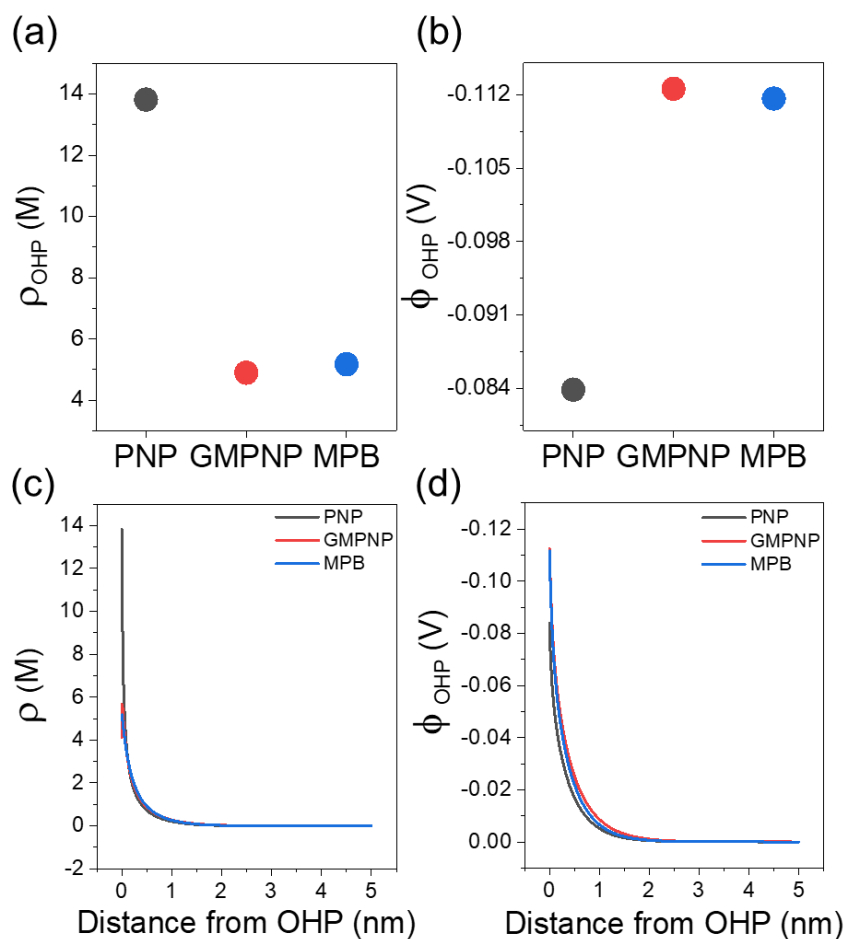


Figure 5.14: Comparison between results obtained from Poisson-Nernst-Planck (PNP) model, a generalized modified PNP (GMPNP) model and modified Poisson-Boltzmann model for (a,c) space charge density (ρ), (b,d) potential (ϕ). Subscript OHP means the measurement at OHP. Considering the difficulty in solving GMPNP numerically, all results are obtained using a planar model with applied potential of -0.4 V vs PZC and the electrolyte of 0.5 M KHCO_3 .

5.5 FEM simulations of $J_{electrolyte}$ behavior

The reaction current density in the electrolyte ($J_{electrolyte}$) near the electrode surface is another important indicator for evaluating the electrochemical performance of an electrode, as it reflects the reaction rate of the electroactive species on the electrode surface. Therefore, a high $J_{electrolyte}$ on the surfaces of an electrode indicates a high electrochemical activity at these areas, which can be regarded as an electrochemical activity indicator to guide the electrocatalyst design. However, the measurement of the local $J_{electrolyte}$ at the nanoscale electrodes are very difficult experimentally under the electrolysis conditions. Moreover, the $J_{electrolyte}$ depends on the interplay of multiple factors such as electrode kinetics, solution resistance, reactant concentration, and mass transfer. Thus, the material and morphology of the electrode, the nature and concentration of the electrolyte, and the nature and concentration of the reactants used in electrolysis all affect the magnitude and the spatial distribution of the $J_{electrolyte}$, which makes it challenging to accurately determine it even using cutting-edge experimental tools. On the other hand, $J_{electrolyte}$ can be calculated using computational simulations, which is an instrumental approach for establishing understanding of the impact of these parameters on the local $J_{electrolyte}$ profile at the electrocatalysts with complex nanoscale morphology.^{13,71} The obtained structure-performance relationships and trends can be used to inform further improvements in the activity of CO₂RR electrocatalysts. In this section, I introduce the commonly used four types of models for the $J_{electrolyte}$ simulations for an electrochemical cell: primary current density (J_{Pri}), secondary current density (J_{Sec}), and tertiary current density (J_{Ter}), as well as one additional modelling approach based on combining J_{Sec} with the mass transport effect (J_{Sec+M}). More specifically, I compare the essential effects accounted for in these modelling approaches and highlight the impact of the electrode kinetics and the bulk concentration of the electrolyte and CO₂ on the spatial profile of $J_{electrolyte}$.

5.5.1 Comparison of various $J_{electrolyte}$ modelling approaches

First, let us consider the simplest model (J_{Pri}) for describing the spatial distribution of the current density, which accounts only for losses due to the solution resistance and treats the solution resistance as a constant. In the J_{Pri} simulation, the electric potential in the electrolyte (ϕ_l) at the electrode-electrolyte interface is defined as: $\phi_l = \phi_s - E_{eq}$, where the ϕ_s is the external applied potential on the electrode and E_{eq} is the equilibrium potential for CO₂RR; the current density J_{Pri} is set to be: $J_{Pri} = -\sigma_l \nabla \phi_l$, where σ_l denotes the conductivity of the electrolyte, which is set to be constant in J_{Pri}

simulation. The electrode kinetics, mass transport, and electrolyte composition variation effects are not involved in the J_{Pri} simulation, making it only applicable to electrochemical systems where the electrolyte concentration is uniform and the electrochemical reactions are sufficiently fast without activation overpotentials. Due to these assumptions, the electrochemical reactions in the J_{Pri} simulation are not kinetically limited, which implies the reaction rate increases linearly with the externally applied potential ϕ_s and can vary in a wide range. Consequently, I observed a very high value of the J_{Pri} (about 100 A/cm^2) around the tips of the nanostar electrode at a potential of -0.3 V vs SHE (Table 5.2) because of omitting the kinetics limitations in the reaction proceeding at the electrode-electrolyte interface.

Table 5.2: Essential effects accounted in the simulation of primary, secondary, tertiary current density and secondary current density coupled with mass transport effect, respectively. All results are obtained for applied potential of -0.3 V vs SHE with the electrolyte of 0.5 M KHCO_3 . All scale bars, 50 nm .

	J_{Pri}	J_{Sec}	J_{Ter}	J_{Sec+M}
Electrode kinetics	✗	✓	✓	✓
Mass transport	✗	✗	✓	✓
Electrolyte variation	✗	✗	✓	✗

In contrast to J_{Pri} , the J_{Sec} model accounts for the influence of the electrode kinetics on the electrochemical reactions as well as the solution resistance effect. The electrode kinetics effect is incorporated in the J_{Sec} simulation by introducing the overpotential η when solving the ϕ_l : $\phi_l = \phi_s - E_{eq} - \eta$. The current density J_{Sec} is solved by using various Butler-Volmer equations as discussed in section of 5.3.2. As the electrode kinetics effect is included in the J_{Sec} model, the electrochemical reactions are considered to be kinetically limited, and the current density is restricted by η instead of linearly changing with ϕ_s . At high local current densities, J_{Sec} would introduce a high local activation overpotential η as discussed in the section 5.3.2, in which case that the electrochemical reactions are limited by the activation potential and can only proceed at a finite rate. As shown in Table 5.2, J_{Sec} on

the electrode surface is less extreme than J_{Pri} (0.25 A/cm^2 vs 100 A/cm^2) in which the electrode kinetics effect is not involved. Thus, J_{Sec} is suitable for modelling the electrochemical reactions in which the activation overpotential cannot be ignored while the concentration overpotential is negligible. The electrode kinetics effect involved in the J_{Sec} model can be described by different current-overpotential $I(\eta)$ relations as seen in Figure 5.10. The discussion about these options for the electrode kinetics effect are covered in the section 5.3.2.

Although the effect of the electrode kinetics is accounted for in the J_{Sec} model, some essential effects are still missing in this model, such as the mass transport and electrolyte composition variation effects. The mass transport effect refers to the influence of the reactant transport on the rate of the electrochemical reaction, especially when there is a depletion of the reactant at the electrolyte-electrode interface. The electrolyte composition variation effect means the impact of the electrolyte composition change on the electrochemical reaction, the solution resistance, and the electrode kinetics. To account for all these essential effects in the simulation, the J_{Ter} model should be applied. The mass transport and electrolyte composition variation effects are considered in the J_{Ter} simulation by solving the Nernst-Planck equations (equation (2.27)) for all species concentrations. The simulation results obtained using the J_{Ter} model are compared to those obtained using the J_{Pri} and J_{Sec} models in Table 5.2. In addition to the reduced magnitude of J_{Ter} compared to that of J_{Pri} with the correction of the electrode kinetic effect, J_{Ter} also shows a more even distribution at the electrode surface compared to J_{Sec} due to the consideration of the mass transport effect and the electrolyte composition variation effect. The application of J_{Ter} produces more accurate results in the case of a complex electrochemical environment with a significant variation of the electrolyte composition, non-linear resistive losses, and reactant-transport-limited electrochemical reaction. However, solving the J_{Ter} is very computationally heavy, especially for 3D models.

To balance the computational time and accuracy, another option for solving $J_{electrolyte}$ is to use a variation of J_{Sec} corrected to account for the mass transport effect, which I refer to as J_{Sec+M} . The electrolyte composition variation effect is ignored in the J_{Sec+M} model. This model is a good choice of simulating $J_{electrolyte}$ in CO₂RR, considering that inert electrolytes are typically used in this case, and therefore their composition does not vary. To understand the accuracy of J_{Sec+M} , I compare the results obtained from J_{Sec+M} to that of J_{Ter} in Table 5.2. The results show that they are very similar to J_{Ter} in terms of the magnitude and distribution of the $J_{electrolyte}$, suggesting that the J_{Sec+M} is a good alternative to J_{Ter} , as it is easier to solve numerically compared to J_{Ter} , since solving the Nernst-Planck

equations for all species concentrations is avoided in J_{Sec+M} . Instead, I only need to solve the Nernst-Planck equations for the reactive species.

5.5.2 Comparison of various electrode kinetic models in $J_{electrolyte}$ simulations

As discussed above, the electrode kinetics is one of the crucial factors in the $J_{electrolyte}$ simulations, as it modifies the reactions in the simulations by introducing the kinetic limitations, which is one of the key features in the realistic electrolysis reactions. Choosing an appropriate electrode kinetics model according to the studied electrochemical setup is crucial for getting reliable results in the $J_{electrolyte}$ simulations while minimizing the complexity of the model and, therefore, the associated computational resources. Mathematically, the electrode kinetics is introduced in the numerical simulations by using various $I(\eta)$ equations as shown in Figure 5.10. The selection of the $I(\eta)$ equation depends on several factors, including the mass transport of the reactants, the applied overpotential. In this section, I compare the effect of various $I(\eta)$ relations on the profile of $J_{electrolyte}$ and discuss the conditions under which they can be applied.

Among all studied $I(\eta)$ relations, the G. B-V equation (equation (2.40)) is a generalized $I(\eta)$ form, which is valid for the cases with and without mass transport limitations under a wide range of overpotentials. However, a generalized form is not always necessary for a given system, and a simplified version can be applied instead to reduce the time and memory storage requirements for the simulations. For instance, when there is no depletion of the reactant on the electrode surface, the mass transport effect in the electrode kinetic expression does not have to be considered. Therefore, in this case the concentration term in equation (2.40) can be ignored, simplifying it to the S. B-V equation (equation 2.41). To illustrate the validity of this simplification, I compare the results obtained from the G. B-V equation and the S. B-V equation in the cases with and without the depletion of the reactant (CO_2). As shown in Figure 5.15, when there is abundant CO_2 at the electrode surface for the electrochemical reaction at the potential of -0.3 V vs SHE (Figure 5.15a and b), the $J_{electrolyte}$ obtained from the G. B-V equation is similar to that obtained from the S. B-V equation (Figure 5.15c and d). However, when there is a depletion of CO_2 at the electrode surface at a more negative potential of -0.6 V vs SHE (Figure 5.15e and f), neglecting the mass transport effect in the electrode kinetics expression of the S. B-V equation results in a 20-fold higher current density than that obtained from the G. B-V equation at the potential of -0.6 V vs SHE (Figure 5.15g and h). This result demonstrates that the S. B-V equation is an accurate simplification of the G. B-V equation only when the electrochemical reaction

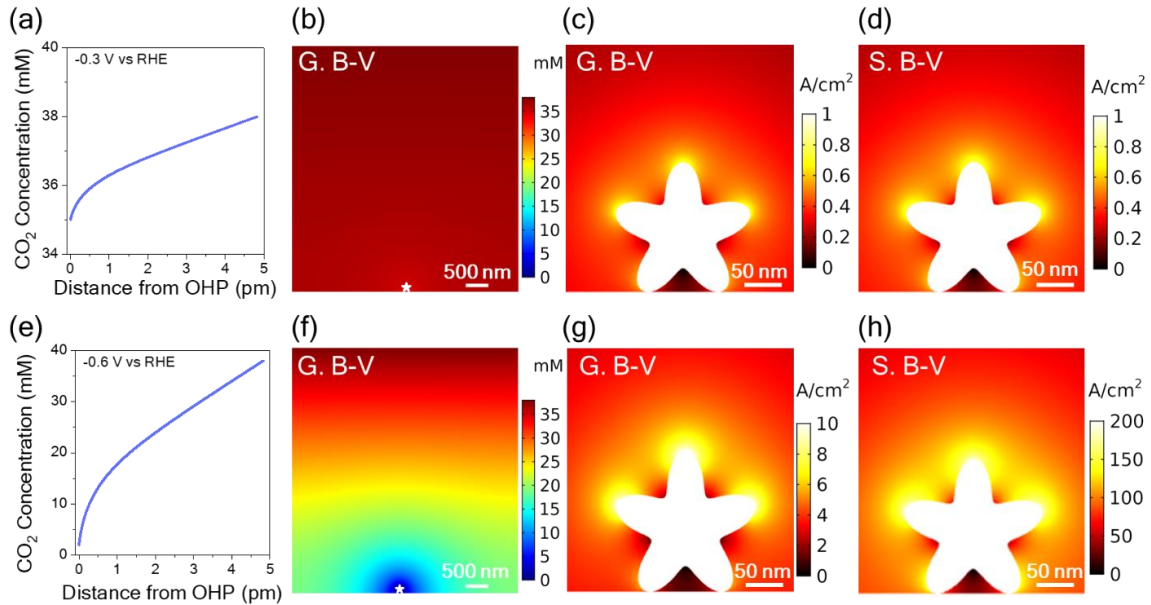


Figure 5.15: Comparison between results of current density obtained from G. B-V equation and S. B-V equation. The results from G. B-V are (a, e) CO_2 concentration drop from catalysts surface, (b, f) CO_2 concentration distribution and (c, g) current density distribution. Current density distributions from S. B-V equation are shown in (d, h). Applied potential of -0.3 V vs SHE is assigned to cathode in (a-d) while -0.6 V vs SHE used in (e-h). The results in this figure are obtained using Tertiary current density.

is controlled by interfacial dynamics instead of the mass transport (that is, when the solution is well-mixed, or the current is kept sufficiently low to prevent the variation in the surface concentrations of reagents compared to the bulk values). In addition, the S. B-V equation can be further simplified to other electrode kinetics expressions such as the L. B-V equation (equation (2.42)) and the Tafel equation (equation (2.43)), depending on the activation overpotential, η . For small values of η , the S. B-V equation can be rearranged as the L. B-V equation, (equation (2.42)), in which the current is linearly dependant on η , while for large values of η , the standard B-V equation can be rearranged as the Tafel equation, (equation (2.43)), in which the contribution of the backward reaction to current is negligible. The net reaction current is the difference in the currents generated in the forward reaction and the backward reaction. When a large overpotential is applied, the reaction rate of the forward reaction is much larger than that of the backward reaction, therefore, the backward reaction can be ignored and does not contribute to the reaction current, which is the case described by the Tafel

equation. Figure 5.16 shows the $J_{electrolyte}$ calculated using the three models under different η , with the equilibrium potential of CO₂ reduction to CO set to be -0.11 V vs SHE. At the applied potential of -0.15 V vs SHE ($\eta = 0.04$ V), one can see that the electrode kinetics models of the S. B-V equation and the L. B-V equations yield very similar results in the $J_{electrolyte}$ simulation (Figure 5.16a and b), while at the applied potential of -0.6 V vs SHE ($\eta = 0.49$ V), the magnitude of $J_{electrolyte}$ obtained from S. B-V equation is 5 order higher than that obtained from L. B-V equation (Figure 5.16d and e). In contrast, the current densities obtained from the S. B-V equation and the Tafel equation are similar only at -0.6 V vs SHE when η is large (Figure 5.16d and f).

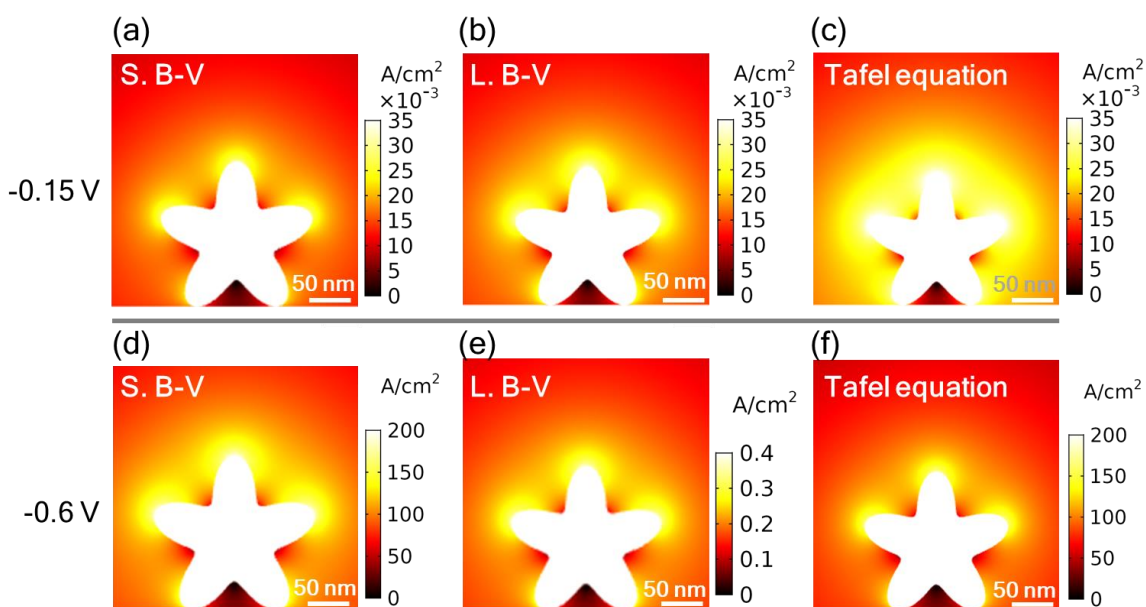


Figure 5.16: Comparison between results of current density obtained from (a, d) S. B-V equation, (b, e) L. B-V equation and (e, f) Tafel equation. Applied potential of -0.15 V vs SHE is assigned to cathode in (a-c), while -0.6 V vs SHE used in (d-f). The results in this figure are obtained using Tertiary current density.

5.5.3 Other essential factors in $J_{electrolyte}$ simulations

In addition to the effects of the electrode kinetics discussed above, other important factors that noticeably affect the calculated $J_{electrolyte}$ in the course of CO₂RR include the bulk concentration of CO₂ and the electrolyte composition. Specifically, CO₂RR on the electrode surface can be influenced by the bulk concentration of CO₂, which affects the Gibbs free energy of CO₂ and the reaction rate of CO₂RR (Figure 5.9b), and also can introduce limitations of the CO₂ mass transport to the electrode surface. In addition to the bulk concentration of CO₂, CO₂RR electrolysis is also affected by the bulk concentration of the electrolyte, as it determines the solution resistance and the transport of the ionic species. To demonstrate the influence of CO₂ and electrolyte concentrations on the $J_{electrolyte}$, J_{Ter} simulations were performed for a nanostar electrode in the solution with various concentrations of CO₂ and KHCO₃ at -0.3 V vs SHE. The results indicate that $J_{electrolyte}$ first linearly increases with increasing CO₂ concentration while it remains below 10 mM, and then slowly increases until the CO₂

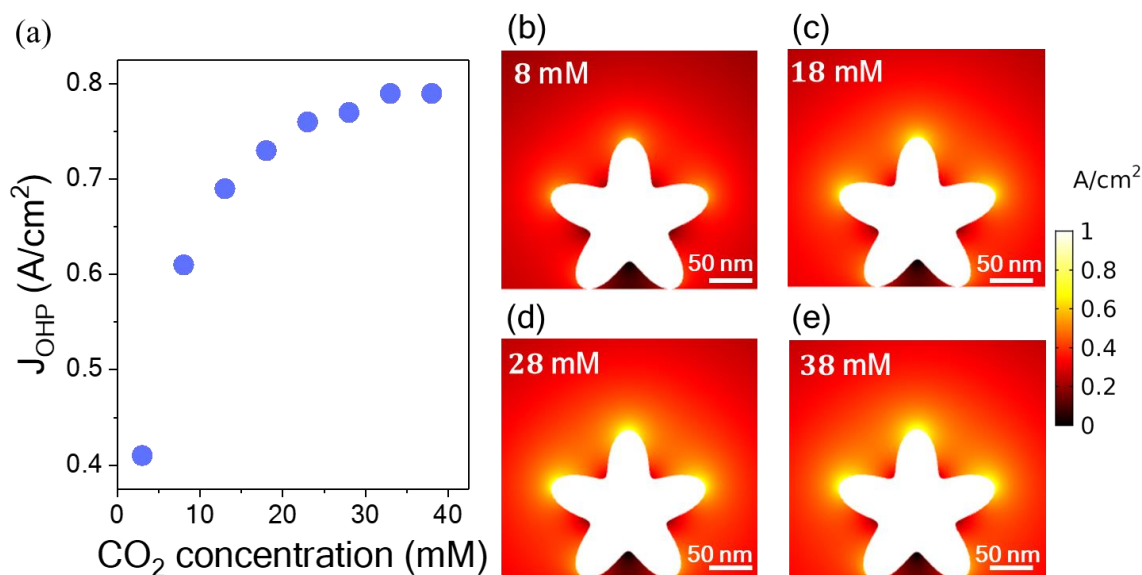


Figure 5.17: Effect of CO₂ concentration on the magnitude and distribution of current density in electrolyte. (a) The magnitudes of current density at OHP (J_{OHP}) are compared using different concentrations of CO₂ from 3 mM to 38 mM. The distribution of current density is shown in (b), (c), (d) and (e) for 8 mM, 18 mM, 28 mM and 38 mM CO₂, respectively. The results in this figure are obtained using Tertiary Current Density with the electrolyte of 500 mM KHCO₃ and the applied potential of -0.3 V vs SHE.

concentration reaches saturation at 38 mM (Figure 5.17a); the $J_{electrolyte}$ for the bulk CO_2 concentrations of 8 mM, 18 mM, 28 mM, and 38 mM are shown in Figure 5.17c-e. This trend suggests that a higher CO_2 bulk concentration can increase the rate of the CO_2RR that occurs at the electrode surface, highlighting the significance of keeping the reaction medium saturated with CO_2 during the electrolysis.

Similarly, $J_{electrolyte}$ at the electrode surface also increases with increasing the bulk electrolyte concentration. However, $J_{electrolyte}$ reaches a steady state when the concentration of the electrolyte is over 100 mM due to the negligible composition variation in the electrolyte with a high bulk concentration at -0.3 V vs SHE (Figure 5.18). Note that $J_{electrolyte}$ greatly depends on the nature and concentration of the electrolyte not only due to the above-mentioned factors, but also because of (1) the electrolyte blocking of the catalytic sites, (2) the chemical interactions between cations and reaction intermediates, (3) the alteration of the interfacial water structure: the water molecules in the first monolayer lie mostly flat on the surface and form a hydrogen bonding network, which can impact chemical processes and the distribution of ions.¹⁵³ Advanced theories such as DFT and molecular

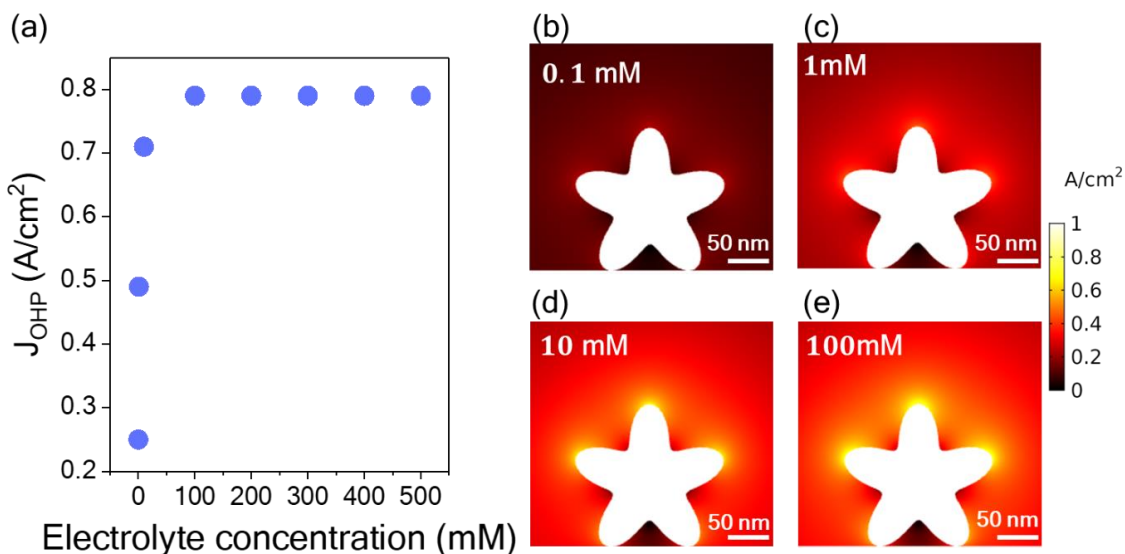


Figure 5.18: Effect of electrolyte concentration on the magnitude and distribution of current density in electrolyte. (a) The magnitudes of current density at OHP (J_{OHP}) are compared using different concentrations of KHCO_3 from 0.1 mM to 500 mM. The distributions of current density are shown in (b), (c), (d) and (e) for 0.1 mM, 1 mM, 10 mM and 100 mM KHCO_3 , respectively. The results in this figure are obtained using Tertiary Current Density with applied potential of -0.3 V vs SHE.

dynamics simulations are required to study these factors, which is beyond the scope of the work presented in this thesis.

5.6 FEM simulations of $J_{electrode}$ behavior

In contrast to thermal catalysis, electrocatalysis is a more complex process, involving charge transfer throughout a solid catalyst, rather than only at the surface-active sites. The flow of electrons in an electrocatalyst could affect the structural stability and cause structural evolution differently compared to the degradation processes occurring in thermal catalysts. Studying the electron flow in electrocatalysts with complex nanomorphology by mapping the current density distribution within the electrode ($J_{electrode}$) can be used to predict the locations of structural instability in these nanomaterials.⁷¹ Specifically, the electron flow in an electrode affects the structural transformation by driving the mass transport of solid metal matter via electromigration (EM) and/or Joule heating.^{157,158} EM is a migration process of metal atoms under applied current caused by the electron wind force, which is a transfer of momentum to the metal atoms from current carriers on their scattering. In the case of nonuniform $J_{electrode}$, EM can be described as a force driving atomic species from higher to lower current density regions to minimize current crowding. The occurrence of EM depends on the magnitude of the $J_{electrode}$ since the current intensity determines the number of the current carriers scattering against the metal atoms. Generally, $J_{electrode} \geq 10^4$ A/cm² are required to cause EM inside the metal, where it is significantly faster along the grain boundaries than in the bulk.⁴⁶ At the same time, EM on surfaces and in thin films can be observed at $J_{electrode} \geq 10$ A/cm², as it is associated with the mobility of less coordinated surface atoms.⁴⁶ In addition, the nanostructure regions with high $J_{electrode}$ and, subsequently, high local power,⁷¹ can be subject to a local temperature increase by Joule heating, which can additionally promote the surface mass transport of the solid catalyst material. This process occurs only when the metal atoms obtain enough thermal energy to diffuse when the localized temperature rises caused by Joule heating, with the diffusion degree depending on the achievable temperature.⁴⁷ Joule heating may be more prominent and therefore should be evaluated in electrodes composed of nanoparticles with insulating surface modifiers or when substrates with low thermal conductivity are used. Regardless of whether the mass transport is induced by EM or Joule heating, they are all closely related to the profile of $J_{electrode}$. Thus, accurate $J_{electrode}$ simulations are necessary for understanding the structural transformations driven by the electron flows in the solid electrocatalysts.

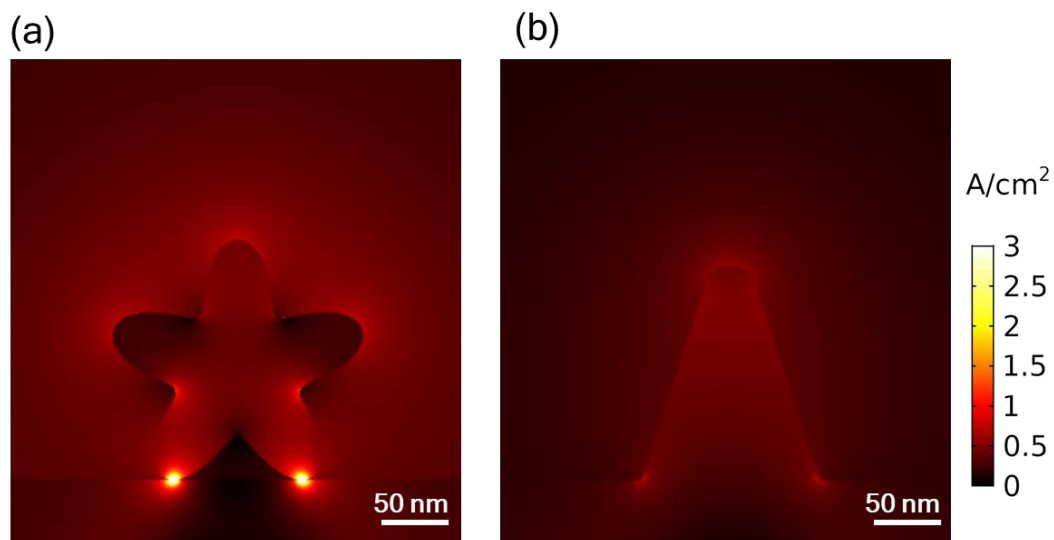


Figure 5.19: Comparison between the results of current density in electrode for nanostar and nanocone. The results in this figure obtained using an average current density of 1 mA/cm² for cathode as boundary condition.

To demonstrate what information is provided by simulating $J_{electrode}$ in nanostructured electrodes, I employed a nanostar and nanocone electrode models. The nanostar model represents a repeat unit in the electrodes comprised of a layer of branched nanoparticles placed on a substrate, while the nanocone model reflects the repeat unit of high-surface-area electrodes obtained by electrodeposition. The simulations of $J_{electrode}$ performed for the nanostar and nanocone models reveal an uneven distribution of $J_{electrode}$ in the metal (Figure 5.19). Specifically, in the nanostar geometry, which has small contact areas with the substrate, the current path is constricted in the metal at the interface with the substrate (Figure 5.19a). Considering that electrocatalysis reactions processing on the electrode surfaces require sufficient supply of electrons to the electrode-electrolyte interface, a large quantity of electrons has to pass through the narrow constrictions at the interface between the nanostars and the substrate, resulting in current crowding (i.e., high $J_{electrode}$) in these constrictions. In contrast, for the $J_{electrode}$ distribution in a structure that does not have narrow features, e.g., a cone with 120-nm-wide base sitting on a flat substrate, I observe a comparatively uniform $J_{electrode}$ distribution in the metal without current crowding (Figure 5.19b). The current crowding in these electrocatalysts could drive the mass transport of solid metal matter via EM, resulting in deformations and sintering in nanoscale features.⁷¹ This example shows that accurate $J_{electrode}$ simulations are instrumental in revealing the current crowding areas prone to structural changes in morphologically-complex electrocatalysts. These simulations can

be used to guide the design of high-performance electrocatalysts by mitigating the negative effects (e.g., deformation) or exploiting the positive effects (e.g., *in situ* activation) of the structural transformations induced via EM.

5.7 Electrochemical simulations for 3D model

Considering the heavy computational demands of 3D simulations, in this chapter I focus on E-field, K^+ concentration, $J_{electrolyte}$, and $J_{electrode}$ simulations using a 2D model, which for many geometries of electrocatalysts is an appropriate simplification. The discussed theories used in these simulations are

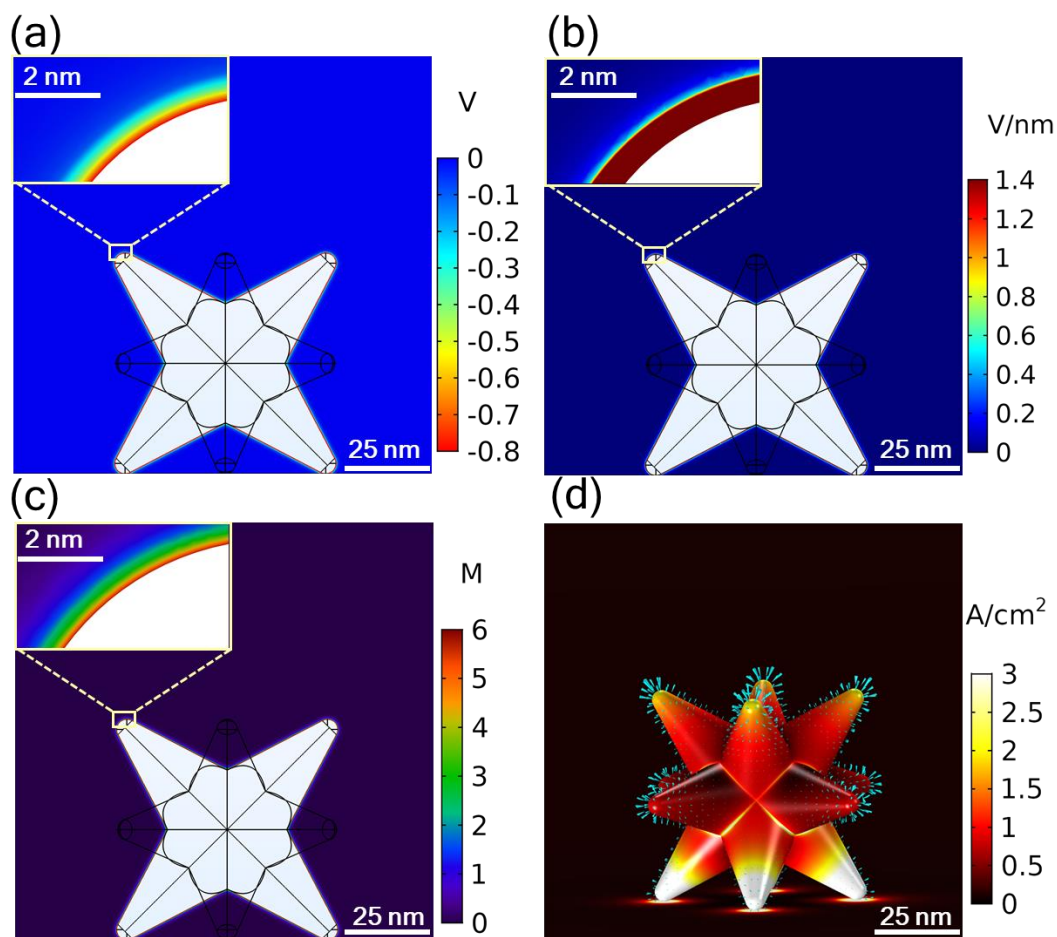


Figure 5.20: Simulations performed for 3D branched nanoparticle: (a) potential, (b) electric field, (c) K^+ concentration and (d) current density in metal ($J_{electrode}$) and adjacent electrolyte ($J_{electrolyte}$). $J_{electrode}$ is shown as color map. $J_{electrolyte}$ is shown as groups of cyan arrows, where the size and direction of each arrow represent the magnitude and direction of the current at the spatial position of the arrow, respectively. The results in (a), (b) and (c) are obtained from MPB & Booth model with the electrolyte of 500 mM $KHCO_3$ and potential of -0.8V vs PZC, the reaction current density ($J_{electrolyte}$) in (d) is calculated using J_{Sec+M} .

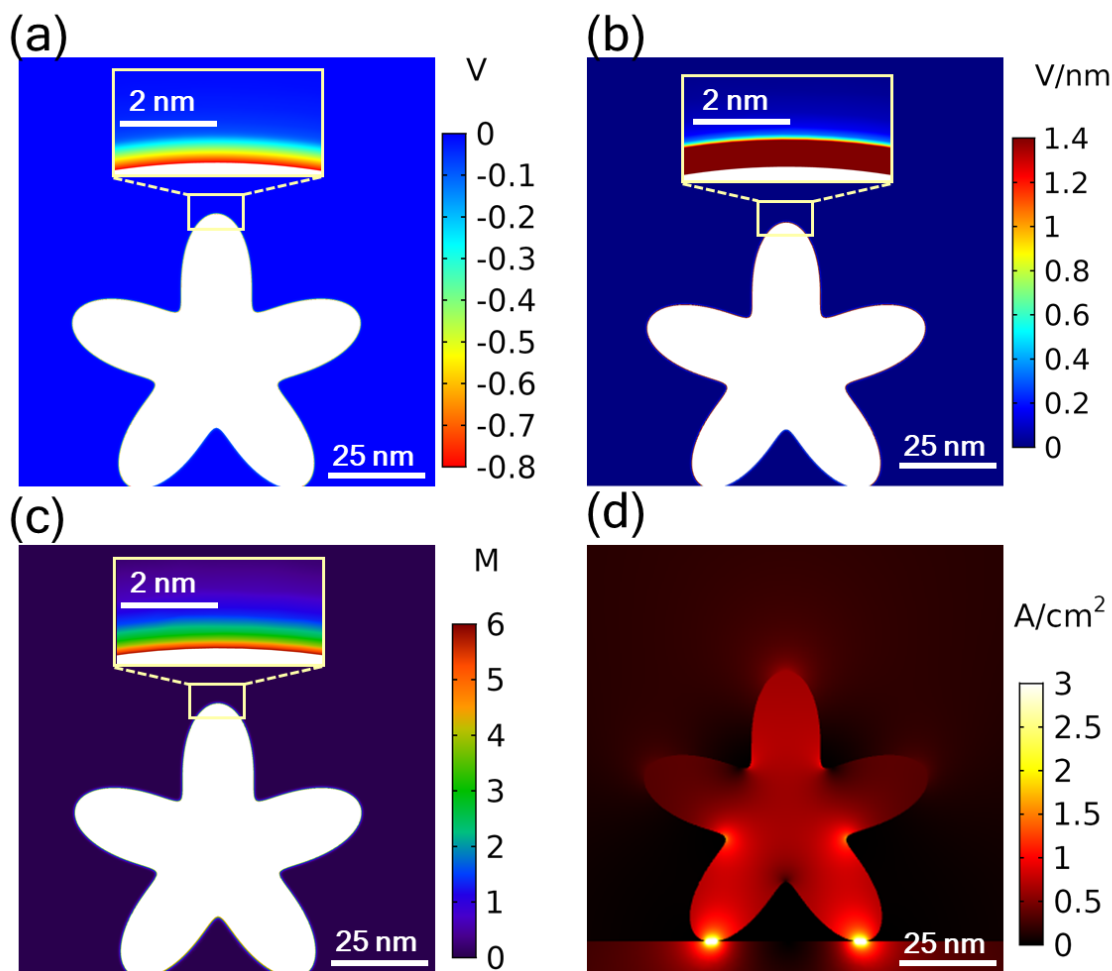


Figure 5.21: Simulations performed for 2D nanostar nanoparticle. (a) The potential (ϕ), (b) electric field (E-field) (c) K⁺ concentration and (d) current density in metal ($J_{electrode}$) and adjacent electrolyte ($J_{electrolyte}$). The results in (a), (b) and (c) are obtained from MPB & Booth model with the electrolyte of 500 mM KHCO₃ and potential of -0.8V vs PZC, the reaction current density ($J_{electrolyte}$) in (d) is calculated using J_{Sec+M} .

equally valid for 3D models and can be easily transferred to 3D simulations. As an illustrative example, the results of simulations for a 3D branched nanoparticle (or nanostar) are shown in Figure 5.20. Specifically, Figure 5.20a-c and d correspond to the simulations based on the combination of the MPB, Booth and J_{Sec+M} models. To accurately compare the applicability of these theoretical models in both 3D and 2D simulations, the above-mentioned simulations were also performed for a 2D nanostar

(Figure 5.21) with the same dimensions as the 3D nanostar (Figure 5.20a-c) at the same conditions, i.e. in 500 mM KHCO_3 electrolyte and the applied potential of -0.8 V vs PZC. As shown in the results obtained from 3D simulations using the MPB and Booth models in Figure 13a-c, the potential sharply drops on the branched nanoparticle surface (Figure 5.20a), leading to high E-field in the electrolyte (about 1nm) close to the surface of the nanoparticle (Figure 5.20b), which can be ascribed to the screening effect of accumulated K^+ on the electrode surface (Figure 5.20c). The results of the potential and E-field in 3D simulations are very similar to those obtained in 2D simulation in Figure 5.21a-c. In addition, when the J_{Sec+M} model and Ohm's law were applied to the 3D model to calculate the $J_{electrolyte}$ and $J_{electrode}$ (Figure 5.20d), the results are also similar to those obtained for 2D model in Figure 5.21d: high $J_{electrolyte}$ appears in the electrolyte at the round tips of the nanostar, while the $J_{electrode}$ showed the current crowding in the area of contact between the metal with the substrate. Although applying the combination of the MPB, Booth and J_{Sec+M} models in 2D and 3D simulations generally generates very similar results under the same conditions, there are still some differences between the results obtained in 2D and in 3D. First, the maximum E-field at OHP obtained in 3D model (Figure 5.20b) is about 2.0 V/nm with that of around 1.9 V/nm observed in 2D model (Figure 5.21b). Second, the hotspots of $J_{electrode}$ in 3D model are larger than those in 2D model. The discrepancies in the E-field and $J_{electrode}$ can be ascribed to the differences in structural representation between 2D and 3D models. Specifically, an equivalent of a 2D model in 3D is a product of extrusion of the 2D planar structure along its normal vector. For example, a 2D nanocone structure represents a 3D ridge as opposed to a 3D tip; similarly, the sharp features seen in the 2D model in Figure S7 correspond to extended ridges in 3D, and not to the vertices of a 12-armed nanostar seen in Figure 13. Therefore, one should be careful when simplifying a 3D model with a 2D model if high-precision results are required. Generally, for 3D structures with uniform extendibility along one dimension, such as cylinders, cuboids and ridges, can be well represented by corresponding 2D slices. More geometrically complex 3D objects, such as 3D branched nanoparticles and nanoframe structures, require accurate 3D representations to produce more accurate numerical results in the simulations.

5.8 Electrochemical performance of various nanostructured electrodes

In the previous sections, I discussed the advanced theoretical models used for the E-field, $J_{electrolyte}$, $J_{electrode}$ simulations using FEM and their application scopes. In this section, I am going to use these theoretical models, especially the $J_{electrolyte}$ and $J_{electrode}$ simulations, for studying the local current behavior of the real electrochemical nanostructures under CO₂RR electrolysis conditions, which combined with the experimental observations (discussed in Chapter 3) and DFT calculations (discussed in Chapter 4) would provide a comprehensive mechanistic understanding of the structural transformations observed in the nanostructures under bias conditions that were discussed in Chapter 3.

In Chapter 3, I found that the morphological changes of the well-defined gold and palladium nanoparticles CCs and BNPs can be accelerated by the RIs of the electrolysis reactions, with the extent and rates of structural transformations depending on the material of the nanostructures and the nature of the electrocatalytic reactions at their surfaces. The RIs- and material-dependent morphological changes in the nanoparticles can be well described by the DFT calculations of migration energy barriers and vacancy formation energies together (Figure 4.1). As demonstrated in Chapter 4, the plot in Figure 4.1 shows the comparatively higher stability of the surface atomic structures in the top-right corner, whereas the structures in the bottom-left corner are relatively more likely to reconstruct. However, these thermodynamic and kinetic aspects consider random hopping of surface atoms and do not reflect any locality or directionality of atomic mobility on the nanoscale. Conversely, the experimental data implied that in some localities of complex nanoscale electrocatalysts the atoms were hopping about more than in other otherwise identical features, suggesting that the impacts exerted on them are associated with the applied bias. Moreover, the experimental evidence revealed structural changes at the interfaces of the particles with the substrate and each other, where the electrolysis is hindered due to apparent mass-transport limitations, further suggesting the presence of additional driving forces for atomic migration (Figure 3.11 and 3.12). To understand the origins of the locality and directionality of atomic mobility in nanocatalysts during electrolysis, I studied how the nanoscale shapes structurally participate in the electrochemical process. I performed spatial FEM simulations of the current-density distributions in both the metal ($J_{electrode}$) and the adjacent electrolyte ($J_{electrolyte}$), using geometric models constructed based on the experimentally studied BNPs and CCs and setting 0.1 A cm⁻² as a boundary condition for the average current density at the anode (Figure 5.22).

The magnitude and direction of the current flow in the electrolyte in the vicinity of the electrocatalyst surface ($J_{electrolyte}$) are shown as a group of yellow arrows in Figure 5.22a–e for a range of gold

models acting as a cathode and supported on a substrate of the same material. In all of the examined structures, the surfaces of the geometries away from the substrate and facing the electrolyte corresponded to high $J_{electrolyte}$ values, suggesting that these areas participate most actively in electrocatalysis. In addition, the surface areas with high curvature displayed the highest $J_{electrolyte}$ values, in agreement with earlier reports on the role of curvature in ultramicro- and nano-electrodes on their electrochemical behaviour^{32,33}. The angle of the BNP branches with respect to the substrate was

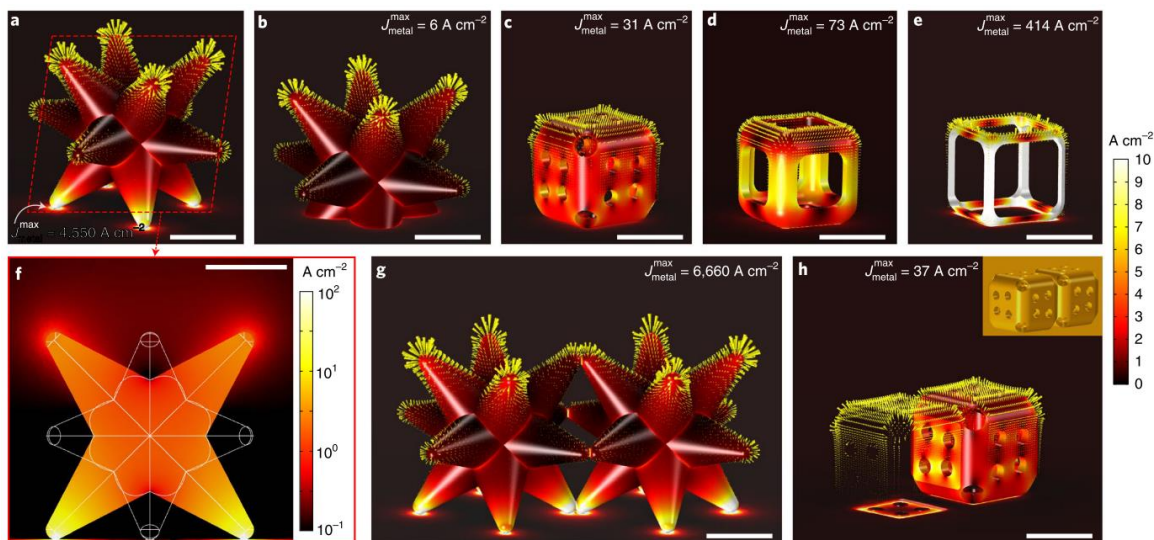


Figure 5.22: Computed current-density distributions of various gold nanoshapes. The current-density distribution within the metal structures ($J_{electrode}$) is shown as colour maps; the current-density distribution in the electrolyte at the nanostructure surface ($J_{electrolyte}$) is shown as groups of yellow arrows, where the size and direction of each arrow represent the magnitude and direction of the current at the spatial position of the arrow, respectively; the average ($J_{electrolyte}$) was set at 0.1 A cm^{-2} . a–e, Structures shown are the symmetric branched (a), anchored branched (b), CC (c), thick (d) and thin (e) frames. f, A 2D-slice of the structure a showing the computed current density in a BNP and the surrounding electrolyte for an apparent comparison of current-density magnitudes in both the metal ($J_{electrode}$) and the adjacent electrolyte ($J_{electrolyte}$). g,h, BNP dimer (g) and CC dimer (h), where the two particles are in direct contact, showing the locations of current crowding at the interfaces between the particles and between a particle and the substrate. In h, the left CC is hidden from the view to reveal the $J_{electrode}$ distribution in the planes of contact, where the inset shows the full geometry of the corresponding CC dimer. All scale bars, 25 nm. Reprinted with permission from ref. [71]. Copyright 2021, Springer Nature.

found to be crucial to the $J_{electrolyte}$ behaviour, with the branches perpendicular to the substrate (that is, pointing directly towards the anode) having the highest $J_{electrolyte}$ accumulation at the tips. Consequently, these highly electrocatalytically active features with adsorbed reaction intermediates increase the likelihood and rate of atomic migration in these features, in contrast with the areas of the

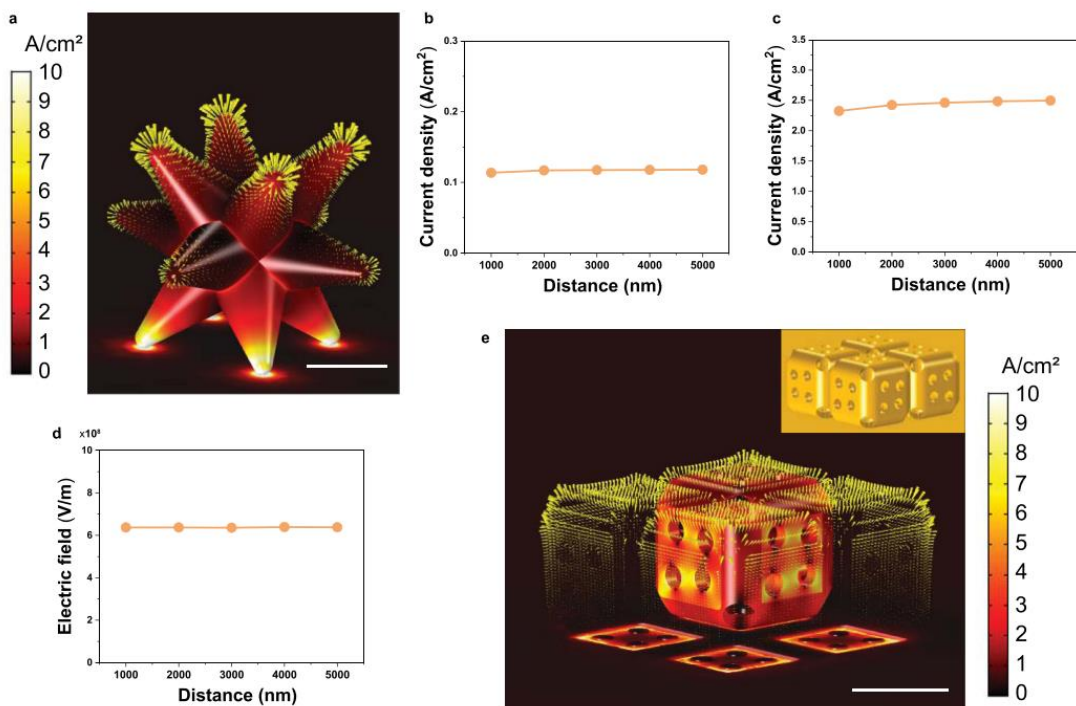


Figure 5.23: Effects of geometry, material, and interelectrode distance on computed current density and E-field. a, Computed current density distribution in Pd BNPs. b-d, average current density within the Debye length, $J_{electrolyte}$ (b), average current density within the electrode, $J_{electrode}$ (c) and average E-field within the Stern layer (d), as the function of the distance between anode and cathode. e, Computed current density distribution in a Au CC tetramer with the geometry shown in the inset; three CCs in the front of the structure are hidden from the view to reveal the current distribution at the interfaces between the particles and at the particle-substrate interfaces. In (a) and (e) $J_{electrode}$ is shown as colour maps, and $J_{electrolyte}$ at the nanostructure surface is shown as a group of yellow arrows, where the size and direction of each arrow represent the magnitude and direction of current at the spatial position of the arrow, respectively. Scale bars are 25 nm. Reprinted with permission from ref. [71]. Copyright 2021, Springer Nature.

structure closer to the substrate, where the reacting species also become depleted due to mass-transport limitations. These trends imply that there is less electrochemical activity at the base of the structure near the substrate, suggesting that other factors facilitate structural changes in these features.

The current-density calculations also revealed an uneven distribution of current density in the metal ($J_{electrode}$), as seen from the colour plots in Figure 5.22a–e. Specifically, in the BNP geometry (Figure 5.22a), which has a small contact area with the substrate, there is considerable current crowding in the metal at the interface with the substrate. The same effect is present in palladium BNPs (Figure 5.23). In the four branches of BNPs at the interface with the substrate, $J_{electrode}$ is orders of magnitude higher than the average $J_{electrolyte}$ associated with the electrochemical activity at the particle surface (Figure 5.22f and 5.23b–d). This $J_{electrode}$ crowding occurs because the current path is constricted, with these areas of limited contact acting as bottlenecks for the carrier flow. Similar $J_{electrode}$ hotspots are observed in geometric constrictions of CCs and other frame geometries (Figure 5.22c–e) and at the interfaces between BNPs (Figure 5.22g) or CCs (Figure 5.22h and 5.23e), as well as between a CC and the substrate (Figure 5.22h and 5.23e).

Constricted current flow in micro- and nano-electronics is known to lead to the mass transport of solid metal matter resulting in deformations and sintering in nanoscale features, which is described by the theory of electromigration.¹⁵⁷ Conceptually, EM is a migration process of metal atoms under applied current caused by the electron wind force, which is a transfer of momentum to the metal atoms from current carriers on their scattering. In the case of nonuniform current density distribution, EM can be described as a force driving atomic species from higher to lower current density regions to minimize current crowding. Generally, $J_{electrode} \geq 10^4$ A/cm² are required to cause EM inside the metal, where it is significantly faster along the grain boundaries than in the bulk. At the same time, EM on surfaces and in thin films can be observed at ≥ 10 A/cm², as it is associated with the mobility of less coordinated surface atoms².

In addition, the nanostructure regions with high current density and, subsequently, high local power (Figure 5.24 and 5.25), can be subject to a local temperature increase by Joule heating, which can additionally promote the surface mass transport of the electrocatalyst material³. However, I found that the temperature increase via Joule heating was negligible in the systems studied in this work (Figure 5.26), due to significant heat dissipation into the substrate metal film. I note that Joule heating may be more prominent and therefore should be evaluated in electrodes composed of nanoparticles with insulating surface modifiers or when substrates with low thermal conductivity are used.

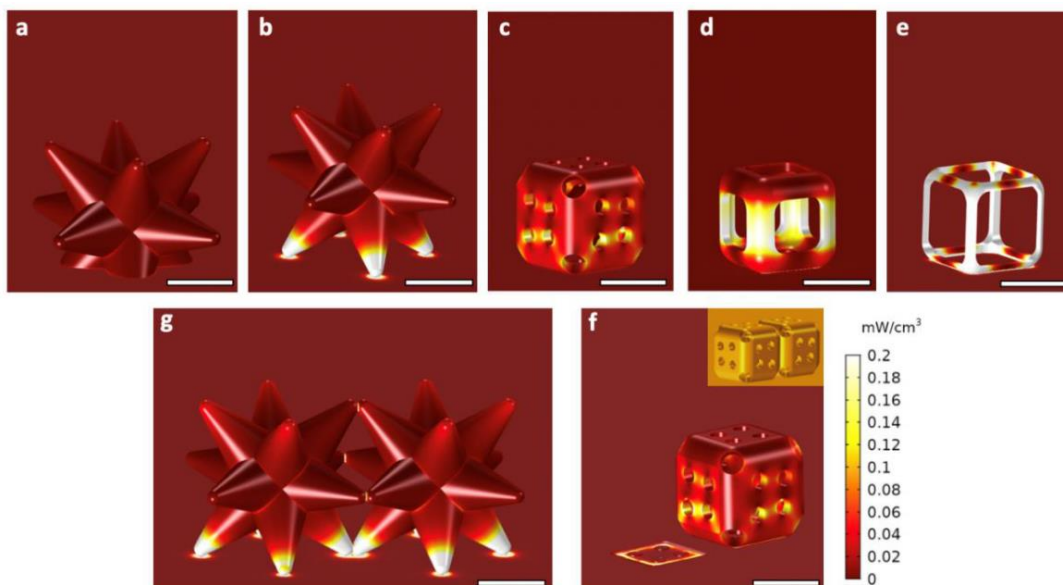


Figure 5.24: Computed power density distribution (shown as colour map) in Au nanostructures of different shapes. The left CC in a dimer in (f) is hidden from view to show the power distribution at the interface between the CC and the substrate, and at the interface between the two CCs; the inset shows the geometry of the dimer. Scale bars are 25 nm. Reprinted with permission from ref. [71]. Copyright 2021, Springer Nature.

As EM is not concerned with the surface electrochemistry per se, it is not generally considered in the field of electrocatalysis. However, in our electrochemical experiments I found that metal mass transfer was pronounced in the areas that showed a high $J_{electrode}$ value: that is, the interfaces of the geometries with the substrate and each other. Based on the FEM simulations, $J_{electrode}$ values in these areas can reach $10\text{--}10^3 \text{ A cm}^{-2}$, depending on the geometry (Figure 5.22f), while the average $J_{electrolyte}$ value within the Debye length is $10^{-1} \text{ A cm}^{-2}$ (Figure 5.23b). The alignment of our experimental observations with the locations of $J_{electrode}$ hotspots suggests that EM is a driving force behind the structural transformations in high $J_{electrode}$ regions.

The particle-particle and particle-substrate interfaces represent noticeable defects from a crystallographic perspective. While I employed nanoparticle synthesis methods that yield single crystalline nanoparticles,¹⁶³ inevitable lattice discontinuities at their interfaces make these areas crystallographically similar to grain boundaries. In the case of CCs, the surfaces of synthesized particles are not perfectly flat, in contrast to the idealized FEM geometric models (Figure 5.22c,h); thus, the imperfect contact at the particle- particle interface may result in even more pronounced current stressing than seen in Figure 5.22. In addition, these NP surface imperfections may contain traces of adsorbates remaining from the synthesis, even though the majority of them was removed. Since the $J_{electrode}$ threshold for EM is a function of not only the metal nature and geometry, but also these nuances at the interfaces, it is difficult to be estimated quantitatively. However, it is reasonable to expect that Pd is more stable against EM than Au as the atomic mobility kinetics and thermodynamics simulations discussed in the DFT section generally show higher stability of Pd against surface mobility than Au (Figure 4.1a).

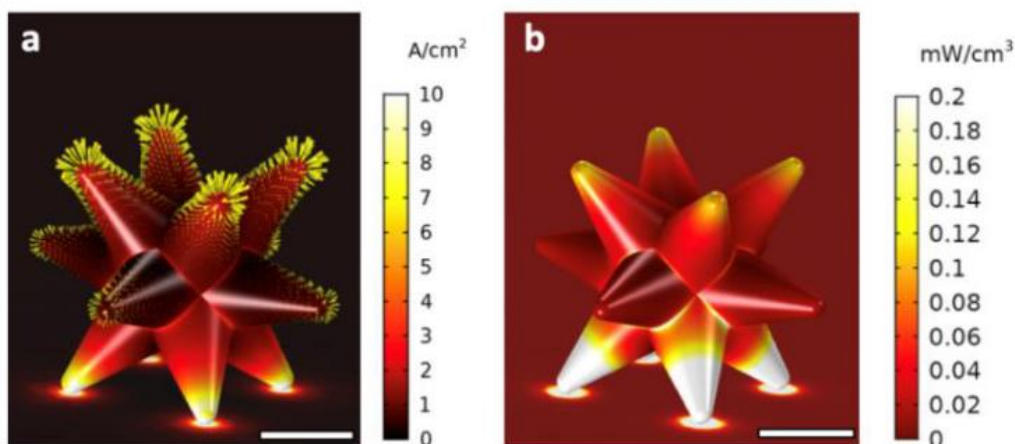


Figure 5.25: Computed current density (a) and power density (b) distributions in Pd BNPs. (a) $J_{electrolyte}$ is shown as groups of arrows, where the size and direction of each arrow represent the magnitude and direction of current at the spatial position of the arrow; $J_{electrode}$ is shown with a colour map. (b) Power density distribution is shown as a colour map. Scale bars are 25 nm. Reprinted with permission from ref. [71]. Copyright 2021, Springer Nature.

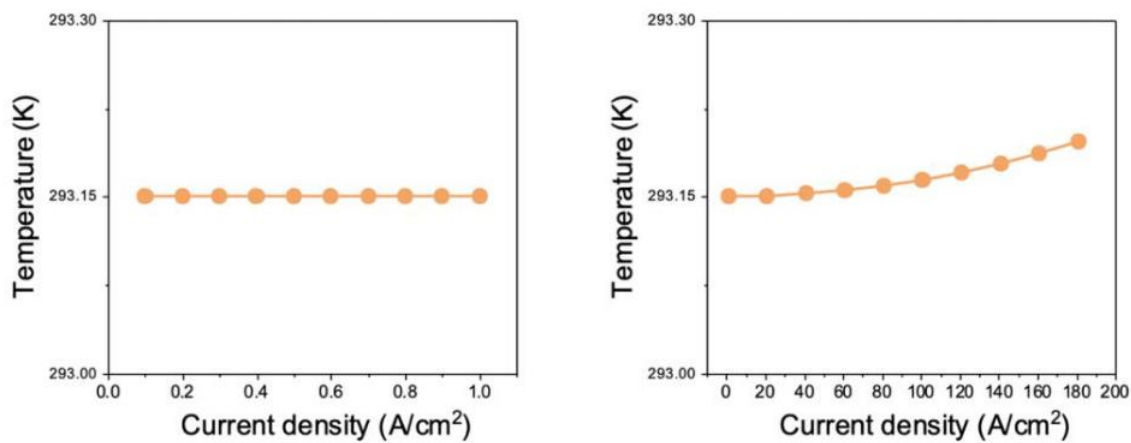


Figure 5.26: The change of averaged temperature of Au BNPs with the average current density with the substrate temperature of 293.15 K as the reference temperature. Reprinted with permission from ref. [71]. Copyright 2021, Springer Nature.

5.9 Applicability and limitations of the discussed models

The combination of *ab initio* and experimental studies have proven to be successful strategies for improving the activity and selectivity of electrocatalysts CO₂RR and other electrocatalytic processes of intense interest by guiding the design of their atomic surface structures including the surface composition and defects.¹ Considering the plethora of nanoscale geometries attainable for electrocatalyst thanks to the progress in synthetic nanochemistry, it is essential to consider rational catalyst design not only on the atomic scale, but also on nanoscale, in order to further enhance the activity, selectivity, and stability of these materials. As I have discussed in this chapter, optimizing the nanoscale shape of the electrocatalysts enables tunability of the E-field, $J_{electrolyte}$ and $J_{electrode}$, and this structural design is gaining increasing attention in the electrocatalysis community. To conclude the systematic discussion of the established theoretical models for the FEM simulations of E-field, $J_{electrolyte}$, and $J_{electrode}$ that are applicable on the nanoscale, in this section I focus on summarizing the applicability and limitations of these models.

5.9.1 Potential and E-field simulations

In section 5.4, I presented three EDL models for simulating the potential and E-field distribution in the vicinity of a nanoscale electrode under electrolysis conditions, including the PNP, GMPNP and MPB models. These models can reveal the influence of the nature and concentration of the electrolytes on the screening effect of the potential and E-field distribution in the EDL. Among the three models, the PNP model can describe the EDL that deviates from the equilibrium state without electrolyte limitations (i.e., regardless whether the electrolyte is symmetric or asymmetric). However, due to the lack of the ion steric effect, the PNP model can only be applied in circumstances where low electric potentials or low-concentration electrolytes are used. In contrast, the ion steric effect is accounted for in the GMPNP model, making the GMPNP model applicable at even more extreme electric potentials or in highly concentration electrolytes. Similarly, the MPB model also considers the steric effect of the ions distributed in EDL, therefore, the MPB model is also suitable for describing EDL at higher electric potentials or in concentrated electrolytes. The difference from the PNP and GMPNP models is that the MPB model only works for the EDL with symmetric electrolyte (such as KHCO₃ and KOH) and at equilibrium state. Among these models, MPB is the most applicable model when studying the potential and E-field distribution for a nanostructured electrode used for CO₂RR electrolysis since the symmetric electrolytes such as KHCO₃ and KOH are commonly used in CO₂RR and the electrochemical performances of an electrode at equilibrium state is of the main interest. However, in the literature, the

EDL model is often not incorporated in these simulations. Consequently, large hotspots of the E-field on the electrode surface are observed in some of the simulation examples shown in Figure 5.1, which is due to the lack of the electrolyte screening effects as demonstrated in Figure 5.11a and 5.11e. Once the EDL model is considered in the simulations of Figure 5.11f, 5.11g and 5.20d using MPB model, the E-field is screened within a narrow area adjacent to the electrode surface. Furthermore, Bohra et al. applied the GMPNP model to simulate the EDL, which resulted in accurate profiles of the potential and E-field at the electrode surface, however, this model is only limited to 1D simulation due to its mathematical complexity and numerical instability. In this chapter, I demonstrated that in order to model EDL for a 2D or 3D nanostructure, the MPB model is the best available option, as it accurately describes the potential and E-field distributions at the nanostructured electrodes with complex morphology (Figure 5.11 and 5.20).

5.9.2 $J_{electrolyte}$ simulations

In section 5.5, I summarized four classes of the $J_{electrolyte}$ simulations: primary current density (J_{Pri}), secondary current density (J_{Sec}), tertiary current density (J_{Ter}), and J_{Sec} combined with mass transport effect (J_{Sec+M}). Each model has its own applicability scope in the $J_{electrolyte}$ simulations, depending on the essential effects considered (Table 5.2). For instance, J_{Pri} simulations are valid to use in electrochemical systems with fast electrolysis reactions and the absence of mass transport limitations, as the activation overpotentials, mass transport and electrolyte composition variation can be ignored in this case. When modelling electrochemical reactions with slow kinetics in which the activation overpotential cannot be ignored while the mass transport limitations and electrolyte composition variation are negligible, J_{Sec} is suitable. When electrochemical reactions proceed with slow kinetics in electrolytes with limited mass transfer, J_{Ter} is appropriate for their modelling, as activation overpotentials, mass transport and electrolyte composition variation are considered in this type of simulations. Lastly, J_{Sec+M} is very similar to J_{Ter} except that the electrolyte composition variation effect is not accounted for in J_{Sec+M} . Typically, inert electrolytes are commonly used in CO₂RR and their composition variation can be ignored. Furthermore, considering a higher numerical efficiency compared to J_{Ter} , J_{Sec+M} is the best option for simulating the 3D spatial distribution of $J_{electrolyte}$ of nanostructured electrodes with complex morphology.

In the $J_{electrolyte}$ simulations, the electrode kinetics is a crucial factor for accurately describing the current density because they determine the electron transfer rate between electrode and reactants. For

accurate $J_{electrolyte}$ results and efficient computation, an appropriate electrode kinetics model should be selected according to the reaction conditions. To this end, in section 5.3.2, I discussed various electrode kinetic models: generalized Butler-Volmer (G. B-V), standard Butler-Volmer (S. B-V), linearized Butler-Volmer (L. B-V) and Tafel equation and highlighted their application scopes. Among these, G. B-V model is the most general form, which can be applied for the cases with and without mass transport limitation under a wide range of overpotentials. However, G. B-V model is computationally heavy due to its complex mathematical formula (equation (2.40)), which can be simplified to different forms under certain conditions to reduce the demand for computational resources. When the surface concentrations of the reactants do not vary significantly from the bulk values, G. B-V model can be simplified to S. B-V model (equation (2.41)), in which the mass transport effect is ignored. Furthermore, when a small overpotential is applied in an electrochemical reaction where the absence of reactant concentration variation is still valid, S. B-V model can be further simplified to L. B-V model (equation (2.42)), in which $J_{electrolyte}$ is assumed to be linearly changing with the overpotential. When a large overpotential is applied, S. B-V model can be simplified to Tafel equation (equation (2.43)), in which the contribution of the backward reaction to current is negligible due to the fact that the reaction rate of the forward reaction is much larger than that of the backward reaction under a large overpotential. If the electrode kinetics model is not selected correctly for a reaction, the resulting $J_{electrolyte}$ varies in a wide range even under similar operation conditions as shown in Figure 5.2 (10^{-9} A/cm² to 10^5 A/cm²). The inconsistency of results is associated with inappropriate electrode kinetics model leading to underestimation or overestimation of the $J_{electrolyte}$ response to the applied overpotentials in a given reaction.

In Table 5.2, I summarize the essential effects accounted for in different classes of the $J_{electrolyte}$ simulations: J_{pri} , J_{sec} , J_{Ter} and J_{Sec} , and their impacts on $J_{electrolyte}$. In Figure 5.15 and 5.16, I compare different options of the electrode kinetics models in the $J_{electrolyte}$ simulations under different conditions as well as their influences on $J_{electrolyte}$. The selection of the class of the $J_{electrolyte}$ and the electrode kinetic models has significant impact on the obtained $J_{electrolyte}$ profile. To obtain reliable $J_{electrolyte}$ results, one should carefully select the electrode kinetics model and the type of $J_{electrolyte}$ according to the operation conditions of the electrochemical cell under study.

5.9.3 $J_{electrode}$ simulations

The current crowding in the metal can cause the structural transformation of electrocatalysts as described by the EM theory. Studying the electron flow in electrocatalysts with complex nanomorphology allows us to evaluate whether there are any current crowding areas that may lead to structural instability in these electrocatalysts. The profile of the electron flow within the electrocatalysts can be described by the $J_{electrode}$ simulations. In contrast to the E-field and $J_{electrolyte}$ simulations, $J_{electrode}$ is comparatively easier to solve since it follows the Ohm's law and changes linearly with the applied potential in a metal. Despite the simplicity of the model, it is applicable for evaluating the $J_{electrode}$ distribution in the electrodes with a specific nanoscale morphology and predicting the intensity and locations of the possible current crowding. By avoiding or taking the advantage of the current crowding, the data obtained from the $J_{electrode}$ simulations can be used to improve stability of electrocatalysts by adjusting their structural geometry or to devise systems capable of *in situ* activation via geometric restructuring.

5.9.4 Other considerations

The theoretical models introduced in this chapter capture some of the essential features of the electrode-electrolyte system, providing an essential reference framework for the studies of E-field, $J_{electrolyte}$, and $J_{electrode}$ spatial distributions in the context of electrocatalysis. However, this theoretical framework is established based on the electrostatic continuum theories without considering the quantum effects, which limits their quantitative accuracy.^{103,104,146} In this subsection, I summarize some important effects observed experimentally or theoretically in electrolysis studies that are not considered in the theoretical models introduced in this chapter: the chemical interaction of the electrolyte cations with the electrode surface and reaction intermediates,¹³ the influence of the interfacial E-field on the neutral species with high dipole moment¹⁶⁴ and, finally, the quantitative description of the electromigration induced by the current crowding.¹⁶⁵

Cations in the electrolyte solution are not only electrostatically attracted to the cathode, but can also chemically interact with the electrode and the reaction intermediates. The chemical interactions can greatly affect the reaction profile of the electrocatalysis. For example, Liu et al. established that adsorbed K^+ lowers the thermodynamic barriers for the reduction of CO_2 to CO on the Au electrode due to the interaction between K^+ and the reaction intermediates of CO_2RR .¹³ Stoffelsma et al. demonstrated that oxidation of CO can be promoted by Li^+ , which is ascribed to the stabilization of

*OH on Pd induced by Li⁺.¹⁶⁶ Furthermore, the electronic structure of the electrode surface can be altered when cations directly interact with the electrode surface, which can also affect the electron transfers between the electrode and reactants.

The interfacial E-field does not only affect the distribution of the cations and reactants, but also the adsorption free energies of the uncharged reaction intermediates with high dipole moments and polarizability, which in turn affects the activation barriers for the reaction steps involving such reaction intermediates.¹⁶⁴ Specifically, Chen et al. found that the adsorption free energies of *CO₂ and *COOH intermediates can be enhanced by 1 eV under E-field of -1 V/Å compared to those without applied E-field during CO₂RR catalysis.¹⁶⁷ The impact of E-field on the adsorption free energy is associated with the large dipole moment and polarizability of *CO₂ (0.96 Å and 0.76 e Å/V, respectively), which leads to its stabilization induced by the electrostatic interactions between *CO₂ and E-field. Furthermore, in the theoretical models covered in this chapter, E-field is assumed to have a homogeneous distribution in the planes parallel to the electrode surface. However, Frumkin suggested that potential gradients in the planes parallel to the electrode surface should be considered due to the discrete nature of the ionic charge.¹⁶⁸ Frumkin's hypothesis was validated by the study of Chen et al., which reveals a heterogeneous distribution of E-field at the planes parallel to the electrode surface in the presence of K⁺ and *CO₂ using DFT calculations.¹⁶⁷ These examples underscore the importance of accounting for heterogeneous E-field distributions in the presence of the cations while the E-field distribution can be assumed to be homogeneous in the areas without cations.

As discussed in section 5.6, current crowding within the catalyst morphology can lead to its structural transformations in electrocatalysts with complex nanoscale geometries via EM. The EM-induced atomic diffusion is driven by the momentum transfer between the electrons and metal ions comprising the electrocatalyst, with the locality and directionality of the EM-induced atomic diffusion resulting in the directional structural changes in the nanostructured geometries of electrocatalysts.¹⁵⁷ These directional effects are strongly correlated with the profile of the current carrier flow, which can be obtained from the $J_{electrode}$ simulations. Furthermore, there are many non-directional EM-induced phenomena that cannot be described by the basic $J_{electrode}$ simulations discussed in this chapter, as they require considering the compositional variation of the material on the atomic and nanoscale. Examples of these phenomena include EM due to supersaturation of alloys,¹⁶⁹ electrorecrystallization,¹⁷⁰ grain rotation,¹⁷¹ dislocation generation¹⁷²⁻¹⁷⁵. These non-directional EM-induced mass transport in electrocatalysts can have significant impacts on the structural stability of

nanostructured electrodes. The accurate description of these phenomena requires advanced theories that can incorporate *ab initio* modelling, continuum-level electromigration modelling and statistical compact modelling. In micro- or nanoscale solid-state electronics, theoretical methods have been developed to some extent for describing the mass transport induced by EM. For example, Lin et al. demonstrated the formation of hillocks and voids induced by EM on Cu materials using a combination of X-ray diffractometry, DFT and FEM methods.¹⁷⁶ Ceric et al. proposed a method for achieving realistic simulations of EM behavior by combining the *ab initio* method with continuum-level electromigration model and the kinetic Monte Carlo model via effective valence.¹⁶⁵ However, EM-induced mass transport in electrocatalysts, a key parameter affecting the structural stability of electrocatalysts, has not been investigated. Only recently have I reported for the first time the extent and rate of EM in metal electrocatalysts determined by the shape and material of the nanostructures under bias conditions using DFT and FEM calculations.⁷¹ While DFT calculations were performed in our work, the DFT was not integrated with describing and characterizing EM processes. To build more predictive computational tools for assessing EM in electrocatalysts, future work in this domain will be on integration of atomic-scale (e.g. DFT), continuum-level (e.g. FEM) and statistical compact (e.g. Monte Carlo) simulations for quantitatively describing the influence of EM on the structures of the electrocatalysts during the electrolysis conditions.

5.10 Summary

In this chapter, I summarized the state-of-the-art theoretical models for simulating the E-field, $J_{electrolyte}$ and $J_{electrode}$ of a nanoscale electrode under electrolysis conditions, established the protocols of these electrochemical physics effect simulations. More importantly, I demonstrated the current-density profiles in nanoparticle-based cathodes with complex nanoscale morphologies influence directional metal mass transfer and enable specific structural transformations in these materials by applying these theoretical models for studying the real electrochemical systems.

Specifically, for E-field simulations, I illustrated the significant screening effect of the EDL on the E-field distribution, which can be further enhanced by adopting the field-dependent dielectric function of the electrolyte in the simulations. Moreover, for $J_{electrolyte}$ simulations, I discussed the effect of electrode kinetics, mass transport and electrolyte composition variation on the $J_{electrolyte}$ distribution and magnitude by comparing different classes of $J_{electrolyte}$ simulations and electrode kinetic models. In particular, the electrode kinetics and mass transport play an important role in describing the effect of electron transfer and reactant transport on the rate of the CO₂RR, respectively, while the electrolyte composition variation can be ignored since inert electrolytes are typically used in this case, and therefore their composition does not vary. Furthermore, for $J_{electrode}$ simulations, I introduced the approach of describing the current density in nanostructured electrodes and demonstrated that current crowding can occur at the narrow constrictions in the nanostructures when electrons pass through these constrictions to supply the surfaces with electrons for the electrolysis reactions.

In addition, I applied the current density simulations ($J_{electrolyte}$ and $J_{electrode}$) for various real electrochemical nanoparticles with complex morphologies, demonstrating that these current-density profiles are geometry-dependent and thus can be modified by the nanoparticle shape design. Generally, in shaped cathodic electrocatalysts, nanoscale curvatures facing the anode form hotspots for electrolysis, which can also promote surface reconstruction by ARIAM. At the same time, geometric constrictions in the cathodic nanostructures lead to current-crowding hotspots in the metal that lead to EM. Structural transformations to minimize the hotspots of both types can occur as long as the surface metal atoms can break the bonds with their neighbours and overcome the energy barrier for surface migration. Finally, I discussed the limitations of the theoretical models discussed in this chapter, highlighting the importance of developing advanced multiscale modelling approaches that integrate atomic-scale (e.g. DFT), continuum-level (e.g. FEM) and statistical compact (e.g. Monte Carlo) simulations in quantitatively simulating the electrochemical physics effects of the nanoelectrocatalysts.

The work introduced in this chapter would navigate electrochemists to conduct appropriate the electrochemical physics effects simulations for analyzing activity and stability of the nanoelectrocatalysts, contributing to a wider adoption of FEM simulations in rational design of advanced electrocatalysts.

Chapter 6

Conclusions and future work

The work presented in this thesis focused on the structural dynamics of complex nanostructured electrodes and the factors affecting their structural transformations under CO₂RR or HER electrolysis conditions, as well as the multiscale simulation approaches of evaluating their structural stability. First, by experimentally exploring structural changes in shape-defined nanoparticle electrocatalysts, this thesis demonstrated that the conditions of electrolysis, the nature of the electrocatalyst material and the current density distribution are the important factors determining the extent of and trends in structural transformation of electrocatalysts under electrolysis conditions. The mechanistic descriptions of the impact of the factors mentioned above on the structural transformation were established using DFT and FEM simulations. Chapter 3 showed the experimental observations of the structural transformations in Cu(II)-derived copper electrodes during the oxidation state changes, and well-defined Au and Pd branched and core-cage nanoparticles without oxidation state changes, and demonstrates the influences of the nature of the environment, nanostructure material and electrolysis reactions on the structural transformations in the electrocatalysts. Chapter 4 explored the impact of the reaction intermediates on the atomic mobility of the metals, including Cu, Ag, Au, Pd, and Cu₃Pd, at atomic scale using DFT and MD simulations, and illustrates that the RIs could accelerate the atomic mobility by lowering the vacancy formation energy and migration energy barrier of metal atoms on the surfaces. Chapter 5 proposed the protocols for reliable simulations of the E-field, $J_{electrolyte}$, $J_{electrode}$, and explored the current density behavior in various real electrochemical nanostructures with complex morphologies, including anchored nanostar, nanostar, core-cages and frames, demonstrating that the current-crowding hotspots at the constricted areas in the metal could lead to the structural transformation in the electrocatalyst via EM.

This thesis explored the influence of nanostructured metallic electrocatalysts' shape and composition on their structural stability. To better understand the intrinsic trends, more shapes and compositions of the electrocatalysts have to be explored, which is especially important for the bimetallic electrocatalysts considering their structural complexity compared to single metals. In literature, various bimetallic electrocatalysts, e.g., CuPt, CuAu, CuSn, AuPt, AuFe, have been synthesized, with either mixed alloy or phase-segregate. Furthermore, these bimetallic electrocatalysts also have very complex nanoscale morphologies, e.g., nanocube, hollow, or double-shelled structures, which combined with various possibilities of compositions and phase-segregation make it very challenging to reveal structure-

stability relationship for the bimetallic electrocatalysts. To quantitatively assessing the influence of the shape of the bimetallic electrocatalysts on their structural stability, future work in this domain will be on integration of atomic-scale (e.g., DFT), continuum-level (e.g., FEM) and statistical compact (e.g., Monte Carlo) simulations for quantitatively describing the influence of EM on the structures of the bimetallic electrocatalysts during the electrolysis conditions. In addition to the shapes, the structural stability of the bimetallic electrocatalysts with more compositions and phases also need to be investigated using DFT and MD simulation, which combined with the advanced EM simulations would contribute to a more comprehensive understanding on the structure-stability relationship of the bimetallic electrocatalysts.

Furthermore, this thesis proposed how to predict the influence of the RIs and nanostructure materials on the atomic mobility of the metals by calculating their energy profiles of the VF and atom migration. However, to have a deeper understanding on the influence of above-mentioned parameters on the atomic mobility, a general model of linking the electronic structures of the transition metal catalysts with their structural stability under the electrolysis conditions is required. In Chapter 4, the DFT calculations showed Pd with higher stability than Au, Ag and Cu, with the later three metal sharing similar stability, which can be ascribed to the more valence electrons of Pd than that of Au, Ag and Cu, suggesting a crucial role of the valence electron of the metals in determining their atomic mobility. More future work will be on developing valence-electron based descriptor for evaluating the atomic mobility of metal-based electrocatalysts.

In addition to the RIs, current density distribution and nanostructure materials mentioned above, there are other factors that may affect the structural dynamics in the electrocatalysts under electrolysis conditions. One of the important factors is the electrolytes, which have shown significant influences on the selectivity and activity of the electrocatalysts during CO₂RR by affecting the adsorption of CO₂ and the interfacial E-field distributions. However, the influence of the electrolytes used for CO₂RR on the structural stability of the electrocatalysts has not been explored yet. The electrolyte ions distribute very close to the electrode surfaces, with both chemical and physical interactions with electrocatalysts in the course of CO₂RR electrolysis. Therefore, the nature and concentration of the electrolyte could affect the interactions of the electrolyte ions with electrocatalysts, and further impact the structural dynamics of the electrocatalyst. In order to have a comprehensive understanding in the mechanisms of the structural dynamics in electrocatalysts, the influence of the electrolyte on the structural behavior of electrocatalysts have to be explored.

Letters of Copyright Permission

3/4/22, 11:38 PM

Rightslink® by Copyright Clearance Center



- Home
- Help ▾
- Email Support
- Sign In
- Create Account

SPRINGER NATURE

Interplay of electrochemical and electrical effects induces structural transformations in electrocatalysts

Author: Feng Li et al
Publication: Nature Catalysis
Publisher: Springer Nature
Date: Jun 3, 2021

Copyright © 2021, The Author(s), under exclusive licence to Springer Nature Limited

Author Request

If you are the author of this content (or his/her designated agent) please read the following. If you are not the author of this content, please click the Back button and select no to the question "Are you the Author of this Springer Nature content?".

Ownership of copyright in original research articles remains with the Author, and provided that, when reproducing the contribution or extracts from it or from the Supplementary Information, the Author acknowledges first and reference publication in the Journal, the Author retains the following non-exclusive rights:

To reproduce the contribution in whole or in part in any printed volume (book or thesis) of which they are the author(s).

The author and any academic institution, where they work, at the time may reproduce the contribution for the purpose of course teaching.

To reuse figures or tables created by the Author and contained in the Contribution in oral presentations and other works created by them.

To post a copy of the contribution as accepted for publication after peer review (in locked Word processing file, of a PDF version thereof) on the Author's own web site, or the Author's institutional repository, or the Author's funding body's archive, six months after publication of the printed or online edition of the Journal, provided that they also link to the contribution on the publisher's website.

Authors wishing to use the published version of their article for promotional use or on a web site must request in the normal way.

If you require further assistance please read Springer Nature's online [author reuse guidelines](#).

For full paper portion: Authors of original research papers published by Springer Nature are encouraged to submit the author's version of the accepted, peer-reviewed manuscript to their relevant funding body's archive, for release six months after publication. In addition, authors are encouraged to archive their version of the manuscript in their institution's repositories (as well as their personal Web sites), also six months after original publication.

v1.0

BACK

CLOSE WINDOW



Combining theory and experiment in electrocatalysis: Insights into materials design

Author: Zhi Wei Seh, Jakob Kibsgaard, Colin F. Dickens, Ib Chorkendorff, et al.

Publication: Science

Publisher: The American Association for the Advancement of Science

Date: Jan 13, 2017

Copyright © 2017, The American Association for the Advancement of Science

Permissions Request

AAAS may not control the rights to the image you wish to use. Please submit your request directly to the publisher by following the guidelines at <https://www.science.org/content/page/reprints-and-permissions>. Please allow 10 to 15 days to receive a response.

BACK

CLOSE WINDOW

SPRINGER NATURE LICENSE TERMS AND CONDITIONS

Aug 02, 2022

This Agreement between Feng Li ("You") and Springer Nature ("Springer Nature") consists of your license details and the terms and conditions provided by Springer Nature and Copyright Clearance Center.

License Number	5361081423438
License date	Aug 02, 2022
Licensed Content Publisher	Springer Nature
Licensed Content Publication	Nature Energy
Licensed Content Title	Co-electrolysis of CO ₂ and glycerol as a pathway to carbon chemicals with improved technoeconomics due to low electricity consumption
Licensed Content Author	Sumit Verma et al
Licensed Content Date	Apr 22, 2019
Type of Use	Thesis/Dissertation
Requestor type	academic/university or research institute
Format	print and electronic
Portion	figures/tables/illustrations
Number of figures/tables/illustrations	1
High-res required	no
Will you be translating?	no
Circulation/distribution	50000 or greater
Author of this Springer Nature content	no
Title	Multiscale Modelling of Structural Transformation in Metal Nanocatalysts for CO ₂ Electroreduction
Institution name	University of Waterloo
Expected presentation date	Aug 2022
Portions	Figure 1

SPRINGER NATURE LICENSE TERMS AND CONDITIONS

Aug 02, 2022

This Agreement between Feng Li ("You") and Springer Nature ("Springer Nature") consists of your license details and the terms and conditions provided by Springer Nature and Copyright Clearance Center.

License Number	5361090090996
License date	Aug 02, 2022
Licensed Content Publisher	Springer Nature
Licensed Content Publication	Nature Catalysis
Licensed Content Title	Designing materials for electrochemical carbon dioxide recycling
Licensed Content Author	Michael B. Ross et al
Licensed Content Date	Jul 1, 2019
Type of Use	Thesis/Dissertation
Requestor type	academic/university or research institute
Format	print and electronic
Portion	figures/tables/illustrations
Number of figures/tables/illustrations	1
High-res required	no
Will you be translating?	no
Circulation/distribution	50000 or greater
Author of this Springer Nature content	no
Title	Multiscale Modelling of Structural Transformation in Metal Nanocatalysts for CO2 Electroreduction
Institution name	University of Waterloo
Expected presentation date	Aug 2022
Portions	Figure 6

SPRINGER NATURE LICENSE TERMS AND CONDITIONS

Aug 02, 2022

This Agreement between Feng Li ("You") and Springer Nature ("Springer Nature") consists of your license details and the terms and conditions provided by Springer Nature and Copyright Clearance Center.

License Number	5361090336726
License date	Aug 02, 2022
Licensed Content Publisher	Springer Nature
Licensed Content Publication	Nature Catalysis
Licensed Content Title	Catalyst electro-redeposition controls morphology and oxidation state for selective carbon dioxide reduction
Licensed Content Author	Phil De Luna et al
Licensed Content Date	Jan 15, 2018
Type of Use	Thesis/Dissertation
Requestor type	academic/university or research institute
Format	print and electronic
Portion	figures/tables/illustrations
Number of figures/tables/illustrations	1
High-res required	no
Will you be translating?	no
Circulation/distribution	50000 or greater
Author of this Springer Nature content	no
Title	Multiscale Modelling of Structural Transformation in Metal Nanocatalysts for CO2 Electroreduction
Institution name	University of Waterloo
Expected presentation date	Aug 2022
Portions	Figure 2



RightsLink

?
Help ▾

✉
Email Support

Potential-induced nanoclustering of metallic catalysts during electrochemical CO2 reduction

SPRINGER NATURE

Author: Jianfeng Huang et al

Publication: Nature Communications

Publisher: Springer Nature

Date: Aug 6, 2018

Copyright © 2018, The Author(s)

Creative Commons

This is an open access article distributed under the terms of the [Creative Commons CC BY](#) license, which permits unrestricted use, distribution, and reproduction in any medium, provided the original work is properly cited.

You are not required to obtain permission to reuse this article.

To request permission for a type of use not listed, please contact [Springer Nature](#)



?
Help ▾

✉
Email Support

SPRINGER NATURE

Phase and structure engineering of copper tin heterostructures for efficient electrochemical carbon dioxide reduction

Author: Pengtang Wang et al
Publication: Nature Communications
Publisher: Springer Nature
Date: Nov 22, 2018

Copyright © 2018, The Author(s)

Creative Commons

This is an open access article distributed under the terms of the [Creative Commons CC BY](#) license, which permits unrestricted use, distribution, and reproduction in any medium, provided the original work is properly cited.

You are not required to obtain permission to reuse this article.
To request permission for a type of use not listed, please contact [Springer Nature](#)



Concave Rhombic Dodecahedral Au Nanocatalyst with Multiple High-Index Facets for CO₂ Reduction

Author: Hye-Eun Lee, Ki Dong Yang, Sang Moon Yoon, et al

Publication: ACS Nano

Publisher: American Chemical Society

Date: Aug 1, 2015

Copyright © 2015, American Chemical Society

PERMISSION/LICENSE IS GRANTED FOR YOUR ORDER AT NO CHARGE

This type of permission/license, instead of the standard Terms and Conditions, is sent to you because no fee is being charged for your order. Please note the following:

- Permission is granted for your request in both print and electronic formats, and translations.
- If figures and/or tables were requested, they may be adapted or used in part.
- Please print this page for your records and send a copy of it to your publisher/graduate school.
- Appropriate credit for the requested material should be given as follows: "Reprinted (adapted) with permission from {COMPLETE REFERENCE CITATION}. Copyright {YEAR} American Chemical Society." Insert appropriate information in place of the capitalized words.
- One-time permission is granted only for the use specified in your RightsLink request. No additional uses are granted (such as derivative works or other editions). For any uses, please submit a new request.

If credit is given to another source for the material you requested from RightsLink, permission must be obtained from that source.

[BACK](#)

[CLOSE WINDOW](#)



?
Help ▾

✉
Email Support

SPRINGER NATURE

Electrochemical Reduction of CO₂ on Hollow Cubic Cu₂O@Au Nanocomposites

Author: Wei Tan et al

Publication: Nanoscale Research Letters

Publisher: Springer Nature

Date: Feb 21, 2019

Copyright © 2019, The Author(s).

Creative Commons

This is an open access article distributed under the terms of the [Creative Commons CC BY](#) license, which permits unrestricted use, distribution, and reproduction in any medium, provided the original work is properly cited.

You are not required to obtain permission to reuse this article.

To request permission for a type of use not listed, please contact [Springer Nature](#)



Hollow Porous Ag Spherical Catalysts for Highly Efficient and Selective Electrocatalytic Reduction of CO₂ to CO

Author: Shao-Qing Liu, Shu-Wen Wu, Min-Rui Gao, et al

Publication: ACS Sustainable Chemistry & Engineering

Publisher: American Chemical Society

Date: Sep 1, 2019

Copyright © 2019, American Chemical Society

PERMISSION/LICENSE IS GRANTED FOR YOUR ORDER AT NO CHARGE

This type of permission/license, instead of the standard Terms and Conditions, is sent to you because no fee is being charged for your order. Please note the following:

- Permission is granted for your request in both print and electronic formats, and translations.
- If figures and/or tables were requested, they may be adapted or used in part.
- Please print this page for your records and send a copy of it to your publisher/graduate school.
- Appropriate credit for the requested material should be given as follows: "Reprinted (adapted) with permission from {COMPLETE REFERENCE CITATION}. Copyright {YEAR} American Chemical Society." Insert appropriate information in place of the capitalized words.
- One-time permission is granted only for the use specified in your RightsLink request. No additional uses are granted (such as derivative works or other editions). For any uses, please submit a new request.

If credit is given to another source for the material you requested from RightsLink, permission must be obtained from that source.

[BACK](#)

[CLOSE WINDOW](#)



Home



Help ▾



Email Support



Feng Li ▾



Most Trusted. Most Cited. Most Read.

Solvothermal Synthesis of Monodisperse PtCu Dodecahedral Nanoframes with Enhanced Catalytic Activity and Durability for Hydrogen Evolution Reaction

Author: Xiao-Fang Zhang, Ai-Jun Wang, Lu Zhang, et al

Publication: ACS Applied Energy Materials

Publisher: American Chemical Society

Date: Sep 1, 2018

Copyright © 2018, American Chemical Society

PERMISSION/LICENSE IS GRANTED FOR YOUR ORDER AT NO CHARGE

This type of permission/license, instead of the standard Terms and Conditions, is sent to you because no fee is being charged for your order. Please note the following:

- Permission is granted for your request in both print and electronic formats, and translations.
- If figures and/or tables were requested, they may be adapted or used in part.
- Please print this page for your records and send a copy of it to your publisher/graduate school.
- Appropriate credit for the requested material should be given as follows: "Reprinted (adapted) with permission from {COMPLETE REFERENCE CITATION}. Copyright {YEAR} American Chemical Society." Insert appropriate information in place of the capitalized words.
- One-time permission is granted only for the use specified in your RightsLink request. No additional uses are granted (such as derivative works or other editions). For any uses, please submit a new request.

If credit is given to another source for the material you requested from RightsLink, permission must be obtained from that source.

[BACK](#)[CLOSE WINDOW](#)



Mesoporous Hollow Cu-Ni Alloy Nanocage from Core-Shell Cu@Ni Nanocube for Efficient Hydrogen Evolution Reaction

Author: Zhenxing Li, Chengcheng Yu, Yangyang Wen, et al

Publication: ACS Catalysis

Publisher: American Chemical Society

Date: Jun 1, 2019

Copyright © 2019, American Chemical Society

PERMISSION/LICENSE IS GRANTED FOR YOUR ORDER AT NO CHARGE

This type of permission/license, instead of the standard Terms and Conditions, is sent to you because no fee is being charged for your order. Please note the following:

- Permission is granted for your request in both print and electronic formats, and translations.
- If figures and/or tables were requested, they may be adapted or used in part.
- Please print this page for your records and send a copy of it to your publisher/graduate school.
- Appropriate credit for the requested material should be given as follows: "Reprinted (adapted) with permission from {COMPLETE REFERENCE CITATION}. Copyright {YEAR} American Chemical Society." Insert appropriate information in place of the capitalized words.
- One-time permission is granted only for the use specified in your RightsLink request. No additional uses are granted (such as derivative works or other editions). For any uses, please submit a new request.

If credit is given to another source for the material you requested from RightsLink, permission must be obtained from that source.

[BACK](#)

[CLOSE WINDOW](#)



Home



Help ▾



Email Support



Feng Li ▾



Enhanced the Hydrogen Evolution Performance by Ruthenium Nanoparticles Doped into Cobalt Phosphide Nanocages

Author: Chong-Dian Si, Ze-Xing Wu, Jing Wang, et al

Publication: ACS Sustainable Chemistry & Engineering

Publisher: American Chemical Society

Date: Jun 1, 2019

Copyright © 2019, American Chemical Society

PERMISSION/LICENSE IS GRANTED FOR YOUR ORDER AT NO CHARGE

This type of permission/license, instead of the standard Terms and Conditions, is sent to you because no fee is being charged for your order. Please note the following:

- Permission is granted for your request in both print and electronic formats, and translations.
- If figures and/or tables were requested, they may be adapted or used in part.
- Please print this page for your records and send a copy of it to your publisher/graduate school.
- Appropriate credit for the requested material should be given as follows: "Reprinted (adapted) with permission from {COMPLETE REFERENCE CITATION}. Copyright {YEAR} American Chemical Society." Insert appropriate information in place of the capitalized words.
- One-time permission is granted only for the use specified in your RightsLink request. No additional uses are granted (such as derivative works or other editions). For any uses, please submit a new request.

If credit is given to another source for the material you requested from RightsLink, permission must be obtained from that source.

[BACK](#)[CLOSE WINDOW](#)



Mesoporous Nanostructured CoFe–Se–P Composite Derived from a Prussian Blue Analogue as a Superior Electrocatalyst for Efficient Overall Water Splitting

Author: Linghao He, Bingbing Cui, Bin Hu, et al

Publication: ACS Applied Energy Materials

Publisher: American Chemical Society

Date: Aug 1, 2018

Copyright © 2018, American Chemical Society

PERMISSION/LICENSE IS GRANTED FOR YOUR ORDER AT NO CHARGE

This type of permission/license, instead of the standard Terms and Conditions, is sent to you because no fee is being charged for your order. Please note the following:

- Permission is granted for your request in both print and electronic formats, and translations.
- If figures and/or tables were requested, they may be adapted or used in part.
- Please print this page for your records and send a copy of it to your publisher/graduate school.
- Appropriate credit for the requested material should be given as follows: "Reprinted (adapted) with permission from {COMPLETE REFERENCE CITATION}. Copyright {YEAR} American Chemical Society." Insert appropriate information in place of the capitalized words.
- One-time permission is granted only for the use specified in your RightsLink request. No additional uses are granted (such as derivative works or other editions). For any uses, please submit a new request.

If credit is given to another source for the material you requested from RightsLink, permission must be obtained from that source.

[BACK](#)

[CLOSE WINDOW](#)



Home



Help ▾



Email Support



Feng Li ▾



Hexagonal-Phase Cobalt Monophosphosulfide for Highly Efficient Overall Water Splitting

Author: Zhengfei Dai, Hongbo Geng, Jiong Wang, et al

Publication: ACS Nano

Publisher: American Chemical Society

Date: Nov 1, 2017

Copyright © 2017, American Chemical Society

PERMISSION/LICENSE IS GRANTED FOR YOUR ORDER AT NO CHARGE

This type of permission/license, instead of the standard Terms and Conditions, is sent to you because no fee is being charged for your order. Please note the following:

- Permission is granted for your request in both print and electronic formats, and translations.
- If figures and/or tables were requested, they may be adapted or used in part.
- Please print this page for your records and send a copy of it to your publisher/graduate school.
- Appropriate credit for the requested material should be given as follows: "Reprinted (adapted) with permission from {COMPLETE REFERENCE CITATION}. Copyright {YEAR} American Chemical Society." Insert appropriate information in place of the capitalized words.
- One-time permission is granted only for the use specified in your RightsLink request. No additional uses are granted (such as derivative works or other editions). For any uses, please submit a new request.

If credit is given to another source for the material you requested from RightsLink, permission must be obtained from that source.

[BACK](#)[CLOSE WINDOW](#)



Nickel Cobalt Sulfide Double-Shelled Hollow Nanospheres as Superior Bifunctional Electrocatalysts for Photovoltaics and Alkaline Hydrogen Evolution

Author: Yiqing Jiang, Xing Qian, Changli Zhu, et al

Publication: Applied Materials

Publisher: American Chemical Society

Date: Mar 1, 2018

Copyright © 2018, American Chemical Society

PERMISSION/LICENSE IS GRANTED FOR YOUR ORDER AT NO CHARGE

This type of permission/license, instead of the standard Terms and Conditions, is sent to you because no fee is being charged for your order. Please note the following:

- Permission is granted for your request in both print and electronic formats, and translations.
- If figures and/or tables were requested, they may be adapted or used in part.
- Please print this page for your records and send a copy of it to your publisher/graduate school.
- Appropriate credit for the requested material should be given as follows: "Reprinted (adapted) with permission from {COMPLETE REFERENCE CITATION}. Copyright {YEAR} American Chemical Society." Insert appropriate information in place of the capitalized words.
- One-time permission is granted only for the use specified in your RightsLink request. No additional uses are granted (such as derivative works or other editions). For any uses, please submit a new request.

If credit is given to another source for the material you requested from RightsLink, permission must be obtained from that source.

[BACK](#)

[CLOSE WINDOW](#)



Home



Help ▾



Email Support



Feng Li ▾



Most Trusted. Most Cited. Most Read.

The Role of Oxidation of Silver in Bimetallic Gold-Silver Nanocages on Electrocatalytic Activity of Nitrogen Reduction Reaction

Author: Mohammadreza Nazemi, Mostafa A. El-Sayed

Publication: The Journal of Physical Chemistry C

Publisher: American Chemical Society

Date: May 1, 2019

Copyright © 2019, American Chemical Society

PERMISSION/LICENSE IS GRANTED FOR YOUR ORDER AT NO CHARGE

This type of permission/license, instead of the standard Terms and Conditions, is sent to you because no fee is being charged for your order. Please note the following:

- Permission is granted for your request in both print and electronic formats, and translations.
- If figures and/or tables were requested, they may be adapted or used in part.
- Please print this page for your records and send a copy of it to your publisher/graduate school.
- Appropriate credit for the requested material should be given as follows: "Reprinted (adapted) with permission from {COMPLETE REFERENCE CITATION}. Copyright {YEAR} American Chemical Society." Insert appropriate information in place of the capitalized words.
- One-time permission is granted only for the use specified in your RightsLink request. No additional uses are granted (such as derivative works or other editions). For any uses, please submit a new request.

If credit is given to another source for the material you requested from RightsLink, permission must be obtained from that source.

[BACK](#)[CLOSE WINDOW](#)



Spiny Rhombic Dodecahedral CuPt Nanoframes with Enhanced Catalytic Performance Synthesized from Cu Nanocube Templates

Author: Lian-Ming Lyu, Ya-Chuan Kao, David A. Cullen, et al

Publication: Chemistry of Materials

Publisher: American Chemical Society

Date: Jul 1, 2017

Copyright © 2017, American Chemical Society

PERMISSION/LICENSE IS GRANTED FOR YOUR ORDER AT NO CHARGE

This type of permission/license, instead of the standard Terms and Conditions, is sent to you because no fee is being charged for your order. Please note the following:

- Permission is granted for your request in both print and electronic formats, and translations.
- If figures and/or tables were requested, they may be adapted or used in part.
- Please print this page for your records and send a copy of it to your publisher/graduate school.
- Appropriate credit for the requested material should be given as follows: "Reprinted (adapted) with permission from {COMPLETE REFERENCE CITATION}. Copyright {YEAR} American Chemical Society." Insert appropriate information in place of the capitalized words.
- One-time permission is granted only for the use specified in your RightsLink request. No additional uses are granted (such as derivative works or other editions). For any uses, please submit a new request.

If credit is given to another source for the material you requested from RightsLink, permission must be obtained from that source.

[BACK](#)

[CLOSE WINDOW](#)



Home



Help ▾



Email Support



Feng Li ▾



Nickel-Ion-Oriented Fabrication of Spiny PtCu Alloy Octahedral Nanoframes with Enhanced Electrocatalytic Performance

Author: Guilin Zhu, Jiawei Liu, Shuo Li, et al

Publication: ACS Applied Energy Materials

Publisher: American Chemical Society

Date: Apr 1, 2019

Copyright © 2019, American Chemical Society

PERMISSION/LICENSE IS GRANTED FOR YOUR ORDER AT NO CHARGE

This type of permission/license, instead of the standard Terms and Conditions, is sent to you because no fee is being charged for your order. Please note the following:

- Permission is granted for your request in both print and electronic formats, and translations.
- If figures and/or tables were requested, they may be adapted or used in part.
- Please print this page for your records and send a copy of it to your publisher/graduate school.
- Appropriate credit for the requested material should be given as follows: "Reprinted (adapted) with permission from {COMPLETE REFERENCE CITATION}. Copyright {YEAR} American Chemical Society." Insert appropriate information in place of the capitalized words.
- One-time permission is granted only for the use specified in your RightsLink request. No additional uses are granted (such as derivative works or other editions). For any uses, please submit a new request.

If credit is given to another source for the material you requested from RightsLink, permission must be obtained from that source.

[BACK](#)[CLOSE WINDOW](#)



High-Density Nanosharp Microstructures Enable Efficient CO₂ Electroreduction

Author: Tina Saberi Safaei, Adam Mepham, Xueli Zheng, et al

Publication: Nano Letters

Publisher: American Chemical Society

Date: Nov 1, 2016

Copyright © 2016, American Chemical Society

PERMISSION/LICENSE IS GRANTED FOR YOUR ORDER AT NO CHARGE

This type of permission/license, instead of the standard Terms and Conditions, is sent to you because no fee is being charged for your order. Please note the following:

- Permission is granted for your request in both print and electronic formats, and translations.
- If figures and/or tables were requested, they may be adapted or used in part.
- Please print this page for your records and send a copy of it to your publisher/graduate school.
- Appropriate credit for the requested material should be given as follows: "Reprinted (adapted) with permission from {COMPLETE REFERENCE CITATION}. Copyright {YEAR} American Chemical Society." Insert appropriate information in place of the capitalized words.
- One-time permission is granted only for the use specified in your RightsLink request. No additional uses are granted (such as derivative works or other editions). For any uses, please submit a new request.

If credit is given to another source for the material you requested from RightsLink, permission must be obtained from that source.

[BACK](#)

[CLOSE WINDOW](#)



Home



Help ▾



Email Support



Feng Li ▾

Atomic-Scale Intercalation of Graphene Layers into MoSe₂ Nanoflower Sheets as a Highly Efficient Catalyst for Hydrogen Evolution Reaction

ACS Publications
Most Trusted. Most Cited. Most Read.

Author: Dezhi Xiao, Chao Huang, Yang Luo, et al

Publication: Applied Materials

Publisher: American Chemical Society

Date: Jan 1, 2020

Copyright © 2020, American Chemical Society

PERMISSION/LICENSE IS GRANTED FOR YOUR ORDER AT NO CHARGE

This type of permission/license, instead of the standard Terms and Conditions, is sent to you because no fee is being charged for your order. Please note the following:

- Permission is granted for your request in both print and electronic formats, and translations.
- If figures and/or tables were requested, they may be adapted or used in part.
- Please print this page for your records and send a copy of it to your publisher/graduate school.
- Appropriate credit for the requested material should be given as follows: "Reprinted (adapted) with permission from {COMPLETE REFERENCE CITATION}. Copyright {YEAR} American Chemical Society." Insert appropriate information in place of the capitalized words.
- One-time permission is granted only for the use specified in your RightsLink request. No additional uses are granted (such as derivative works or other editions). For any uses, please submit a new request.

If credit is given to another source for the material you requested from RightsLink, permission must be obtained from that source.

[BACK](#)[CLOSE WINDOW](#)



Fluorine Doped Cagelike Carbon Electrocatalyst: An Insight into the Structure-Enhanced CO Selectivity for CO₂ Reduction at High Overpotential

Author: Wei Ni, Yifei Xue, Xiaogang Zang, et al

Publication: ACS Nano

Publisher: American Chemical Society

Date: Feb 1, 2020

Copyright © 2020, American Chemical Society

PERMISSION/LICENSE IS GRANTED FOR YOUR ORDER AT NO CHARGE

This type of permission/license, instead of the standard Terms and Conditions, is sent to you because no fee is being charged for your order. Please note the following:

- Permission is granted for your request in both print and electronic formats, and translations.
- If figures and/or tables were requested, they may be adapted or used in part.
- Please print this page for your records and send a copy of it to your publisher/graduate school.
- Appropriate credit for the requested material should be given as follows: "Reprinted (adapted) with permission from {COMPLETE REFERENCE CITATION}. Copyright {YEAR} American Chemical Society." Insert appropriate information in place of the capitalized words.
- One-time permission is granted only for the use specified in your RightsLink request. No additional uses are granted (such as derivative works or other editions). For any uses, please submit a new request.

If credit is given to another source for the material you requested from RightsLink, permission must be obtained from that source.

[BACK](#)

[CLOSE WINDOW](#)



Home



Help ▾



Email Support



Feng Li ▾



Most Trusted. Most Cited. Most Read.

Hierarchical Copper with Inherent Hydrophobicity Mitigates Electrode Flooding for High-Rate CO₂ Electroreduction to Multicarbon Products

Author: Zhuang-Zhuang Niu, Fei-Yue Gao, Xiao-Long Zhang, et al

Publication: Journal of the American Chemical Society

Publisher: American Chemical Society

Date: Jun 1, 2021

Copyright © 2021, American Chemical Society

PERMISSION/LICENSE IS GRANTED FOR YOUR ORDER AT NO CHARGE

This type of permission/license, instead of the standard Terms and Conditions, is sent to you because no fee is being charged for your order. Please note the following:

- Permission is granted for your request in both print and electronic formats, and translations.
- If figures and/or tables were requested, they may be adapted or used in part.
- Please print this page for your records and send a copy of it to your publisher/graduate school.
- Appropriate credit for the requested material should be given as follows: "Reprinted (adapted) with permission from {COMPLETE REFERENCE CITATION}. Copyright {YEAR} American Chemical Society." Insert appropriate information in place of the capitalized words.
- One-time permission is granted only for the use specified in your RightsLink request. No additional uses are granted (such as derivative works or other editions). For any uses, please submit a new request.

If credit is given to another source for the material you requested from RightsLink, permission must be obtained from that source.

[BACK](#)[CLOSE WINDOW](#)



Protecting Copper Oxidation State via Intermediate Confinement for Selective CO₂ Electroreduction to C₂ Fuels

Author: Peng-Peng Yang, Xiao-Long Zhang, Fei-Yue Gao, et al

Publication: Journal of the American Chemical Society

Publisher: American Chemical Society

Date: Apr 1, 2020

Copyright © 2020, American Chemical Society

PERMISSION/LICENSE IS GRANTED FOR YOUR ORDER AT NO CHARGE

This type of permission/license, instead of the standard Terms and Conditions, is sent to you because no fee is being charged for your order. Please note the following:

- Permission is granted for your request in both print and electronic formats, and translations.
- If figures and/or tables were requested, they may be adapted or used in part.
- Please print this page for your records and send a copy of it to your publisher/graduate school.
- Appropriate credit for the requested material should be given as follows: "Reprinted (adapted) with permission from {COMPLETE REFERENCE CITATION}. Copyright {YEAR} American Chemical Society." Insert appropriate information in place of the capitalized words.
- One-time permission is granted only for the use specified in your RightsLink request. No additional uses are granted (such as derivative works or other editions). For any uses, please submit a new request.

If credit is given to another source for the material you requested from RightsLink, permission must be obtained from that source.

[BACK](#)

[CLOSE WINDOW](#)



This is a License Agreement between Feng Li ("User") and Copyright Clearance Center, Inc. ("CCC") on behalf of the Rightsholder identified in the order details below. The license consists of the order details, the CCC Terms and Conditions below, and any Rightsholder Terms and Conditions which are included below.

All payments must be made in full to CCC in accordance with the CCC Terms and Conditions below.

Order Date	04-Jun-2022	Type of Use	Republish in a
Order License ID	1228917-1	Publisher	thesis/dissertation
ISSN	2052-1553	Portion	Royal Society of Chemistry Chart/graph/table/figure

LICENSED CONTENT

Publication Title	Inorganic Chemistry Frontiers	Rightsholder	Royal Society of Chemistry
Article Title	Thin-walled hollow Au-Cu nanostructures with high efficiency in electrochemical reduction of CO ₂ to CO	Publication Type	e-Journal
Author/Editor	Beijing da xue,, Zhongguo hua xue hui (Beijing, China),, Royal Society of Chemistry (Great Britain),	Start Page	1524
Date	01/01/2014	End Page	1532
Language	English	Issue	7
Country	United Kingdom of Great Britain and Northern Ireland	Volume	5

REQUEST DETAILS

Portion Type	Chart/graph/table/figure	Distribution	Worldwide
Number of charts / graphs / tables / figures requested	1	Translation	Original language of publication
Format (select all that apply)	Print, Electronic	Copies for the disabled?	No
Who will republish the content?	Academic Institution	Minor editing privileges?	Yes
Duration of Use	Life of current edition	Incidental promotional use?	No
Lifetime Unit Quantity	Up to 750,000	Currency	USD
Rights Requested	Main product		

NEW WORK DETAILS

Title	Multiscale Modelling of Structural Transformation in Metal Nanocatalysts for CO ₂ Electroreduction	Institution name	University of Waterloo
		Expected presentation date	2022-08-01

Instructor name Anna Klinkova

ADDITIONAL DETAILS

Order reference number	N/A	The requesting person / organization to appear on the license	Feng Li
------------------------	-----	---	---------

REUSE CONTENT DETAILS

Title, description or numeric reference of the portion(s)	Scheme 1	Title of the article/chapter the portion is from	Thin-walled hollow Au-Cu nanostructures with high efficiency in electrochemical reduction of CO ₂ to CO
Editor of portion(s)	Zhou, Jun-Hao; Lan, Da-Wei; Yang, Sheng-Song; Guo, Yu; Yuan, Kun; Dai, Lin-Xiu; Zhang, Ya-Wen	Author of portion(s)	Zhou, Jun-Hao; Lan, Da-Wei; Yang, Sheng-Song; Guo, Yu; Yuan, Kun; Dai, Lin-Xiu; Zhang, Ya-Wen
Volume of serial or monograph	5	Issue, if republishing an article from a serial	7
Page or page range of portion	1524-1532	Publication date of portion	2018-01-01

CCC Terms and Conditions

- Description of Service; Defined Terms. This Republication License enables the User to obtain licenses for republication of one or more copyrighted works as described in detail on the relevant Order Confirmation (the "Work(s)"). Copyright Clearance Center, Inc. ("CCC") grants licenses through the Service on behalf of the rightsholder identified on the Order Confirmation (the "Rightsholder"). "Republication", as used herein, generally means the inclusion of a Work, in whole or in part, in a new work or works, also as described on the Order Confirmation. "User", as used herein, means the person or entity making such republication.
- The terms set forth in the relevant Order Confirmation, and any terms set by the Rightsholder with respect to a particular Work, govern the terms of use of Works in connection with the Service. By using the Service, the person transacting for a republication license on behalf of the User represents and warrants that he/she/it (a) has been duly authorized by the User to accept, and hereby does accept, all such terms and conditions on behalf of User, and (b) shall inform User of all such terms and conditions. In the event such person is a "freelancer" or other third party independent of User and CCC, such party shall be deemed jointly a "User" for purposes of these terms and conditions. In any event, User shall be deemed to have accepted and agreed to all such terms and conditions if User republishes the Work in any fashion.
- Scope of License; Limitations and Obligations.
 - All Works and all rights therein, including copyright rights, remain the sole and exclusive property of the Rightsholder. The license created by the exchange of an Order Confirmation (and/or any invoice) and payment by User of the full amount set forth on that document includes only those rights expressly set forth in the Order Confirmation and in these terms and conditions, and conveys no other rights in the Work(s) to User. All rights not expressly granted are hereby reserved.
 - General Payment Terms: You may pay by credit card or through an account with us payable at the end of the month. If you and we agree that you may establish a standing account with CCC, then the following terms apply: Remit Payment to: Copyright Clearance Center, 29118 Network Place, Chicago, IL 60673-1291. Payments Due: Invoices are payable upon their delivery to you (or upon our notice to you that they are

**JOHN WILEY AND SONS LICENSE
TERMS AND CONDITIONS**

Jun 04, 2022

This Agreement between Feng Li ("You") and John Wiley and Sons ("John Wiley and Sons") consists of your license details and the terms and conditions provided by John Wiley and Sons and Copyright Clearance Center.

License Number 5322030444737

License date Jun 04, 2022

Licensed Content
Publisher John Wiley and Sons

Licensed Content
Publication Small

Licensed Content
Title Porous Copper Microspheres for Selective Production of Multicarbon
Fuels via CO₂ Electroreduction

Licensed Content
Author Xi-Wen Du, Cunku Dong, Hui Liu, et al

Licensed Content
Date Aug 25, 2019

Licensed Content
Volume 15

Licensed Content
Issue 42

Licensed Content
Pages 7

6/4/22, 1:23 PM

RightsLink Printable License

Type of use	Dissertation/Thesis
Requestor type	University/Academic
Format	Print and electronic
Portion	Figure/table
Number of figures/tables	1
Will you be translating?	No
Title	Multiscale Modelling of Structural Transformation in Metal Nanocatalysts for CO2 Electroreduction
Institution name	University of Waterloo
Expected presentation date	Aug 2022
Portions	Table 3.1



This is a License Agreement between Feng Li ("User") and Copyright Clearance Center, Inc. ("CCC") on behalf of the Rightsholder identified in the order details below. The license consists of the order details, the CCC Terms and Conditions below, and any Rightsholder Terms and Conditions which are included below.

All payments must be made in full to CCC in accordance with the CCC Terms and Conditions below.

Order Date	04-Jun-2022	Type of Use	Republish in a
Order License ID	1228916-1	Publisher	thesis/dissertation
ISSN	1463-9262	Portion	ROYAL SOC OF CHEM Chart/graph/table/figure

LICENSED CONTENT

Publication Title	Green chemistry	Rightsholder	Royal Society of Chemistry
Article Title	Rethinking Co(CO3)0.5(OH)·0.11H2O: a new property for highly selective electrochemical reduction of carbon dioxide to methanol in aqueous solution	Publication Type	Journal
Author/Editor	Royal Society of Chemistry (Great Britain)	Start Page	2967
Date	01/01/1999	End Page	2972
Language	English	Issue	13
Country	United Kingdom of Great Britain and Northern Ireland	Volume	20

REQUEST DETAILS

Portion Type	Chart/graph/table/figure	Distribution	Worldwide
Number of charts / graphs / tables / figures requested	1	Translation	Original language of publication
Format (select all that apply)	Print, Electronic	Copies for the disabled?	No
Who will republish the content?	Academic institution	Minor editing privileges?	Yes
Duration of Use	Life of current edition	Incidental promotional use?	No
Lifetime Unit Quantity	Up to 1,500,000	Currency	USD
Rights Requested	Main product		

NEW WORK DETAILS

Title	Multiscale Modelling of Structural Transformation in Metal Nanocatalysts for CO2 Electroreduction	Institution name	University of Waterloo
		Expected presentation date	2022-08-01

Instructor name Anna Klinkova

ADDITIONAL DETAILS

Order reference number	N/A	The requesting person / organization to appear on the license	Feng Li
------------------------	-----	---	---------

REUSE CONTENT DETAILS

Title, description or numeric reference of the portion(s)	TOC	Title of the article/chapter the portion is from	Rethinking Co(CO3)0.5(OH)·0.11H2O: a new property for highly selective electrochemical reduction of carbon dioxide to methanol in aqueous solution
Editor of portion(s)	Huang, Jianzhi; Hu, Qiong; Guo, Xinrong; Zeng, Qiang; Wang, Lishi	Author of portion(s)	Huang, Jianzhi; Hu, Qiong; Guo, Xinrong; Zeng, Qiang; Wang, Lishi
Volume of serial or monograph	20	Issue, if republishing an article from a serial	13
Page or page range of portion	2967-2972	Publication date of portion	2018-01-01

CCC Terms and Conditions

1. Description of Service; Defined Terms. This Republication License enables the User to obtain licenses for republication of one or more copyrighted works as described in detail on the relevant Order Confirmation (the "Work(s)"). Copyright Clearance Center, Inc. ("CCC") grants licenses through the Service on behalf of the rightsholder identified on the Order Confirmation (the "Rightsholder"). "Republication", as used herein, generally means the inclusion of a Work, in whole or in part, in a new work or works, also as described on the Order Confirmation. "User", as used herein, means the person or entity making such republication.
2. The terms set forth in the relevant Order Confirmation, and any terms set by the Rightsholder with respect to a particular Work, govern the terms of use of Works in connection with the Service. By using the Service, the person transacting for a republication license on behalf of the User represents and warrants that he/she/it (a) has been duly authorized by the User to accept, and hereby does accept, all such terms and conditions on behalf of User, and (b) shall inform User of all such terms and conditions. In the event such person is a "freelancer" or other third party independent of User and CCC, such party shall be deemed jointly a "User" for purposes of these terms and conditions. In any event, User shall be deemed to have accepted and agreed to all such terms and conditions if User republishes the Work in any fashion.
3. Scope of License; Limitations and Obligations.
 - 3.1. All Works and all rights therein, including copyright rights, remain the sole and exclusive property of the Rightsholder. The license created by the exchange of an Order Confirmation (and/or any invoice) and payment by User of the full amount set forth on that document includes only those rights expressly set forth in the Order Confirmation and in these terms and conditions, and conveys no other rights in the Work(s) to User. All rights not expressly granted are hereby reserved.
 - 3.2. General Payment Terms: You may pay by credit card or through an account with us payable at the end of the month. If you and we agree that you may establish a standing account with CCC, then the following terms apply: Remit Payment to: Copyright Clearance Center, 29118 Network Place, Chicago, IL 60673-1291.

SPRINGER NATURE LICENSE TERMS AND CONDITIONS

Jun 04, 2022

This Agreement between Feng Li ("You") and Springer Nature ("Springer Nature") consists of your license details and the terms and conditions provided by Springer Nature and Copyright Clearance Center.

License Number	5322021374338
License date	Jun 04, 2022
Licensed Content Publisher	Springer Nature
Licensed Content Publication	Nano Research
Licensed Content Title	Fabrication of bilayer Pd-Pt nanocages with sub-nanometer thin shells for enhanced hydrogen evolution reaction
Licensed Content Author	Yihe Wang et al
Licensed Content Date	Mar 7, 2019
Type of Use	Thesis/Dissertation
Requestor type	academic/university or research institute
Format	print and electronic
Portion	figures/tables/illustrations
Number of figures/tables/illustrations	1
Will you be translating?	no
Circulation/distribution	50000 or greater
Author of this Springer Nature content	no
Title	Multiscale Modelling of Structural Transformation in Metal Nanocatalysts for CO2 Electroreduction
Institution name	University of Waterloo
Expected presentation date	Aug 2022
Portions	Table 3.2



This is a License Agreement between Feng Li ("User") and Copyright Clearance Center, Inc. ("CCC") on behalf of the Rightsholder identified in the order details below. The license consists of the order details, the CCC Terms and Conditions below, and any Rightsholder Terms and Conditions which are included below.

All payments must be made in full to CCC in accordance with the CCC Terms and Conditions below.

Order Date	04-Jun-2022	Type of Use	Republish in a
Order License ID	1228914-1	Publisher	thesis/dissertation
ISSN	2050-7488	Portion	Royal Society of Chemistry Chart/graph/table/figure

LICENSED CONTENT

Publication Title	Journal of materials chemistry	Rightsholder	Royal Society of Chemistry
Article Title	Metal-organic framework-derived CoSe ₂ /(NiCo)Se ₂ box-in-box hollow nanocubes with enhanced electrochemical properties for sodium-ion storage and hydrogen evolution	Publication Type	Journal
Author/Editor	Royal Society of Chemistry (Great Britain)	Start Page	18823
Date	01/01/2012	End Page	18830
Language	English	Issue	35
Country	United Kingdom of Great Britain and Northern Ireland	Volume	5

REQUEST DETAILS

Portion Type	Chart/graph/table/figure	Distribution	Worldwide
Number of charts / graphs / tables / figures requested	1	Translation	Original language of publication
Format (select all that apply)	Print, Electronic	Copies for the disabled?	No
Who will republish the content?	Academic Institution	Minor editing privileges?	Yes
Duration of Use	Life of current edition	Incidental promotional use?	No
Lifetime Unit Quantity	Up to 69,999	Currency	CAD
Rights Requested	Main product		

NEW WORK DETAILS

Title	Multiscale Modelling of Structural Transformation in Metal Nanocatalysts for CO ₂ Electroreduction	Institution name	University of Waterloo
		Expected presentation date	2022-08-01

Instructor name Anna Klinkova

ADDITIONAL DETAILS

Order reference number	N/A	The requesting person / organization to appear on the license	Feng Li
------------------------	-----	---	---------

REUSE CONTENT DETAILS

Title, description or numeric reference of the portion(s)	Figure 1	Title of the article/chapter the portion is from	Metal-organic framework-derived CoSe ₂ /(NiCo)Se ₂ box-in-box hollow nanocubes with enhanced electrochemical properties for sodium-ion storage and hydrogen evolution
Editor of portion(s)	Park, Seung-Keun; Kim, Jin Koo; Chan Kang, Yun	Author of portion(s)	Park, Seung-Keun; Kim, Jin Koo; Chan Kang, Yun
Volume of serial or monograph	5	Issue, if republishing an article from a serial	35
Page or page range of portion	18823-18830	Publication date of portion	2017-09-21

CCC Terms and Conditions

1. Description of Service; Defined Terms. This Republication License enables the User to obtain licenses for republication of one or more copyrighted works as described in detail on the relevant Order Confirmation (the "Work(s)"). Copyright Clearance Center, Inc. ("CCC") grants licenses through the Service on behalf of the rightsholder identified on the Order Confirmation (the "Rightsholder"). "Republication", as used herein, generally means the inclusion of a Work, in whole or in part, in a new work or works, also as described on the Order Confirmation. "User", as used herein, means the person or entity making such republication.
2. The terms set forth in the relevant Order Confirmation, and any terms set by the Rightsholder with respect to a particular Work, govern the terms of use of Works in connection with the Service. By using the Service, the person transacting for a republication license on behalf of the User represents and warrants that he/she/it (a) has been duly authorized by the User to accept, and hereby does accept, all such terms and conditions on behalf of User, and (b) shall inform User of all such terms and conditions. In the event such person is a "freelancer" or other third party independent of User and CCC, such party shall be deemed jointly a "User" for purposes of these terms and conditions. In any event, User shall be deemed to have accepted and agreed to all such terms and conditions if User republishes the Work in any fashion.
3. Scope of License; Limitations and Obligations.
 - 3.1. All Works and all rights therein, including copyright rights, remain the sole and exclusive property of the Rightsholder. The license created by the exchange of an Order Confirmation (and/or any invoice) and payment by User of the full amount set forth on that document includes only those rights expressly set forth in the Order Confirmation and in these terms and conditions, and conveys no other rights in the Work(s) to User. All rights not expressly granted are hereby reserved.
 - 3.2. General Payment Terms: You may pay by credit card or through an account with us payable at the end of the month. If you and we agree that you may establish a standing account with CCC, then the following terms apply: Remit Payment to: Copyright Clearance Center, 29118 Network Place, Chicago, IL 60673-1291. Payments Due: Invoices are payable upon their delivery to you (or upon our notice to you that they are

**ELSEVIER LICENSE
TERMS AND CONDITIONS**

Jun 04, 2022

This Agreement between Feng Li ("You") and Elsevier ("Elsevier") consists of your license details and the terms and conditions provided by Elsevier and Copyright Clearance Center.

License Number	5322020561332
License date	Jun 04, 2022
Licensed Content Publisher	Elsevier
Licensed Content Publication	Nano Energy
Licensed Content Title	Enhancing the rate of electrochemical nitrogen reduction reaction for ammonia synthesis under ambient conditions using hollow gold nanocages
Licensed Content Author	Mohammadreza Nazemi, Sajanalal R. Panikkanvalappil, Mostafa A. El-Sayed
Licensed Content Date	Jul 1, 2018
Licensed Content Volume	49
Licensed Content Issue	n/a
Licensed Content Pages	8
Start Page	316
End Page	323

Type of Use	reuse in a thesis/dissertation
Portion	figures/tables/illustrations
Number of figures/tables/illustrations	1
Format	both print and electronic
Are you the author of this Elsevier article?	No
Will you be translating?	No
Title	Multiscale Modelling of Structural Transformation in Metal Nanocatalysts for CO2 Electroreduction
Institution name	University of Waterloo
Expected presentation date	Aug 2022
Portions	Table 3.3

**ELSEVIER LICENSE
TERMS AND CONDITIONS**

Jun 04, 2022

This Agreement between Feng Li ("You") and Elsevier ("Elsevier") consists of your license details and the terms and conditions provided by Elsevier and Copyright Clearance Center.

License Number	5322020404756
License date	Jun 04, 2022
Licensed Content Publisher	Elsevier
Licensed Content Publication	Nano Energy
Licensed Content Title	Pt4PdCu0.4 alloy nanoframes as highly efficient and robust bifunctional electrocatalysts for oxygen reduction reaction and formic acid oxidation
Licensed Content Author	Wei Ye, Shuangming Chen, Mengshan Ye, Chenhao Ren, Jun Ma, Ran Long, Chengming Wang, Jian Yang, Li Song, Yujie Xiong
Licensed Content Date	Sep 1, 2017
Licensed Content Volume	39
Licensed Content Issue	n/a
Licensed Content Pages	7
Start Page	532
End Page	538

Type of Use reuse in a thesis/dissertation

Portion figures/tables/illustrations

Number of figures/tables/illustrations 1

Format both print and electronic

Are you the author of this Elsevier article? No

Will you be translating? No

Title Multiscale Modelling of Structural Transformation in Metal Nanocatalysts for CO2 Electroreduction

Institution name University of Waterloo

Expected presentation date Aug 2022

Portions Table 3.3

**JOHN WILEY AND SONS LICENSE
TERMS AND CONDITIONS**

Jun 04, 2022

This Agreement between Feng Li ("You") and John Wiley and Sons ("John Wiley and Sons") consists of your license details and the terms and conditions provided by John Wiley and Sons and Copyright Clearance Center.

License Number 5322020320607

License date Jun 04, 2022

Licensed Content
Publisher John Wiley and SonsLicensed Content
Publication ChemSusChemLicensed Content
Title Platinum Cubic Nanoframes with Enhanced Catalytic Activity and
Durability Toward Oxygen ReductionLicensed Content
Author Younan Xia, Madeline Vara, Helan Wang, et alLicensed Content
Date Sep 15, 2016Licensed Content
Volume 9Licensed Content
Issue 19Licensed Content
Pages 7

6/4/22, 12:55 PM

RightsLink Printable License

Type of use	Dissertation/Thesis
Requestor type	University/Academic
Format	Print and electronic
Portion	Figure/table
Number of figures/tables	1
Will you be translating?	No
Title	Multiscale Modelling of Structural Transformation in Metal Nanocatalysts for CO2 Electroreduction
Institution name	University of Waterloo
Expected presentation date	Aug 2022
Portions	Table 3.3

**JOHN WILEY AND SONS LICENSE
TERMS AND CONDITIONS**

Jun 04, 2022

This Agreement between Feng Li ("You") and John Wiley and Sons ("John Wiley and Sons") consists of your license details and the terms and conditions provided by John Wiley and Sons and Copyright Clearance Center.

License Number 5322011259255

License date Jun 04, 2022

Licensed Content
Publisher John Wiley and Sons

Licensed Content
Publication Advanced Materials

Licensed Content
Title Atomic-Scale Preparation of Octopod Nanoframes with High-Index Facets as Highly Active and Stable Catalysts

Licensed Content
Author Siyu Ye, Pei Kang Shen, Min Tang, et al

Licensed Content
Date Sep 26, 2016

Licensed Content
Volume 29

Licensed Content
Issue 8

Licensed Content
Pages 6

6/4/22, 12:46 PM

RightsLink Printable License

Type of use	Dissertation/Thesis
Requestor type	University/Academic
Format	Print and electronic
Portion	Figure/table
Number of figures/tables	1
Will you be translating?	No
Title	Multiscale Modelling of Structural Transformation in Metal Nanocatalysts for CO2 Electroreduction
Institution name	University of Waterloo
Expected presentation date	Aug 2022
Portions	Table 3.3

**SPRINGER NATURE LICENSE
TERMS AND CONDITIONS**

Jun 04, 2022

This Agreement between Feng Li ("You") and Springer Nature ("Springer Nature") consists of your license details and the terms and conditions provided by Springer Nature and Copyright Clearance Center.

License Number	5322000541168
License date	Jun 04, 2022
Licensed Content Publisher	Springer Nature
Licensed Content Publication	Nature
Licensed Content Title	Enhanced electrocatalytic CO2 reduction via field-induced reagent concentration
Licensed Content Author	Min Liu et al
Licensed Content Date	Aug 3, 2016
Type of Use	Thesis/Dissertation
Requestor type	academic/university or research institute
Format	print and electronic
Portion	figures/tables/illustrations
Number of figures/tables/illustrations	2

High-res required	no
Will you be translating?	no
Circulation/distribution	50000 or greater
Author of this Springer Nature content	no
Title	Multiscale Modelling of Structural Transformation in Metal Nanocatalysts for CO2 Electroreduction
Institution name	University of Waterloo
Expected presentation date	Aug 2022
Portions	Figure 1 and Extended Data Figure 2

**ELSEVIER LICENSE
TERMS AND CONDITIONS**

Jun 04, 2022

This Agreement between Feng Li ("You") and Elsevier ("Elsevier") consists of your license details and the terms and conditions provided by Elsevier and Copyright Clearance Center.

License Number	5321990511071
License date	Jun 04, 2022
Licensed Content Publisher	Elsevier
Licensed Content Publication	Nano Energy
Licensed Content Title	Shape-controlled bismuth nanoflakes as highly selective catalysts for electrochemical carbon dioxide reduction to formate
Licensed Content Author	Sungjoo Kim,Wan Jae Dong,Seungo Gim,Woonbae Sohn,Jae Yong Park,Chul Jong Yoo,Ho Won Jang,Jong-Lam Lee
Licensed Content Date	Sep 1, 2017
Licensed Content Volume	39
Licensed Content Issue	n/a
Licensed Content Pages	9
Start Page	44
End Page	52

6/4/22, 11:43 AM

RightsLink Printable License

Type of Use	reuse in a thesis/dissertation
Portion	figures/tables/illustrations
Number of figures/tables/illustrations	1
Format	both print and electronic
Are you the author of this Elsevier article?	No
Will you be translating?	No
Title	Multiscale Modelling of Structural Transformation in Metal Nanocatalysts for CO2 Electroreduction
Institution name	University of Waterloo
Expected presentation date	Aug 2022
Portions	Figure 6

**JOHN WILEY AND SONS LICENSE
TERMS AND CONDITIONS**

Jun 04, 2022

This Agreement between Feng Li ("You") and John Wiley and Sons ("John Wiley and Sons") consists of your license details and the terms and conditions provided by John Wiley and Sons and Copyright Clearance Center.

License Number 5321990746671

License date Jun 04, 2022

Licensed Content Publisher John Wiley and Sons

Licensed Content Publication Angewandte Chemie International Edition

Licensed Content Title High-Curvature Transition-Metal Chalcogenide Nanostructures with a Pronounced Proximity Effect Enable Fast and Selective CO₂ Electroreduction

Licensed Content Author Shu-Hong Yu, Min-Rui Gao, Jun-Fa Zhu, et al

Licensed Content Date Feb 3, 2020

Licensed Content Volume 59

Licensed Content Issue 22

Licensed
Content Pages 7

Type of use Dissertation/Thesis

Requestor
type University/Academic

Format Print and electronic

Portion Figure/table

Number of
figures/tables 1

Will you be
translating? No

Title Multiscale Modelling of Structural Transformation in Metal Nanocatalysts
for CO2 Electroreduction

Institution
name University of Waterloo

Expected
presentation
date Aug 2022

Portions Figure 1

**ELSEVIER LICENSE
TERMS AND CONDITIONS**

Jun 04, 2022

This Agreement between Feng Li ("You") and Elsevier ("Elsevier") consists of your license details and the terms and conditions provided by Elsevier and Copyright Clearance Center.

License Number	5321990858004
License date	Jun 04, 2022
Licensed Content Publisher	Elsevier
Licensed Content Publication	Chemosphere
Licensed Content Title	Electrochemical reduction of carbon dioxide to formate via nano-prism assembled CuO microspheres
Licensed Content Author	Da Li, Linlin Huang, Tongtong Liu, Jia Liu, Liang Zhen, Jing Wu, Yujie Feng
Licensed Content Date	Dec 1, 2019
Licensed Content Volume	237
Licensed Content Issue	n/a
Licensed Content Pages	1
Start Page	124527
End Page	0

6/4/22, 11:49 AM

RightsLink Printable License

Type of Use	reuse in a thesis/dissertation
Portion	figures/tables/illustrations
Number of figures/tables/illustrations	1
Format	both print and electronic
Are you the author of this Elsevier article?	No
Will you be translating?	No
Title	Multiscale Modelling of Structural Transformation in Metal Nanocatalysts for CO2 Electroreduction
Institution name	University of Waterloo
Expected presentation date	Aug 2022
Portions	figure 5



This is a License Agreement between Feng Li ("User") and Copyright Clearance Center, Inc. ("CCC") on behalf of the Rightsholder identified in the order details below. The license consists of the order details, the CCC Terms and Conditions below, and any Rightsholder Terms and Conditions which are included below.

All payments must be made in full to CCC in accordance with the CCC Terms and Conditions below.

Order Date	04-Jun-2022	Type of Use	Republish in a thesis/dissertation
Order License ID	1228909-1	Publisher Portion	Royal Society of Chemistry Chart/graph/table/figure
ISSN	2050-7488		

LICENSED CONTENT

Publication Title	Journal of materials chemistry	Rightsholder	Royal Society of Chemistry
Article Title	Multifunctional nanostructures of Au-Bi ₂ O ₃ fractals for CO ₂ reduction and optical sensing	Publication Type	Journal
Author/Editor	Royal Society of Chemistry (Great Britain)	Start Page	11233
Date	01/01/2012	End Page	11245
Language	English	Issue	22
Country	United Kingdom of Great Britain and Northern Ireland	Volume	8

REQUEST DETAILS

Portion Type	Chart/graph/table/figure	Distribution	Worldwide
Number of charts / graphs / tables / figures requested	1	Translation	Original language of publication
Format (select all that apply)	Print, Electronic	Copies for the disabled?	No
Who will republish the content?	Academic institution	Minor editing privileges?	Yes
Duration of Use	Life of current edition	Incidental promotional use?	No
Lifetime Unit Quantity	Up to 750,000	Currency	CAD
Rights Requested	Main product		

NEW WORK DETAILS

Title	Multiscale Modelling of Structural Transformation in Metal Nanocatalysts for CO ₂ Electroreduction	Institution name	University of Waterloo
Instructor name	Anna Klinkova	Expected presentation date	2022-08-02

ADDITIONAL DETAILS

Order reference number	N/A	The requesting person / organization to appear on the license	Feng Li
------------------------	-----	---	---------

REUSE CONTENT DETAILS

Title, description or numeric reference of the portion(s)	Figure 4	Title of the article/chapter the portion is from	Multifunctional nanostructures of Au-Bi2O3 fractals for CO2 reduction and optical sensing
Editor of portion(s)	Tran-Phu, Thanh; Daiyan, Rahman; Fusco, Zelio; Ma, Zhipeng; Rahim, Lina Raihana Abd; Kiy, Alexander; Kluth, Patrick; Guo, Xuyun; Zhu, Ye; Chen, Hongjun; Amal, Rose; Tricoli, Antonio	Author of portion(s)	Tran-Phu, Thanh; Daiyan, Rahman; Fusco, Zelio; Ma, Zhipeng; Rahim, Lina Raihana Abd; Kiy, Alexander; Kluth, Patrick; Guo, Xuyun; Zhu, Ye; Chen, Hongjun; Amal, Rose; Tricoli, Antonio
Volume of serial or monograph	8	Issue, if republishing an article from a serial	22
Page or page range of portion	11233-11245	Publication date of portion	2020-01-01

CCC Terms and Conditions

1. Description of Service; Defined Terms. This Republication License enables the User to obtain licenses for republication of one or more copyrighted works as described in detail on the relevant Order Confirmation (the "Work(s)"). Copyright Clearance Center, Inc. ("CCC") grants licenses through the Service on behalf of the rightsholder identified on the Order Confirmation (the "Rightsholder"). "Republication", as used herein, generally means the inclusion of a Work, in whole or in part, in a new work or works, also as described on the Order Confirmation. "User", as used herein, means the person or entity making such republication.
2. The terms set forth in the relevant Order Confirmation, and any terms set by the Rightsholder with respect to a particular Work, govern the terms of use of Works in connection with the Service. By using the Service, the person transacting for a republication license on behalf of the User represents and warrants that he/she/it (a) has been duly authorized by the User to accept, and hereby does accept, all such terms and conditions on behalf of User, and (b) shall inform User of all such terms and conditions. In the event such person is a "freelancer" or other third party independent of User and CCC, such party shall be deemed jointly a "User" for purposes of these terms and conditions. In any event, User shall be deemed to have accepted and agreed to all such terms and conditions if User republishes the Work in any fashion.
3. Scope of License; Limitations and Obligations.
 - 3.1. All Works and all rights therein, including copyright rights, remain the sole and exclusive property of the Rightsholder. The license created by the exchange of an Order Confirmation (and/or any invoice) and payment by User of the full amount set forth on that document includes only those rights expressly set forth in the Order Confirmation and in these terms and conditions, and conveys no other rights in the Work(s) to User. All rights not expressly granted are hereby reserved.
 - 3.2. General Payment Terms: You may pay by credit card or through an account with us payable at the end of the month. If you and we agree that you may establish a standing account with CCC, then the following terms apply: Remit Payment to: Copyright Clearance Center, 29118 Network Place, Chicago, IL 60673-1291.

**JOHN WILEY AND SONS LICENSE
TERMS AND CONDITIONS**

Jun 04, 2022

This Agreement between Feng Li ("You") and John Wiley and Sons ("John Wiley and Sons") consists of your license details and the terms and conditions provided by John Wiley and Sons and Copyright Clearance Center.

License Number	5322000814701
License date	Jun 04, 2022
Licensed Content Publisher	John Wiley and Sons
Licensed Content Publication	ChemElectroChem
Licensed Content Title	Highly Selective Electrochemical Conversion of CO ₂ to HCOOH on Dendritic Indium Foams
Licensed Content Author	Yang Hou, Zhongjian Li, Lecheng Lei, et al
Licensed Content Date	Nov 29, 2017
Licensed Content Volume	5
Licensed Content Issue	2
Licensed Content Pages	7

6/4/22, 12:13 PM

RightsLink Printable License

Type of use	Dissertation/Thesis
Requestor type	University/Academic
Format	Print and electronic
Portion	Figure/table
Number of figures/tables	1
Will you be translating?	No
Title	Multiscale Modelling of Structural Transformation in Metal Nanocatalysts for CO2 Electroreduction
Institution name	University of Waterloo
Expected presentation date	Aug 2022
Portions	Figure 9

**JOHN WILEY AND SONS LICENSE
TERMS AND CONDITIONS**

Jun 04, 2022

This Agreement between Feng Li ("You") and John Wiley and Sons ("John Wiley and Sons") consists of your license details and the terms and conditions provided by John Wiley and Sons and Copyright Clearance Center.

License Number 5322001034412

License date Jun 04, 2022

Licensed Content
Publisher John Wiley and SonsLicensed Content
Publication ChemCatChemLicensed Content
Title Copper-Palladium Tetrapods with Sharp Tips as a Superior Catalyst for the Oxygen Reduction ReactionLicensed Content
Author Jie Zeng, Shiming Zhou, Yunjiao Zhang, et alLicensed Content
Date Jan 26, 2018Licensed Content
Volume 10Licensed Content
Issue 5Licensed Content
Pages 6

6/4/22, 12:17 PM

RightsLink Printable License

Type of use	Dissertation/Thesis
Requestor type	University/Academic
Format	Print and electronic
Portion	Figure/table
Number of figures/tables	1
Will you be translating?	No
Title	Multiscale Modelling of Structural Transformation in Metal Nanocatalysts for CO2 Electroreduction
Institution name	University of Waterloo
Expected presentation date	Aug 2022
Portions	Figure 4



This is a License Agreement between Feng Li ("User") and Copyright Clearance Center, Inc. ("CCC") on behalf of the Rightsholder identified in the order details below. The license consists of the order details, the CCC Terms and Conditions below, and any Rightsholder Terms and Conditions which are included below.

All payments must be made in full to CCC in accordance with the CCC Terms and Conditions below.

Order Date	04-Jun-2022	Type of Use	Republish in a
Order License ID	1228911-1	Publisher	thesis/dissertation
ISSN	2050-7488	Portion	Royal Society of Chemistry Image/photo/illustration

LICENSED CONTENT

Publication Title	Journal of materials chemistry	Rightsholder	Royal Society of Chemistry
Article Title	Sharp Cu@Sn nanocones on Cu foam for highly Selective and efficient electrochemical reduction of CO ₂ to formate	Publication Type	Journal
Author/Editor	Royal Society of Chemistry (Great Britain)	Start Page	19621
Date	01/01/2012	End Page	19630
Language	English	Issue	40
Country	United Kingdom of Great Britain and Northern Ireland	Volume	6

REQUEST DETAILS

Portion Type	Image/photo/illustration	Distribution	Worldwide
Number of images / photos / illustrations	1	Translation	Original language of publication
Format (select all that apply)	Print, Electronic	Copies for the disabled?	No
Who will republish the content?	Academic institution	Minor editing privileges?	Yes
Duration of Use	Life of current edition	Incidental promotional use?	No
Lifetime Unit Quantity	More than 2,000,000	Currency	CAD
Rights Requested	Main product		

NEW WORK DETAILS

Title	Multiscale Modelling of Structural Transformation in Metal Nanocatalysts for CO ₂ Electroreduction	Institution name	University of Waterloo
Instructor name	Anna Klinkova	Expected presentation date	2022-08-01

ADDITIONAL DETAILS

Order reference number	figure 4	The requesting person / organization to appear on the license	Feng Li
------------------------	----------	---	---------

REUSE CONTENT DETAILS

Title, description or numeric reference of the portion(s)	Figure 4	Title of the article/chapter the portion is from	Sharp Cu@Sn nanocones on Cu foam for highly Selective and efficient electrochemical reduction of CO2 to formate
Editor of portion(s)	Chen, Chengzhen; Cheng, Zhenmin; Pang, Yuanjie; Zhang, Bo; Zhang, Fanghua; Zhong, Ju Hua	Author of portion(s)	Chen, Chengzhen; Cheng, Zhenmin; Pang, Yuanjie; Zhang, Bo; Zhang, Fanghua; Zhong, Ju Hua
Volume of serial or monograph	6	Issue, if republishing an article from a serial	40
Page or page range of portion	19621-19630	Publication date of portion	2018-01-01

CCC Terms and Conditions

1. Description of Service; Defined Terms. This Republication License enables the User to obtain licenses for republication of one or more copyrighted works as described in detail on the relevant Order Confirmation (the "Work(s)"). Copyright Clearance Center, Inc. ("CCC") grants licenses through the Service on behalf of the rightsholder identified on the Order Confirmation (the "Rightsholder"). "Republication", as used herein, generally means the inclusion of a Work, in whole or in part, in a new work or works, also as described on the Order Confirmation. "User", as used herein, means the person or entity making such republication.
2. The terms set forth in the relevant Order Confirmation, and any terms set by the Rightsholder with respect to a particular Work, govern the terms of use of Works in connection with the Service. By using the Service, the person transacting for a republication license on behalf of the User represents and warrants that he/she/it (a) has been duly authorized by the User to accept, and hereby does accept, all such terms and conditions on behalf of User, and (b) shall inform User of all such terms and conditions. In the event such person is a "freelancer" or other third party independent of User and CCC, such party shall be deemed jointly a "User" for purposes of these terms and conditions. In any event, User shall be deemed to have accepted and agreed to all such terms and conditions if User republishes the Work in any fashion.
3. Scope of License; Limitations and Obligations.
 - 3.1. All Works and all rights therein, including copyright rights, remain the sole and exclusive property of the Rightsholder. The license created by the exchange of an Order Confirmation (and/or any invoice) and payment by User of the full amount set forth on that document includes only those rights expressly set forth in the Order Confirmation and in these terms and conditions, and conveys no other rights in the Work(s) to User. All rights not expressly granted are hereby reserved.
 - 3.2. General Payment Terms: You may pay by credit card or through an account with us payable at the end of the month. If you and we agree that you may establish a standing account with CCC, then the following terms apply: Remit Payment to: Copyright Clearance Center, 29118 Network Place, Chicago, IL 60673-1291. Payments Due: Invoices are payable upon their delivery to you (or upon our notice to you that they are available to you for downloading). After 30 days, outstanding amounts will be subject to a service charge of 1-1/2% per month or, if less, the maximum rate allowed by applicable law. Unless otherwise specifically set forth in the Order Confirmation or in a separate written agreement signed by CCC, invoices are due and



This is a License Agreement between Feng Li ("User") and Copyright Clearance Center, Inc. ("CCC") on behalf of the Rightsholder identified in the order details below. The license consists of the order details, the CCC Terms and Conditions below, and any Rightsholder Terms and Conditions which are included below.

All payments must be made in full to CCC in accordance with the CCC Terms and Conditions below.

Order Date	04-Jun-2022	Type of Use	Republish in a thesis/dissertation
Order License ID	1228912-1	Publisher Portion	Royal Society of Chemistry
ISSN	2050-7488		Image/photo/illustration

LICENSED CONTENT

Publication Title	Journal of materials chemistry	Rightsholder	Royal Society of Chemistry
Article Title	Confined Cavity on a Mass-Produced Wrinkle Film Promotes the Selective CO ₂ Reduction	Publication Type	Journal
Author/Editor	Royal Society of Chemistry (Great Britain)	Start Page	14592
Date	01/01/2012	End Page	14599
Language	English	Issue	29
Country	United Kingdom of Great Britain and Northern Ireland	Volume	8

REQUEST DETAILS

Portion Type	Image/photo/illustration	Distribution	Worldwide
Number of images / photos / illustrations	1	Translation	Original language of publication
Format (select all that apply)	Print, Electronic	Copies for the disabled?	No
Who will republish the content?	Academic institution	Minor editing privileges?	Yes
Duration of Use	Life of current edition	Incidental promotional use?	No
Lifetime Unit Quantity	More than 2,000,000	Currency	CAD
Rights Requested	Main product		

NEW WORK DETAILS

Title	Multiscale Modelling of Structural Transformation in Metal Nanocatalysts for CO ₂ Electroreduction	Institution name	University of Waterloo
Instructor name	Anna Klinkova	Expected presentation date	2022-08-01

ADDITIONAL DETAILS

Order reference number	N/A	The requesting person / organization to appear on the license	Feng Li
------------------------	-----	---	---------

REUSE CONTENT DETAILS

Title, description or numeric reference of the portion(s)	Figure 4	Title of the article/chapter the portion is from	Confined Cavity on a Mass-Produced Wrinkle Film Promotes the Selective CO2 Reduction
Editor of portion(s)	Cho, Kyeong Min; Jung, Woo-Bin; Kim, Donggyu; Kim, Ju Ye; Kim, Yesol; Yun, Geun-Tae; Ryu, Seunghwa; Gereige, Issam; Saggaf, Ahmed; Jung, Hee-Tae	Author of portion(s)	Cho, Kyeong Min; Jung, Woo-Bin; Kim, Donggyu; Kim, Ju Ye; Kim, Yesol; Yun, Geun-Tae; Ryu, Seunghwa; Gereige, Issam; Saggaf, Ahmed; Jung, Hee-Tae
Volume of serial or monograph	8	Issue, if republishing an article from a serial	29
Page or page range of portion	14592-14599	Publication date of portion	2020-01-01

CCC Terms and Conditions

1. Description of Service; Defined Terms. This Republication License enables the User to obtain licenses for republication of one or more copyrighted works as described in detail on the relevant Order Confirmation (the "Work(s)"). Copyright Clearance Center, Inc. ("CCC") grants licenses through the Service on behalf of the rightsholder identified on the Order Confirmation (the "Rightsholder"). "Republication", as used herein, generally means the inclusion of a Work, in whole or in part, in a new work or works, also as described on the Order Confirmation. "User", as used herein, means the person or entity making such republication.
2. The terms set forth in the relevant Order Confirmation, and any terms set by the Rightsholder with respect to a particular Work, govern the terms of use of Works in connection with the Service. By using the Service, the person transacting for a republication license on behalf of the User represents and warrants that he/she/it (a) has been duly authorized by the User to accept, and hereby does accept, all such terms and conditions on behalf of User, and (b) shall inform User of all such terms and conditions. In the event such person is a "freelancer" or other third party independent of User and CCC, such party shall be deemed jointly a "User" for purposes of these terms and conditions. In any event, User shall be deemed to have accepted and agreed to all such terms and conditions if User republishes the Work in any fashion.
3. Scope of License; Limitations and Obligations.
 - 3.1. All Works and all rights therein, including copyright rights, remain the sole and exclusive property of the Rightsholder. The license created by the exchange of an Order Confirmation (and/or any invoice) and payment by User of the full amount set forth on that document includes only those rights expressly set forth in the Order Confirmation and in these terms and conditions, and conveys no other rights in the Work(s) to User. All rights not expressly granted are hereby reserved.
 - 3.2. General Payment Terms: You may pay by credit card or through an account with us payable at the end of the month. If you and we agree that you may establish a standing account with CCC, then the following terms apply: Remit Payment to: Copyright Clearance Center, 29118 Network Place, Chicago, IL 60673-1291. Payments Due: Invoices are payable upon their delivery to you (or upon our notice to you that they are available to you for downloading). After 30 days, outstanding amounts will be subject to a service charge of 1-1/2% per month or, if less, the maximum rate allowed by applicable law. Unless otherwise specifically set forth in the Order Confirmation or in a separate written agreement signed by CCC, invoices are due and payable on "net 30" terms. While User may exercise the rights licensed immediately upon issuance of the

**JOHN WILEY AND SONS LICENSE
TERMS AND CONDITIONS**

Jun 04, 2022

This Agreement between Feng Li ("You") and John Wiley and Sons ("John Wiley and Sons") consists of your license details and the terms and conditions provided by John Wiley and Sons and Copyright Clearance Center.

License Number 5322010387304

License date Jun 04, 2022

Licensed
Content
Publisher John Wiley and SonsLicensed
Content
Publication Angewandte Chemie International EditionLicensed
Content Title Nanoconfinement Engineering over Hollow Multi-Shell Structured Copper towards Efficient Electrocatalytical C-C couplingLicensed
Content Author Chunxiao Liu, Menglu Zhang, Jiawei Li, et alLicensed
Content Date Dec 2, 2021Licensed
Content Volume 61Licensed
Content Issue 3Licensed
Content Pages 6

6/4/22, 12:31 PM

RightsLink Printable License

Type of use Dissertation/Thesis

Requestor type University/Academic

Format Print and electronic

Portion Figure/table

Number of
figures/tables 1

Will you be
translating? No

Title Multiscale Modelling of Structural Transformation in Metal Nanocatalysts
for CO2 Electroreduction

Institution name University of Waterloo

Expected
presentation date Aug 2022

Portions Figure 1

**SPRINGER NATURE LICENSE
TERMS AND CONDITIONS**

Jun 04, 2022

This Agreement between Feng Li ("You") and Springer Nature ("Springer Nature") consists of your license details and the terms and conditions provided by Springer Nature and Copyright Clearance Center.

License Number	5322010736956
License date	Jun 04, 2022
Licensed Content Publisher	Springer Nature
Licensed Content Publication	Nature Catalysis
Licensed Content Title	Copper nanocavities confine intermediates for efficient electrosynthesis of C3 alcohol fuels from carbon monoxide
Licensed Content Author	Tao-Tao Zhuang et al
Licensed Content Date	Oct 29, 2018
Type of Use	Thesis/Dissertation
Requestor type	academic/university or research institute
Format	print and electronic
Portion	figures/tables/illustrations
Number of figures/tables/illustrations	2

6/4/22, 12:37 PM

RightsLink Printable License

High-res required no

Will you be translating? no

Circulation/distribution 50000 or greater

Author of this Springer
Nature content no

Title Multiscale Modelling of Structural Transformation in Metal
Nanocatalysts for CO2 Electroreduction

Institution name University of Waterloo

Expected presentation
date Aug 2022

Portions Figure 1 and 2

Bibliography

- (1) Seh, Z. W.; Kibsgaard, J.; Dickens, C. F.; Chorkendorff, I.; Nørskov, J. K.; Jaramillo, T. F. *Science* **2017**, *355*, 146, DOI: 10.1126/science.aad4998.
- (2) Lin, S.; Diercks, C. S.; Zhang, Y. B.; Kornienko, N.; Nichols, E. M.; Zhao, Y.; Paris, A. R.; Kim, D.; Yang, P.; Yaghi, O. M.; Chang, C. J. *Science* **2015**, *349*, 1208–1213, DOI: 10.1126/science.aac8343.
- (3) Verma, S.; Lu, S.; Kenis, P. J. A. *Nat. Energy* **2019**, *4*, 466–474, DOI: 10.1038/S41560-019-0374-6.
- (4) Zhang, Y.-J.; Sethuraman, V.; Michalsky, R.; A. Peterson, A. *ACS Catal.* **2014**, *4*, 3742–3748, DOI: 10.1021/cs5012298.
- (5) Goyal, A.; Marcandalli, G.; Mints, V. A.; Koper, M. T. M. *J. Am. Chem. Soc.* **2020**, *142*, 4154–4161, DOI: 10.1021/jacs.9b10061.
- (6) Xu, Y.; Edwards, J. P.; Zhong, J.; O'Brien, C. P.; Gabardo, C. M.; McCallum, C.; Li, J.; Dinh, C. T.; Sargent, E. H.; Sinton, D. *Energy Environ. Sci.* **2020**, *13*, 554–561, DOI: 10.1039/c9ee03077h.
- (7) Gao, D.; Arán-Ais, R. M.; Jeon, H. S.; Roldan Cuenya, B. *Nat. Catal.* **2019**, *2*, 198–210, DOI: 10.1038/s41929-019-0235-5.
- (8) Verdaguier-Casadevall, A.; Li, C. W.; Johansson, T. P.; Scott, S. B.; McKeown, J. T.; Kumar, M.; Stephens, I. E. L.; Kanan, M. W.; Chorkendorff, I. *J. Am. Chem. Soc.* **2015**, *137*, 9808–9811, DOI: 10.1021/jacs.5b06227.
- (9) Eilert, A.; Cavalca, F.; Roberts, F. S.; Osterwalder, J.; Liu, C.; Favaro, M.; Crumlin, E. J.; Ogasawara, H.; Friebel, D.; Pettersson, L. G. M.; Nilsson, A. *J. Phys. Chem. Lett.* **2017**, *8*, 285–290, DOI: 10.1021/acs.jpcllett.6b02273.
- (10) Zheng, W.; Yang, J.; Chen, H.; Hou, Y.; Wang, Q.; Gu, M.; He, F.; Xia, Y.; Xia, Z.; Li, Z.; Yang, B.; Lei, L.; Yuan, C.; He, Q.; Qiu, M.; Feng, X. *Adv. Funct. Mater.* **2020**, *30*, 1–10, DOI: 10.1002/adfm.201907658.
- (11) Ross, M. B.; De Luna, P.; Li, Y.; Dinh, C.-T.; Kim, D.; Yang, P.; Sargent, E. H. *Nat. Catal.* **2019**, *2*, 648–658, DOI: 10.1038/s41929-019-0306-7.

- (12) Vasileff, A.; Xu, C.; Jiao, Y.; Zheng, Y.; Qiao, S.-Z. *Chem* **2018**, *4*, 1809–1831, DOI: 10.1016/j.chempr.2018.05.001.
- (13) Liu, M.; Pang, Y.; Zhang, B.; De Luna, P.; Voznyy, O.; Xu, J.; Zheng, X.; Dinh, C. T.; Fan, F.; Cao, C.; De Arquer, F. P. G.; Safaei, T. S.; Mepham, A.; Klinkova, A.; Kumacheva, E.; Filletter, T.; Sinton, D.; Kelley, S. O.; Sargent, E. H. *Nature* **2016**, *537*, 382–386, DOI: 10.1038/nature19060.
- (14) Zhuang, T. T.; Pang, Y.; Liang, Z. Q.; Wang, Z.; Li, Y.; Tan, C. S.; Li, J.; Dinh, C. T.; De Luna, P.; Hsieh, P. L.; Burdyny, T.; Li, H. H.; Liu, M.; Wang, Y.; Li, F.; Proppe, A.; Johnston, A.; Nam, D. H.; Wu, Z. Y.; Zheng, Y. R.; Ip, A. H.; Tan, H.; Chen, L. J.; Yu, S. H.; Kelley, S. O.; Sinton, D.; Sargent, E. H. *Nat. Catal.* **2018**, *1*, 946–951, DOI: 10.1038/s41929-018-0168-4.
- (15) Wang, Y.; Zhang, L.; Hu, C.; Yu, S.; Yang, P.; Cheng, D.; Zhao, Z.-J.; Gong, J. *Nano Res.* **2019**, *12*, 2268–2274, DOI: 10.1007/s12274-019-2312-y.
- (16) Li, Z.; Yu, C.; Wen, Y.; Gao, Y.; Xing, X.; Wei, Z.; Sun, H.; Zhang, Y.-W.; Song, W. *ACS Catal.* **2019**, *9*, 5084–5095, DOI: 10.1021/acscatal.8b04814.
- (17) Si, C.-D.; Wu, Z.-X.; Wang, J.; Lu, Z.-H.; Xu, X.-F.; Li, J.-S. *ACS Sustain. Chem. & Eng.* **2019**, *7*, 9737–9742, DOI: 10.1021/acssuschemeng.9b00817.
- (18) Nazemi, M.; Panikkanvalappil, S. R.; El-Sayed, M. A. *Nano Energy* **2018**, *49*, 316–323, DOI: 10.1016/J.NANOEN.2018.04.039.
- (19) Nazemi, M.; A. El-Sayed, M. *J. Phys. Chem. C* **2019**, *123*, 11422–11427, DOI: 10.1021/acs.jpcc.9b01107.
- (20) Ye, W.; Chen, S.; Ye, M.; Ren, C.; Ma, J.; Long, R.; Wang, C.; Yang, J.; Song, L.; Xiong, Y. *Nano Energy* **2017**, *39*, 532–538, DOI: 10.1016/j.nanoen.2017.07.025.
- (21) Ye, W.; Chen, S.; Ye, M.; Ren, C.; Ma, J.; Long, R.; Wang, C.; Yang, J.; Song, L.; Xiong, Y. *Nano Energy* **2017**, *39*, 532–538, DOI: 10.1016/J.NANOEN.2017.07.025.
- (22) Chen, C.; Kang, Y.; Huo, Z.; Zhu, Z.; Huang, W.; Xin, H. L.; Snyder, J. D.; Li, D.; Herron, J. A.; Mavrikakis, M.; Chi, M.; More, K. L.; Li, Y.; Markovic, N. M.; Somorjai, G. A.; Yang, P.; Stamenkovic, V. R. *Science* **2014**, *343*, 1339–1343, DOI: 10.1126/science.1249061.
- (23) Luo, S.; Tang, M.; Shen, P. K.; Ye, S. *Adv. Mater.* **2017**, *29*, 1601687, DOI:

10.1002/adma.201601687.

- (24) Lyu, L. M.; Kao, Y. C.; Cullen, D. A.; Sneed, B. T.; Chuang, Y. C.; Kuo, C. H. *Chem. Mater.* **2017**, *29*, 5681–5692, DOI: 10.1021/acs.chemmater.7b01550.
- (25) Zhu, G.; Liu, J.; Li, S.; Zuo, Y.; Li, D.; Han, H. *ACS Appl. Energy Mater.* **2019**, *2*, 2862–2869, DOI: 10.1021/acsaem.9b00205.
- (26) Zhang, X.-F.; Wang, A.-J.; Zhang, L.; Yuan, J.; Li, Z.; Feng, J.-J. *ACS Appl. Energy Mater.* **2018**, *1*, 5054–5061, DOI: 10.1021/acsaem.8b01065.
- (27) He, L.; Cui, B.; Hu, B.; Liu, J.; Tian, K.; Wang, M.; Song, Y.; Fang, S.; Zhang, Z.; Jia, Q. *ACS Appl. Energy Mater.* **2018**, *1*, 3915–3928, DOI: 10.1021/acsaem.8b00663.
- (28) Lee, H.-E.; Dong Yang, K.; Moon Yoon, S.; Ahn, H.-Y.; Young Lee, Y.; Chang, H.; Hong Jeong, D.; Lee, Y.-S.; Young Kim, M.; Tae Nam, K. *ACS Nano* **2015**, *9*, 8384–8393, DOI: 10.1021/acsnano.5b03065.
- (29) Wang, P.; Qiao, M.; Shao, Q.; Pi, Y.; Zhu, X.; Li, Y.; Huang, X. *Nat. Commun.* **2018**, *9*, 1–10, DOI: 10.1038/s41467-018-07419-z.
- (30) Zhou, J. H.; Lan, D. W.; Yang, S. S.; Guo, Y.; Yuan, K.; Dai, L. X.; Zhang, Y. W. *Inorg. Chem. Front.* **2018**, *5*, 1524–1532, DOI: 10.1039/C8QI00297E.
- (31) Tan, W.; Cao, B.; Xiao, W.; Zhang, M.; Wang, S.; Xie, S.; Xie, D.; Cheng, F.; Guo, Q.; Liu, P. *Nanoscale Res. Lett.* **2019**, *14*, 63, DOI: 10.1186/s11671-019-2892-3.
- (32) Liu, S.-Q.; Wu, S.-W.; Gao, M.-R.; Li, M.-S.; Fu, X.-Z.; Luo, J.-L. *ACS Sustain. Chem. Eng.* **2019**, *7*, 14443–14450, DOI: 10.1021/acssuschemeng.9b01635.
- (33) Park, S.-K.; Kim, J. K.; Chan Kang, Y. *J. Mater. Chem. A* **2017**, *5*, 18823–18830, DOI: 10.1039/C7TA05571D.
- (34) Dai, Z.; Geng, H.; Wang, J.; Luo, Y.; Li, B.; Zong, Y.; Yang, J.; Guo, Y.; Zheng, Y.; Wang, X.; Yan, Q. *ACS Nano* **2017**, *11*, 11031–11040, DOI: 10.1021/acsnano.7b05050.
- (35) Jiang, Y.; Qian, X.; Zhu, C.; Liu, H.; Hou, L. *ACS Appl. Mater. & Interfaces* **2018**, *10*, 9379–9389, DOI: 10.1021/acsami.7b18439.
- (36) Zou, C.; Xi, C.; Wu, D.; Mao, J.; Liu, M.; Liu, H.; Dong, C.; Du, X. *Small* **2019**, *15*, 1902582, DOI: 10.1002/smll.201902582.

- (37) Huang, J.; Hu, Q.; Guo, X.; Zeng, Q.; Wang, L. *Green Chem.* **2018**, *20*, 2967–2972, DOI: 10.1039/C7GC03744A.
- (38) Park, J.; Kwon, T.; Kim, J.; Jin, H.; Kim, H. Y.; Kim, B.; Joo, S. H.; Lee, K. *Chem. Soc. Rev.* **2018**, *47*, 8173–8202, DOI: 10.1039/C8CS00336J.
- (39) Zhang, L.; Chen, S.; Dai, Y.; Shen, Z.; Wei, M.; Huang, R.; Li, H.; Zheng, T.; Zhang, Y.; Zhou, S.; Zeng, J. *ChemCatChem* **2018**, *10*, 925–930, DOI: 10.1002/cctc.201701578.
- (40) Chen, C.; Pang, Y.; Zhang, F.; Zhong, J.; Zhang, B.; Cheng, Z. *J. Mater. Chem. A* **2018**, *6*, 19621–19630, DOI: 10.1039/c8ta06826g.
- (41) Li, D.; Huang, L.; Liu, T.; Liu, J.; Zhen, L.; Wu, J.; Feng, Y. *Chemosphere* **2019**, *237*, 124527, DOI: 10.1016/j.chemosphere.2019.124527.
- (42) Saberi Safaei, T.; Mepham, A.; Zheng, X.; Pang, Y.; Dinh, C. T.; Liu, M.; Sinton, D.; Kelley, S. O.; Sargent, E. H. *Nano Lett.* **2016**, *16*, 7224–7228, DOI: 10.1021/acs.nanolett.6b03615.
- (43) Xiao, D.; Huang, C.; Luo, Y.; Tang, K.; Ruan, Q.; Wang, G.; Chu, P. K. *ACS Appl. Mater. Interfaces* **2020**, *12*, 2460–2468, DOI: 10.1021/acsami.9b18302.
- (44) Kim, S.; Dong, W. J.; Gim, S.; Sohn, W.; Park, J. Y.; Yoo, C. J.; Jang, H. W.; Lee, J. L. *Nano Energy* **2017**, *39*, 44–52, DOI: 10.1016/j.nanoen.2017.05.065.
- (45) Xia, Z.; Freeman, M.; Zhang, D.; Yang, B.; Lei, L.; Li, Z.; Hou, Y. *ChemElectroChem* **2018**, *5*, 253–259, DOI: 10.1002/celec.201700935.
- (46) Zhang, X.; Guo, S. X.; Gandionco, K. A.; Bond, A. M.; Zhang, J. *Mater. Today Adv.* **2020**, *7*, 100074, DOI: 10.1016/j.mtadv.2020.100074.
- (47) Niu, Z.; Becknell, N.; Yu, Y.; Kim, D.; Chen, C.; Kornienko, N.; Somorjai, G. A.; Yang, P. *Nat. Mater.* **2016**, *15*, 1188–1194, DOI: 10.1038/nmat4724.
- (48) Spöri, C.; Kwan, J. T. H.; Bonakdarpour, A.; Wilkinson, D. P.; Strasser, P. *Angew. Chemie* **2017**, *129*, 6088–6117, DOI: 10.1002/ange.201608601.
- (49) Li, C. W.; Ciston, J.; Kanan, M. W. *Nature* **2014**, *508*, 504–507, DOI: 10.1038/nature13249.
- (50) Lum, Y.; Yue, B.; Lobaccaro, P.; Bell, A. T.; Ager, J. W. *J. Phys. Chem. C* **2017**, *121*, 14191–14203, DOI: 10.1021/acs.jpcc.7b03673.
- (51) De Luna, P.; Quintero-Bermudez, R.; Dinh, C.-T.; Ross, M. B.; Bushuyev, O. S.; Todorović,

- P.; Regier, T.; Kelley, S. O.; Yang, P.; Sargent, E. H. *Nat. Catal.* **2018**, *1*, 103–110, DOI: 10.1038/s41929-017-0018-9.
- (52) Li, C. W.; Kanan, M. W. *J. Am. Chem. Soc.* **2012**, *134*, 7231–7234, DOI: 10.1021/ja3010978.
- (53) Chen, Y.; Li, C. W.; Kanan, M. W. *J. Am. Chem. Soc.* **2012**, *134*, 19969–19972, DOI: 10.1021/ja309317u.
- (54) Jiang, K.; Sandberg, R. B.; Akey, A. J.; Liu, X.; Bell, D. C.; Nørskov, J. K.; Chan, K.; Wang, H. *Nat. Catal.* **2018**, *1*, 111–119, DOI: 10.1038/s41929-017-0009-x.
- (55) Kim, D.; Kley, C. S.; Li, Y.; Yang, P. *Proc. Natl. Acad. Sci. U. S. A.* **2017**, *114*, 10560–10565, DOI: 10.1073/pnas.1711493114.
- (56) Li, Y.; Kim, D.; Louisia, S.; Xie, C.; Kong, Q.; Yu, S.; Lin, T.; Aloni, S.; Fakra, S. C.; Yang, P. *Proc. Natl. Acad. Sci.* **2020**, *117*, 9194–9201, DOI: 10.1073/pnas.1918602117.
- (57) K. Pattadar, D.; P. Zamborini, F. *J. Am. Chem. Soc.* **2018**, *140*, 14126–14133, DOI: 10.1021/jacs.8b06830.
- (58) T. Osowiecki, W.; J. Nussbaum, J.; A. Kamat, G.; Katsoukis, G.; Ledendecker, M.; Frei, H.; T. Bell, A.; Paul Alivisatos, A. *ACS Appl. Energy Mater.* **2019**, *2*, 7744–7749, DOI: 10.1021/acsaem.9b01714.
- (59) Manthiram, K.; Surendranath, Y.; Paul Alivisatos, A. *J. Am. Chem. Soc.* **2014**, *136*, 7237–7240, DOI: 10.1021/ja502628r.
- (60) Popović, S.; Smiljanić, M.; Jovanović, P.; Vavra, J.; Buonsanti, R.; Hodnik, N. *Angew. Chemie* **2020**, *132*, 14844–14854, DOI: 10.1002/ange.202000617.
- (61) Liu, L.; Corma, A. *Nat. Rev. Chem.* **2021**, *5*, 256–276, DOI: 10.1038/s41570-021-00255-8.
- (62) Kim, D.; Kley, C. S.; Li, Y.; Yang, P. *Proc. Natl. Acad. Sci.* **2017**, *114*, 10560–10565, DOI: 10.1073/pnas.1711493114.
- (63) Huang, J.; Hörmann, N.; Oveisi, E.; Loiudice, A.; De Gregorio, G. L.; Andreussi, O.; Marzari, N.; Buonsanti, R. *Nat. Commun.* **2018**, *9*, 3117, DOI: 10.1038/s41467-018-05544-3.
- (64) Eren, B.; Weatherup, R. S.; Liakakos, N.; Somorjai, G. A.; Salmeron, M. *J. Am. Chem. Soc.* **2016**, *138*, 8207–8211, DOI: 10.1021/jacs.6b04039.
- (65) O'Connor, C. R.; Duanmu, K.; Patel, D. A.; Muramoto, E.; van Spronsen, M. A.; Stacchiola,

- D.; Sykes, E. C. H.; Sautet, P.; Madix, R. J.; Friend, C. M. *Proc. Natl. Acad. Sci.* **2020**, *117*, 22657–22664, DOI: 10.1073/pnas.2010413117.
- (66) Wang, J.; McEntee, M.; Tang, W.; Neurock, M.; Baddorf, A. P.; Maksymovych, P.; Yates, J. T. *J. Am. Chem. Soc.* **2016**, *138*, 1518–1526, DOI: 10.1021/jacs.5b09052.
- (67) Cinquini, F.; Delbecq, F.; Sautet, P. *Phys. Chem. Chem. Phys.* **2009**, *11*, 11546, DOI: 10.1039/b914418h.
- (68) Henkelman, G.; Uberuaga, B. P.; Jónsson, H. *J. Chem. Phys.* **2000**, *113*, 9901–9904, DOI: 10.1063/1.1329672.
- (69) Li, M.; Hua, B.; Wang, L.-C.; Sugar, J. D.; Wu, W.; Ding, Y.; Li, J.; Ding, D. *Nat. Catal.* **2021**, *4*, 274–283, DOI: 10.1038/s41929-021-00590-5.
- (70) Wang, Y.-G.; C. Cantu, D.; Lee, M.-S.; Li, J.; Glezakou, V.-A.; Rousseau, R. *J. Am. Chem. Soc.* **2016**, *138*, 10467–10476, DOI: 10.1021/jacs.6b04187.
- (71) Li, F.; Medvedeva, X. V.; Medvedev, J. J.; Khairullina, E.; Engelhardt, H.; Chandrasekar, S.; Guo, Y.; Jin, J.; Lee, A.; Thérien-Aubin, H.; Ahmed, A.; Pang, Y.; Klinkova, A. *Nat. Catal.* **2021**, *4*, 479–487, DOI: 10.1038/s41929-021-00624-y.
- (72) Gao, F.; Hu, S.; Zhang, X.; Zheng, Y.; Wang, H.; Niu, Z.; Yang, P.; Bao, R.; Ma, T.; Dang, Z.; Guan, Y.; Zheng, X.; Zheng, X.; Zhu, J.; Gao, M.; Yu, S. *Angew. Chemie* **2020**, *132*, 8784–8790, DOI: 10.1002/ange.201912348.
- (73) Tran-Phu, T.; Daiyan, R.; Fusco, Z.; Ma, Z.; Rahim, L. R. A.; Kiy, A.; Kluth, P.; Guo, X.; Zhu, Y.; Chen, H.; Amal, R.; Tricoli, A. *J. Mater. Chem. A* **2020**, *8*, 11233–11245, DOI: 10.1039/d0ta01723j.
- (74) Saraj, C. S.; Singh, S. C.; Verma, G.; Rahul, A. R.; Wei, L.; Guo, C. *Opto-electronic Adv.* **2021**, *1*, 1, DOI: <https://doi.org/10.48550/arXiv.2112.07044>.
- (75) Ni, W.; Xue, Y.; Zang, X.; Li, C.; Wang, H.; Yang, Z.; Yan, Y. M. *ACS Nano* **2020**, *14*, 2014–2023, DOI: 10.1021/acsnano.9b08528.
- (76) Niu, Z. Z.; Gao, F. Y.; Zhang, X. L.; Yang, P. P.; Liu, R.; Chi, L. P.; Wu, Z. Z.; Qin, S.; Yu, X.; Gao, M. R. *J. Am. Chem. Soc.* **2021**, *143*, 8011–8021, DOI: 10.1021/jacs.1c01190.
- (77) Yang, P. P.; Zhang, X. L.; Gao, F. Y.; Zheng, Y. R.; Niu, Z. Z.; Yu, X.; Liu, R.; Wu, Z. Z.;

- Qin, S.; Chi, L. P.; Duan, Y.; Ma, T.; Zheng, X. S.; Zhu, J. F.; Wang, H. J.; Gao, M. R.; Yu, S. *H. J. Am. Chem. Soc.* **2020**, *142*, 6400–6408, DOI: 10.1021/jacs.0c01699.
- (78) Cho, K. M.; Jung, W. Bin; Kim, D.; Kim, J. Y.; Kim, Y.; Yun, G. T.; Ryu, S.; Al-Saggaf, A.; Gereige, I.; Jung, H. T. *J. Mater. Chem. A* **2020**, *8*, 14592–14599, DOI: 10.1039/d0ta03400b.
- (79) Zhou, Y.; Chen, S.; Xi, S.; Wang, Z.; Deng, P.; Yang, F.; Han, Y.; Pang, Y.; Xia, B. Y. *Cell Reports Phys. Sci.* **2020**, *1*, 100182, DOI: 10.1016/j.xcrp.2020.100182.
- (80) Liu, C.; Zhang, M.; Li, J.; Xue, W.; Zheng, T.; Xia, C.; Zeng, J. *Angew. Chem. Int. Ed. Engl.* **2022**, *61*, e202113498, DOI: 10.1002/anie.202113498.
- (81) LaGrow, A. P.; Sinatra, L.; Elshewy, A.; Huang, K.-W.; Katsiev, K.; Kirmani, A. R.; Amassian, A.; Anjum, D. H.; Bakr, O. M. *J. Phys. Chem. C* **2014**, *118*, 19374–19379, DOI: 10.1021/jp503612k.
- (82) Cai, R.; Yang, D.; Peng, S.; Chen, X.; Huang, Y.; Liu, Y.; Hou, W.; Yang, S.; Liu, Z.; Tan, W. *J. Am. Chem. Soc.* **2015**, *137*, 13957–13963, DOI: 10.1021/jacs.5b09337.
- (83) Khairullina, E.; Mosina, K.; Choueiri, R. M.; Paradis, A. P.; Petruk, A. A.; Sciaini, G.; Krivoschapkina, E.; Lee, A.; Ahmed, A.; Klinkova, A. *Nanoscale* **2019**, *11*, 44, DOI: 10.1039/c8nr09731c.
- (84) Choi, S.; Moon, Y.; Yoo, H. *J. Colloid Interface Sci.* **2016**, *469*, 269–276, DOI: 10.1016/J.JCIS.2016.02.019.
- (85) Klinkova, A.; M. Larin, E.; Prince, E.; H. Sargent, E.; Kumacheva, E. *Chem. Mater.* **2016**, *28*, 3196–3202, DOI: 10.1021/acs.chemmater.6b00936.
- (86) Min, X.; Chen, Y.; Kanan, M. W. *Phys. Chem. Chem. Phys.* **2014**, *16*, 13601–13604, DOI: 10.1039/C4CP01337A.
- (87) Kresse, G.; Hafner, J. *Phys. Rev. B* **1993**, *47*, 558–561, DOI: 10.1103/PhysRevB.47.558.
- (88) Kresse, G.; Furthmüller, J. *Comput. Mater. Sci.* **1996**, *6*, 15–50, DOI: 10.1016/0927-0256(96)00008-0.
- (89) Kresse, G.; Furthmüller, J. *Phys. Rev. B* **1996**, *54*, 11169–11186, DOI: 10.1103/PhysRevB.54.11169.
- (90) Payne, M. C.; Teter, M. P.; Allan, D. C.; Arias, T. A.; Joannopoulos, J. D. *Rev. Mod. Phys.*

- 1992**, *64*, 1045–1097, DOI: 10.1103/RevModPhys.64.1045.
- (91) Blöchl, P. E. *Phys. Rev. B* **1994**, *50*, 17953–17979, DOI: 10.1103/PhysRevB.50.17953.
- (92) Joubert, D. *Phys. Rev. B - Condens. Matter Mater. Phys.* **1999**, *59*, 1758–1775, DOI: 10.1103/PhysRevB.59.1758.
- (93) Monkhorst, H. J.; Pack, J. D. *Phys. Rev. B* **1976**, *13*, 5188–5192, DOI: 10.1103/PhysRevB.13.5188.
- (94) Presnyakov, A. A.; Dautova, L. I.; Dzhanbusinov, E. A. *APL. Mater.* **1963**, *16*, 52–55, .
- (95) Bader, R. F. W. *Chem. Rev.* **1991**, *91*, 893–928, DOI: 10.1021/cr00005a013.
- (96) Tang, W.; Sanville, E.; Henkelman, G. *J. Phys. Condens. Matter* **2009**, *21*, 084204, DOI: 10.1088/0953-8984/21/8/084204.
- (97) Nosé, S. *J. Chem. Phys.* **1984**, *81*, 511–519, DOI: 10.1063/1.447334.
- (98) Hoover, W. G. *Phys. Rev. A* **1985**, *31*, 1695–1697, DOI: 10.1103/PhysRevA.31.1695.
- (99) Nosé, S. *Prog. Theor. Phys. Suppl.* **1991**, *103*, 1–46, DOI: 10.1143/PTPS.103.1.
- (100) Gafner, S. L.; Redel, L. V.; Gafner, Y. Y. *J. Exp. Theor. Phys.* **2009**, *108*, 784–799, DOI: 10.1134/S1063776109050070.
- (101) Bard, A. J.; Faulkner, L. R. *Electrochemical Methods : Fundamentals and Applications*, 2nd ed.; Harris, D., Ed.; John Wiley & Sons, Inc.: New York, 2001.
- (102) Wang, H.; Pilon, L. *J. Phys. Chem. C* **2011**, *115*, 16711–16719, DOI: 10.1021/jp204498e.
- (103) Kilic, M. S.; Bazant, M. Z.; Ajdari, A. *Phys. Rev. E - Stat. Nonlinear, Soft Matter Phys.* **2007**, *75*, 1–14, DOI: 10.1103/PhysRevE.75.021503.
- (104) Borukhov, I.; Andelman, D.; Orland, H. *Phys. Rev. Lett.* **1997**, *79*, 435–438, DOI: 10.1103/PhysRevLett.79.435.
- (105) Booth, F. *J. Chem. Phys.* **1951**, *19*, 391–394, DOI: 10.1063/1.1748233.
- (106) Booth, F. *J. Chem. Phys.* **1955**, *23*, 453–457, DOI: 10.1063/1.1742009.
- (107) Paunov, V. N.; Dimova, R. I.; Kralchevsky, P. A.; Broze, G.; Mehreteab, A. *J. Colloid Interface Sci.* **1996**, *182*, 239–248, DOI: 10.1006/jcis.1996.0456.

- (108) Aguilera-Arzo, M.; Andrio, A.; Aguilera, V. M.; Alcaraz, A. *Phys. Chem. Chem. Phys.* **2009**, *11*, 358–365, DOI: 10.1039/B812775A.
- (109) Serway Jewett, John W., R. A. *Principles of Physics*; Saunders College Publ.: Fort Worth, Tex., 1998.
- (110) Matula, R. A. *J. Phys. Chem. Ref. Data* **1979**, *8*, 1147–1298, DOI: 10.1063/1.555614.
- (111) Basiratnia, A.; Rempel, J.; Li, F.; Pogodaev, A.; Zienchuk, T. A.; Klinkova, A. *Phys. Chem. Chem. Phys.* **2019**, *21*, 5894–5897, DOI: 10.1039/c8cp07891b.
- (112) Persson, K. A.; Waldwick, B.; Lazic, P.; Ceder, G. *Phys. Rev. B* **2012**, *85*, 235438, DOI: 10.1103/PhysRevB.85.235438.
- (113) Korzhavyi, P. A.; Soroka, I. L.; Isaev, E. I.; Lilja, C.; Johansson, B. *Proc. Natl. Acad. Sci.* **2012**, *109*, 686–689, DOI: 10.1073/pnas.1115834109.
- (114) De Luna, P.; Quintero-Bermudez, R.; Dinh, C.-T.; Ross, M. B.; Bushuyev, O. S.; Todorović, P.; Regier, T.; Kelley, S. O.; Yang, P.; Sargent, E. H. *Nat. Catal.* **2018**, *1*, 103–110, DOI: 10.1038/s41929-017-0018-9.
- (115) Roberts, F. S.; Kuhl, K. P.; Nilsson, A. *Angew. Chemie Int. Ed.* **2015**, *54*, 5179–5182, DOI: 10.1002/anie.201412214.
- (116) Gao, D.; Zegkinoglou, I.; J. Divins, N.; Scholten, F.; Sinev, I.; Grosse, P.; Roldan Cuenya, B. *ACS Nano* **2017**, *11*, 4825–4831, DOI: 10.1021/acsnano.7b01257.
- (117) Durand, W. J.; Peterson, A. A.; Studt, F.; Abild-Pedersen, F.; Nørskov, J. K. *Surf. Sci.* **2011**, *605*, 1354–1359, DOI: 10.1016/J.SUSC.2011.04.028.
- (118) Wen, Y. N.; Zhang, J. M. *Solid State Commun.* **2007**, *144*, 163–167, DOI: 10.1016/j.ssc.2007.07.012.
- (119) Tao, A. R.; Habas, S.; Yang, P. *Small* **2008**, *4*, 310–325, DOI: 10.1002/smll.200701295.
- (120) Yoo, S.-H.; Lee, J.-H.; Delley, B.; Soon, A. *Phys. Chem. Chem. Phys.* **2014**, *16*, 18570–18577, DOI: 10.1039/C4CP02384F.
- (121) Redmond, P. L.; Hallock, A. J.; Brus, L. E. *Nano Lett.* **2005**, *5*, 131–135, DOI: 10.1021/nl048204r.
- (122) Plieth, W. J. *J. Phys. Chem.* **1982**, *86*, 3166–3170, DOI: 10.1021/j100213a020.

- (123) Burdyny, T.; Graham, P. J.; Pang, Y.; Dinh, C.-T.; Liu, M.; Sargent, E. H.; Sinton, D. *ACS Sustain. Chem. Eng.* **2017**, *5*, 4031–4040, DOI: 10.1021/acssuschemeng.7b00023.
- (124) Herrero, E.; Buller, L. J.; Abruña, H. D. *Chem. Rev.* **2001**, *101*, 1897–1930, DOI: 10.1021/cr9600363.
- (125) Hamelin, A. *J. Electroanal. Chem. Interfacial Electrochem.* **1979**, *101*, 285–290, DOI: 10.1016/S0022-0728(79)80242-9.
- (126) Hamelin, A.; Katayama, A. *J. Electroanal. Chem. Interfacial Electrochem.* **1981**, *117*, 221–232, DOI: 10.1016/S0022-0728(81)80084-8.
- (127) Hamelin, A. *J. Electroanal. Chem.* **1984**, *165*, 167–180, DOI: 10.1016/S0022-0728(84)80095-9.
- (128) Hamelin, A.; Lipkowski, J. *J. Electroanal. Chem. Interfacial Electrochem.* **1984**, *171*, 317–330, DOI: 10.1016/0022-0728(84)80123-0.
- (129) Hernández, J.; Solla-Gullón, J.; Herrero, E. *J. Electroanal. Chem.* **2004**, *574*, 185–196, DOI: 10.1016/j.jelechem.2003.10.039.
- (130) Shah, A. H.; Wang, Y.; Woldu, A. R.; Lin, L.; Iqbal, M.; Cahen, D.; He, T. *J. Phys. Chem. C* **2018**, *122*, 18528–18536, DOI: 10.1021/acs.jpcc.8b05348.
- (131) Calvino, K. U. D.; Laursen, A. B.; Yap, K. M. K.; Goetjen, T. A.; Hwang, S.; Murali, N.; Mejia-Sosa, B.; Lubarski, A.; Teeluck, K. M.; Hall, E. S.; Garfunkel, E.; Greenblatt, M.; Dismukes, G. C. *Energy Environ. Sci.* **2018**, *11*, 2550–2559, DOI: 10.1039/C8EE00936H.
- (132) Li, F.; Zhou, C.; Feygin, E.; Roy, P.-N.; Chen, L. D.; Klinkova, A. *Phys. Chem. Chem. Phys.* **2022**, DOI: 10.1039/D2CP02075K.
- (133) Sen, S.; Liu, D.; Palmore, G. T. R. *ACS Catal.* **2014**, *4*, 3091–3095, DOI: 10.1021/cs500522g.
- (134) Lu, Q.; Rosen, J.; Zhou, Y.; Hutchings, G. S.; Kimmel, Y. C.; Chen, J. G.; Jiao, F. *Nat. Commun.* **2014**, *5*, 1–6, DOI: 10.1038/ncomms4242.
- (135) Feng, X.; Jiang, K.; Fan, S.; Kanan, M. W. *J. Am. Chem. Soc.* **2015**, *137*, 4606–4609, DOI: 10.1021/ja5130513.
- (136) He, Q.; Lee, J. H.; Liu, D.; Liu, Y.; Lin, Z.; Xie, Z.; Hwang, S.; Kattel, S.; Song, L.; Chen, J. G. *Adv. Funct. Mater.* **2020**, *30*, 1–8, DOI: 10.1002/adfm.202000407.

- (137) Ma, S.; Sadakiyo, M.; Heim, M.; Luo, R.; Haasch, R. T.; Gold, J. I.; Yamauchi, M.; Kenis, P. J. A. *J. Am. Chem. Soc.* **2017**, *139*, 47–50, DOI: 10.1021/jacs.6b10740.
- (138) Capelo, R. G.; Leppert, L.; Albuquerque, R. Q. *J. Phys. Chem. C* **2014**, *118*, 21647–21654, DOI: 10.1021/jp5058258.
- (139) Nanba, Y.; Tsutsumi, T.; Ishimoto, T.; Koyama, M. *J. Phys. Chem. C* **2017**, *121*, 14611–14617, DOI: 10.1021/acs.jpcc.7b03137.
- (140) Johansson, M.; Skúlason, E.; Nielsen, G.; Murphy, S.; Nielsen, R. M.; Chorkendorff, I. *Surf. Sci.* **2010**, *604*, 718–729, DOI: 10.1016/j.susc.2010.01.023.
- (141) *CRC Handbook of Chemistry and Physics*, 102nd Edit.; Rumble, J. R., Ed.; CRC Press/Taylor & Francis, Boca Raton, 2021.
- (142) Hori, Y.; Wakebe, H.; Tsukamoto, T.; Koga, O. *Electrochim. Acta* **1994**, *39*, 1833–1839, DOI: 10.1016/0013-4686(94)85172-7.
- (143) Loiudice, A.; Lobaccaro, P.; Kamali, E. A.; Thao, T.; Huang, B. H.; Ager, J. W.; Buonsanti, R. *Angew. Chemie - Int. Ed.* **2016**, *55*, 5789–5792, DOI: 10.1002/anie.201601582.
- (144) Pang, Y.; Li, J.; Wang, Z.; Tan, C. S.; Hsieh, P. L.; Zhuang, T. T.; Liang, Z. Q.; Zou, C.; Wang, X.; De Luna, P.; Edwards, J. P.; Xu, Y.; Li, F.; Dinh, C. T.; Zhong, M.; Lou, Y.; Wu, D.; Chen, L. J.; Sargent, E. H.; Sinton, D. *Nat. Catal.* **2019**, *2*, 251–258, DOI: 10.1038/s41929-019-0225-7.
- (145) Sandberg, R. B.; Montoya, J. H.; Chan, K.; Nørskov, J. K. *Surf. Sci.* **2016**, *654*, 56–62, DOI: 10.1016/j.susc.2016.08.006.
- (146) Bohra, D.; Chaudhry, J. H.; Burdyny, T.; Pidko, E. A.; Smith, W. A. *Energy Environ. Sci.* **2019**, *12*, 3380–3389, DOI: 10.1039/c9ee02485a.
- (147) Chen, Q. X.; Liu, Y. H.; Qi, X. Z.; Liu, J. W.; Jiang, H. J.; Wang, J. L.; He, Z.; Ren, X. F.; Hou, Z. H.; Yu, S. H. *J. Am. Chem. Soc.* **2019**, *141*, 10729–10735, DOI: 10.1021/jacs.9b03617.
- (148) Shukla, A.; Rehage, H. *Langmuir* **2008**, *24*, 8507–8513, DOI: 10.1021/la800816e.
- (149) Helmholtz, H. *Ann. der Phys. und Chemie* **1879**, *243*, 337–382, DOI: 10.1002/andp.18792430702.

- (150) Grahame, D. C. *Chem. Rev.* **1947**, *41*, 441–501, DOI: 10.1021/cr60130a002.
- (151) Gouy, M. *J. Phys. Théorique Appliquée* **1910**, *9*, 457–468, DOI: 10.1051/jphystap:019100090045700.
- (152) Chapman, D. L. *London, Edinburgh, Dublin Philos. Mag. J. Sci.* **1913**, *25*, 475–481, DOI: 10.1080/14786440408634187.
- (153) Waegele, M. M.; Gunathunge, C. M.; Li, J.; Li, X. *J. Chem. Phys.* **2019**, *151*, 160902, DOI: 10.1063/1.5124878.
- (154) Stern, O. *Zeitschrift fur Elektrochemie* **1924**, *30*, 508–516, DOI: <https://doi.org/10.1002/bbpc.192400182>.
- (155) Nakamura, M.; Sato, N.; Hoshi, N.; Sakata, O. *ChemPhysChem* **2011**, *12*, 1430–1434, DOI: 10.1002/cphc.201100011.
- (156) Favaro, M.; Jeong, B.; Ross, P. N.; Yano, J.; Hussain, Z.; Liu, Z.; Crumlin, E. J. *Nat. Commun.* **2016**, *7*, 1–8, DOI: 10.1038/ncomms12695.
- (157) Yasunaga, H.; Natori, A. *Surf. Sci. Rep.* **1992**, *15*, 205–280, DOI: 10.1016/0167-5729(92)90007-X.
- (158) Song, T. Bin; Chen, Y.; Chung, C. H.; Yang, Y.; Bob, B.; Duan, H. S.; Li, G.; Tu, K. N.; Huang, Y. *ACS Nano* **2014**, *8*, 2804–2811, DOI: 10.1021/nn4065567.
- (159) Peljo, P.; Manzanares, J. A.; Girault, H. H. *Chem. Sci.* **2017**, *8*, 4795–4803, DOI: 10.1039/c7sc00848a.
- (160) Le, J.; Iannuzzi, M.; Cuesta, A.; Cheng, J. *Phys. Rev. Lett.* **2017**, *119*, 016801, DOI: 10.1103/PhysRevLett.119.016801.
- (161) Clark, M. L.; Ge, A.; Videla, P. E.; Rudshiteyn, B.; Miller, C. J.; Song, J.; Batista, V. S.; Lian, T.; Kubiak, C. P. *J. Am. Chem. Soc.* **2018**, *140*, 17643–17655, DOI: 10.1021/jacs.8b09852.
- (162) Nightingale, E. R. *J. Phys. Chem.* **1959**, *63*, 1381–1387, DOI: 10.1021/j150579a011.
- (163) Xia, Y.; Xiong, Y.; Lim, B.; Skrabalak, S. E. *Angew. Chemie Int. Ed.* **2009**, *48*, 60–103, DOI: 10.1002/anie.200802248.
- (164) Che, F.; Gray, J. T.; Ha, S.; Kruse, N.; Scott, S. L.; McEwen, J.-S. *ACS Catal.* **2018**, *8*, 5153–5174, DOI: 10.1021/acscatal.7b02899.

- (165) Ceric, H.; De Orio, R. L.; Zisser, W. H.; Selberherr, S. Ab Initio Method for Electromigration Analysis. In *2012 19th IEEE International Symposium on the Physical and Failure Analysis of Integrated Circuits*; IEEE, 2012; pp 1–4.
- (166) Stoffelsma, C.; Rodriguez, P.; Garcia, G.; Garcia-Araez, N.; Strmcnik, D.; Marković, N. M.; Koper, M. T. M. *J. Am. Chem. Soc.* **2010**, *132*, 16127–16133, DOI: 10.1021/ja106389k.
- (167) Chen, L. D.; Urushihara, M.; Chan, K.; Nørskov, J. K. *ACS Catal.* **2016**, *6*, 7133–7139, DOI: 10.1021/acscatal.6b02299.
- (168) Frumkin, A. N. *Trans. Faraday Soc.* **1959**, *55*, 156–167, DOI: 10.1039/tf9595500156.
- (169) Chiu, Y. T.; Liu, C. H.; Lin, K. L.; Lai, Y. S. *Scr. Mater.* **2011**, *65*, 615–617, DOI: 10.1016/j.scriptamat.2011.06.041.
- (170) Chiu, Y. T.; Lin, K. L.; Wu, A. T.; Jang, W. L.; Dong, C. L.; Lai, Y. S. *J. Alloys Compd.* **2013**, *549*, 190–194, DOI: 10.1016/j.jallcom.2012.08.138.
- (171) Wu, A. T.; Gusak, A. M.; Tu, K. N.; Kao, C. R. *Appl. Phys. Lett.* **2005**, *86*, 1–3, DOI: 10.1063/1.1941456.
- (172) Chen, K.; Tamura, N.; Valek, B. C.; Tu, K. N. *J. Appl. Phys.* **2008**, *104*, 013513, DOI: 10.1063/1.2952073.
- (173) Valek, B. C.; Tamura, N.; Spolenak, R.; Caldwell, W. A.; MacDowell, A. A.; Celestre, R. S.; Padmore, H. A.; Bravman, J. C.; Batterman, B. W.; Nix, W. D.; Patel, J. R. *J. Appl. Phys.* **2003**, *94*, 3757–3761, DOI: 10.1063/1.1600843.
- (174) Budiman, A. S.; Nix, W. D.; Tamura, N.; Valek, B. C.; Gadre, K.; Maiz, J.; Spolenak, R.; Patel, J. R. *Appl. Phys. Lett.* **2006**, *88*, 2004–2007, DOI: 10.1063/1.2210451.
- (175) Takahashi, Y.; Nishino, Y.; Furukawa, H.; Kubo, H.; Yamauchi, K.; Ishikawa, T.; Matsubara, E. *J. Appl. Phys.* **2009**, *105*, 124911, DOI: 10.1063/1.3151855.
- (176) Lin, S. K.; Liu, Y. C.; Chiu, S. J.; Liu, Y. T.; Lee, H. Y. *Sci. Rep.* **2017**, *7*, 1–10, DOI: 10.1038/s41598-017-03324-5.

Appendices

Appendix A: Optimized geometry structures

A.1 Optimized geometry structures for initial, transition and final states of metal atom migration

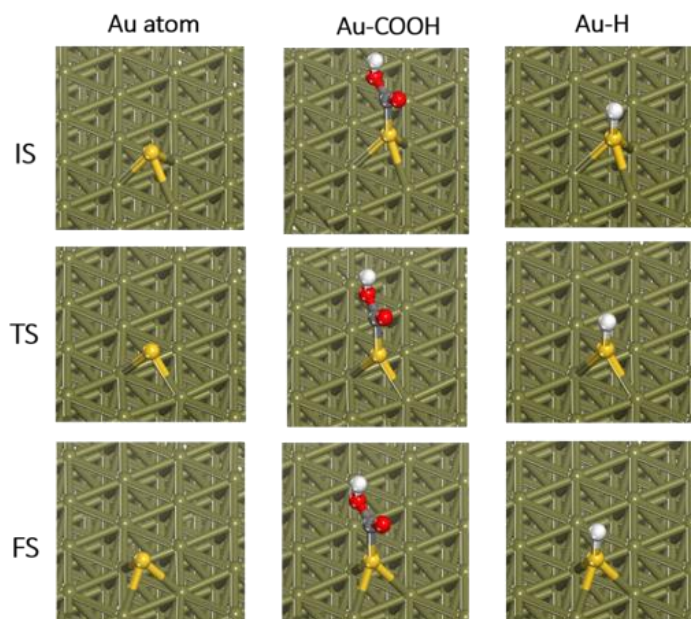


Figure A.1: Optimized geometry structures for initial, transition and final states of migration for Au atom and intermediate-bound Au atoms of Au-COOH(CO₂RR) and Au-H(HER) on Au(111) surface respectively. The olive color atoms represent Au substrate surfaces, with yellow, grey, red and white color atoms representing hopping Au, C, O and H atoms respectively. Reprinted with permission from ref. [71]. Copyright 2021, Springer Nature.

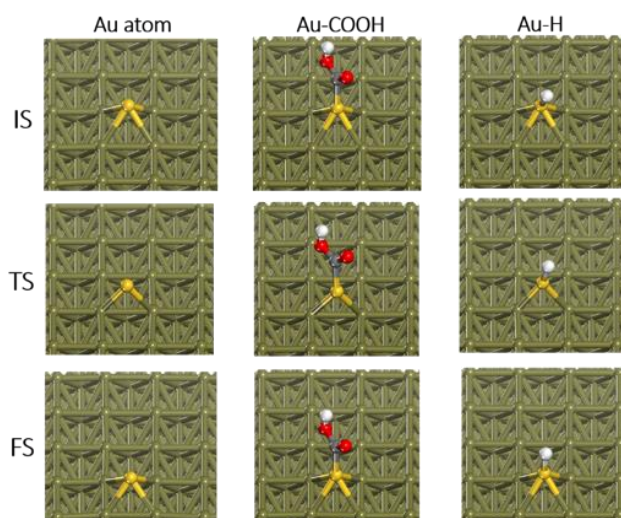


Figure A.2: Optimized geometry structures for initial, transition and final states of migration for Au atom and intermediate-bound Au atoms of Au-COOH(CO₂RR) and Au-H(HER) on Au(100) surface, respectively. Reprinted with permission from ref. [71]. Copyright 2021, Springer Nature.

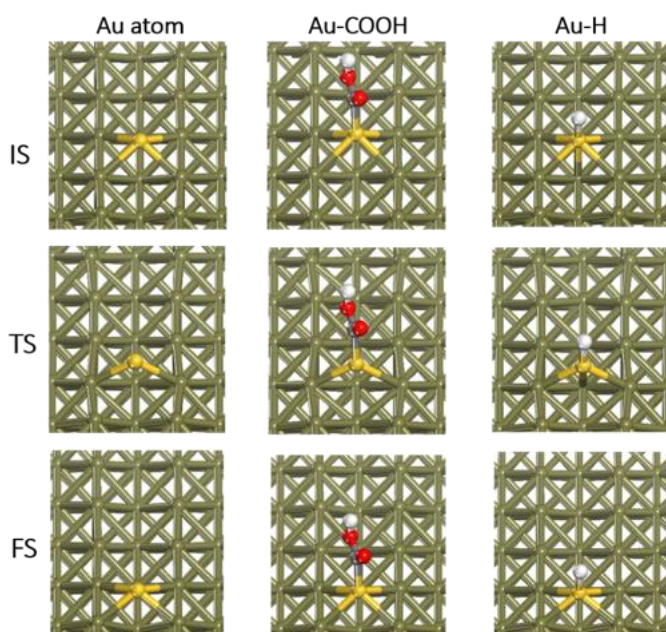


Figure A.3: Optimized geometry structures for initial, transition and final states of migration for Au atom and intermediate-bound Au atoms of Au-COOH(CO₂RR) and Au-H(HER) on Au(110) surface, respectively. Reprinted with permission from ref. [71]. Copyright 2021, Springer Nature.

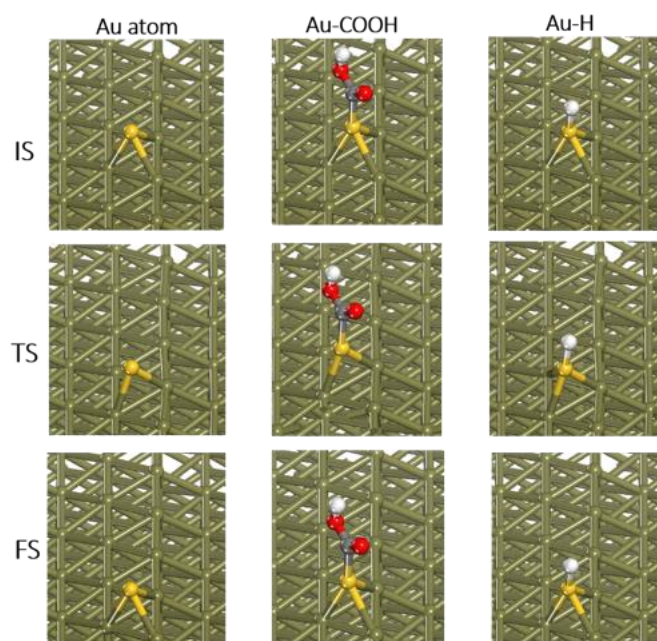


Figure A.4: Optimized geometry structures for initial, transition and final states of migration for Au atom and intermediate-bound Au atoms of Au-COOH(CO₂RR) and Au-H(HER) on Au(211) surface, respectively. Reprinted with permission from ref. [71]. Copyright 2021, Springer Nature.

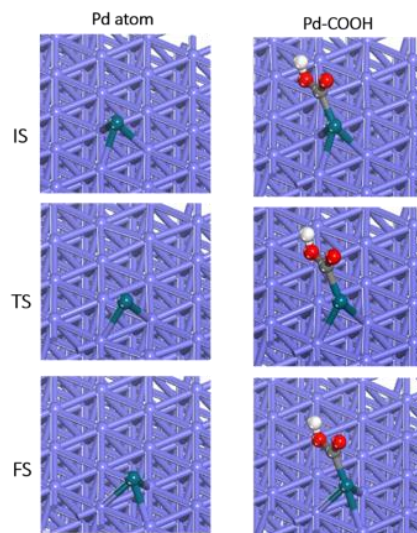


Figure A.5: Optimized geometry structures for initial, transition and final states of migration for Pd atom and intermediate-bound Pd atom of Pd-COOH(CO₂RR) on Pd(111) surface respectively. The lavender color atoms represent Pd surfaces, with teal, grey, red and white color atoms representing hooping Au, C, O and H atoms, respectively. Reprinted with permission from ref. [71]. Copyright 2021, Springer Nature.

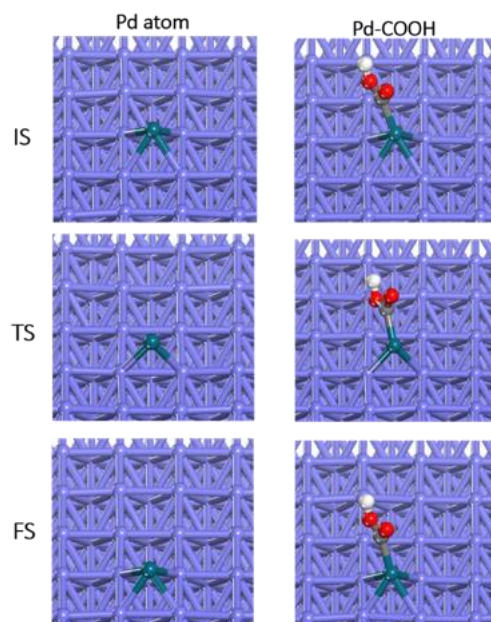


Figure A.6: Optimized geometry structures for initial, transition and final states of migration for Pd atom and intermediate-bound Pd atom of Pd-COOH(CO₂RR) on Pd(100) surface, respectively. Reprinted with permission from ref. [71]. Copyright 2021, Springer Nature.

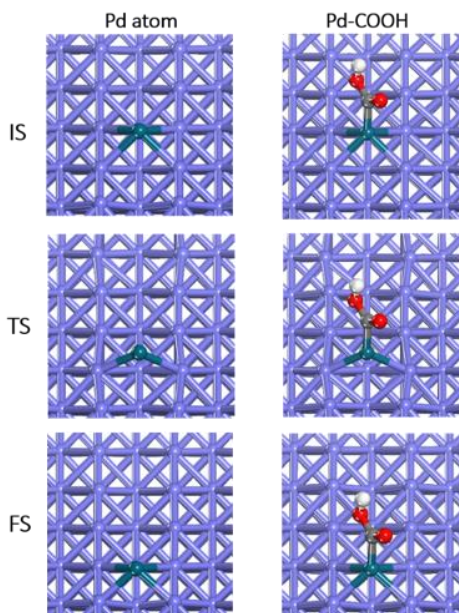


Figure A.7: Optimized geometry structures for initial, transition and final states of migration for Pd atom and intermediate-bound Pd atom of Pd-COOH(CO₂RR) on Pd(110) surface, respectively. Reprinted with permission from ref. [71]. Copyright 2021, Springer Nature.

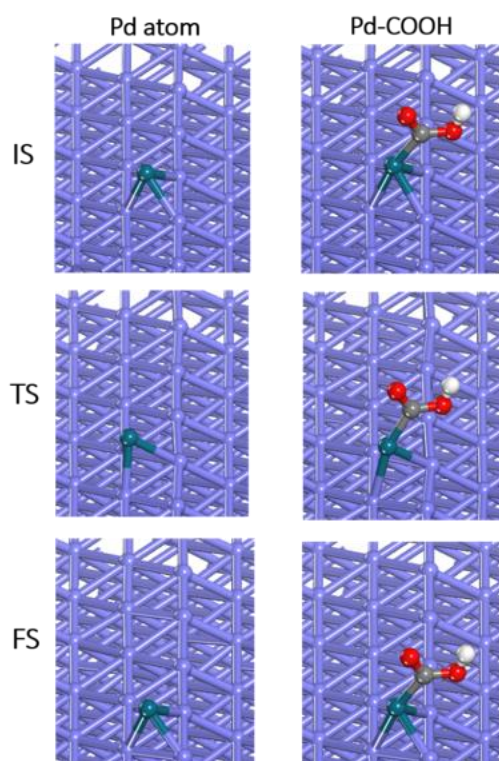


Figure A.8: Optimized geometry structures for initial, transition and final states of migration for Pd atom and intermediate-bound Pd atom of Pd-COOH(CO₂RR) on Pd(211) surface, respectively. Reprinted with permission from ref. [71]. Copyright 2021, Springer Nature.

A.2 Optimized geometry structures for reaction-intermediate-adsorbed metal surfaces

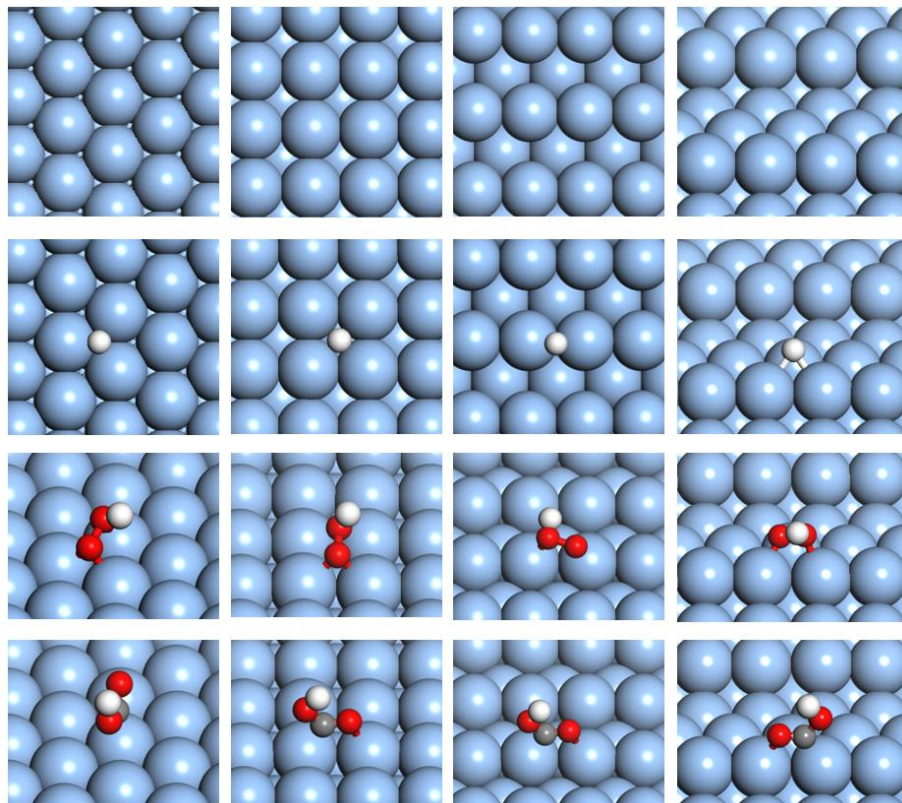


Figure A.9: Optimized geometries of Ag(111), Ag(100), Ag(110), and Ag(211) surfaces without (top panels) and with (bottom panels) adsorbed *H, *OOH and *COOH. Reprinted with permission from ref. [132]. Copyright 2022, Royal Society of Chemistry.

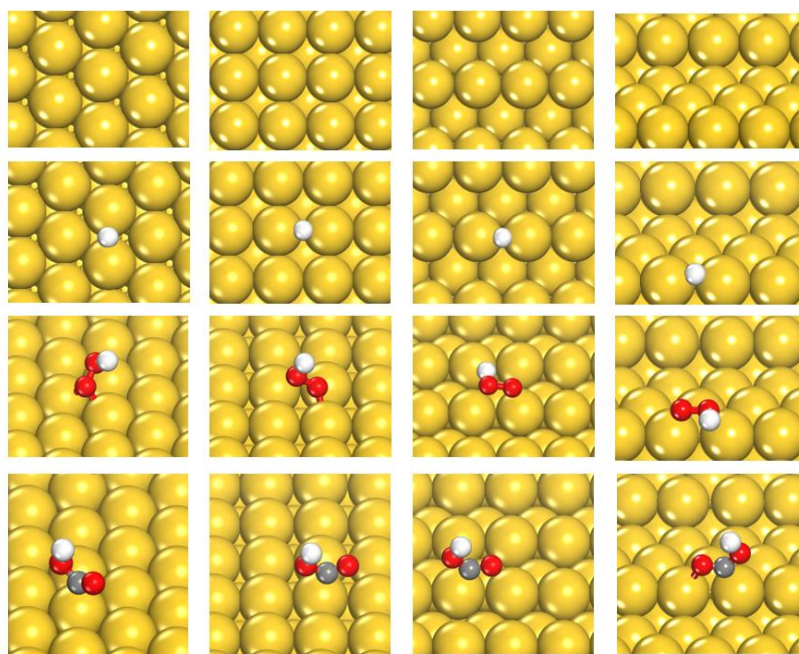


Figure A.10: Optimized geometries of on Au(111), Au(100), Au(110), and Au(211) surfaces without (top panels) and with (bottom panels) absorbed $*\text{H}$, $*\text{OOH}$ and $*\text{COOH}$. Reprinted with permission from ref. [132]. Copyright 2022, Royal Society of Chemistry.

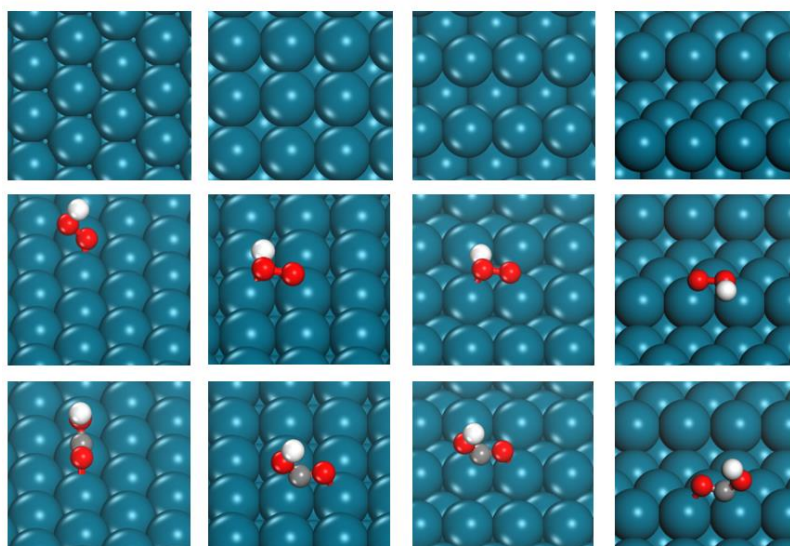


Figure A.11: Optimized geometries of Pd(111), Pd(100), Pd(110), and Pd(211) surfaces without (top panels) and with (bottom panels) absorbed $*\text{OOH}$ and $*\text{COOH}$. Reprinted with permission from ref. [132]. Copyright 2022, Royal Society of Chemistry.

A.3 Optimized geometry structures for metal surfaces with single atom vacancy

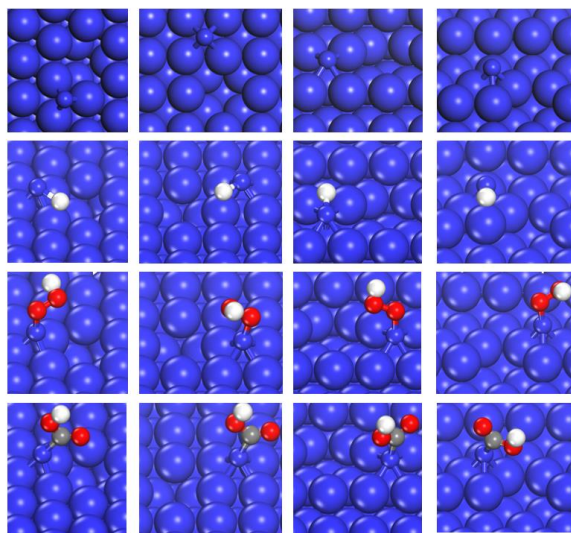


Figure A.12: Optimized singe-atom vacancy on Cu(111), Cu(100), Cu(110), and Cu(211) surfaces without (top panels) and with (bottom panels) absorbed *H, *OOH and *COOH. Reprinted with permission from ref. [132]. Copyright 2022, Royal Society of Chemistry.

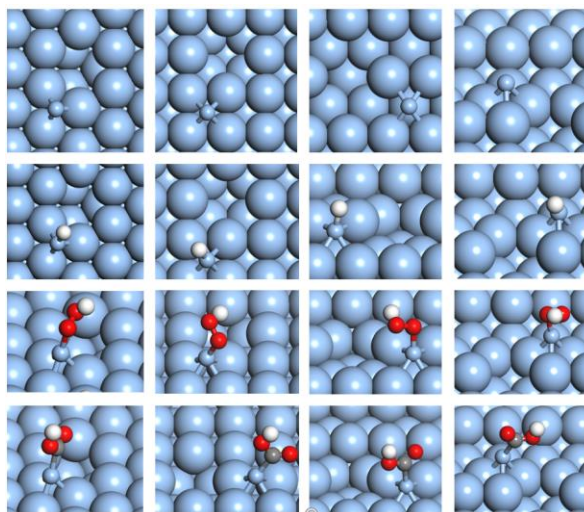


Figure A.13: Optimized singe-atom vacancy on Ag(111), Ag(100), Ag(110), and Ag(211) surfaces without (top panels) and with (bottom panels) absorbed *H, *OOH and *COOH. Reprinted with permission from ref. [132]. Copyright 2022, Royal Society of Chemistry.

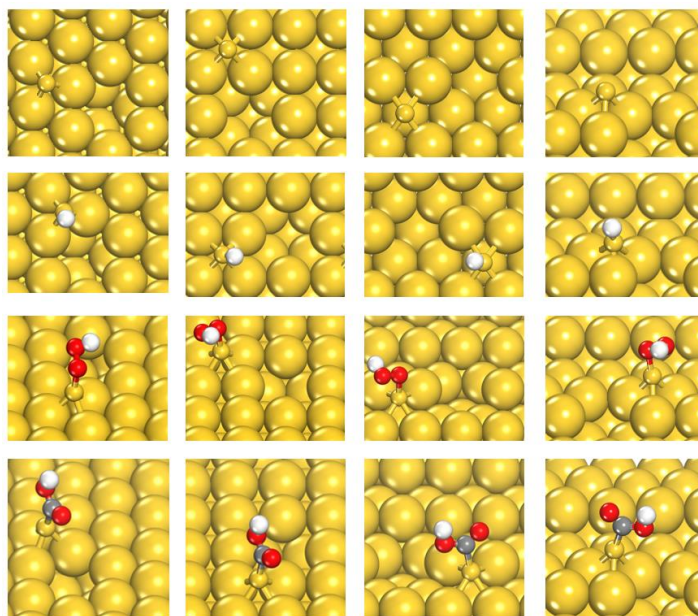


Figure A.14: Optimized singe-atom vacancy on Au(111), Au(100), Au(110), and Au(211) surfaces without (top panels) and with (bottom panels) absorbed *H, *OOH and *COOH. Reprinted with permission from ref. [132]. Copyright 2022, Royal Society of Chemistry.

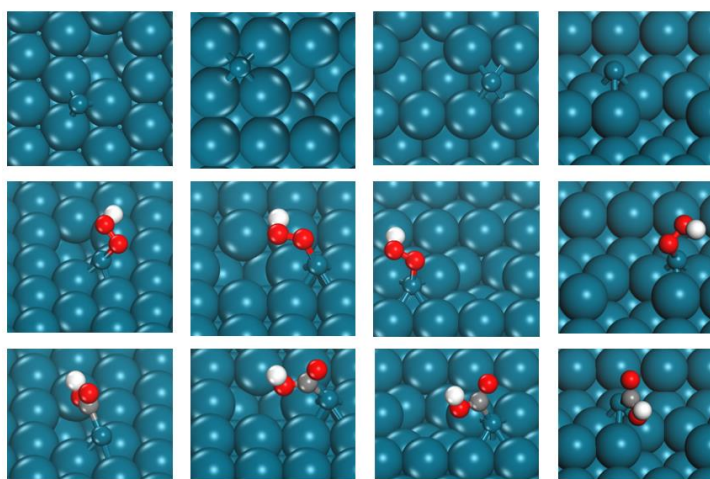


Figure A.15: Optimized singe-atom vacancy on Pd(111), Pd((100), Pd((110), and Pd((211) surfaces without (top panels) and with (bottom panels) absorbed *OOH and *COOH. Reprinted with permission from ref. [132]. Copyright 2022, Royal Society of Chemistry.

Appendix B: Calculated energy barriers

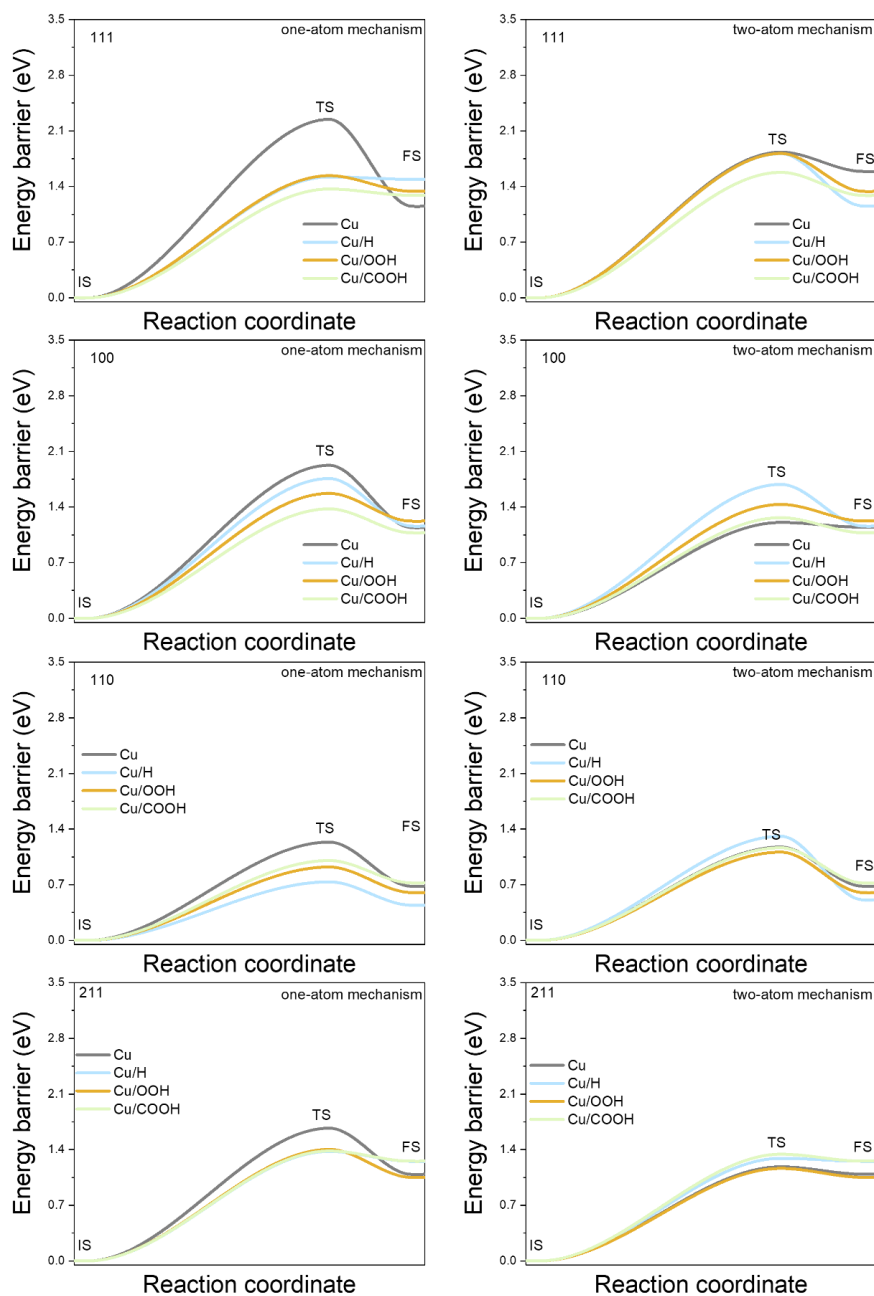


Figure B.1: Calculated kinetic barriers of two VF mechanisms on Cu(111), Cu(100), Cu(110), and Cu(211) surfaces. Reprinted with permission from ref. [132]. Copyright 2022, Royal Society of Chemistry.

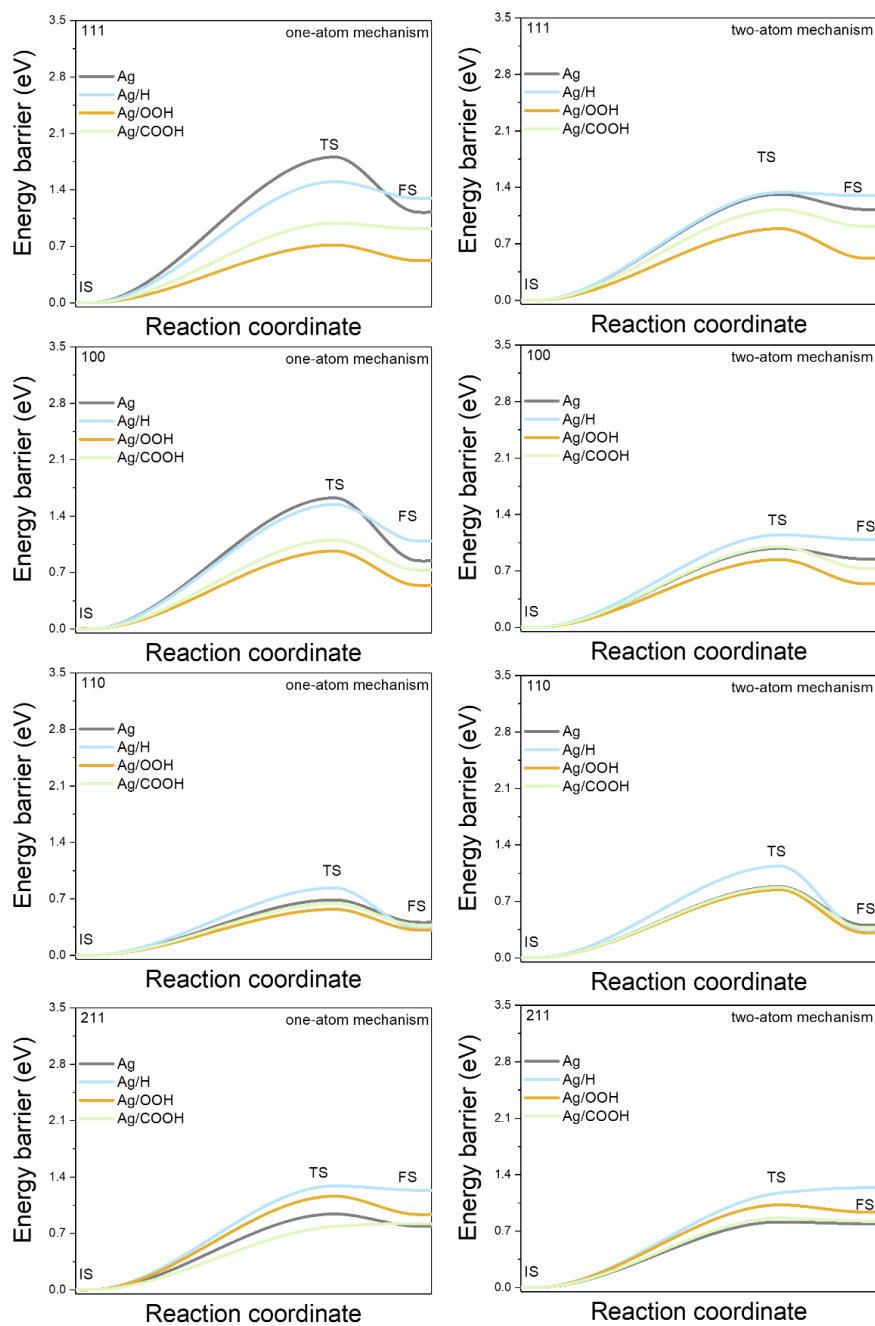


Figure B.2: Calculated kinetic barriers of two VF mechanisms on Ag(111), Ag(100), Ag(110), and Ag(211) surfaces. Reprinted with permission from ref. [132]. Copyright 2022, Royal Society of Chemistry.

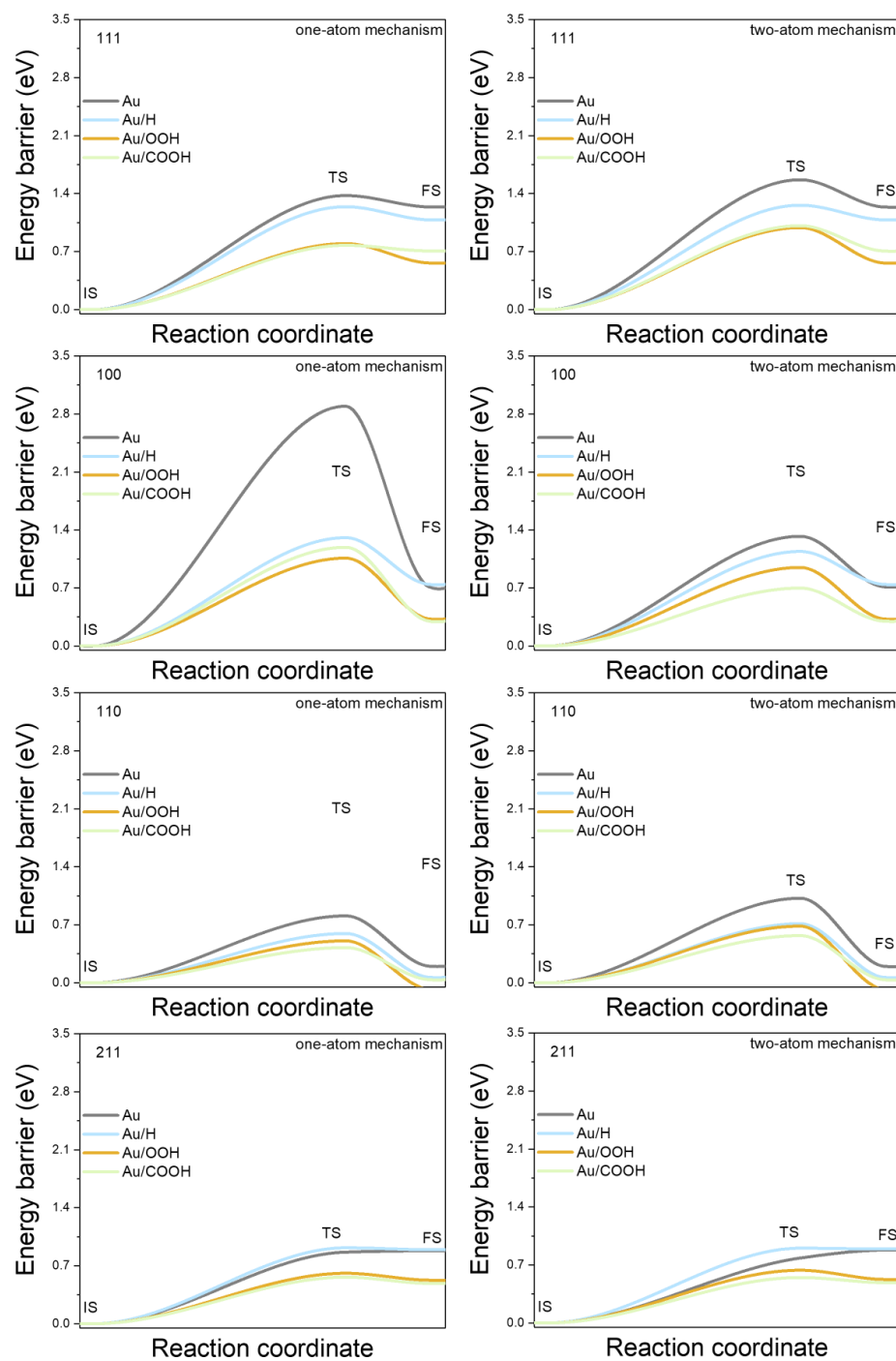


Figure B.3: Calculated kinetic barriers of two VF mechanisms on Au(111), Au(100), Au(110), and Au(211) surfaces. Reprinted with permission from ref. [132]. Copyright 2022, Royal Society of Chemistry.

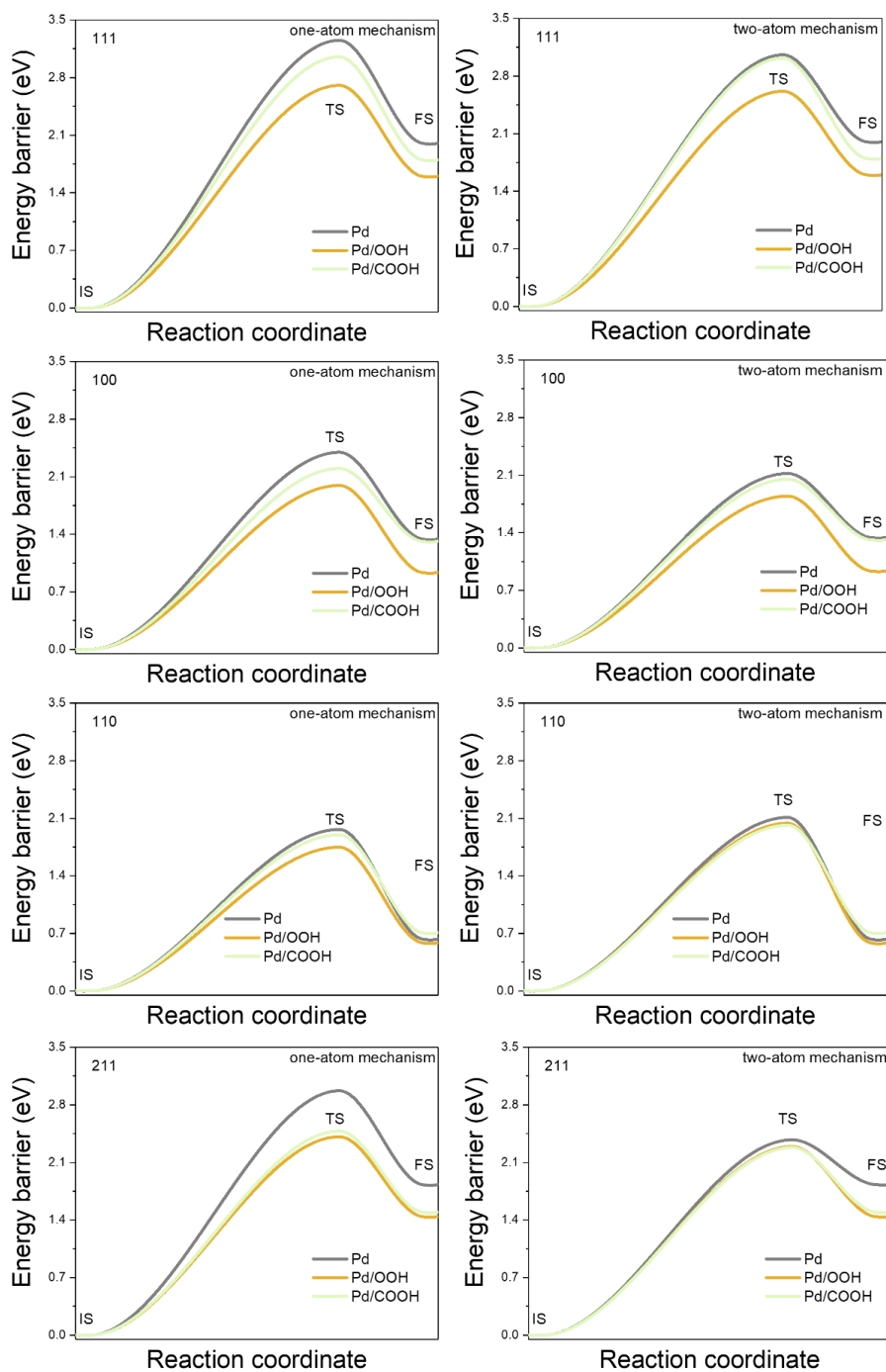


Figure B.4: Calculated kinetic barriers of two VF mechanisms on Pd(111), Pd(100), Pd(110), and Pd(211) surfaces. Reprinted with permission from ref. [132]. Copyright 2022, Royal Society of Chemistry.

Appendix C: Calculated MSD, RDF, and Lindemann index

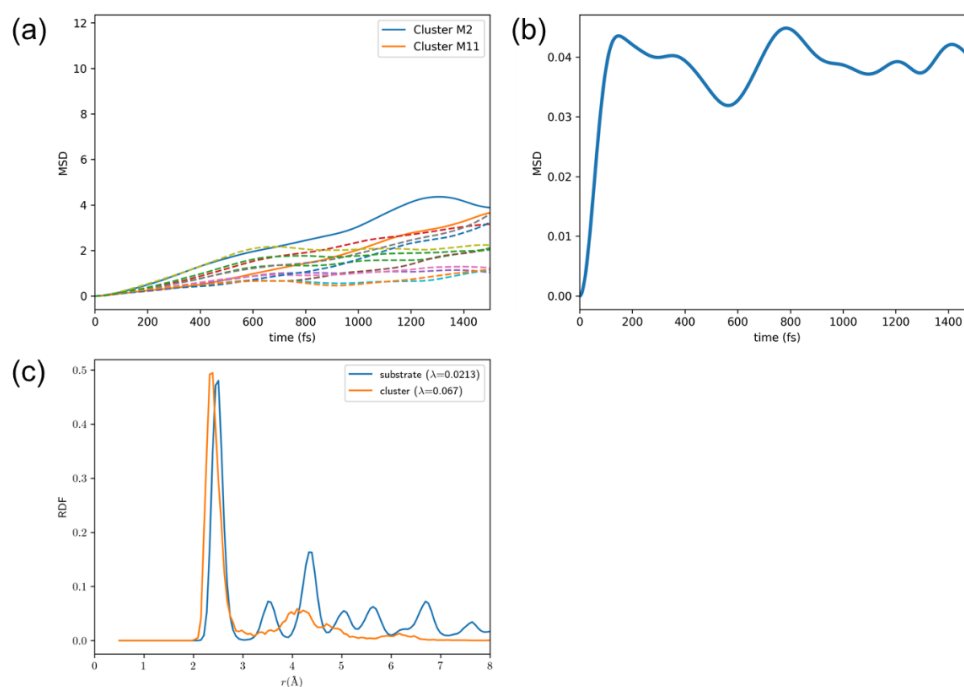


Figure C.1: Profiles of time-averaged mean-square displacement (TA-MSD) and radial distribution function (RDF) for Cu cluster supported on Cu(111) surface. (a) TA-MSDs for cluster Cu atoms. TA-MSD for the first 2 most mobile cluster atoms is shown in solid line, with the rest shown in dash line. (b) Averaged TA-MSD for all substrate metal atoms. (c) RDF and Lindemann index of the metal cluster and substrate. Reprinted with permission from ref. [132]. Copyright 2022, Royal Society of Chemistry.

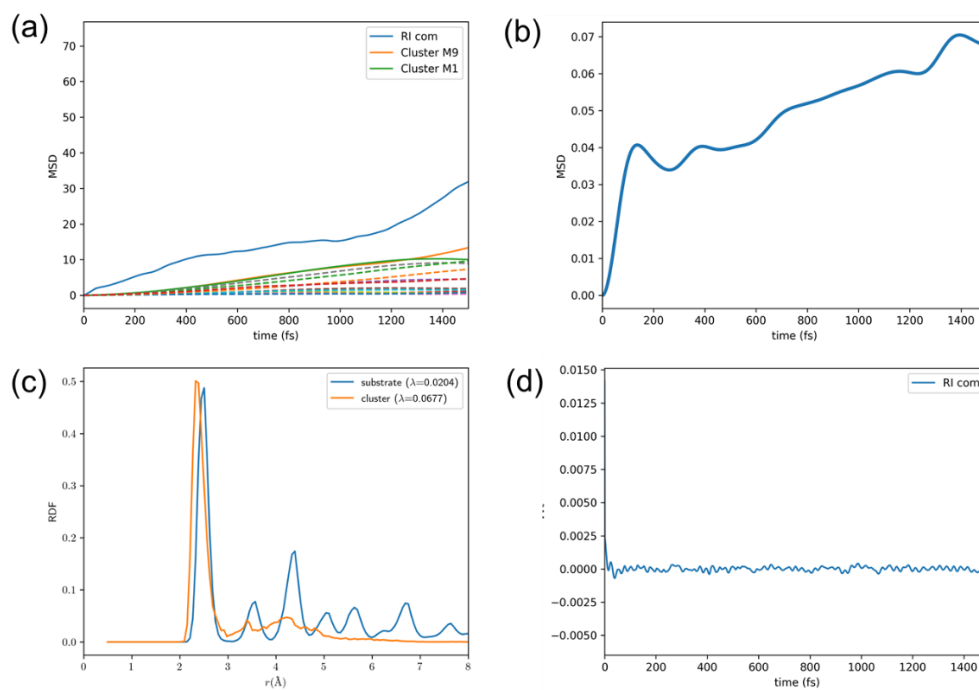


Figure C.2: Profiles of time-averaged mean-square displacement (TA-MSD), radial distribution function (RDF), and vvt for H-bound Cu cluster supported on Cu(111) surface. (a) TA-MSDs for cluster Cu atoms. TA-MSD for the first 2 most mobile cluster atoms is shown in solid line, with the rest shown in dashed line. (b) Averaged TA-MSD for all substrate metal atoms. (c) RDF and Lindemann index of the metal cluster and substrate, and the RDF of the reaction intermediate. (d) vvt for reaction intermediate of H. Reprinted with permission from ref. [132]. Copyright 2022, Royal Society of Chemistry.

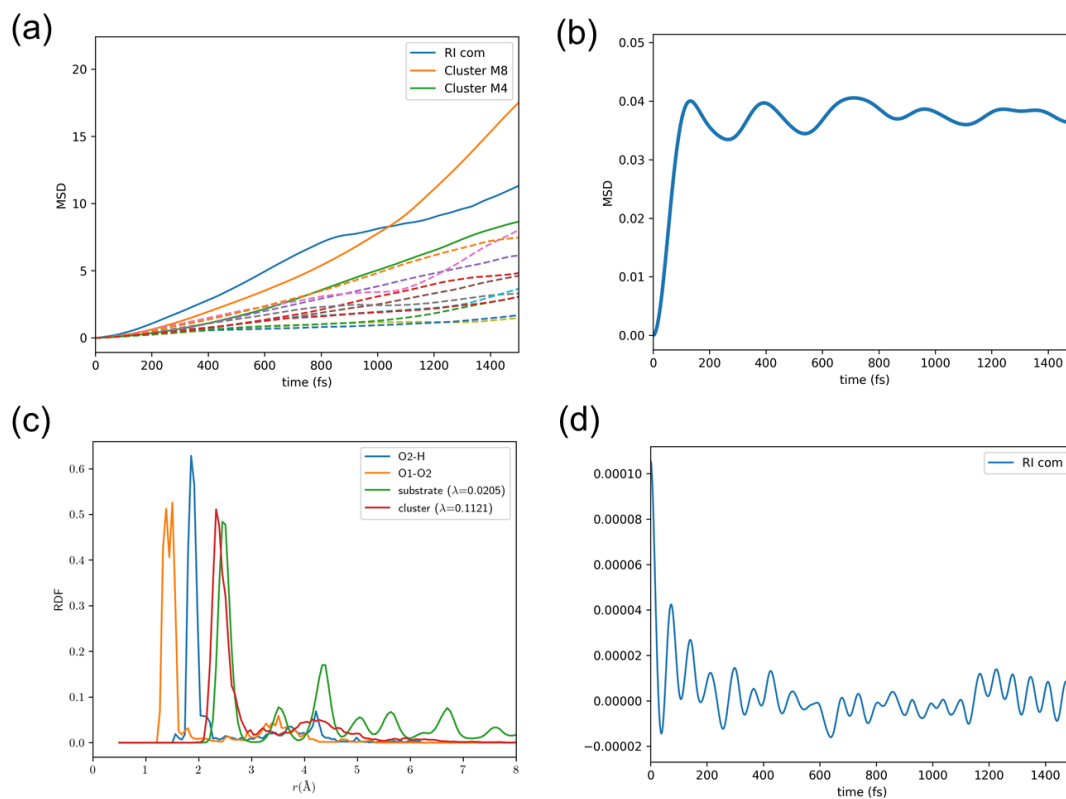


Figure C.3: Profiles of time-averaged mean-square displacement (TA-MSD), radial distribution function (RDF), and vvt for OOH-bound Cu cluster supported on Cu(111) surface. (a) TA-MSDs for cluster Cu atoms. TA-MSD for the first 2 most mobility cluster atoms is shown in solid line, with the rest shown in dash line. (b) Averaged TA-MSD for all substrate metal atoms. (c) RDF and Lindemann index of the metal cluster and substrate, and RDF of the reaction intermediate. (d) vvt for reaction intermediate of OOH. Reprinted with permission from ref. [132]. Copyright 2022, Royal Society of Chemistry.

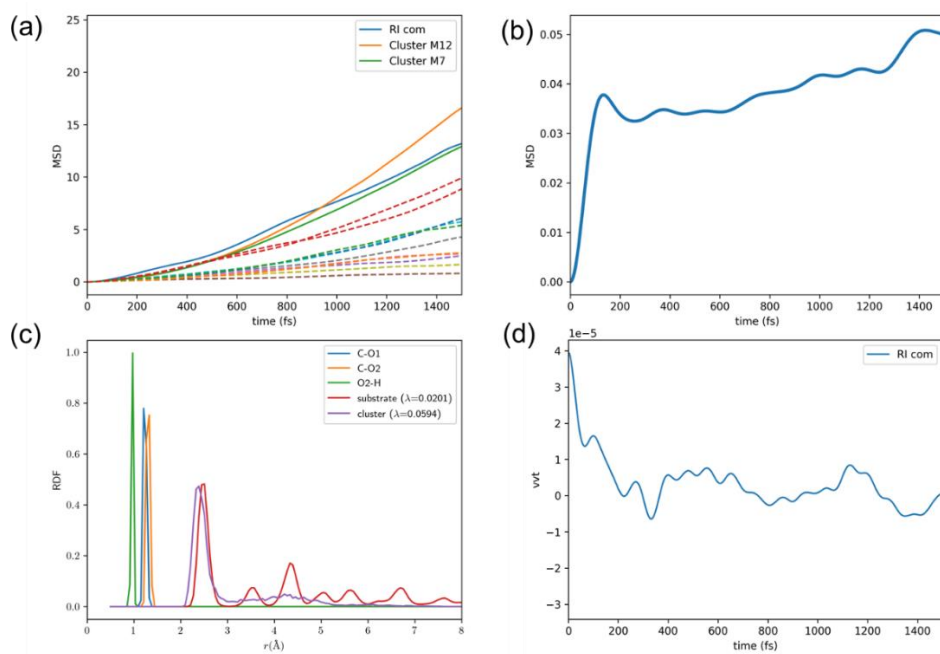


Figure C.4: Profiles of time-averaged mean-square displacement (TA-MSD), radial distribution function (RDF), and vvt for COOH-bound Cu cluster supported on Cu(111) surface. (a) TA-MSDs for cluster Cu atoms. TA-MSD for the first 2 most mobile cluster atoms is shown in solid line, with the rest shown in dash line. (b) Averaged TA-MSD for all substrate metal atoms. (c) RDF and Lindemann index of the metal cluster and substrate, and the RDF of the reaction intermediate. (d) vvt for reaction intermediate of COOH. Reprinted with permission from ref. [132]. Copyright 2022, Royal Society of Chemistry.

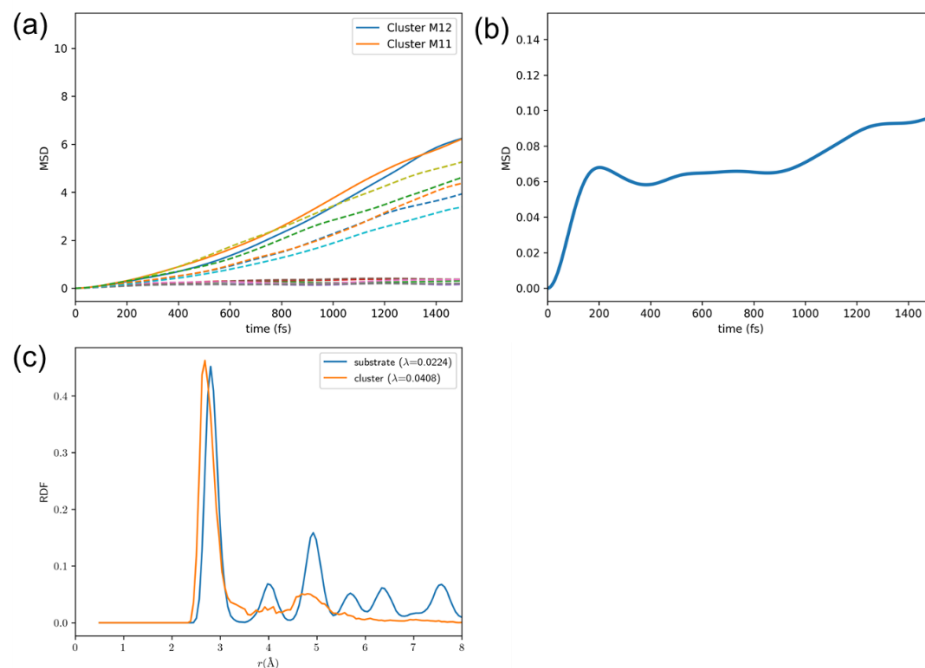


Figure C.5: Profiles of time-averaged mean-square displacement (TA-MSD) and radial distribution function (RDF) for Ag cluster supported on Ag(111) surface. (a) TA-MSDs for cluster Ag atoms. TA-MSD for the first 2 most mobile cluster atoms is shown in solid line, with the rest shown in dash line. (b) Averaged TA-MSD for all substrate metal atoms. (c) RDF and Lindemann index of the metal cluster and substrate. Reprinted with permission from ref. [132]. Copyright 2022, Royal Society of Chemistry.

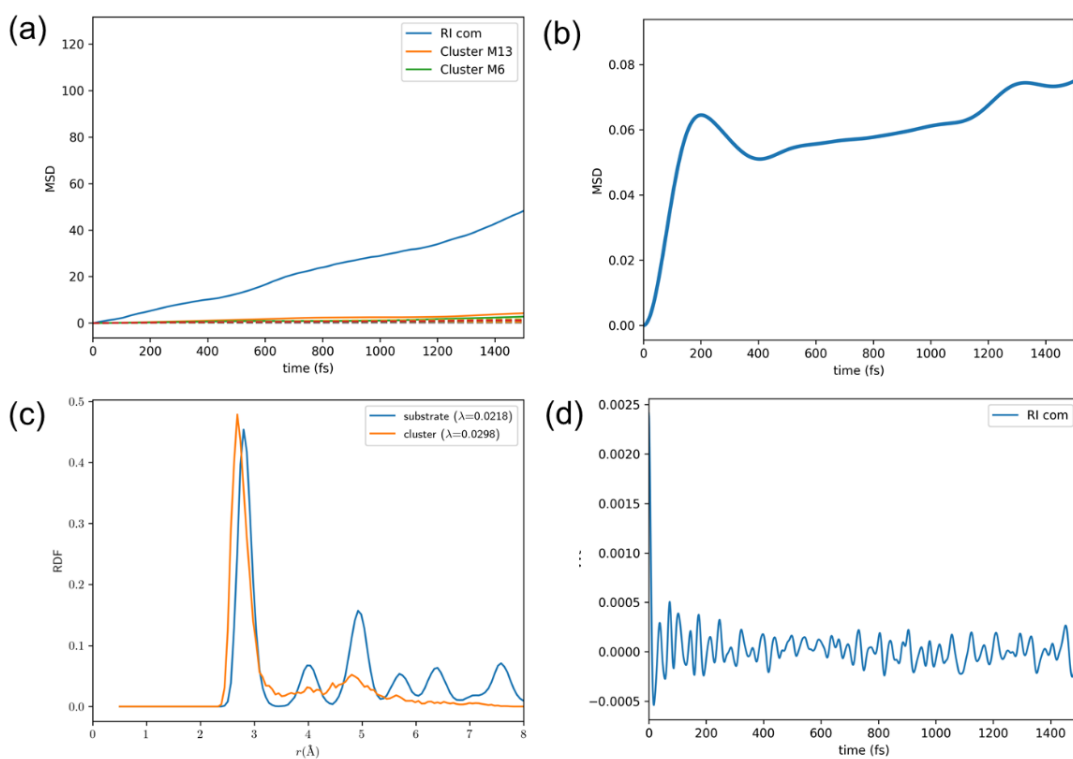


Figure C.6: Profiles of time-averaged mean-square displacement (TA-MSD), radial distribution function (RDF), and vvt for H-bound Ag cluster supported on Ag(111) surface. (a) TA-MSDs for cluster Ag atoms. TA-MSD for the first 2 most mobility cluster atoms is shown in solid line, with the rest shown in dash line. (b) Averaged TA-MSD for all substrate metal atoms. (c) RDF and Lindemann index of the metal cluster and substrate, and the RDF of the reaction intermediate. (d) vvt for reaction intermediate of H. Reprinted with permission from ref. [132]. Copyright 2022, Royal Society of Chemistry.

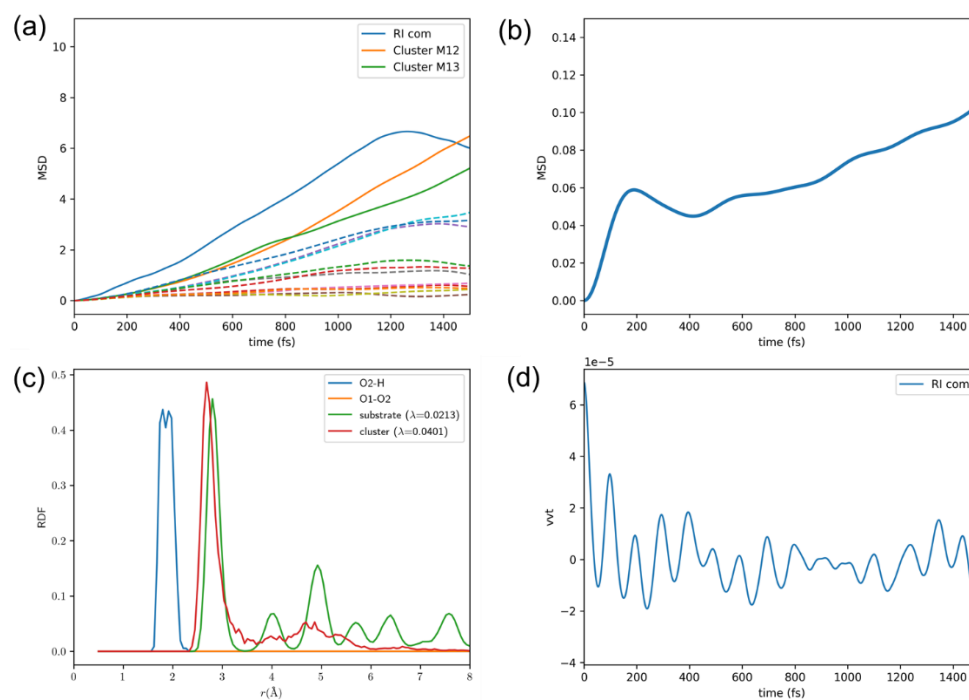


Figure C.7: Profiles of time-averaged mean-square displacement (TA-MSD), radial distribution function (RDF), and vvt for OOH-bound Ag cluster supported on Ag(111) surface. (a) TA-MSDs for cluster Ag atoms. TA-MSD for the first 2 most mobility cluster atoms is shown in solid line, with the rest shown in dash line. (b) Averaged TA-MSD for all substrate metal atoms. (c) RDF and Lindemann index of the metal cluster and substrate, and the RDF of the reaction intermediate. (d) vvt for reaction intermediate of OOH. Reprinted with permission from ref. [132]. Copyright 2022, Royal Society of Chemistry.

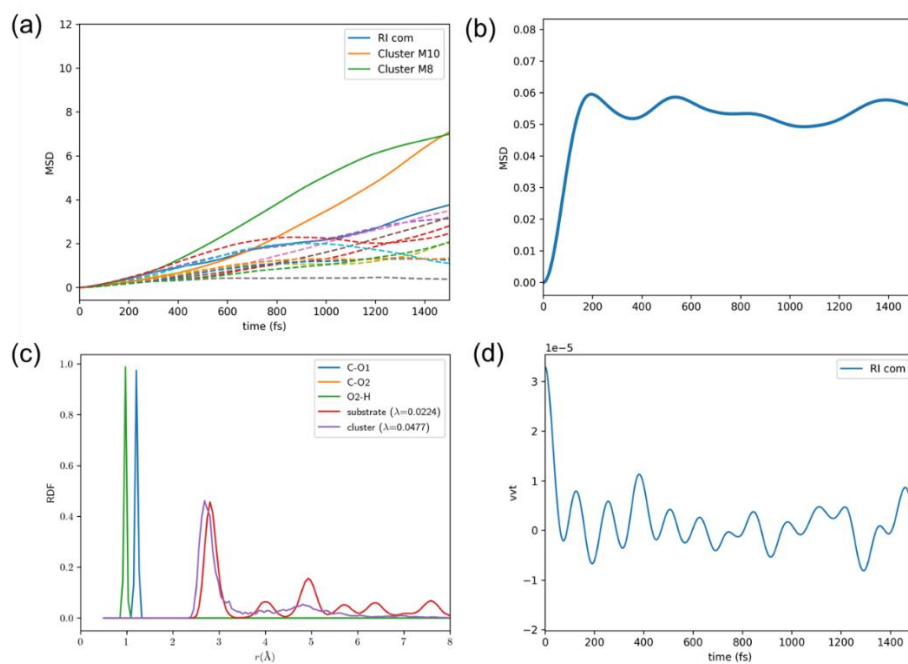


Figure C.8: Profiles of time-averaged mean-square displacement (TA-MSD), radial distribution function (RDF), and vvt for COOH-bound Ag cluster supported on Ag(111) surface. (a) TA-MSDs for cluster Ag atoms. TA-MSD for the first 2 most mobility cluster atoms is shown in solid line, with the rest shown in dash line. (b) Averaged TA-MSD for all substrate metal atoms. (c) RDF and Lindemann index of the metal cluster and substrate, and the RDF of the reaction intermediate. (d) vvt for reaction intermediate of OOH. Reprinted with permission from ref. [132]. Copyright 2022, Royal Society of Chemistry.

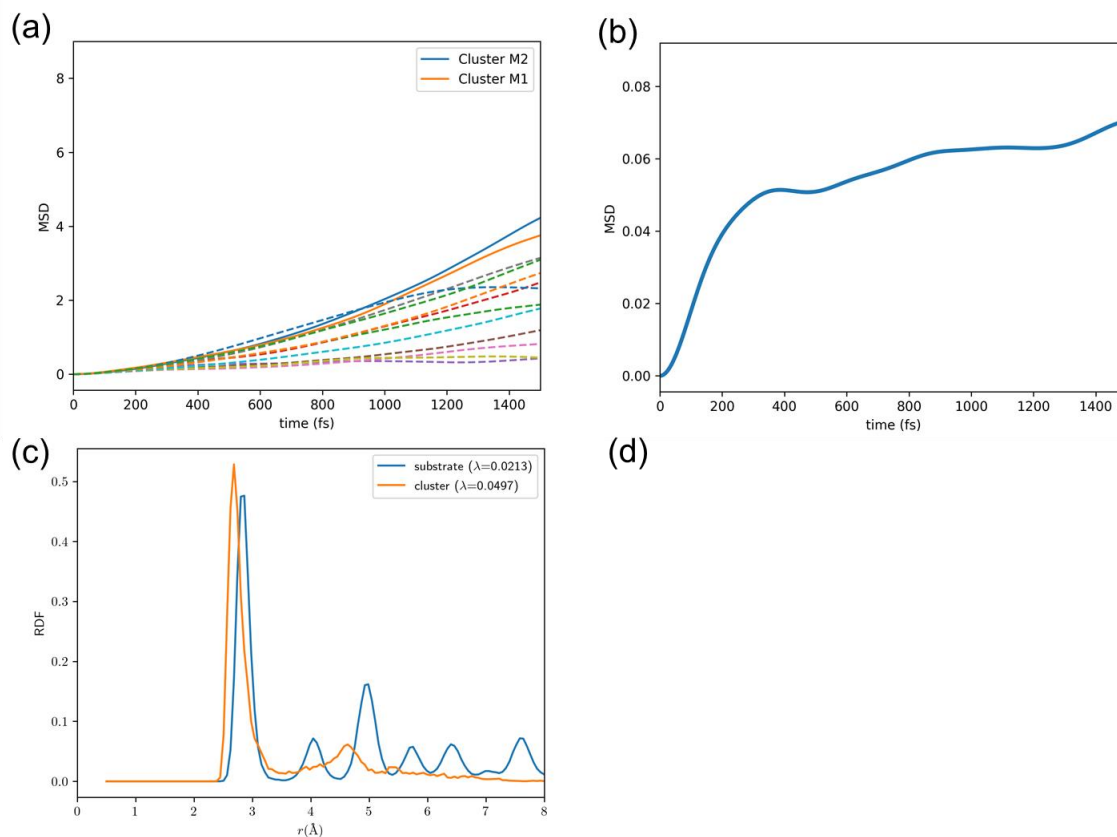


Figure C.9: Profiles of time-averaged mean-square displacement (TA-MSD) and radial distribution function (RDF) for Au cluster supported on Au(111) surface. (a) TA-MSDs for cluster Au atoms. TA-MSD for the first 2 most mobile cluster atoms is shown in solid line, with the rest shown in dash line. (b) Averaged TA-MSD for all substrate metal atoms. (c) RDF and Lindemann index of the metal cluster and substrate. Reprinted with permission from ref. [132]. Copyright 2022, Royal Society of Chemistry.

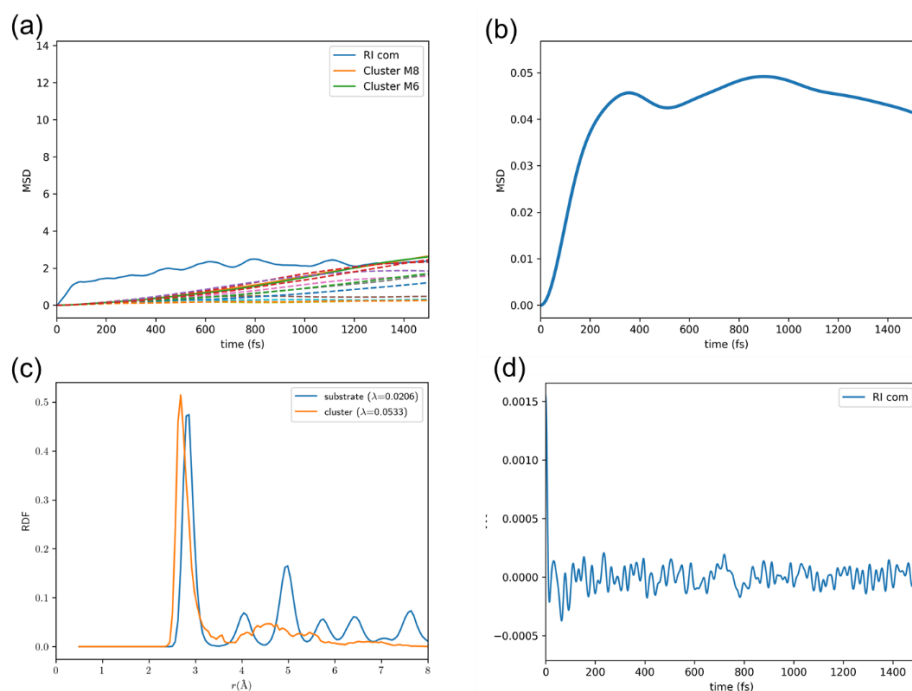


Figure C.10: Profiles of time-averaged mean-square displacement (TA-MSD), radial distribution function (RDF), and vvt for H-bound Au cluster supported on Au(111) surface. (a) TA-MSDs for cluster Au atoms. TA-MSD for the first 2 most mobile cluster atoms is shown in solid line, with the rest shown in dashed line. (b) Averaged TA-MSD for all substrate metal atoms. (c) RDF and Lindemann index of the metal cluster and substrate, and the RDF of the reaction intermediate. (d) vvt for reaction intermediate of H. Reprinted with permission from ref. [132]. Copyright 2022, Royal Society of Chemistry.

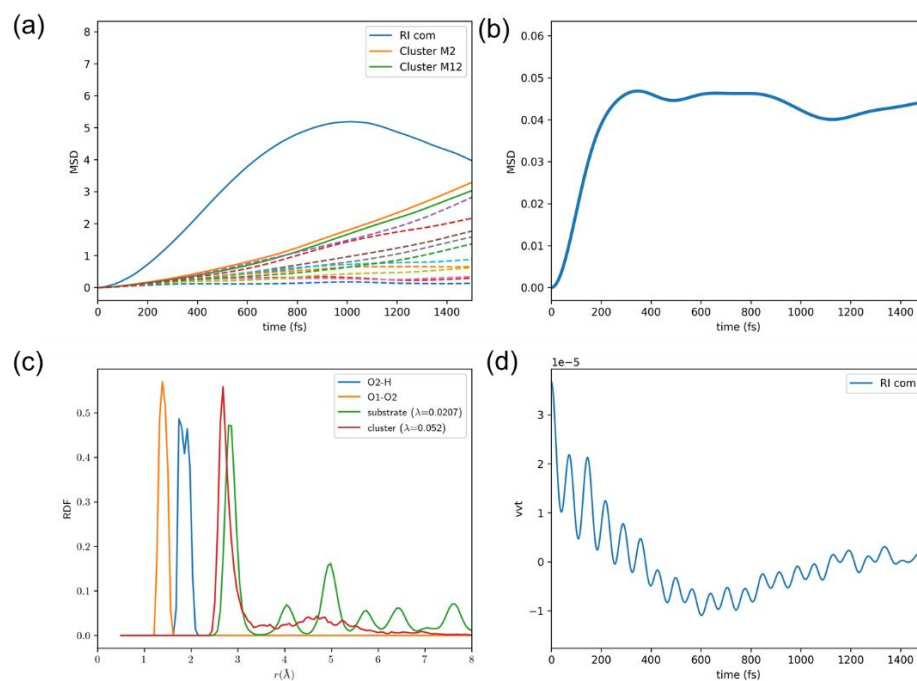


Figure C.11: Profiles of time-averaged mean-square displacement (TA-MSD), radial distribution function (RDF), and vvt for OOH-bound Au cluster supported on Au(111) surface. (a) TA-MSDs for cluster Au atoms. TA-MSD for the first 2 most mobility cluster atoms is shown in solid line, with the rest shown in dash line. (b) Averaged TA-MSD for all substrate metal atoms. (c) RDF and Lindemann index of the metal cluster and substrate, and the RDF of the reaction intermediate. (d) vvt for reaction intermediate of OOH. Reprinted with permission from ref. [132]. Copyright 2022, Royal Society of Chemistry.

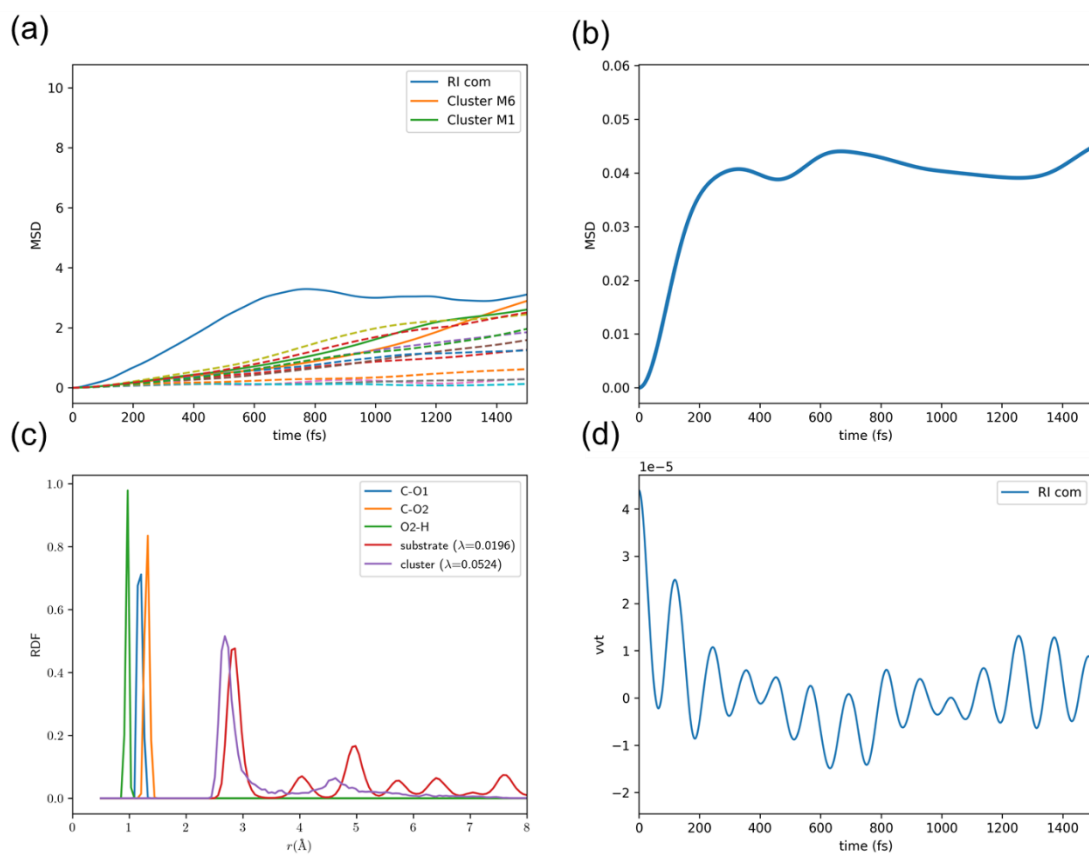


Figure C.12: Profiles of time-averaged mean-square displacement (TA-MSD), radial distribution function (RDF), and vvt for COOH-bound Au cluster supported on Au(111) surface. (a) TA-MSDs for cluster Au atoms. TA-MSD for the first 2 most mobility cluster atoms is shown in solid line, with the rest shown in dash line. (b) Averaged TA-MSD for all substrate metal atoms. (c) RDF and Lindemann index of the metal cluster and substrate, and the RDF of the reaction intermediate. (d) vvt for reaction intermediate of COOH. Reprinted with permission from ref. [132]. Copyright 2022, Royal Society of Chemistry.

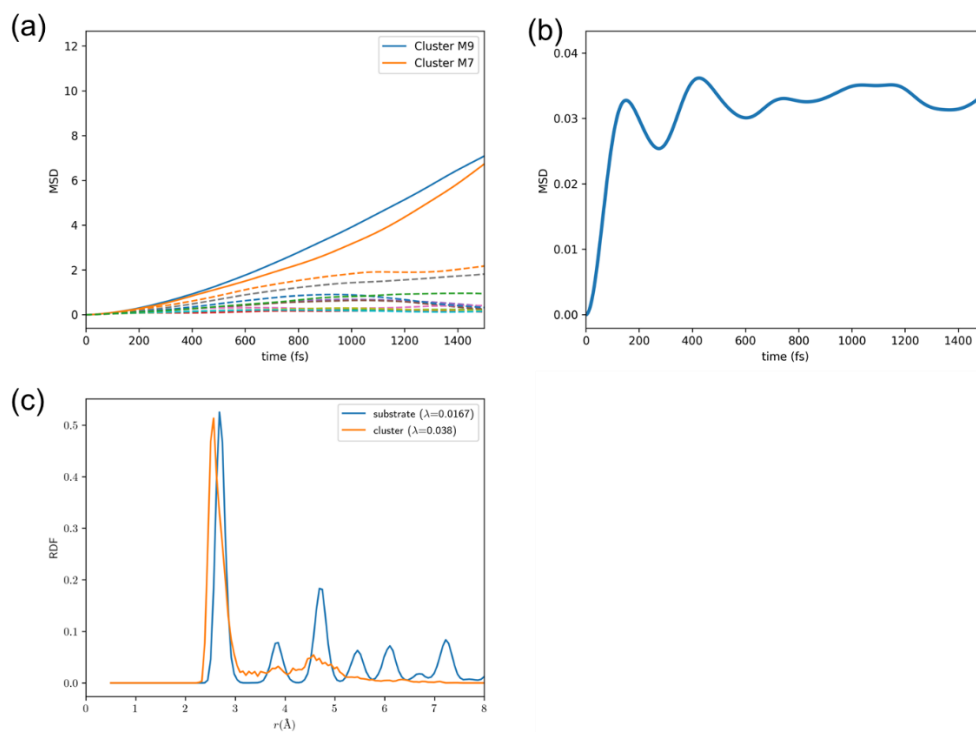


Figure C.13: Profiles of time-averaged mean-square displacement (TA-MSD) and radial distribution function (RDF) for Pd cluster supported on Pd(111) surface. (a) TA-MSDs for cluster Ag atoms. TA-MSD for the first 2 most mobile cluster atoms is shown in solid line, with the rest shown in dash line. (b) Averaged TA-MSD for all substrate metal atoms. (c) RDF and Lindemann index of the metal cluster and substrate. Reprinted with permission from ref. [132]. Copyright 2022, Royal Society of Chemistry.

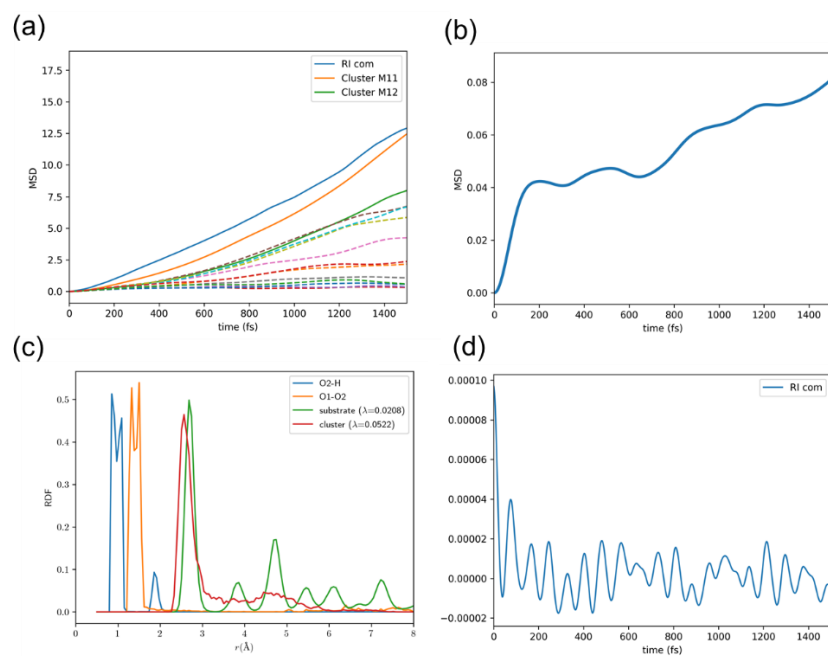


Figure C.14: Profiles of time-averaged mean-square displacement (TA-MSD), radial distribution function (RDF), and vvt for OOH-bound Pd cluster supported on Pd(111) surface. (a) TA-MSDs for cluster Au atoms. TA-MSD for the first 2 most mobile cluster atoms is shown in solid line, with the rest shown in dash line. (b) Averaged TA-MSD for all substrate metal atoms. (c) RDF and Lindemann index of the metal cluster and substrate, and the RDF of the reaction intermediate. (d) vvt for reaction intermediate of OOH. Reprinted with permission from ref. [132]. Copyright 2022, Royal Society of Chemistry.

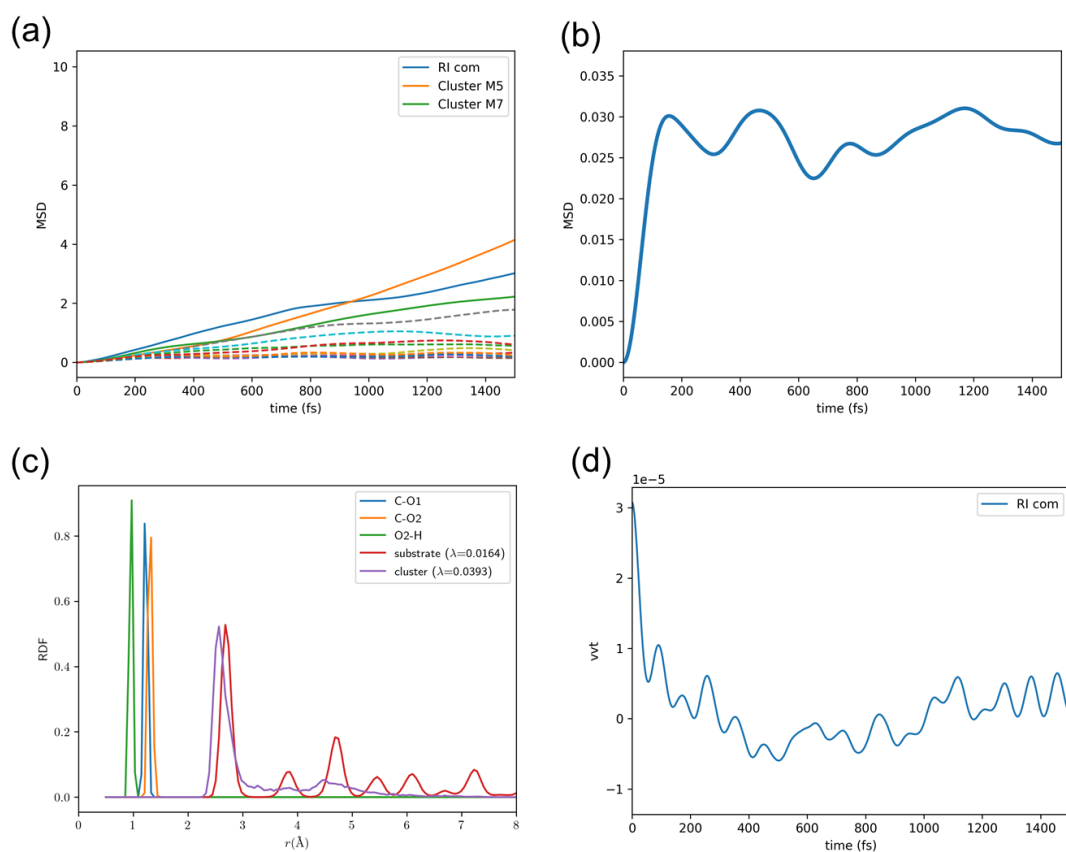


Figure C.15: Profiles of time-averaged mean-square displacement (TA-MSD), radial distribution function (RDF), and vvt for COOH-bound Pd cluster supported on Pd(111) surface. (a) TA-MSDs for cluster Au atoms. TA-MSD for the first 2 most mobile cluster atoms is shown in solid line, with the rest shown in dash line. (b) Averaged TA-MSD for all substrate metal atoms. (c) RDF and Lindemann index of the metal cluster and substrate, and the RDF of the reaction intermediate. (d) vvt for reaction intermediate of COOH. Reprinted with permission from ref. [132]. Copyright 2022, Royal Society of Chemistry.

Appendix D: Derivation of PB, PNP, MPB and GMPNP models

Derivation of the Poisson-Boltzmann (PB) equation

In the Poisson-Boltzmann model, the distribution of ionic species, $\rho(\mathbf{r})$, at equilibrium follows the Boltzmann distribution:

$$\rho(\mathbf{r}) = \sum_i \rho_i(\mathbf{r}) = \sum_i z_i F C_i^* e^{-\left(\frac{z_i F \phi(\mathbf{r})}{RT}\right)} \quad (D1)$$

Here z_i and C_i^* are the charge and the bulk concentration of the i^{th} ion species, $\phi(\mathbf{r})$ is the electric potential within the electrolyte, T is the temperature of the system, F is the Faraday constant, and R is the ideal gas constant. Note that z_i is positive for cations and negative for anions. The second ingredient of the model is the Poisson's equation:

$$\nabla \cdot (\varepsilon_0 \varepsilon_r \nabla \phi(\mathbf{r})) = -\rho(\mathbf{r}) \quad (D2)$$

In equation D2, ε_0 and ε_r are the vacuum permittivity and the relative permittivity of the media (in aqueous solutions, ε_r is the relative permittivity for water). Substitute equation D1 into D2, one obtains the Poisson-Boltzmann (PB) equation:

$$\nabla \cdot (\varepsilon_0 \varepsilon_r \nabla \phi(\mathbf{r})) = - \sum_i z_i F C_i^* e^{-\left(\frac{z_i F}{RT} \phi(\mathbf{r})\right)} \quad (D3a)$$

For symmetrical binary electrolyte ($z_+ = -z_- = z$, $C_{cation}^* = C_{anion}^* = C^*$), the PB equation can be further simplified to a hyperbolic form:

$$\nabla \cdot (\varepsilon_0 \varepsilon_r \nabla \phi(\mathbf{r})) = 2zFC^* \sinh\left(\frac{zF}{RT} \phi(\mathbf{r})\right) \quad (D3b)$$

Derivation of the Poisson-Nernst-Planck (PNP) equation (without magnetic force)

The principle of the PNP model is mass conservation. For any point in electrolyte within a time period, the concentration change of a species equals the difference between the species flow inside the point and that flow outside. In the context of electrolysis, only the diffusion and the electric migration are usually considered, resulting in the following differential equation:

$$\frac{\partial C_i(\mathbf{r})}{\partial t} = -\nabla \cdot \mathbf{J}_i(\mathbf{r}) = -\nabla \cdot \left(-D_i \nabla C_i(\mathbf{r}) - \frac{D_i z_i F C_i(\mathbf{r})}{RT} \nabla \phi(\mathbf{r}) \right) \quad (D4)$$

In equation D4, J_i , C_i , and D_i are the flux, the concentration, and the diffusion coefficient of the i^{th} species, while the definition of other variables follows those in the derivation of PB equation. In

this work, we are interested in an equilibrium state, in which the concentration of ionic species does not change with respect to time. This gives the PNP equation:

$$\frac{\partial C_i(\mathbf{r})}{\partial t} = \nabla \cdot \left(D_i \nabla C_i(\mathbf{r}) + \frac{D_i z_i F C_i(\mathbf{r})}{RT} \nabla \phi(\mathbf{r}) \right) = 0 \quad (\text{D4a})$$

The Lattice Gas Approximation^{103,104}

In both the PB and the PNP model, the ions are treated as point charge and thus can aggregate to form unphysically high ion concentration at high electrode voltage. To correct this, the size of the ions is introduced to the PB and the PNP model via the lattice gas approximation. In this approximation, the electrolyte is divided into small cubic cells of size a . Each cell is assumed to have only three possible contents: a cation, an anion, or solvent. To better validate this assumption, the parameter a is chosen close to the diameter of the ionic species. Given the logic of the lattice gas approximation, it is worth noting that despite the parameter a being usually referred to as the ‘diameter of the ionic species’, it is actually associated with the fineness of the three-state cell, and is chosen according to the size of the ions. In additionally, methods derived using the lattice gas approximation only applies to the electrolyte systems whose cations and anions are of similar size.

Using the lattice gas approximation, the internal energy, U , and the entropy, S , of an electrolyte system can be written as follows:

$$U = \int d\mathbf{r} \left(-\frac{\varepsilon}{2} |\nabla \psi|^2 + z_+ e C_+ \psi + z_- e C_- \psi - \mu_+ C_+ - \mu_- C_- \right) \quad (\text{D5})$$

In equation D5, the definition of z , C , and ψ follows those in the previous derivation. The chemical potential is denoted in μ . e is the elementary charge. The ε parameter is the product of ε_0 and ε_r for a given medium. The ‘+’ and the ‘-’ subscript denotes the property of cationic and anionic species, respectively.

The first term in equation D6 is the electric self-energy, while the following two terms arise from charge separation of ionic species under external electric potential. The last two are the chemical potential of ionic species.

The entropy of the system can be obtained from the Gibbs entropy:

$$-S = k_B \sum_{i=(+,-,w)} p_i \ln(p_i) \quad (\text{D6})$$

In equation D6, k_B is the Boltzmann’s constant, and p_i is the probability of the system in the i^{th} state. According to the lattice gas approximation, a cell has three states. The probability of the cell being

occupied by a cation, an anion, and water is denoted p_+ , p_- , and p_w . Obviously, p_+ and p_- can be calculated from the concentration of the ionic species, and p_w can be calculated from the fact that the three probabilities sum up to unity.

$$p_+ = C_+ a^3 \quad (D7a)$$

$$p_- = C_- a^3 \quad (D7b)$$

$$p_w = 1 - p_+ - p_- \quad (D7c)$$

The Gibbs entropy of the electrolyte system is:

$$\begin{aligned} S &= -k_B \sum_{cell} (p_+ \ln p_+ + p_- \ln p_- + p_w \ln p_w) \\ &= -\frac{k_B}{a^3} \int d\mathbf{r} [C_+ a^3 \ln(C_+ a^3) + C_- a^3 \ln(C_- a^3) \\ &\quad + (1 - C_+ a^3 - C_- a^3) \ln(1 - C_+ a^3 - C_- a^3)] \end{aligned} \quad (D8)$$

The Helmholtz free energy of the system is

$$F = U - TS \quad (D9)$$

For an equilibrium state, F should be minimized with respect to the change of the electric potential and the ion concentrations, thus

$$\frac{\partial F}{\partial \psi} = 0, \frac{\partial F}{\partial C_+} = 0, \frac{\partial F}{\partial C_-} = 0 \quad (D10)$$

Derivation of Modified Poisson-Boltzmann (MPB) Equation¹⁰⁴

In the following derivation, we evaluate the three equations in equation D10 to establish the MPB equation. For the simplicity of the mathematical derivation, we consider symmetric binary electrolyte of charge z ($z_+ = -z_- = z$), and bulk concentration C^* .

1) Evaluating $\partial F/\partial \psi=0$

Since C_+ , C_- , and ψ are three independent variables, S does not have dependence on ψ , thus $\partial S/\partial \psi=0$.

At low electric potential, $\partial \varepsilon/\partial \psi = 0$, too. Thus, the Helmholtz free energy becomes:

$$\frac{\partial F}{\partial \psi} = \frac{\partial U}{\partial \psi} = \int d\mathbf{r} \left[\left(-\frac{1}{2} (|\nabla \psi|^2 \frac{\partial \varepsilon}{\partial \psi} - 2\varepsilon \nabla^2 \psi) + zeC_+ - zeC_- \right) \right] = 0 \quad (D10a)$$

Assume low electric potential such that $\partial \varepsilon/\partial \psi=0$, we get the Poisson's Equation:

$$\varepsilon \nabla^2 \psi = -ze[C_+ - C_-] \quad (D10b)$$

2) Evaluating $\partial F/\partial C_+=0$ and $\partial F/\partial C_-=0$:

$$\frac{\partial F}{\partial C_+} = \frac{\partial U}{\partial C_+} - T \frac{\partial S}{\partial C_+} = \int dr \left(ze\psi - \mu_+ - C_+ \frac{\partial \mu_+}{\partial C_+} + k_B T \ln \frac{C_+ a^3}{1 - C_+ a^3 - C_- a^3} \right) = 0 \quad (\text{D10c})$$

Similarly:

$$\frac{\partial F}{\partial C_-} = \frac{\partial U}{\partial C_-} - T \frac{\partial S}{\partial C_-} = \int dr \left(-ze\psi - \mu_- - C_- \frac{\partial \mu_-}{\partial C_-} + k_B T \ln \frac{C_- a^3}{1 - C_+ a^3 - C_- a^3} \right) = 0 \quad (\text{D10d})$$

Furthermore, we assume μ_+ and μ_- are constants, which is $\partial \mu_{\pm}/\partial C_{\pm} = 0$. When there is no external electric potential ($\psi = 0$), the equilibrium state of the electrolyte can be described as $C_+ = C_- = C^*$. Meanwhile, the derivative of F with respect to C_+ and C_- are both 0. Substituting the condition into equation D10c and D10d, one get:

$$\left. \frac{\partial F}{\partial C_+} \right|_{C_+=C^*} = -\mu_+ + k_B T \ln \frac{C^* a^3}{1 - 2C^* a^3} = 0 \quad (\text{D10e})$$

$$\left. \frac{\partial F}{\partial C_-} \right|_{C_-=C^*} = -\mu_- + k_B T \ln \frac{C^* a^3}{1 - 2C^* a^3} = 0 \quad (\text{D10f})$$

Solve equation D10e and equation D10f, one gets

$$\mu_+ = \mu_- = k_B T \ln \frac{C^* a^3}{1 - 2C^* a^3} \quad (\text{D10g})$$

Substitute equation D10g back to equation D10c, one gets

$$ze\psi - k_B T \ln \frac{C^* a^3}{1 - 2C^* a^3} + k_B T \ln \frac{C_+ a^3}{1 - C_+ a^3 - C_- a^3} = 0 \quad (\text{D10h})$$

Rearrange equation D10h, one can eventually get

$$\begin{aligned} \frac{ze\psi}{k_B T} &= \ln \left(\frac{C^* a^3}{1 - 2C^* a^3} \frac{1 - C_+ a^3 - C_- a^3}{C_+ a^3} \right) \\ e^{-\frac{ze\psi}{k_B T}} &= \frac{C_+}{C^*} \frac{1 - 2C^* a^3}{1 - C_+ a^3 - C_- a^3} \\ C_+ &= C^* e^{-\frac{ze\psi}{k_B T}} \frac{1 - C_+ a^3 - C_- a^3}{1 - 2C^* a^3} \end{aligned} \quad (\text{D10i})$$

Similarly, one can obtain

$$C_- = C^* e^{\frac{ze\psi}{k_B T}} \frac{1 - C_+ a^3 - C_- a^3}{1 - 2C^* a^3} \quad (\text{D10j})$$

In principle, by aligning equation D10i and D10j, one can solve for C_+ and C_- . The mathematical procedure to obtain the solution is listed in Entry D of the Derivation Entries. The solution is:

$$C_+ = \frac{C^* e^{-\frac{ze\psi}{k_B T}}}{1 - 2C^* a^3 + C^* a^3 e^{-\frac{ze\psi}{k_B T}} + C^* a^3 e^{\frac{ze\psi}{k_B T}}} \quad (\text{D10k})$$

$$C_- = \frac{C^* e^{\frac{ze\psi}{k_B T}}}{1 - 2C^* a^3 + C^* a^3 e^{-\frac{ze\psi}{k_B T}} + C^* a^3 e^{\frac{ze\psi}{k_B T}}} \quad (\text{D10l})$$

Substitute equation D10k and D10l into equation D10b, we get the formula of the MPB model for symmetrical binary electrolyte of charge z and concentration C^* .

$$\begin{aligned} \varepsilon \nabla^2 \psi &= -ze[C_+ - C_-] \\ &= -ze \left[\frac{C^* e^{-\frac{ze\psi}{k_B T}} - C^* e^{\frac{ze\psi}{k_B T}}}{1 - 2C^* a^3 + C^* a^3 e^{-\frac{ze\psi}{k_B T}} + C^* a^3 e^{\frac{ze\psi}{k_B T}}} \right] \\ &= 2zeC^* \left[\frac{\sinh\left(\frac{ze\psi}{k_B T}\right)}{1 - 2C^* a^3 + 2C^* a^3 \cosh\left(\frac{ze\psi}{k_B T}\right)} \right] \end{aligned} \quad (\text{D10m})$$

Derivation of the Generalized Modified Poisson Nernst Planck (GMPNP) equation¹⁰³

We start from the chemical potential established in equation X10c and equation X10d with the assumption that the chemical potential are constants ($\partial\mu_{\pm}/\partial C_{\pm} = 0$). The expression for chemical potential is then:

$$\mu_{\pm} = \frac{\partial F}{\partial C_{\pm}} = \pm ze\psi + k_B T \ln\left(\frac{C_{\pm} a^3}{1 - C_+ a^3 - C_- a^3}\right) \quad (\text{D11})$$

The GMPNP model relies the following postulate for near equilibrium mass transport:

$$\frac{\partial C_{\pm}}{\partial t} = \nabla \cdot J_{\pm} = \nabla \cdot (b_{\pm} C_{\pm} \nabla \mu_{\pm}) = 0 \quad (\text{D12})$$

In equation D12, J_{\pm} and b_{\pm} is the flux and the mobility of the ionic species. Substituting equation D11 into equation D12:

$$\begin{aligned} J_{\pm} &= b_{\pm} c_{\pm} \nabla \left(\pm z e \psi + k_B T \ln \left(\frac{c_{\pm} a^3}{1 - c_+ a^3 - c_- a^3} \right) \right) \\ &= b_{\pm} c_{\pm} \left(\nabla (\pm z e \psi) + k_B T \nabla \left(\ln \left(\frac{c_{\pm} a^3}{1 - c_+ a^3 - c_- a^3} \right) \right) \right) \\ &= \frac{\pm z e D_{\pm} c_{\pm} \nabla \psi}{k_B T} + D_{\pm} c_{\pm} \nabla \ln \left(\frac{c_{\pm} a^3}{1 - c_+ a^3 - c_- a^3} \right) \\ &= \frac{\pm z e D_{\pm} c_{\pm} \nabla \psi}{k_B T} + D_{\pm} c_{\pm} \left(\frac{\nabla c_{\pm}}{c_{\pm}} + \frac{a^3 (\nabla c_+ + \nabla c_-)}{(1 - c_+ a^3 - c_- a^3)} \right) \\ &= \frac{\pm z e D_{\pm} c_{\pm} \nabla \psi}{k_B T} + D_{\pm} \nabla c_{\pm} + D_{\pm} c_{\pm} \left(\frac{a^3 (\nabla c_+ + \nabla c_-)}{(1 - c_+ a^3 - c_- a^3)} \right) \end{aligned} \quad (\text{D12a})$$

In equation D12a, $D_{\pm} = k_B T b_{\pm}$ is the diffusion coefficient of the ionic species. See Entry E of the Derivation Entries for more details on the derivation of equation D12a. For an equilibrium state, the total flux of the ionic species should be 0, which gives

$$\frac{\pm z e D_{\pm} c_{\pm} \nabla \psi}{k_B T} + D_{\pm} \nabla c_{\pm} + D_{\pm} c_{\pm} \left(\frac{a^3 (\nabla c_+ + \nabla c_-)}{(1 - c_+ a^3 - c_- a^3)} \right) = 0 \quad (\text{D12b})$$

Note that the Poisson equation is still valid

$$\varepsilon \nabla^2 \psi = -[z_+ e C_+ - z_- e C_-] \quad (\text{D13})$$

The GMPNP model is then established by solving the equation set composed of equation D12b and D13.